TRANSACTIONS
OF THE ASME
Series C

Journal of HEAT TRANSFER

November 1960

RADIATION • CONDUCTION • CONVECTION • COMPLEX SYSTEMS • PHASE CHANGES AND MIXTURES • TRANSIENT PHENOMENA • THERMOPHYSICAL PROPERTIES • EXPERIMENTAL TECHNIQUES • THERMOMETRY • ANALOG METHODS • ANALYTICAL AND NUMERICAL METHODS • APPLICATIONS • DESIGN TECHNIQUES • HEAT EXCHANGERS • INSULATION • ECONOMIC FACTORS BIOTECHNOLOGY • ASTRONAUTICS

Published Quarterly by
THE AMERICAN SOCIETY OF MECHANICAL ENGINEERS

TRANSACTIONS OF THE ASME
Series C

Journal of
HEAT TRANSFER
VOL. 82 • SERIES C • NO. 4
November 1960

EDITORIAL DEPARTMENT
Editor, J. J. JAKLITSCH, JR.
Consulting Editor, LEO BLODGETT
Production, JEAN NORTH
Production Asst., CARMEN L. CABRANES
Art Editor, HENRY BALFOUR

HEAT TRANSFER DIVISION
Chairman, H. A. JOHNSON
Secretary, S. OSTRACH
Papers Review, J. P. HARTNETT
Consulting Editor, S. P. KEZIOS

OFFICERS OF THE ASME
President, W. L. CISLER
Secretary, O. B. SCHIER, II
Treasurer, E. J. KATES
Assistant Treasurer, H. J. SAUER

PUBLICATIONS COMMITTEE
Chairman, S. G. A. SKROTZKI
HENDLEY N. BLACKMON
R. D. MINDLIN
MARTIN GOLAND
VITO L. SALERNO
Junior Representatives
A. S. GOLDSTEIN
J. W. FOLLANSBEE

REGIONAL ADVISORY BOARD
Region I, H. M. ROGERS, JR.
Region II, GLENN R. FRYLING
Region III, F. J. HEINZE
Region IV, FRANCIS C. SMITH
Region V, H. M. CATHER
Region VI, C. R. EARLE
Region VII, M. S. UMBENHAUER
Region VIII, CARL J. ECKHARDT

Published quarterly by The American Society of Mechanical Engineers. Publication office at 20th and Northampton Streets, Easton, Pa. The editorial department is located at the headquarters of the Society, 29 West Thirty-Ninth Street, New York 18, N. Y. Cable address, "Mechaneer," New York. Price $3.00 a copy, $10.00 annually; to members, $1.50 a copy, $5.00 annually. Add 50 cents for postage to all countries outside the United States and Canada. Changes of address must be received at Society headquarters seven weeks before they are to be effective on the mailing list. Please send old as well as new address. . . . By-Law: The Society shall not be responsible for statements or opinions advanced in papers or . . . printed in its publications (B13, Par. 4). . . . Second-class mail privileges authorized at Easton, Penna. . . . This publication is authorized to be mailed at the special rates of postage prescribed by Section 132.122 . . . © Copyrighted, 1960, by The American Society of Mechanical Engineers. Reprints from this publication may be made on condition that full credit be given the TRANSACTIONS OF THE ASME, Series C—Journal of Heat Transfer, and the author, and that date of publication be stated.

TRANSACTIONS OF THE ASME
is indexed by the Engineering Index, Inc.

CONTENTS

265 **A Variable Density Single-Fluid Model for Two-Phase Flow With Particular Reference to Steam-Water Flow** (59—HT-7)
S. G. Bankoff

273 **Transient Temperatures and Thermal Stresses in Hollow Cylinders Due to Heat Generation** (59—A-144)
John E. Schmidt and George Sonnemann

279 **Thermal-Contact Resistance in Finned Tubing** (59—A-135)
Karl A. Gardner and T. C. Carnavos

294 **Mass Transfer, Flow, and Heat Transfer About a Rotating Disk** (59—A-107)
E. M. Sparrow and J. L. Gregg

303 **Heat Transfer and Effectiveness for a Turbulent Boundary Layer With Tangential Fluid Injection** (59—A-177)
R. A. Seban

313 **Sublimation Mass Transfer Through Compressible Boundary Layers on a Flat Plate** (59—A-137)
T. K. Sherwood and Olev Träss

325 **Laminar Skin Friction and Heat Transfer on Flat Plates With Wedge-Shaped Grooves in Flow Direction** (59—A-143)
T. F. Irvine, Jr., and E. R. G. Eckert

333 **Heat Transfer to Liquid Metals With Variable Properties** (59—A-148)
R. Viskanta and Y. S. Touloukian

341 **A Summary of Experiments on Turbulent Heat Transfer From a Nonisothermal Flat Plate** (59—A-157)
W. C. Reynolds, W. M. Kays, and S. J. Kline

349 **An Experimental Study of the Effects of Nonuniform Wall Temperature on Heat Transfer in Laminar and Turbulent Axisymmetric Flow Along a Cylinder** (59—A-151)
R. Eichhorn, E. R. G. Eckert, and A. D. Anderson

360 **Geometric Factors for Radiative Heat Transfer Through an Absorbing Medium in Cartesian Co-ordinates** (59—A-206)
A. K. Oppenheim and J. T. Bevans

369 **Thermal Radiation From a Cylindrical Enclosure With Specified Wall Heat Flux** (59—A-159)
C. M. Usiskin and R. Siegel

375 **Application of Variational Methods to Radiation Heat-Transfer Calculations** (59—A-120)
E. M. Sparrow

381 **Certain Thermodynamic and Transport Properties of the Atmospheres of Venus, Mars, and Jupiter** (59—A-102)
W. E. Ibele and T. F. Irvine, Jr.

TECHNICAL BRIEFS

387 **Heat Transfer to Boiling Mercury**
F. E. Romie, S. W. Brovarney, and W. H. Giedt

389 **Temperature Distribution and Heat-Transfer Results for an Internally Cooled, Heat-Generating Solid**
E. M. Sparrow

392 **Effects of Initial Boundary-Layer Thickness on a Tangential Injection System**
R. A. Seban

393 **The Mechanism of Sound Field Effects on Heat Transfer**
J. P. Holman

396 **A Transducer for the Measurement of Heat-Flow Rate**
Robert Gardon

TRANSACTIONS OF THE ASME Series B

Journal of
ENGINEERING FOR INDUSTRY

Volume 82 • Series B • Number 4

CONTENTS FOR NOVEMBER, 1960

283 Tensile and Short-Time Creep Properties of N-155 Alloy Sheet, by E. C. Bernett. (59—A-27)
303 A Photoelastic Analysis of Machining Stresses, by E. Usui and H. Takeyama. (59—A-37)
309 Correlation of Bendability of Materials With Their Tensile Properties, by J. Datsko and C. T. Yang. (59—A-110)
315 Comparisons Between the Shearing Properties of Alpha-Brass as Derived From the Cutting Process and From Static and Impact Torsion Tests, by S. S. Chang and W. B. Heginbotham. (59—A-38)
324 The Role of Friction in Metal Cutting, by S. Kobayashi and E. G. Thomsen. (59—A-132)
333 A Critical Comparison of Metal-Cutting Theories With New Experimental Data, by S. Kobayashi, R. P. Herzog, D. M. Eggleston, and E. G. Thomsen. (59—A-131)
348 New Developments in the Theory of the Metal-Cutting Process, Part I, by P. Albrecht. (59—A-243)
359 Structural Weight Approximation for a Bell-Nozzle Divergent Section, by G. D. Brewer and E. Levin. (59—A-69)
363 Optimum Tolerances of Sheet Materials for Flight Vehicles, by G. A. Hoffman. (59—A-70)
369 Mechanical Vibration Filters With Nonlinear Characteristics, by W. J. Worley. (59—A-42)
377 Refinement of Finite Difference Calculations in Kinematic Analysis, by B. W. Shaffer and I. Krause. (59—A-53)
382 The Measurement of Very Low Frictional Torques in Rotating Equipment, by M. Zaid and I. S. Tolins. (59—A-43)
387 Design by Quantitative Factor of Safety, by Hsuan-Loh Su. (59—A-48)
393 Study of Critical Velocity of Stick-Slip Sliding, by B. R. Singh. (59—A-146)
399 Inertial Effects in a Multiple-Ball Transmission, by W. S. Rouverol. (59—A-14)
407 Some Applications of the Cycloid in Machine Design, by E. P. Pollitt. (59—A-134)
415 A Discussion of the Vibration Characteristics of a Simple Mechanical Connection, by Arthur Sorensen, Jr. (59—A-41)
423 Deformation and Moments in Elastically Restrained Circular Plates Under Arbitrary Load or Linear Thermal Gradient, by M. Zaid and M. Farray. (59—A-39)
439 Dimensionless Parameters for Helical Compression Springs, by R. J. Erisman. (59—A-30)
444 Errata on previously published paper by R. C. Brewer.

TRANSACTIONS OF THE ASME Series A

Journal of
ENGINEERING FOR POWER

Volume 82 • Series A • Number 4

CONTENTS FOR OCTOBER, 1960

247 Throat Tap Nozzles Used for Accurate Flow Measurements, by K. C. Cotton and J. C. Westcott. (59—A-174)
264 Water-Treatment, Corrosion, and Internal-Deposit Studies for Eddystone, by R. C. Ulmer, H. A. Grabowski, and R. C. Patterson. (59—A-147)
275 The Selection of Materials and Fabricating Techniques for the Eddystone Boiler and Sulzer Control Valves, by E. C. Chapman and R. E. Lorentz, Jr. (59—A-318)
286 Development Associated With the Superpressure Turbine for Eddystone Station Unit No. 1, by W. E. Trumpler, Jr., A. F. LeBreton, E. A. Fox, and R. B. Williamson. (59—A-288)
293 Material Selection and Fabrication, Main Steam Piping for Eddystone No. 1, 1200-F and 5000-Psi Service, by R. H. Caughey and W. G. Benz, Jr. (59—A-327)
315 Solar Turbo Power-Plant Design, by D. B. Mackay and E. L. Leventhal. (59—A-74)
325 Analysis of Solar-Furnace Performance in Mechanical Testing at Extremely High Temperatures, by G. S. Leon and M. E. Shank. (59—A-79)

TRANSACTIONS OF THE ASME Series D

Journal of
BASIC ENGINEERING

Vol. 82 • Series D • No. 3

CONTENTS FOR SEPTEMBER, 1960

505 Theoretical and Experimental Analysis of Hydrostatic Thrust Bearings, by R. C. Elwell and B. Sternlicht. (59—A-152)
513 Precise Measurement of Clothes Insulation During Controlled Operation of the Human, by A. S. Iberall. (59—A-197)
528 Radial Distributions of Temporal-Mean Peripheral Velocity and Pressure for Fully Developed Turbulent Flow in Curved Channels, by A. W. Marris. (59—A-51)
539 Flow Phenomena of Partially Enclosed Rotating Disks, by L. A. Maroti, G. Deak, and F. Kreith. (59—A-49)
553 Roughness Effects on Frictional Resistance of Enclosed Rotating Disks, by R. E. Nece and J. W. Daily. (59—A-55)
563 Rotating Wakes in Vaneless Diffusers, by R. C. Dean, Jr., and Y. Senoo. (59—A-104)
575 Incidence and Deviation-Angle Correlations for Compressor Cascades, by Seymour Lieblein. (59—A-171)
588 A Study of Boundary-Layer Characteristics of Turbomachine Blade Rows and Their Relation to Over-All Blade Loss, by W. L. Stewart, W. J. Whitney, and R. Y. Wong. (59—A-23)
593 Laminar Boundary Layers in Oscillatory Flow, by P. G. Hill and A. H. Stenning. (59—A-265)
609 Experimental Determination of Statistical Properties of Two-Phase Turbulent Motion, by S. L. Soo, H. K. Ihrig, Jr., and A. F. El Kouh. (59—A-59)
622 The Turbulent Boundary Layer at a Plane of Symmetry in a Three-Dimensional Flow, by J. P. Johnston. (59—A-72)
629 Heat-Transfer Characteristics of Hot-Film Sensing Element Used in Flow Measurement, by S. C. Ling. (59—A-172)
635 The Adiabatic Bulk Modulus of Normal Paraffin Hydrocarbons From Hexane to Hexadecane, by R. E. Rolling and C. J. Vogt. (59—A-169)
645 Variable Flow Resistance With Adjustable Multihole Orifice Plates in Series, by J. Sherman, F. A. Grochowski, and J. E. Sharbaugh. (59—A-182)
654 Cycle-Dependent Stress Relaxation of A-286 Alloy, by A. S. Ross and JoDean Morrow. (59—A-116)

Journal of
BASIC ENGINEERING
Vol. 82 • Series D • No. 3

CONTENTS FOR SEPTEMBER, 1960
(CONTINUED)

661 Low-Cycle Fatigue of Two Nickel-Base Alloys by Thermal-Stress Cycling, by F. J. Mehringer and R. P. Felgar. (59—A-58)
671 The Stability of Metals Under Cyclic Plastic Strain, by L. F. Coffin, Jr. (59—A-100)
683 Roll-Force and Torque Coefficients for Hot-Strip Steel Mill, by B. N. Garudachar and H. A. Peterson. (59—A-153)
689 Steady-State Creep of a Thick-Walled Cylinder Under Combined Axial Load and Internal Pressure, by Iain Finnie. (59—A-57)
695 Burst Strengths and Deformations of Welded Composite Turbine Wheels as Related to Weld Quality and Plasticity Calculations, by A. G. Holms and A. J. Repko. (59—A-28)
710 The Twin Throat Venturi: A New Fluid-Flow Measuring Device, by A. A. Kalinske. (59—A-154)
717 A Study of Viscosity Effect and Its Compensation on Turbine-Type Flowmeters, by W. F. Z. Lee and Henning Karlby. (59—A-105)
729 The Quadrant Edge Orifice—A Fluid Meter for Low Reynolds Numbers, by M. Bogema and P. L. Monkmeyer. (59—A-140)
735 Small-Diameter-Orifice Metering, by T. J. Fitzban and W. A. Griffin. (59—A-101)
741 Analysis of Axially Loaded Annular Shells With Applications to Welded Bellows, by M. Hetenyi and R. J. Timms. (59—A-175)
756 Cavitation Problems in Cryogenics, by R. B. Jacobs and K. B. Martin.

TRANSACTIONS OF THE ASME Series E

Journal of
APPLIED MECHANICS
Volume 82 • Series E • No. 3

CONTENTS FOR SEPTEMBER, 1960

381 On Three and Two-Dimensional Disturbances of Pipe Flow, Kurt Spielberg and Hans Timan. (60—APM-12)
390 On the Indeterminateness of the Boundary Conditions for the Mixing of Two Parallel Streams, K. T. Yen. (59—A-68)
393 Thermal Transfer in Turbulent Gas Streams. Effect of Turbulence on Local Transport From Spheres, W. W. Short, R. A. S. Brown, and B. H. Sage. (60—APM-30)
403 Hydrodynamic Entrance Lengths for Incompressible Laminar Flow in Rectangular Ducts, L. S. Han. (59—A-82)
410 Stability of a Turbine-Generator Rotor Including the Effects of Certain Types of Steam and Bearing Excitations, A. H. Landzberg. (60—APM-9)
417 On Saint Venant's Principle: Elastic Shells and Plates, P. M. Naghdi. (60—APM-11)
423 On the Airy Stress Functions of Plane Dislocation Problems, F. D. Ju. (60—APM-14)
429 The Effect of Pressure on the Bending Characteristics of an Actuator System, Paul Seide. (60—APM-16)
438 The Contact Problem for Viscoelastic Bodies, E. H. Lee and J. R. M. Radok. (59—A-83)
445 Stresses in Curved Beams of Noncircular Center Line, M. M. Abbassi. (60—APM-21)
455 Shear Buckling of Bars, G. Herrmann and A. E. Armenakas. (59—A-91)
458 Buckling of Circular Cones Under Axial Compression, Leslie Lackman and Joseph Penzien. (60—APM-17)
461 The Additional Deflection of a Cantilever Due to the Elasticity of the Support, W. J. O'Donnell. (60—APMW-3)
465 Thermoelastic Stresses in Beams, E. S. Barrekette. (60—APM-28)
474 Elastic Instability of Rectangular Sandwich Panel of Orthotropic Core With Different Face Thicknesses and Materials, C. C. Chang and I. K. Ebcioglu. (60—APM-26)
481 Transient and Residual Thermal Stresses in an Elastic-Plastic Cylinder, H. G. Landau and E. E. Zwicky, Jr. (60—APM-4)
489 On Strain-Hardened Circular Cylindrical Shells, Nicholas Perrone and P. G. Hodge, Jr. (60—APM-20)
496 The Elastoplastic Thick-Walled Sphere Subjected to a Radial Temperature Gradient, G. R. Cowper. (60—APM-22)
501 Rupture Instability of Plane Membranes and Solids, S. F. Borg. (60—APM-1)
505 Expansion of Thick-Walled Cylinders Fabricated From Cold Bent Plates, Irwin Berman. (60—APMW-2)
513 Dispersion of Flexural Waves in an Elastic, Circular Cylinder, Yih-Hsing Pao and R. D. Mindlin. (59—A-84)
521 Modeling of Large Transient Elastic and Plastic Deformations of Structures Subjected to Blast Loading, W. E. Baker. (60—APM-18)
528 Shock Spectra of a Nonlinear System, W. T. Thomson. (60—APM-23)
535 Forced Flexural Vibrations of Sandwich Plates in Plane Strain, Yi-Yuan Yu.
541 Extensional Vibrations and Waves in a Circular Disk and a Semi-Infinite Plate, D. C. Gazis and R. D. Mindlin. (60—APM-3)
548 Effect of Small Hub-Radius Change on Bending Frequencies of a Rotating Beam, Hsu Lo, J. E. Goldberg, and J. L. Bogdanoff. (60—APMW-5)
551 Forced Lateral Vibration of a Uniform Cantilever Beam With Internal and External Damping, Ho Chong Lee. (60—APM-15)
557 A Method for Investigating Certain Eigenvalue Problems of the Buckling and Vibration of Plates, H. D. Conway and A. W. Leissa. (60—APM-25)
559 Dynamical Response of an Elastic Half-Space to Tangential Surface Loadings, Chi-Chang Chao. (60—APM-29)
568 On a Special Class of Self-Sustained Oscillations, K. Klotter and E. Kreyszig.
575 Random Excitation of a Loaded Nonlinear String, T. K. Caughey. (60—APMW-1)
579 On the Use of Nonsinusoidal Approximating Functions for Nonlinear Oscillation Problems, K. Klotter and P. R. Cobb.

S. G. BANKOFF
Department of Chemical Engineering,
Northwestern University,
Evanston, Ill.
Mem. ASME

A Variable Density Single-Fluid Model for Two-Phase Flow With Particular Reference to Steam-Water Flow

Turbulent cocurrent flow of a liquid and a gaseous phase through a pipe or channel is characterized by several regimes. If the volumetric rate of flow of the gas is much greater than that of the liquid, the gas will flow as a continuous phase. The liquid in this case will be either a continuous or a dispersed phase, depending upon the mass velocities, the pipe diameter, and the orientation of the flow axis. In horizontal flow at relatively low mass velocities, the liquid flows along the bottom of the pipe (stratified flow). As the mass velocities are increased, keeping the ratio of the volumetric flow rates constant, the interface becomes quite wavy; and eventually a portion of the liquid is entrained as droplets in the gas. If the gas mass velocity only is increased, the liquid tends to spread out into an annular film over the walls of the pipe (annular flow). On the other hand, if both mass velocities are increased, so that the liquid and gas are flowing at comparable volumetric flow rates, the gas phase becomes discontinuous, resulting in a coarse suspension of bubbles in the liquid. The bubbles are not uniformly distributed except near the critical pressure, where the densities of the phases are nearly equal, or at very high Reynolds numbers, where the turbulent stresses are very much larger than the buoyant forces. This mode of flow ("bubble flow") is especially observed in vertical pipes at void fractions less than approximately 0.8. The bubbles are, in general, not uniformly distributed across the pipe cross section except when the difference in the densities of the phases is small, or when the turbulent intensity is large. In vertical flow the vapor tends to concentrate near the pipe axis. The diffusion of vapor toward the center of the pipe is due to the lift force resulting from the unequal flow of the viscous liquid around any individual bubble in the presence of the pipe wall. As the vapor content increases the bubbles tend to coalesce near the center of the pipe; at still higher concentrations of vapor the flow eventually changes to either "slug" flow (alternate slugs of liquid and vapor completely filling the pipe cross section) or annular flow, depending upon the Froude and Weber numbers. For small pipes and velocities where the surface tension forces are comparable to the inertial forces, the slug flow regime is stable. At larger pipe diameters or gas velocities annular flow results.

Because of the severe requirements for their existence, annular flow (completely separated) and homogeneous flow (completely mixed) may be considered to be special cases of bubble flow (partially mixed). Bubble flow is present in conventional and nuclear boilers with vertical channels, and in many other systems of engineering interest. This regime is, however, quite difficult to analyze; and until recently attempts to calculate frictional pressure drops and slip velocities have been based upon consideration of one or the other limiting case. In the homogeneous flow model the two-phase mixture is considered to be a single fluid, so that the mean velocities of the two phases are exactly equal, which is rarely the case. A number of variations of the completely separated flow model have been presented. Levy [1][1] has given a complete analysis of the annular-flow model with various combinations of turbulent and laminar flow of the liquid and gas. For turbulent flow a seventh-power distribution law was assumed. The interface between the liquid and gas was considered to be smooth. The slip velocities predicted by this analysis were higher than experiment, however, except for improbable combinations, such as a turbulent liquid annulus and a laminar gaseous core. The results can be considerably improved by empirical modifications of the friction factor and hydraulic radii of the hypothetical flow conduits for liquid and gas. Two of

Contributed by the Heat Transfer Division of The American Society of Mechanical Engineers and presented at the ASME-AIChE Heat Transfer Conference, Storrs, Conn., August 9–12, 1959. Manuscript received at ASME Headquarters, May 13, 1959. Paper No. 59—HT-7.

[1] Numbers in brackets designate References at end of paper.

Nomenclature

a = bubble radius; also cylinder radius, Equation (35), ft
A = constant defined by Equation (43)
C_1 = constant defined by Equation (48)
C_2 = constant defined by Equation (49)
c = local bubble concentration, Equation (37), no. of bubbles/cu ft
D_b = bubble diffusivity, Equation (38), sq ft/hr
G = total mass velocity, lb/(sq ft)(hr)
g = acceleration due to gravity, ft/hr^2
J = bubble flux in direction normal to wall, bubbles/(sq ft)(hr)
K = dimensionless parameter, Equation (9), for tube flow
K' = dimensionless parameter, Equation (33), for flow between flat plates
m = dimensionless exponent, Equation (1)
N_b = Bond and Newton number
n = dimensionless exponent, Equation (2)
P = pressure, lb force/sq in absolute
R = tube radius or channel half-width, ft
s = y/R, dimensionless distance from wall
u = velocity of two-phase mixture at distance y from wall, ft/hr
u^* = u/u_m, dimensionless mixture velocity
$\bar{u}_G$ = mean velocity of vapor, ft/hr
$\bar{u}_L$ = mean velocity of liquid, ft/hr
u_L = liquid velocity in x-direction, ft/hr
u_m = velocity of two-phase mixture at tube centerline, ft/hr
v_b = transverse bubble velocity, ft/hr

(Continued on next page)

the more successful of these empirical correlations are those of Martinelli and Nelson [2] and Armand [3].[1]

Nevertheless, these models at opposite ends of the mixing spectrum do not provide an adequate physical picture of the bubble flow regime, which encompasses most cases of practical interest. In the model proposed herein it is conceived that the mixture flows as a suspension of bubbles in the liquid, where radial gradients exist in the concentration of bubbles. The bubble concentration is maximum at the center of the pipe, decreases monotonically in a radial direction, and vanishes at the pipe wall. An important concept which is introduced is that the gas and liquid have the same velocity at any radial position, the relative velocity of the bubbles with respect to the surrounding liquid being considered to be negligible compared to the stream velocity. The average velocity of the gaseous phase is greater than that of the liquid phase only because the gas is concentrated in the regions of higher velocity. Because the slippage at any point is considered to be negligible the mixture may be considered to be a single fluid whose density is a function of radial position.

The exact form of the radial distribution function for voids cannot be determined without more information on turbulent diffusivities of bubbles and of momentum in these mixtures. Since buoyancy, inertial, and surface tension forces all play a part, it is to be expected that the Froude, Reynolds, and Weber numbers will determine this function. The pressure, volumetric flow rates of the two phases, and the physical properties of the two phases will therefore enter into this function. Some insight into the relevant parameters may be obtained by a simplified analysis of the forces on a two-dimensional bubble as given in the Appendix.

Statement of Model

Consider the flow of a suspension of bubbles in a liquid through a circular pipe under steady-state conditions. A power law distribution is assumed for both the velocity and the void fraction:

$$u^* = s^{\frac{1}{m}} \tag{1}$$

$$\alpha^* = s^{\frac{1}{n}} \tag{2}$$

where $u^* = u/u_m$; $\alpha^* = \alpha/\alpha_m$; $s = y/R$; and m and n are positive constants.

The liquid and gas mass-flow rates are given by

$$W_L = 2\pi R^2 \rho_L u_m \int_0^1 (1 - s)(1 - \alpha_m \alpha^*) u^* ds \tag{3}$$

$$W_G = 2\pi R^2 \rho_G u_m \int_0^1 (1 - s)\alpha_m \alpha^* u^* ds \tag{4}$$

The qunlity, or mass fraction of gaseous phase, is

$$X = \frac{W_G}{W_L + W_G} \tag{5}$$

Finally, the average void fraction $\bar{\alpha}$ across the cross section is given by

$$\bar{\alpha} = 2\alpha_m \int_0^1 \alpha^*(1 - s) ds \tag{6}$$

Upon substituting Equations (1) and (2) into Equations (3) to (6), one obtains

$$\frac{\bar{\alpha}}{\alpha_m} = \frac{2n^2}{(n + 1)(2n + 1)} \tag{7}$$

$$\frac{1}{X} = 1 - \frac{1}{\beta}\left(1 - \frac{K}{\bar{\alpha}}\right) \tag{8}$$

where $\beta = \rho_G/\rho_L$, and the flow parameter K is

$$K = \frac{2(m + n + mn)(m + n + 2mn)}{(n + 1)(2n + 1)(m + 1)(2m + 1)} \tag{9}$$

The symmetry of Equation (9) in m and n is noteworthy. From Fig. 1 it is seen that the range of variation of K is about 0.6 — 1.0; for nearly all reasonable velocity and void-fraction profiles, the range of variation is considerably less.

From a material balance and Equation (9) a particularly simple expression is obtained for the slip velocity ratio, Φ

$$\Phi \equiv \frac{u_G}{u_L} = \frac{1 - \bar{\alpha}}{K - \bar{\alpha}} \tag{10}$$

It is easily shown [4] from Equation (8) or (10) that

$$K = \bar{\alpha}/\frac{V_G}{V_T} \equiv C \tag{11}$$

where V_G/V_T is the ratio of the gas volumetric flow rate to the total volumetric flow rate, and C is the Armand flow parameter [3].

Wall Shear Stress

The gas-liquid mixture has been considered to be so intimate that at any point the two phases have the same velocity and can be considered to flow as a single fluid whose physical properties are, however, dependent upon the radial position. In general, the

[1] The writer is indebted to Dr. Novak Zuber for calling his attention to the Armand data and to the equivalence of the Armand flow parameter C and the flow parameter K derived in this work.

Nomenclature

V = bubble rise velocity through surrounding liquid, ft/hr
W_G = weight rate of steam flow, lb/hr
W_L = weight rate of liquid flow, lb/hr
W_T = weight rate of flow, total, lb/hr
X = quality, lb steam/lb fluid flowing
y = distance from wall, ft
$\bar{\alpha}$ = void fraction, average over cross section
α = void fraction
α^* = α/α_m
α_m = void fraction at tube centerline
β = ρ_G/ρ_L
ϵ = eddy diffusivity for momentum, sq ft/hr
κ = universal constant, defined by Equation (40)
λ = lift component, defined by Equation (35), lb force/ft
$\bar{\mu}$ = apparent mixture viscosity, averaged across the cross section, lb mass/(ft)(hr)
μ_L = liquid viscosity, lb mass/(ft)(hr)
ν_L = kinematic viscosity of liquid, sq ft/hr
ρ = density of two-phase mixture, lb/cu ft
ρ_G = density of vapor, lb/cu ft
ρ_L = density of liquid, lb/cu ft
σ = surface tension, lb force/ft
τ = wall shear stress in two-phase system, lb force/sq ft
τ_{sp} = wall shear stress if liquid were flowing at same total weight rate, lb force/sq ft
Υ = kinetic energy correction factor, Equation (13)
ψ = sphericity factor, Equation (36)
Φ = slip velocity ratio, Equation (10)
ω = circulation around cylindrical bubble, sq ft/hr

Superscripts

$\bar{}$ = volumetric average across the cross section

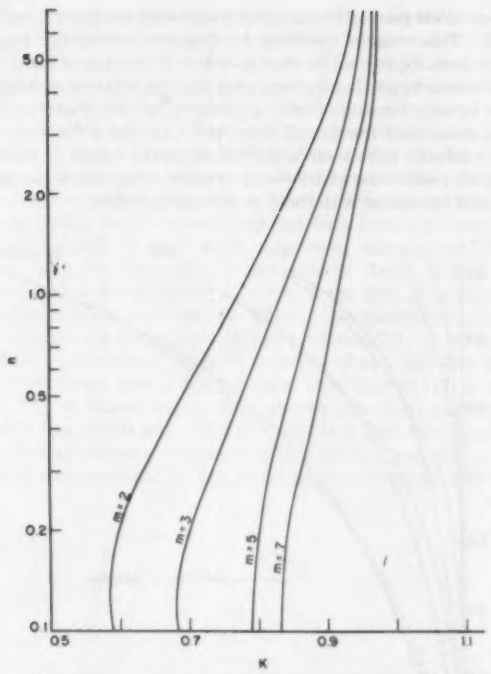

Fig. 1 Flow parameter K as a function of the velocity distribution exponent m and the void-fraction distribution exponent s

drag force exerted by a turbulent fluid flowing past solid boundaries may be expressed as the product of a friction factor, a characteristic area, and the mean kinetic energy per unit volume. For circular pipes this may be written

$$F_D = f_L(\pi DL)(\tfrac{1}{2}\rho_L \bar{u}^2\gamma) \tag{12}$$

where the kinetic energy correction factor is defined as

$$\gamma = \frac{\int_0^1 u_L^3(1-s)ds}{\left[\int_0^1 u_L(1-s)ds\right]^3} = \frac{\overline{(u_L^3)}}{(\bar{u}_L)^3} \tag{13}$$

and may be taken equal to unity for turbulent flow. In terms of the wall shear stress this becomes

$$\tau_{sp} = \tfrac{1}{2} f_L \rho_L \bar{u}_L^2 \tag{14}$$

Based upon correlation of extensive data on liquids flowing in circular pipes, Blasius [5] proposed the following equation for $\mathrm{Re} < 10^5$:

$$f_L(\mathrm{Re})^{1/4} = f_L\left(\frac{D\bar{u}_L\rho_L}{\mu_L}\right)^{1/4} = B_1 \tag{15}$$

where B_1 is a constant which depends only upon the dimensionless wall roughness. By analogy to Equation (14) a two-phase friction factor is now defined:

$$f = \frac{\tau}{\tfrac{1}{2}\bar{\rho}\bar{u}^2} \tag{16}$$

Equation (14) has been extended to noncircular ducts with good results, although based originally upon circular pipe data. A similar extension is herein made to flow of a single fluid with position-dependent physical properties. It is assumed therefore that

$$f\left(\frac{D\bar{u}\bar{\rho}}{\bar{\mu}}\right)^{1/4} = B_1 \tag{17}$$

The ratio of the two-phase wall shear stress to the wall shear stress which would be exerted by the liquid only flowing at the same mass flow rate is therefore:

$$\frac{\tau}{\tau_{sp}} = \left(\frac{\bar{\rho}}{\rho_L}\right)^{1/4}\left(\frac{\bar{u}}{\bar{u}_L}\right)^{1/4}\left(\frac{\bar{\mu}}{\mu_L}\right)^{1/4} \tag{18}$$

Equations (14) and (15) may be combined and rearranged to express a dimensionless average velocity in terms of a friction Reynolds number:

$$\frac{\bar{u}_L}{v_{*,L}} = B_2\left(\frac{R\rho_L v_{*,L}}{\mu_L}\right)^{1/7} \tag{19}$$

with a friction velocity defined as

$$v_{*,L} = \left(\frac{\tau_{sp}}{\rho_L}\right)^{1/2} \tag{20}$$

and the new constant of proportionality is

$$B_2 = \left(\frac{32}{B_1^4}\right)^{1/7} \tag{21}$$

Equation (19) is sometimes used to justify the one-seventh power velocity distribution law in single-phase turbulent flow. Assuming that Equation (19) can be applied at any distance from the wall, with the friction velocity being considered to be a constant parameter, one obtains

$$\frac{u_L}{v_{*,L}} \sim \left(\frac{\rho_L v_{*,L} y}{\mu_L}\right)^{1/7} \tag{22}$$

Similarly, one may define a two-phase friction velocity:

$$v_* = \left(\frac{\tau}{\rho_L}\right)^{1/2} \tag{23}$$

where the shear stress and the density are again evaluated at the wall. Analogously to Equation (22), one obtains

$$\frac{u}{v_*} \sim \left(\frac{\rho v_* y}{\mu}\right)^{1/7} \tag{24}$$

If the friction velocity can again be considered to be a constant parameter this represents a modified one-seventh power law in which the velocity at any point is proportional to the one-seventh power of the ratio of the distance from the wall to the kinematic viscosity of the two-phase mixture

The mean density averaged over the cross section is given by

$$\bar{\rho} = 2\int_0^1 [(1-\alpha)\rho_L + \alpha\rho_G](1-s)ds \tag{25}$$

Upon employing Equations (2) and (7) this leads to

$$\frac{\bar{\rho}}{\rho_L} = 1 - \bar{\alpha}(1-\beta) \tag{26}$$

Similarly, it follows from the preceding equation and the condition that the mass flow rates be equal in the two-phase and single-phase systems that

$$\frac{\bar{u}_L}{\bar{u}} = 1 - \frac{\bar{\alpha}}{K}[1-\beta] \tag{27}$$

The flow parameter K can be eliminated from this equation by means of Equation (8) to give

$$\frac{\bar{u}}{\bar{u}_L} = 1 - X\left[1 - \frac{1}{\beta}\right] \tag{28}$$

The proper form for the viscosity ratio is less easily obtained. Minute bubbles act hydrodynamically as solid particles, the upper limits of bubble radius a being given by the Bond and Newton number [6], $N_b = (\rho_L - \rho_G)a^2 g\sigma^{-1}$, where σ is the surface tension. For small values of N_b, therefore, the viscosity of the two-phase mixture at any point is given by the Einstein [7] expression for the apparent viscosity of a suspension of solid spheres in a liquid:

$$\mu = \mu_L(1 + 2.5\alpha) \tag{29}$$

On the other hand, if the bubbles are large and easily deformed, the apparent mixture viscosity may be approximated by a volumetric average across the channel cross section, of the form

$$\frac{\bar{\mu}}{\mu_L} = 1 - \bar{\alpha}(1 - \beta) \tag{30}$$

Thus for N_b small, $\bar{\mu}/\mu_L > 1$; and for N_b large, $\bar{\mu}/\mu_L < 1$. The spectrum of bubble radii is usually not known; and since the viscosity ratio enters to the one-fourth power, it is permissible to take this ratio to be unity. Substituting Equations (27) and (29) into Equation (19)

$$\frac{\tau}{\tau_{sp}} = [1 - \bar{\alpha}(1 - \beta)]^{3/4}\left[1 - X\left(1 - \frac{1}{\beta}\right)\right]^{7/4} \tag{31}$$

Similar expressions can be derived for a two-phase mixture flowing between two infinite, flat walls whose distance apart is $2R$. For this case

$$\frac{1}{X} = 1 - \frac{1}{\beta}\left(1 - \frac{K'}{\alpha}\right) \tag{32}$$

where

$$K' = \frac{m + n + mn}{(m + 1)(n + 1)} \tag{33}$$

Comparison With Experiment

Although the principle herein proposed, of the equivalence of an intimately mixed gas-liquid flow in a conduit to the flow of a single fluid with position-dependent physical properties, is a general concept, the present interest in this work is in steam-water flows. This concept implies that the local relative slip of the phases at any point is zero. Two Equations (8) and (31) have been derived which make possible the prediction of the mean void fraction and the frictional pressure drop for the flow of a steam-water mixture of known quality at a given pressure. The predicted quantities are related to the characteristic parameters of the flow, taken as the exponents of the velocity and void-fraction radial distributions, through a derived parameter K which is symmetrical in these exponents. Experimental methods have not yet been sufficiently refined to enable accurate measurement of velocity and void-fraction profiles in steam-water flows. It is necessary, therefore, to choose appropriate values of K by comparison with experimental data on pressure drop and mean void fraction. The void-fraction distribution exponent should be a function of the pressure, since the tendency for the gas to concentrate in the center depends on the relative density of the phases. Hence one would expect the pressure to have some effect on the flow parameter K. The mass flow rate and the quality may also influence this parameter, although less is known about these dependencies.

In Figs. 2 and 3 the predictions of this theory are compared with the well-known Martinelli-Nelson correlation using a constant average value of 0.89 for K. The agreement is good between the two sets of predictions over a range of pressures from 100 to 2500 psia and a range of mean void fractions from 0 to 0.85. This range of variation for $\bar{\alpha}$ is dictated by the requirement from Equation (10) that $\bar{\alpha} < K$. This range of mean void fractions is in good agreement with the observations of Armand, who noted a departure from a constant value of C, Equation (11), at a mean void fraction of about 0.9. In Fig. 4 the local wall shear stresses have been integrated along the length of the tube to give predictions of frictional pressure drop which are again in good agreement with those of Martinelli-Nelson.

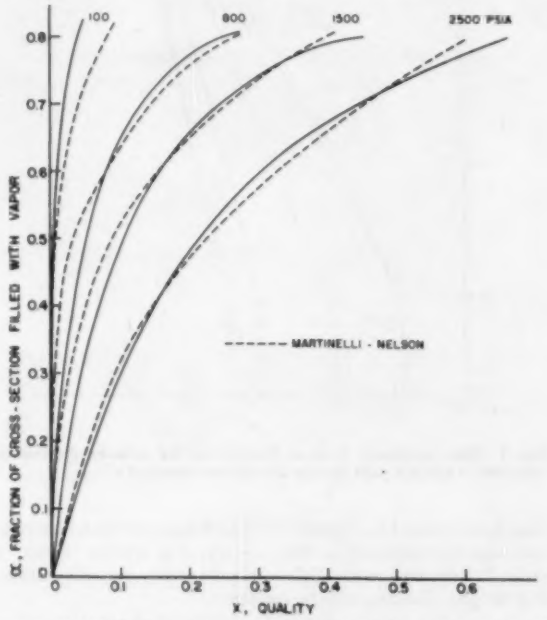

Fig. 2 Void fraction versus quality in steam-water flow: Comparison of Equation (8) with Martinelli-Nelson correlation

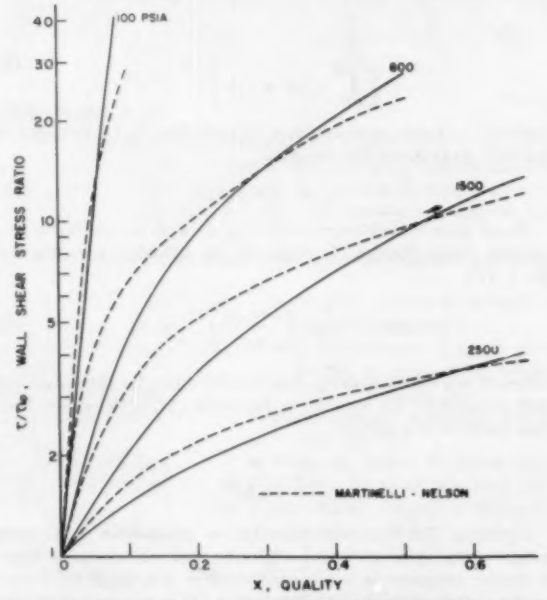

Fig. 3 Wall shear stress ratio versus quality in steam-water flow: Comparison of Equation (31) with Martinelli-Nelson correlation

More recently a momentum exchange theory has been proposed by Levy [8] which assumes that frictional and head loss of the liquid is equal to the frictional and head loss of the gas. This theory has the advantage of not requiring any parameters which are not measurable by present experimental techniques. It implies, however, a basic difference in the flow structure in horizontal and vertical flow, since in horizontal flow the frictional losses of the two phases are equal while in vertical flow the frictional losses are considerably different. This momentum exchange theory was compared with test data from the literature. Figs. 5 through 10 show these same data, taken from Levy's paper, with the predictions of the present theory and of the momentum exchange theory. In Fig. 5 the data of Larson [9] for a horizontal pipe at 1000 psia without heat addition are shown. Fig. 6 shows the data of Sher [10] and Schwarz [11] for unheated vertical and horizontal pipes at pressures of 14.7 and 1180 psia. Fig. 7 shows the data of Egen, Dingee, and Chastain [12] at 2000 psia, Fig. 8 Marchaterre's data at 115 psia [13], and Fig. 9 Cook's data at 600 psia [14]. It is seen that both theories agree with the experimental void-fraction data within the scatter of this type of measurement. In Fig. 10 frictional pressure drop data of Moen [15] and of Larson are shown. Again both theories are in good agreement with experimental results. The pressure dependency for the flow parameter found in this way is given by the equation

$$K = 0.71 + 0.0001P \tag{34}$$

where P is the pressure in psia. This result is compared with the pressure dependency found by Armand [3] and Kholodovski [16], as reported by Zuber [4], in Fig. 11. It is seen that the agree-

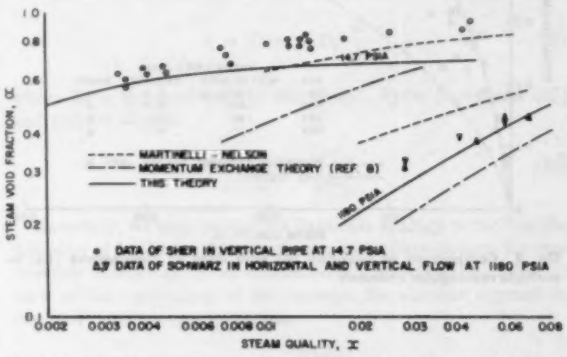
STEAM VOID FRACTION, α
STEAM QUALITY, x
MARTINELLI - NELSON
MOMENTUM EXCHANGE THEORY (REF 8)
THIS THEORY
• DATA OF SHER IN VERTICAL PIPE AT 14.7 PSIA
Δ▽ DATA OF SCHWARZ IN HORIZONTAL AND VERTICAL FLOW AT 1180 PSIA

Fig. 6 Comparison of Equation (8) with quality data of Sher [10] and Schwarz [11] for steam-water flow in unheated vertical and horizontal pipes

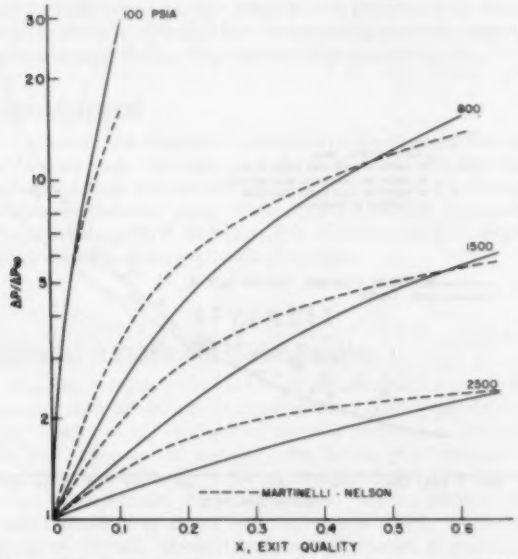

Fig. 4 Frictional pressure drop ratio versus quality: Comparison of Equation (31) with Martinelli-Nelson correlation

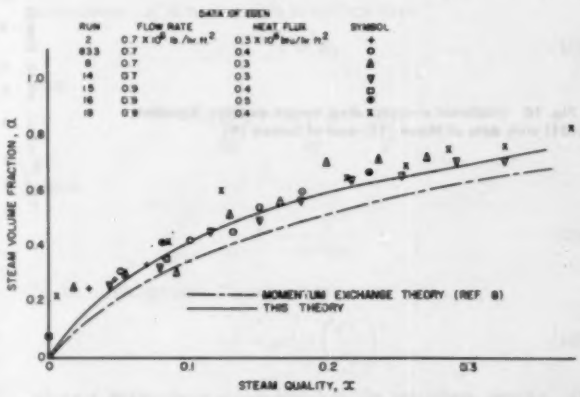

Fig. 7 Comparison of Equation (8) with data of Egen, Dingee, and Chastain [12] at 2000 psia

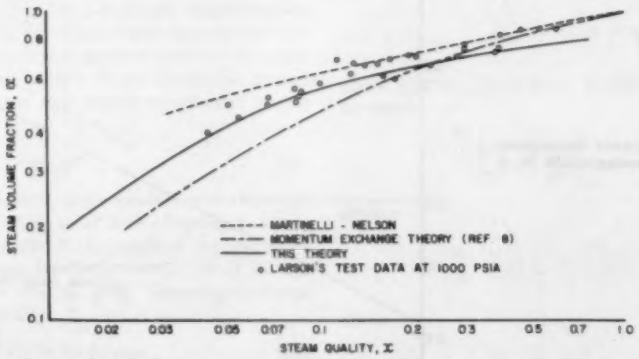
STEAM VOLUME FRACTION, α
STEAM QUALITY, x
MARTINELLI - NELSON
MOMENTUM EXCHANGE THEORY (REF 8)
THIS THEORY
○ LARSON'S TEST DATA AT 1000 PSIA

Fig. 5 Comparison of Equation (8) with data of Larson [9] in horizontal steam-water flow at 1000 psi without heat addition

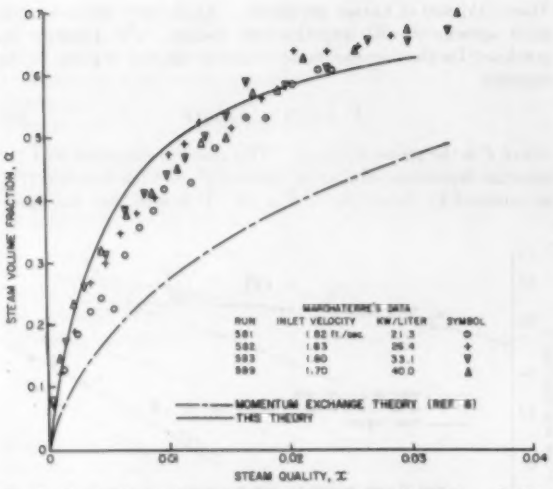
STEAM VOLUME FRACTION, Q
STEAM QUALITY, Σ
MARCHATERRE'S DATA
RUN | INLET VELOCITY | KW/LITER | SYMBOL
581 | 1.82 ft./sec. | 21.3 | ○
582 | 1.85 | 26.4 | +
583 | 1.80 | 33.1 | ▽
589 | 1.70 | 40.0 | △
MOMENTUM EXCHANGE THEORY (REF. 8)
THIS THEORY

Fig. 8 Comparison of Equation (8) with data of Marchaterre [13] in multiple rectangular channels

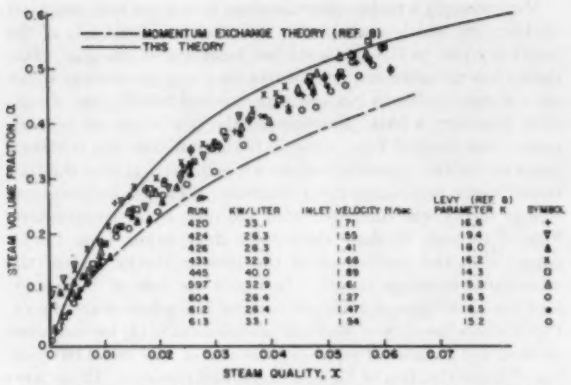
MOMENTUM EXCHANGE THEORY (REF. 8)
THIS THEORY
STEAM VOLUME FRACTION, Q
STEAM QUALITY, Σ
RUN | KW/LITER | INLET VELOCITY ft/sec. | LEVY (REF. 8) PARAMETER K | SYMBOL
420 | 33.1 | 1.71 | 16.6 | +
424 | 26.3 | 1.85 | 19.4 | ▽
426 | 26.3 | 1.41 | 18.0 | △
433 | 32.9 | 1.66 | 16.2 | x
445 | 40.0 | 1.89 | 14.3 | □
597 | 32.9 | 1.61 | 15.3 | △
604 | 26.4 | 1.37 | 16.5 | ○
612 | 26.4 | 1.47 | 18.5 | ●
613 | 33.1 | 1.94 | 15.2 | ○

Fig. 9 Comparison of Equation (8) with data of Cook [14] at 600 psia

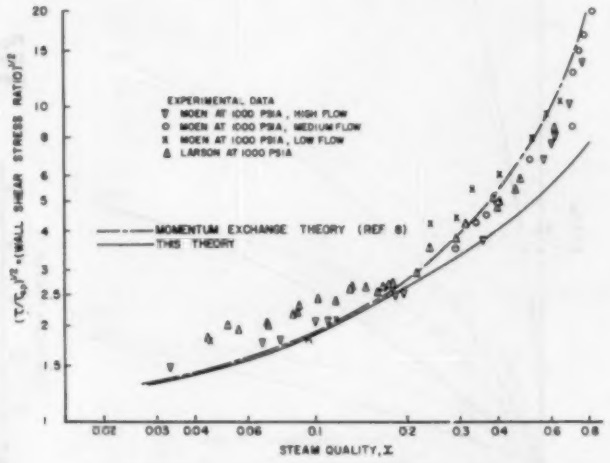
EXPERIMENTAL DATA
▽ MOEN AT 1000 PSIA, HIGH FLOW
○ MOEN AT 1000 PSIA, MEDIUM FLOW
x MOEN AT 1000 PSIA, LOW FLOW
△ LARSON AT 1000 PSIA
MOMENTUM EXCHANGE THEORY (REF. 8)
THIS THEORY
STEAM QUALITY, Σ

Fig. 10 Frictional pressure drop versus quality: Equation (31) with data of Moen [15] and of Larson [9]

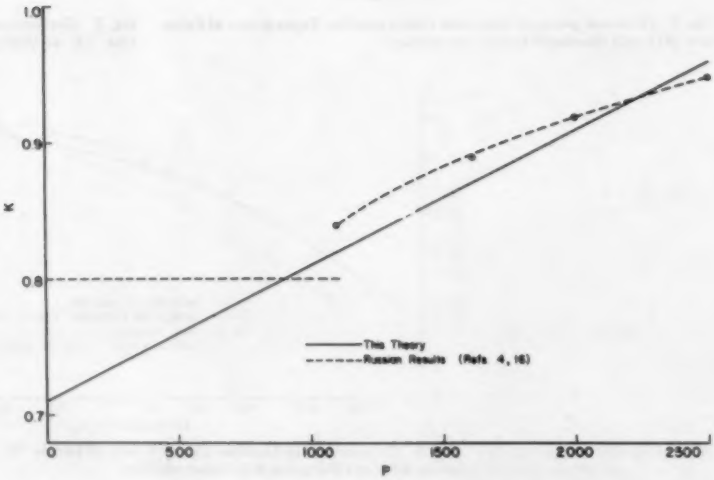

Fig. 11 Comparison of the pressure dependency of the flow parameter K with Russian results [3, 4, 16]

ment again is quite good. These results lend confidence in the utility of the proposed model.

Discussion and Summary

A physical model has been proposed for the bubble flow regime of liquid-gas flow which is in good agreement with the important features of the process. Some interesting questions are raised by this model as follows:

1 The flow parameter assumes different forms for flow in circular pipes and for flow between two flat plates. The equivalent diameter concept has been justified experimentally for single-phase turbulent flows although some deviation has been observed for narrow wedge-shaped passages in which the laminar sublayer is relatively thick [17]. It has not been demonstrated, however, that the equivalent diameter concept is equally valid for two-phase turbulent flow.

2 The wall has been assumed to be wetted by a liquid so that the void fraction at the wall itself is zero, Equation (2). If, however, the vapor is being generated at the walls, as in boiling channels, some fraction of the wall will be continuously in contact with bubbles. It may be expected that these bubbles will act as additional roughnesses and that therefore the pressure drop characteristics would be different than for nonboiling channels under the same flow conditions. This question is as yet unresolved.

Acknowledgment

Portions of this work were performed at the Argonne National Laboratory under the auspices of the U. S. Atomic Energy Commission, at Rose Polytechnic Institute with the aid of a National Science Foundation grant, and at Northwestern University. The assistance of R. P. Anderson, P. T. Eubank, and L. G. Neal in the calculations is gratefully acknowledged.

APPENDIX

Derivation of Bubble Distribution Function

Consider a single, small bubble of radius a, which is placed in a liquid of semi-infinite extent at a distance y from a vertical wall. The velocity of the undisturbed liquid is everywhere parallel to the wall. Because of buoyancy the bubble rises through the liquid; or equivalently, if the co-ordinate axes are fixed at the center of the bubble, the liquid streams past the bubble. The viscous liquid flows around the bubble less rapidly on the side closest to the wall. Hence a lift force is developed, in addition to the drag force, which propels the bubble away from the wall. This flow, being neither axisymmetric nor irrotational, is difficult to solve analytically, even if the inertial terms are omitted from the Navier-Stokes equation [18, 19]. A simple approximation can be made, however, using two-dimensional nonviscous flow theory [20]. If a nonviscous liquid streams past a cylindrical bubble of radius a with a mean velocity V, the circulation around the bubble being ω, the lift per unit length experienced by the bubble is

$$\lambda = -\pi\rho_L a^2 V\omega \tag{35}$$

If the cylinder is of finite length, there will be a disturbance of the flow due to end effects, but no axial force component, on account of symmetry. In particular, if the length of the cylinder is $2a$, the transverse force given by Equation (35) may be approximately equated to the viscous drag, assuming uniform, creeping motion in the y-direction

$$-2\pi\rho_L a^2 V\omega = 6\pi\psi\mu_L v_b a \tag{36}$$

where μ_L is the liquid viscosity, v_b is the transverse bubble velocity, and ψ is a sphericity factor, representing the ratio of the viscous Stokes drag of a right cylinder of equal diameter and height to a sphere of the same diameter. The flux of bubbles across any plane parallel to the x-axis is then:

$$J = cv_b = \frac{ca^2V\omega}{3\psi\nu_L} \tag{37}$$

where c is the local concentration of bubbles, and ν_L is the kinematic viscosity of the liquid. At steady state this flux can be equated to the flux due to the bubble concentration gradient:

$$J = J' = -D_b\frac{dc}{dy} \tag{38}$$

where D_b is the local bubble diffusivity. From Equations (37) and (38) we obtain:

$$\frac{D_b}{c}\frac{dc}{dy} = \frac{a^2V\omega}{3\psi\nu_L} \tag{39}$$

Hopefully, we may extend the Reynolds analogy to include the diffusion of bubbles. Many semiempirical formulations for momentum diffusivity in turbulent liquids are available; but in view of the uncertainty of the analogy, the simplest expression, due to Prandtl, seems preferable

$$\epsilon = \kappa^2 y^2\left|\frac{du_L}{dy}\right| \tag{40}$$

where κ is a universal constant and ϵ is the eddy diffusivity for momentum. If it is allowable to assume that

$$\epsilon = D_b \tag{41}$$

then

$$\frac{d\ln c}{dy} = \frac{d\ln\alpha}{dy} = \frac{Au_L}{y^2} \tag{42}$$

where

$$A = \frac{a^2}{3\kappa^2\psi\nu_L} \tag{43}$$

In the turbulent core, Equation (40) gives

$$\tau = \rho\kappa^2 y^2\left(\frac{du_L}{dy}\right)^2 \tag{44}$$

where τ is the shear stress and ρ is the two-phase density. If τ/ρ is assumed to be constant, this gives the well-known logarithmic velocity law:

$$u_m - u_L = \frac{1}{\kappa}\sqrt{\frac{\tau}{\rho}}\ln\frac{R}{y} \tag{45}$$

where R is the pipe radius. Combining Equations (42) and (45) we obtain

$$\frac{d\ln\alpha}{dy} = \frac{A}{y^2}\left(u_m - \frac{1}{\kappa}\sqrt{\frac{\tau}{\rho}}\ln\frac{R}{y}\right) \tag{46}$$

whence

$$\ln\frac{\alpha_m}{\alpha} = C_1\left(\frac{s-1}{s}\right) + \frac{C_2\ln s}{s} = -\ln\alpha^* \tag{47}$$

where

$$C_1 = \frac{A}{R}\left[u_m + \frac{1}{\kappa}\sqrt{\frac{\tau}{\rho_L}}\right] \tag{48}$$

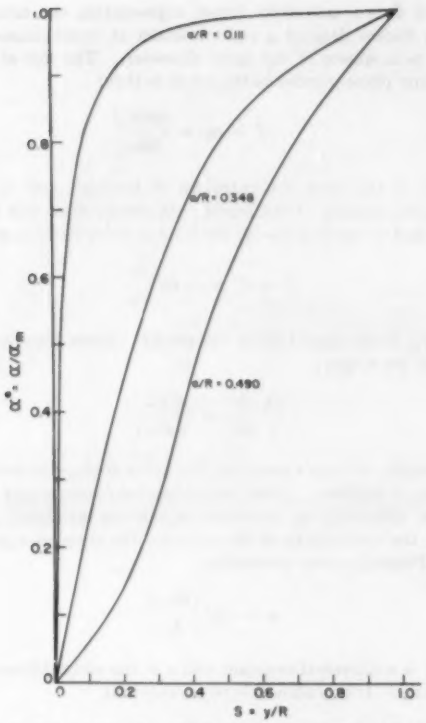

Fig. 12 Radial void-fraction distribution calculated from Equation (47) for various ratios of mean bubble to pipe radius

and

$$C_2 = \frac{-A}{\kappa}\sqrt{\frac{\tau}{\rho_L}} \tag{49}$$

To obtain some idea of the shape of the curves predicted by Equation (47), we assume some typical values of the parameters: $\kappa = 0.4$; $\psi = 1$; $R = 0.5$ in.; $\nu_L = 0.17$ ft²/sec; $u_m = 3$ ft/sec; and $a/R = 0.111$, 0.348, and 0.490. The Reynolds analogy gives

$$\sqrt{\frac{\tau}{\rho}} = \sqrt{\frac{f}{2}}\, u_m \tag{50}$$

where f, the friction factor, is found to be 0.005 for the assumed values of the parameters. The resulting curves are shown in Fig. 12. It is seen that the distribution curve is very strongly dependent on a/R, the ratio of the mean bubble radius to the pipe radius. A logarithmic plot (Fig. 13) of the same curves shows that they are reasonably well approximated by straight lines, substantiating the power-law assumption given by Equation (2).

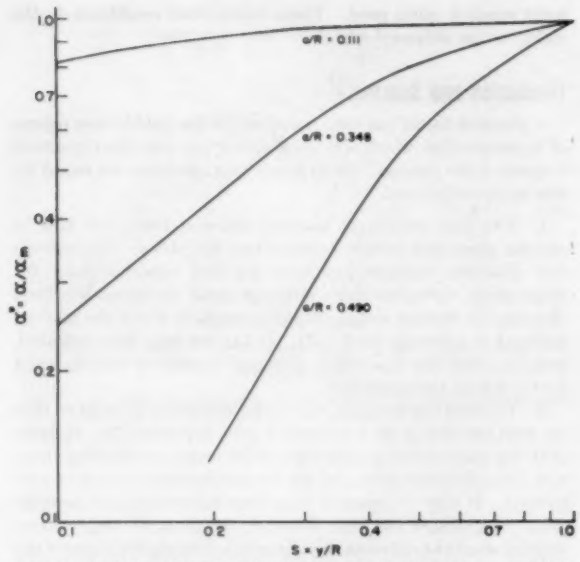

Fig. 13 Radial void-fraction distribution calculated from Equation (47) for various ratios of mean bubble to pipe radius

References

1 S. Levy, "Theory of Pressure Drop and Heat Transfer for Two-Phase-Component Annular Flow in Pipes," Ohio State University, Engineering Experimental Station Bulletin No. 149, Proceedings of Second Midwestern Conference of Fluid Mechanics, 337, 1952.

2 R. C. Martinelli and D. B. Nelson, "Prediction of Pressure Drop During Forced-Circulation Boiling of Water," TRANS. ASME, vol. 70, 1948, p. 695.

3 A. A. Armand and G. G. Treschev, "Investigation of the Resistance During the Movement of Vapor-Water Mixtures in Heated Pipes at High Pressure," *Izv. Vsesou. Teplotek. Inst.*, no. 4, 1–5, AERE Lib/Trans. 816.

4 N. Zuber, "On the Variable-Density Single-Fluid Model," submitted for publication.

5 H. Schlichting, "Boundary Layer Theory," Pergamon Press, Limited, London, England, 1955.

6 W. N. Bond and D. A. Newton, "Bubbles, Drops, and Stokes' Law," *Philosophical Magazine*, vol. 5, 1928, p. 794.

7 A. Einstein, "New Determination of Molecular Dimensions," *Annalen der Physik*, vol. 19, 1906, p. 289.

8 S. Levy, "Steam Slip—Theoretical Prediction From Momentum Model," JOURNAL OF HEAT TRANSFER, TRANS. ASME, Series C, vol. 82, 1960, p. 113.

9 H. C. Larson, "Void Fractions of Two-Phase Steam-Water Mixture," MS thesis, University of Minnesota, 1957.

10 H. S. Isbin, N. C. Sher, and K. C. Eddy, "Void Fractions in Two-Phase Steam Water Flow," *AIChE Journal*, March, 1957.

11 K. Schwarz, "Untersuchungen Uber die Wichteverteiling, die Wasser und Dampfgeschwindigkeit fur den Reibungsdrucksfall in Lotrechen und Wasgerechten Kesselsteigrohren," VDI Forschungsheft 455, 1954.

12 R. A. Egen, D. A. Dingee, and J. W. Chastain, "Vapor Formation and Behavior in Boiling Heat Transfer," Battelle Memorial Institute Report No. 1163, February, 1957.

13 J. F. Marchaterre, "The Effect of Pressure on Boiling Density in Multiple Rectangular Channels," Argonne National Laboratory Report No. 5522, February, 1956.

14 W. H. Cook, "Boiling Density in Vertical Rectangular Multi-Channel Sections With Natural Circulation," Argonne National Laboratory Report No. 5621, November, 1956.

15 R. H. Moen, "An Investigation of the Steam-Water System at High Pressures and High Temperatures," PhD thesis, University of Minnesota, 1956.

16 G. E. Kholodovski, "New Method for Correlating Experimental Data for the Flow of Steam-Water Mixtures in Vertical Pipes," *Teploenergetiks*, vol. 4, no. 7, 1957, p. 68–72.

17 C. C. Lin, editor, "Turbulent Flows and Heat Transfer," vol. V, High Speed Aerodynamics and Jet Propulsion, Princeton University Press, Princeton, N. J., 1959.

18 M. J. Lighthill, "Drift," *Journal of Fluid Mechanics*, vol. 1, 1956, pp. 31–35.

19 I. M. Hall, "The Displacement Effect of a Sphere in a Two-Dimensional Shear Flow," *Journal of Fluid Mechanics*, vol. 1, 1956, pp. 142–162.

20 L. M. Milne-Thomson, "Theoretical Hydrodynamics," third edition, The Macmillan Company, New York, N. Y., 1955, p. 182.

JOHN E. SCHMIDT
Engineer, Westinghouse Bettis Atomic Power Division, Pittsburgh, Pa.
Assoc. Mem. ASME

GEORGE SONNEMANN
Westinghouse Professor of Mechanical Engineering, University of Pittsburgh, Pittsburgh, Pa. Mem. ASME

Transient Temperatures and Thermal Stresses in Hollow Cylinders Due to Heat Generation[1]

A general solution for the transient temperatures and thermal stress is obtained for a right circular cylinder with internal heat generation varying exponentially with the radius by use of Hankel transforms. Curves for the maximum thermal stresses are presented for diameter ratios up to 1.2 and for a variety of internal heat-generation rates for internal heat-generation transients with both cylinder walls maintained at zero reference temperature at all times.

Introduction

Operation of nuclear reactors produces radiation, principally in the form of neutrons and gamma rays, which upon collision with the materials in the vicinity of the reactor lose energy giving rise to heat in the material at the point of collision. This internal radiation heating induces thermal stresses, and these thermal stresses are especially serious in the structural members nearest to the nuclear reactor, the core barrel, thermal shields, and pressure vessel.

Steady-state thermal-stress analysis with a decaying exponential radial variation with axial symmetry was presented by Sonnemann and Davis [1][2] and with angular variation by Kraus and Sonnemann [2]. Transient thermal stresses in reactor pressure vessels with constant internal heat-generation rate were evaluated in a paper by Heisler [3].

Statement of the Problem

This paper determines the transient temperature and the tangential, radial, and axial stress distributions in a long, hollow, circular cylinder with internal heat generation. The radially dependent internal heat generation is a decaying exponential function and represents the energy-loss characteristics of nuclear-reactor radiations. To restrict the problem to one dimension, no variations axially or azimuthally will be considered in this internal heat generation. Furthermore, to make the problem tractable, the material properties will be assumed temperature independent and the material will be treated as being elastic, isotropic, and homogeneous. In addition, the analysis will utilize the plane-strain assumption, thereby restricting the validity of the results to regions far removed from the ends of the cylinder.

Steps in Obtaining Solution

After nondimensionalizing the transient heat-conduction equation applicable to the cylinder with internal heat generation, this equation is operated upon by a finite Hankel transform. The resulting linear differential equation is then integrated to yield the steady-state and transient transformed temperatures. Inversion of the integrated equation yields the nondimensionalized temperature.

Stresses are computed from these temperature distributions by integrating the thermal-stress equations.

Solution of the Temperature Problem

For the cylinder in the presence of internal heat generation and with radial and axial symmetry, the heat-conduction equation is:[3]

$$\frac{\partial^2(\Delta T)}{\partial r^2} + \frac{1}{r}\frac{\partial(\Delta T)}{\partial r} - \frac{1}{\alpha_d}\frac{\partial(\Delta T)}{\partial t} = -\frac{H_i(r,t)}{k}. \quad (1)$$

Expressing the internal heat-generation rate $H_i(r, t)$ by

$$H_i(t) = f(t)e^{-\beta(r-a)} = G_i f(\tau)e^{-\beta(r-a)} \quad (2)$$

with G_i defined later, and introducing the same nondimensional quantities as in the previous paper [1, 2] yields for Equation (1).

[1] Based on a thesis submitted by J. E. Schmidt to the Graduate Faculty of the Schools of Engineering and Mines, University of Pittsburgh, in partial fulfillment of the requirements for the degree of Master of Science in Mechanical Engineering.

[2] Numbers in brackets designate References at end of paper.

Contributed by the Heat Transfer Division and presented at the Annual Meeting, Atlantic City, N. J., November 29–December 4, 1959, of The American Society of Mechanical Engineers.

Note: Statements and opinions advanced in papers are to be understood as individual expressions of their authors and not those of the Society. Manuscript received at ASME Headquarters, May 21, 1959. Paper No. 59—A-144.

[3] See Nomenclature for definition of symbols.

Nomenclature

a = inner radius of cylinder, in.
b = outer radius of cylinder, in.
B_0 = $1/y$ times kernel of Hankel transform
E = modulus of elasticity, lb/in.^{2}
$\bar{f}_{(\alpha)}$ = finite Hankel transform of $f(r)$
$g_{(\alpha)}$ = finite Hankel transform of $g(y)$
$G_i(\tau) = \frac{ma^2}{\alpha}$ = modified heat generation at inner surface, Btu/sec/in.^{3}
H_i = internal heat-generation rate at inner surface, Btu/sec/in.^{3}
J_0, Y_0 = Bessel function of order zero, first and second kind
k = thermal conductivity, Btu/sec/in/deg F
p_n = nth root of transcendental equation
r = radius of a point in cylinder wall, in.
t = time, sec
ΔT = temperature difference, deg F
X = time and position independent term in nondimensional temperature equations
$y = r/a$ = nondimensional radius to a point in the wall divided by the inner radius of the cylinder

(*Continued on next page*)

$$\left[\frac{\partial^2\theta}{\partial y^2} + \frac{1}{y}\frac{\partial\theta}{\partial y}\right] - \frac{\partial\theta}{\partial\tau} = -f(\tau)\beta_i^2 e^{-\beta(y-1)} \quad (3)$$

Solution of Equation (3) is obtained by using the finite Hankel transform defined by [4]

$$\bar{g}(p_n) = \int_1^{y_0} g(y) y B_0(p_n y) dy, \quad (1 < y < y_0), \quad (4)$$

with

$$B_0(p_n y) = J_0(p_n y) Y_0(p_n) - Y_0(p_n y) J_0(p_n), \quad (5)$$

and the parameter p_n for each value of n is the root of the equation

$$J_0(p_n y_0) Y_0(p_n) = J_0(p_n) Y_0(p_n y_0) \quad (6)$$

Applying the transform to Equation (3) results in the linear first-order differential equation in the time variable

$$\left\{\frac{2}{\pi}\left[\theta_b(\tau)\frac{J_0(p_n)}{J_0(p_n y_0)} - \theta_a(\tau)\right] - p_n^2\bar{\Omega}(p_n, \tau)\right\} - \frac{\partial\bar{\Omega}}{\partial\tau}(p_n, \tau) = -\beta_i^2 f(\tau)\bar{f}(p_n) \quad (7)$$

in which $\bar{\Omega}(p_n, \tau)$ is the transformed temperature and

$$\bar{f}(p_n) = \int_1^{y_0} y e^{-\beta_i(y-1)} B_0(p_n y) dy. \quad (8)$$

Rearrangement of Equation (7) leads to the differential equation

$$\frac{\partial\bar{\Omega}(p_n\tau)}{\partial\tau} + p_n^2\bar{\Omega}(p_n, \tau) = Q(\tau) \quad (9)$$

with

$$Q(\tau) = \beta_i^2 f(\tau)\bar{f}(p_n) + \frac{2}{\pi}\left[\theta_b(\tau)\frac{J_0(p_n)}{J_0(p_n y_0)} - \theta_a(\tau)\right] \quad (10)$$

for which the solution is [5]

$$\bar{\Omega}(p_n, \tau) = e^{-p_n^2\tau}\int_0^\tau Q(\tau) e^{p_n^2\tau} d\tau + ce^{-p_n^2\tau} \quad (11)$$

With the inversion formula for the finite Hankel transform [6]

$$g(y) = \frac{\pi^2}{2}\sum_{p_n}\frac{p_n^2 J_0^2(p_n y_0)}{J_0^2(p_n) - J_0^2(p_n y_0)} B_0(p_n y)\,\bar{g}(p_n) \quad (12)$$

Equation (13) becomes the solution for the nondimensionalized temperature

$$\theta(y, \tau) = \frac{\pi^2}{2}\sum_{p_n}\frac{p_n^2 J_0^2(p_n y_0)}{J_0^2(p_n) - J_0^2(p_n y_0)} B_0(p_n y)\bar{\Omega}(p_n, \tau). \quad (13)$$

The boundary and initial conditions are taken as

$$\theta(a, \tau) = \theta_a(\tau)$$

$$\theta(b, \tau) = \theta_b(\tau)$$

and

$$\theta(y, 0) = 0$$

so that the nondimensional temperature distribution becomes, after substituting for $\bar{\Omega}(p_n, \tau)$,

$$\theta(y, \tau) = \frac{\pi^2}{2}\sum_{p_n}\frac{p_n^2 J_0^2(p_n y_0)}{J_0^2(p_n) - J_0^2(p_n y_0)} B_0(p_n y) \times \left[+\frac{2}{\pi}e^{-p_n^2\tau}\int_0^\tau \theta_b(\tau)\frac{J_0(p_n)}{J_0(p_n y_0)} e^{p_n^2\tau} d\tau - \frac{2}{\pi}e^{-p_n^2\tau}\int_0^\tau \theta_a(\tau) e^{p_n^2\tau} d\tau + e^{-p_n^2\tau}\bar{f}(p_n)\beta_i^2\int_0^\tau f(\tau) e^{p_n^2\tau} d\tau\right] \quad (14)$$

with

$$\bar{f}(p_n) = \int_1^{y_0} e^{\beta_i(y-1)}\, y B_0(p_n y) dy, \quad (15)$$

This nondimensional temperature consists of three separable components; namely, the inner wall temperature transient $\theta_a(\tau)$, the outer wall transient $\theta_b(\tau)$, and the internal heat generation transient $f(\tau)$. As a consequence of the linearity of the differential equation, any physical transient can be obtained by a suitable superposition of linear functions of time.

In general, then

$$f(t) = mt$$

or nondimensionalizing time

$$f(t) = \left[\frac{ma^2}{\alpha}\right]\tau = G_i\tau$$

Thus taking

$$f(\tau) = \frac{f(t)}{G_i} = \tau \quad (16)$$

allows a simple relation in τ with G_i containing both the time

Nomenclature

y_0 = b/a = outer radius divided by inner radius

Y = time-dependent term in nondimensional temperature equations

α = coefficient of thermal expansion, in/in/deg F

α_d = thermal diffusivity, in²/sec

β_i = βa = dimensionless logarithmic decrement

ζ_1 = $[(y^3 - 1)/y^3]/[(y_0^3 - 1)/y_0^3]$ = coefficients in stress equations

ζ_2 = $[(y^2 + 1)/y^2]/[(y_0^2 - 1)/y_0^2]$ = coefficients in stress equations

ζ_3 = $(1/y_0^2) - 1$ = coefficients in stress equations

θ = $\Delta T\dfrac{k\beta^2}{Gi}$ = dimensionless temperature difference

$\theta_a(\tau)$ = dimensionless temperature of inner wall

$\theta_b(\tau)$ = dimensionless temperature of outer wall

Θ = weighted average temperature difference

λ = $\dfrac{E\alpha G_i(\tau)}{(1-\nu)k\beta^2}$ = dimensional conversion factor, lb/in.²

ν = Poisson's ratio

σ_R = σ_r/λ = dimensionless radial stress

σ_A = σ_a/λ = dimensionless axial stress

σ_T = σ_s/λ = dimensionless tangential stress

τ = $(\alpha/a^2)t$ = Fourier modulus

$\bar{\Omega}$ = finite Hankel transform of nondimensional temperature

conversion and functional rotation. Consequently, it is possible to write for any of the transient occurrences, which may take place either separately or simultaneously,

$$\left.\begin{aligned} f(\tau) &= \tau \\ \theta_a(\tau) &= \tau \\ \theta_b(\tau) &= \tau \end{aligned}\right\} \quad (17)$$

To further simplify the subsequent numerical integration, the Bessel functions appearing in the solution of the nondimensional temperature are approximated by the asymptotic expansions since the zeros of Equation (6), for diameter ratios y_0 lying in the range of 1.0 to 1.2, are sufficiently large to permit this expansion [7]. Introducing the asymptotic expansions

$$J_0(p_n y) = \sqrt{\frac{2}{\pi\, p_n y}} \cos\left(p_n y - \frac{\pi}{4}\right), \quad (18)$$

$$Y_0(p_n y) = \sqrt{\frac{2}{\pi\, p_n y}} \sin\left(p_n y - \frac{\pi}{4}\right), \quad (19)$$

as well as linear relations for the temperature transients into Equation (13), leads, after some simplification, to the three temperature transients:

Internal Heat Generation

$$\theta_{H_i}(y, \tau) = \sum_{p_n} X(p_n) Y(p_n, \tau) \left[\frac{\sin p_n(y-1)}{\sqrt{y}}\right] [\bar{f}(p_n)] \quad (20)$$

Inner Wall Temperature

$$\theta_a(y, \tau) = \sum_{p_n} X(p_n) Y(p_n, \tau) \left[\frac{\sin p_n(y-1)}{\sqrt{y}}\right] [-\theta_a(1, 1)] \quad (21)$$

Outer Wall Temperature

$$\theta_b(y, \tau) = \sum_{p_n} X(p_n)\, Y(p_n, \tau) \left[\frac{\sin p_n(y-1)}{\sqrt{y}}\right] \times \left[\theta_b(y_0, 1) \frac{\sqrt{y_0}\cos\left(p_n - \frac{\pi}{4}\right)}{\cos\left(p_n y_0 - \frac{\pi}{4}\right)}\right] \quad (22)$$

with

$$X(p_n) = \left[\frac{2}{y_0 \dfrac{\cos^2\left(p_n - \frac{\pi}{4}\right)}{\cos^2\left(p_n y_0 - \frac{\pi}{4}\right)} - 1}\right]^{1/p_n^2} \quad (23)$$

and

$$Y(p_n, \tau) = \frac{p_n^2 \tau - 1 + e^{-p_n^2 \tau}}{p_n^2} \quad (24)$$

Solution of the Stress Problem

Thermal stress induced in the long hollow circular resulting from the radial temperature distributions given in Equations (20) to (22) are evaluated from [8]:

$$\sigma_z = \frac{\alpha E}{1-\nu} \frac{1}{r^2} \left(\frac{r^2 - a^2}{b^2 - a^2} \int_a^b Trdr - \int_a^r Trdr\right) \quad (25)$$

$$\sigma_y = \frac{\alpha E}{1-\nu} \frac{I}{r^2} \left(\frac{r^2 + a^2}{b^2 - a^2} \int_a^b Trdr + \int_a^r Trdr - Tr^2\right) \quad (26)$$

$$\sigma_x = \frac{\alpha E}{1-\nu} \left(\frac{2}{b^2 - a^2} \int_a^b Trdr - T\right) \quad (27)$$

Rearrangement of these equations into a dimensionless form results in

$$\sigma_R = \sigma_x/\lambda = [-\Theta(y) - \zeta_1 \Theta(y_0)] \quad (28)$$

$$\sigma_T = \sigma_y/\lambda = [\Theta(y) + \zeta_2 \Theta(y_0) - \theta] \quad (29)$$

$$\sigma_A = \sigma_z/\lambda = [\zeta_3 \Theta(y_0) - \theta] \quad (30)$$

with the weighted average temperature difference

$$\Theta(y) = \frac{1}{y^2} \int_1^y \theta y dy \quad (31)$$

and the other symbols defined in the Nomenclature.

For each of the three temperature transient problems discussed so far, it is the weighted average temperature which is required in the analysis. Substitution of the requisite temperature equations into Equation (31) gives rise to:[4]

For the internal heat generation transient,

$$\Theta_{H_i}(y, t) = \sum_{p_n} X(p_n) Y(p_n, \tau)\, I(p_n y) \bar{f}(p_n); \quad (32)$$

For the inner wall temperature transient,

$$\Theta_a(y, \tau) = -\sum_{p_n} X(p_n) Y(p_n, \tau) I(p_n y) \theta_a(1, 1); \quad (33)$$

For the outer wall temperature transient,

$$\Theta_b(y, \tau) = \sum_{p_n} [X(p_n) Y(p_n, \tau) I(p_n y) \theta_b(y_0, 1)] \times \left[\frac{\sqrt{y_0}\cos\left(p_n - \frac{\pi}{4}\right)}{\cos\left(p_n y_0 - \frac{\pi}{4}\right)}\right] \quad (34)$$

with

$$I(p_n y) = \frac{1}{y^2} \int_1^y \sqrt{y}\, \sin p_n(y-1) dy \quad (35)$$

General Nondimensional Solution and Curves

Evaluation of the nondimensional transient thermal stresses for various values of the parameters y_0 (ratio of outer to inner radius) and β_1 (nondimensional decay constant) can be undertaken through the equations developed in the preceding paragraphs. Only response characteristics, i.e., transient temperatures and stresses, induced by a transient power internal heat generation excursion, were evaluated with both wall temperatures maintained at zero reference temperature. Though the other transient cases are of great interest, the magnitude of the computation prevented their evaluation particularly since this effort was an unsponsored activity and all computations were made possible through the kind co-operation of Mr. W. B. Kehl, Director, University of Pittsburgh Computation Center. These temperatures and thermal stresses were evaluated from the appropriate equations by means of the IBM 650 digital computer.

Only the maximum circumferential stresses occurring at the inner boundary, as shown in Fig. 1, which is a representative

[4] Integration prior to insertion of the asymptotic expansion for the Bessel functions is possible but was not done. Check of accuracy of solution with reference [1] for steady-state stress values shows that no additional error is incurred by the procedure employed in the paper.

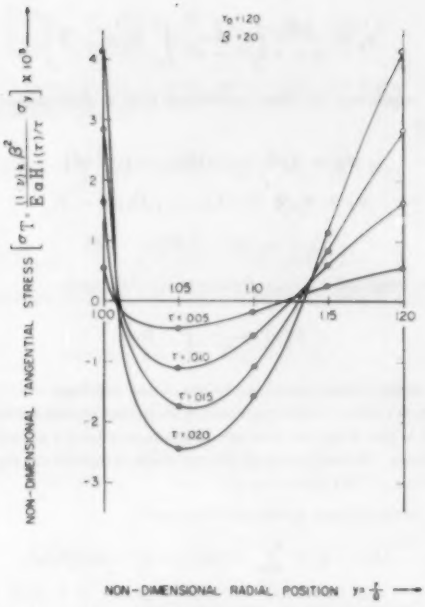

Fig. 1 Dimensionless tangential stress distribution (σ_T) through cylinder wall for several values of dimensionless time (τ)

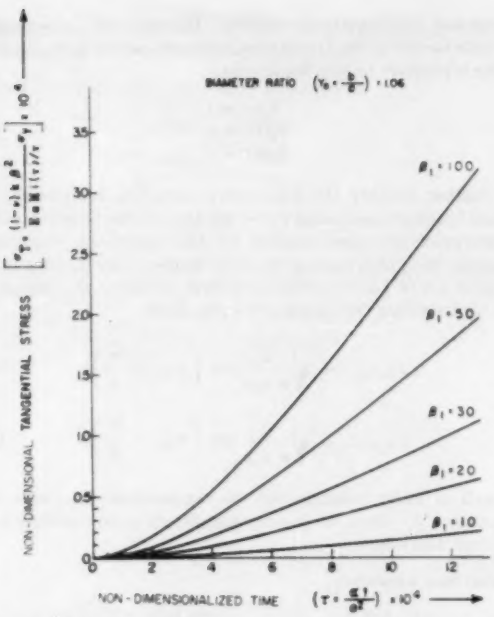

Fig. 3 Response curves for the maximum tangential stress in hollow cylinders having radial exponential internal heat generation with the nondimensional logarithmic decrement β_1 as a parameter

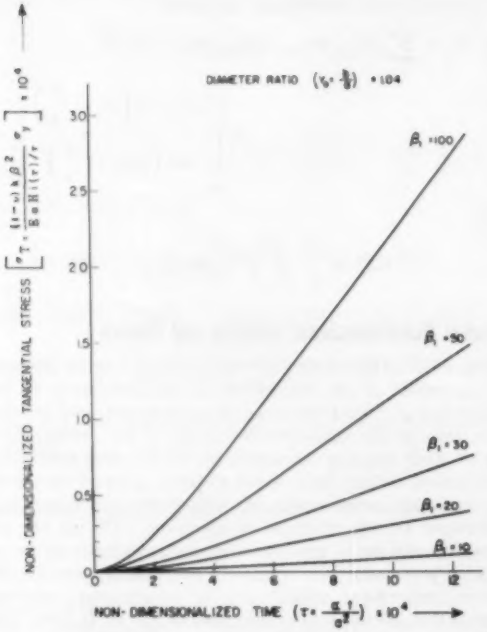

Fig. 2 Response curves for the maximum tangential stress in hollow cylinders having radial exponential internal heat generation with the nondimensional logarithmic decrement β_1 as a parameter

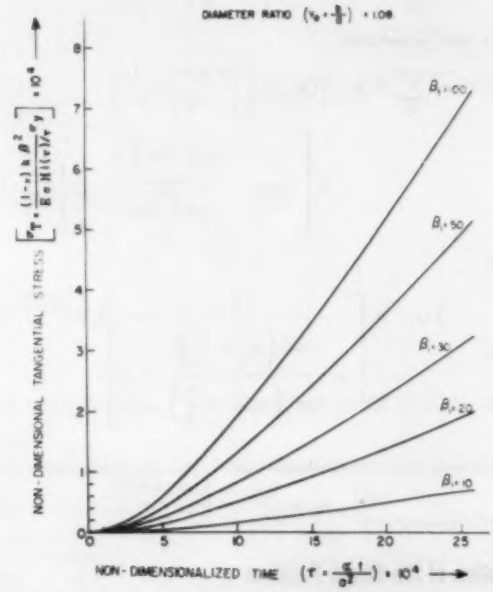

Fig. 4 Response curves for the maximum tangential stress in hollow cylinders having radial exponential internal heat generation with the nondimensional logarithmic decrement β_1 as a parameter

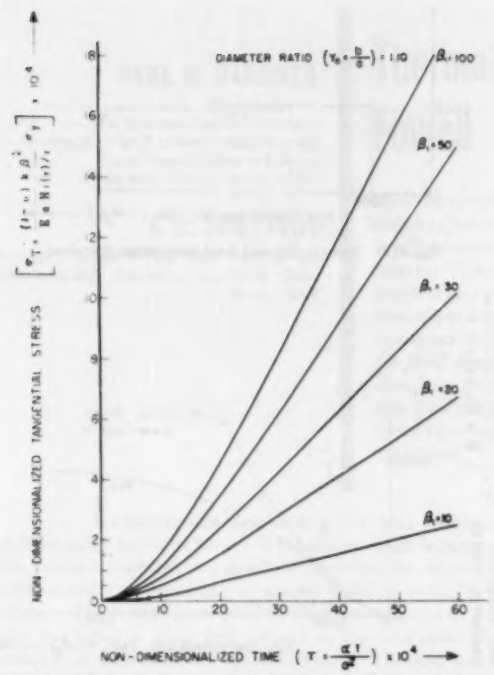
DIAMETER RATIO $(\gamma_0 = \frac{b}{a}) = 1.10$
$\beta_1 = 100$
$\beta_1 = 50$
$\beta_1 = 30$
$\beta_1 = 20$
$\beta_1 = 10$
NON-DIMENSIONALIZED TANGENTIAL STRESS $\left[\sigma_T = \frac{(1-\nu)\,k\,\beta^2}{E\,\alpha\,W_1(\tau)/\tau}\,\sigma_y\right] \times 10^4$
NON-DIMENSIONALIZED TIME $(\tau = \frac{\alpha\,t}{a^2}) \times 10^4$

Fig. 5 Response curves for the maximum tangential stress in hollow cylinders having radial exponential internal heat generation with the nondimensional logarithmic decrement β_1 as a parameter

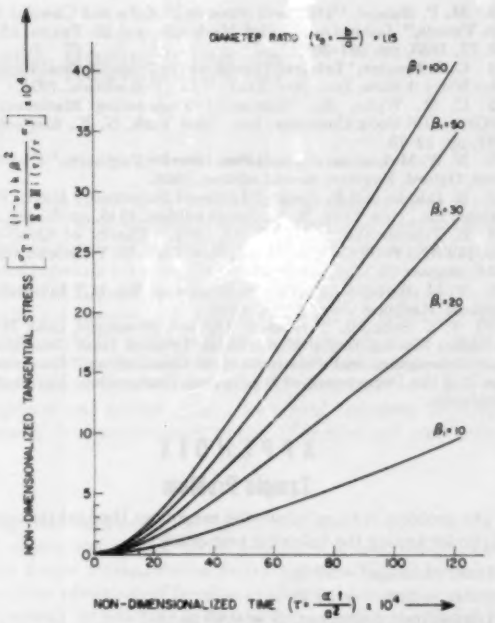
DIAMETER RATIO $(\gamma_0 = \frac{b}{a}) = 1.15$
$\beta_1 = 100$
$\beta_1 = 50$
$\beta_1 = 30$
$\beta_1 = 20$
$\beta_1 = 10$
NON-DIMENSIONALIZED TANGENTIAL STRESS $\left[\sigma_T = \frac{(1-\nu)\,k\,\beta^2}{E\,\alpha\,W_1(\tau)/\tau}\,\sigma_y\right] \times 10^4$
NON-DIMENSIONALIZED TIME $(\tau = \frac{\alpha\,t}{a^2}) \times 10^4$

Fig. 6 Response curves for the maximum tangential stress in hollow cylinders having radial exponential internal heat generation with the nondimensional logarithmic decrement β_1 as a parameter

sample, are of interest since the radial stress is zero at the inner boundary in the absence of pressure stresses. Each of the curves in Figs. 2 through 7 is for a given diameter ratio and presents the maximum stress as a function of the time (nondimensionalized) with the logarithmic decrement as parameter. These curves can be used to predict the thermal stress caused by any arbitrary power excursion, as is shown in Appendix A, provided the boundary conditions are met.

Results and Conclusions

Rapid calculation of the transient thermal stresses in long hollow cylinders experiencing a power transient due to radiation heating changes has been made possible by means of the graphs presented and these should facilitate establishment of limits on operating power transients in nuclear reactor power plants.

These curves of the nondimensional tangential stress due to a linearly increasing internal heat generation rate were obtained for the boundary condition of zero surface reference temperatures at all times of the transient. Superposition of this solution permits analysis for arbitrary start-up and operating stress transients in thermal shields. In the true start-up problem, the convective behavior at the inner surface of the pressure vessel would have to be accounted for as well as the large gradient of temperature which can occur in a rapid start-up. For this reason care must be exercised in the application of this paper and the interpretation of results.

For all the parameter variations considered, excellent agreement was obtained with the steady-state calculations for the tangential stresses presented by Sonnemann and Davis [1]. Additional data can be obtained by using a Wolontis code [9] for the IBM-650 which has been written for the temperatures and tangential stresses [10]. Presently, work is in progress to evaluate the transient stresses when the convective character at the boundary is accounted for during the thermal transient.

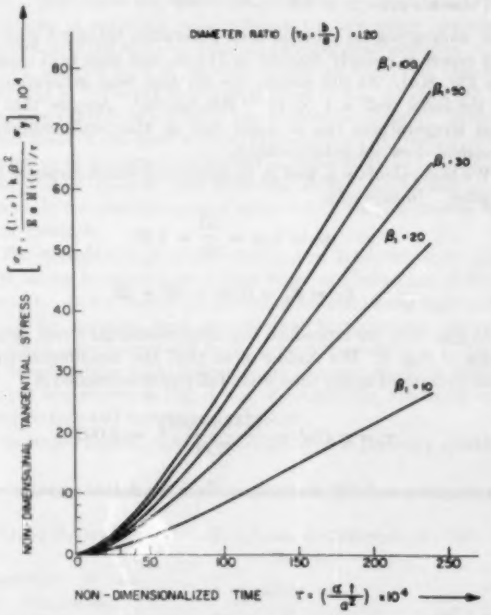
DIAMETER RATIO $(\gamma_0 = \frac{b}{a}) = 1.20$
$\beta_1 = 100$
$\beta_1 = 50$
$\beta_1 = 30$
$\beta_1 = 20$
$\beta_1 = 10$
NON-DIMENSIONAL TANGENTIAL STRESS $\left[\sigma_T = \frac{(1-\nu)\,k\,\beta^2}{E\,\alpha\,W_1(\tau)/\tau}\,\sigma_y\right] \times 10^4$
NON-DIMENSIONALIZED TIME $(\tau = \frac{\alpha\,t}{a^2}) \times 10^4$

Fig. 7 Response curves for the maximum tangential stress in hollow cylinders having radial exponential internal heat generation with the nondimensional logarithmic decrement β_1 as a parameter

References

1 G. Sonnemann and D. M. Davis, "Stresses in Long Thick-Walled Cylinders Caused by Pressure and Temperature," ASME Paper No. 57—A-256.

2 H. Kraus and G. Sonnemann, "Stresses in Hollow Cylinders Due to Asymmetrical Heat Generation," *Journal of Engineering for Power*, TRANS. ASME, Series A, vol. 81, 1959, pp. 449–454.

3 M. P. Heisler, "Transient Stresses in Slabs and Circular Pressure Vessels," *Journal of Applied Mechanics*, vol. 20, TRANS. ASME, vol. 75, 1953, pp. 261–269.
4 C. J. Tranter, "Integral Transforms in Mathematical Physics," John Wiley & Sons, Inc., New York, N. Y., first edition, 1951.
5 C. R. Wylie, Jr., "Advanced Engineering Mathematics," McGraw-Hill Book Company, Inc., New York, N. Y., first edition, 1951, pp. 12–13.
6 N. W. McLachlan, "Bessel Functions for Engineers," Clarendon Press, Oxford, England, second edition, 1955.
7 E. Jahnke and F. Emde, "Tables of Functions," Dover Publications, Inc., New York, N. Y., fourth edition, 1945, pp. 36 and 204.
8 S. Timoshenko and J. N. Goodier, "Theory of Elasticity," McGraw-Hill Book Company, Inc., New York, N. Y., second edition, 1951, chapter 14.
9 V. M. Wolontis, "Technical Newsletter No. 11," International Business Machines Corporation, 1956.
10 J. E. Schmidt, "Transient Thermal Stresses in Long Hollow Cylinders Having Radial Exponential, Internal Heat Generation—Code Description and Presentation of Calculations," Research Report 3 of the Department of Mechanical Engineering, University of Pittsburgh.

APPENDIX

Sample Problem

The problem is to calculate the maximum thermal stresses for a cylinder having the following properties:

Inner radius, $a = 50$ in.
Outer radius, $b = 60$ in.
Logarithmic decrement, $\beta = 0.40$ in.$^{-1}$
Coefficient of thermal expansion, $\alpha = 0.07 \times 10^{-4}$ in/in/deg F
Thermal diffusivity, $\alpha_d = 0.007$ in^2/sec
Modulus of elasticity, $E = 30 \times 10^6$ lb/in.^{2}
Poisson's ratio, $\nu = 0.3$

and undergoing an internal heat generation transient such that full power is linearly reached in 714 sec and then held constant, see Fig. 8(*a*). At full power, the internal heat generation rate at the inner wall is 1×10^{-13} Btu/sec/in^3. Assume that both wall temperatures rise at same rate so that wall temperature transient does not enter problem.

We first calculate y_0 and β_1 to determine which response curve applies. In this case,

$$y_0 = b/a = \frac{60}{50} = 1.20$$

$$\beta_1 = \beta_a = 0.40 \times 50 = 20$$

In Fig. 8(*b*), we reproduce the nondimensional stress response curve of Fig. 7. We further note that the nondimensionalized time equivalent to the time when full power is reached is

$$\tau = \alpha_d t/a^2 = \frac{(714)(0.007)}{2500} = 0.002$$

Starting at $\tau = 0.002$, we subtract from the dotted response curve

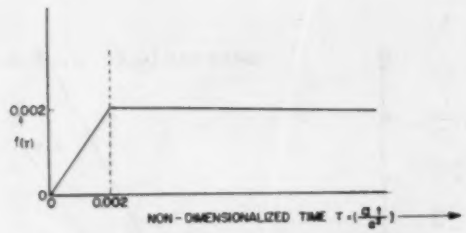

Fig. 8(*a*) Sample internal heat generation transient

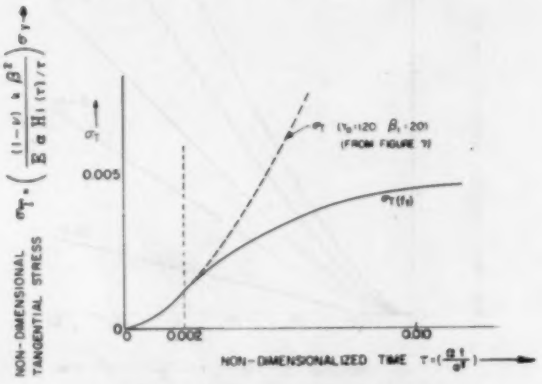

Fig. 8(*b*) Sample tangential stress transient

in Fig. 8(*b*); we subtract from this the same response curve with a dimensionless time delay ($\Delta\tau$) equal to 0.002. The result is the nondimensional tangential stress shown by the solid line in Fig. 8(*b*).

From this curve, the tangential stress one hour ($\tau = 0.01$) after the internal heat generation started is:

$$\sigma_y = 1.51 \times 10^4 \times 0.00045 = 675 \text{ lb/in}^2.$$

Since

$$G_i = \frac{ma^2}{\alpha_d} = \frac{(H_i/t)a^2}{\alpha d} = \frac{[(1 \times 10^{-3})/(714)]\,(50)^2}{(0.007)} = \frac{1}{2}$$

and

$$\lambda = \frac{E\alpha G_i}{(1-\nu)k\beta^2} = \frac{(30 \times 10^6)(7 \times 10^{-6})(1/2)}{(1-0.3)(6 \times 10^{-4})(0.40)^2} = 1.51 \times 10^4$$

It should be observed that the relatively low stress in this problem is due to the original assumption that the wall temperatures rise equally.

KARL A. GARDNER
Chief Engineer,
The Griscom-Russell Company;
(presently, Vice-President—Engineering,
Yuba Consolidated Industries,
Palo Alto, Calif.) Mem. ASME

T. C. CARNAVOS
Manager, Research-Test Department, The Griscom-Russell Company, Massillon, Ohio.
Mem. ASME

Thermal-Contact Resistance in Finned Tubing

Interference-fit finned tubes depend for their heat-transfer capability upon a contact pressure between fin and tube. The bond resistance under such conditions is relatively small compared to the other resistances in the heat-flow path. At elevated temperatures, however, differential thermal expansion between fins and tubes completely relaxes the contact pressure and introduces an additional gap resistance; this may become a significant part of the total resistance to heat transfer. A theoretical method for predicting the gap resistance is derived in terms of the fin and tube dimensions, their physical properties, the fluid temperatures and heat-transfer coefficients, and the initial contact pressure. Test data on five finned-tube units representing embedded, tension-wound, and muff-type fins are given in graphical and tabular form. Very good agreement is found between theory and test in two of the interference-fit units. The other two show only fair agreement.

EXTENDED-SURFACE tubing for heat exchangers is made by many methods but tends to take two basic forms; i.e., one with parallel fins extending axially of the tube, the other with circumferential fins consisting of spaced disks or helically wound ribbon. The former is adapted to fluid flow parallel to the tube axes, the latter to cross flow normal to the tube axes. Several examples of each form are shown in Fig. 1. Gardner and Gould [1][1] have listed and discussed the various methods of manufacture of extended surface and some of their respective advantages and shortcomings.

Briefly, the types of attachment between fins and tubes are:

I Integral.
II Mechanically embedded.
III Welded, brazed, or soldered.
IV Interference fit.
V Mechanically embedded and brazed (II and III).
VI Tension wound and soldered (III and IV).
VII Interference fit bimetal muff (I and IV).

Examples of attachment types II, IV, V, and VII are shown in magnified cross section in Figs. 2, 3, 4, and 5. Each has its field of application within whose bounds it is completely suitable. The simple tension-wound finned tubes in Fig. 3, for example, have the advantage of freedom of choice of tube and fin materials separately, to suit fluid environments and still retain high fin conductivity. The same is true of the extruded muff type of bimetal tube shown in Fig. 5 which may have, for some environments, the added advantage of a protective covering over the core-tube surface. Both have the disadvantage, however, that certain combinations of materials cannot retain the necessary compressive contact between fins and tubes at elevated temperatures.

The integral type of fin—not shown as such, but essentially identical to the outer finned muff alone in Fig. 5—does not have the disadvantage of potential loss of fin-tube contact. However, when made of the most suitable high-conductivity metals, usually copper or aluminum, it is limited in application to suitable combinations of fin-side and tube-side environments and to the moderate temperature ranges within which these materials retain their strength.

The embedded type of finned tube, Fig. 2, has the same advantage as the integral type in that there can be no loss of fin-tube contact. It has the added advantage of combining high-conductivity fin material with any desired high-strength, corrosion-resistant material suitable to the tube-side conditions. The type of finned tubing with embedded and brazed stainless-steel-clad copper fins shown in Fig. 4 was developed for extremely severe temperature and corrosion conditions.

As stated before, each finned-tube type is perfectly suitable to

[1] Numbers in brackets designate References at end of paper.

Contributed by the Heat Transfer Division and presented at the Annual Meeting, Atlantic City, N. J., November 29–December 4, 1959, of THE AMERICAN SOCIETY OF MECHANICAL ENGINEERS.

NOTE: Statements and opinions advanced in papers are to be understood as individual expressions of their authors and not those of the Society. Manuscript received at ASME Headquarters, August 17, 1959. Paper No. 59—A-135.

Nomenclature

a = empirical constant
A_o = total outside surface of test unit, sq ft
b = base contact length per fin, in.
C_1, C_2 = arbitrary constants
d = outside diameter of tube, in.
D = outside diameter of fin, in.
E_f = elastic modulus of fin, psi
E_t = elastic modulus of tube, psi
g = radial gap between fin and tube, in.
G = air-mass velocity at minimum flow area, lb/sec/sq ft
k = thermal conductivity of bulk air stream, Btu/hr/sq ft/(deg F/ft)
k_e = thermal conductivity of entrapped fluid, Btu/hr/sq ft/(deg F/ft)
k_f = thermal conductivity of fin material, Btu/hr/sq ft/(deg F/ft)
K = dimensionless constant, equation (12)
n = empirical constant
p_c = contact pressure between fin base and tube, psi
p_{co} = contact pressure as fabricated between fin base and tube, psi
Q = heat transferred in test unit Btu/hr
r = radius, in.
r_c^* = contact resistance, (Btu/hr/sq ft/deg F)$^{-1}$
r_f = fin-metal resistance, (Btu/hr/sq ft/deg F)$^{-1}$
r_g = gap resistance, (Btu/hr/sq ft/deg F)$^{-1}$
r_{go} = initial gap resistance, (Btu/hr/sq ft/deg F)$^{-1}$

(Continued on next page)

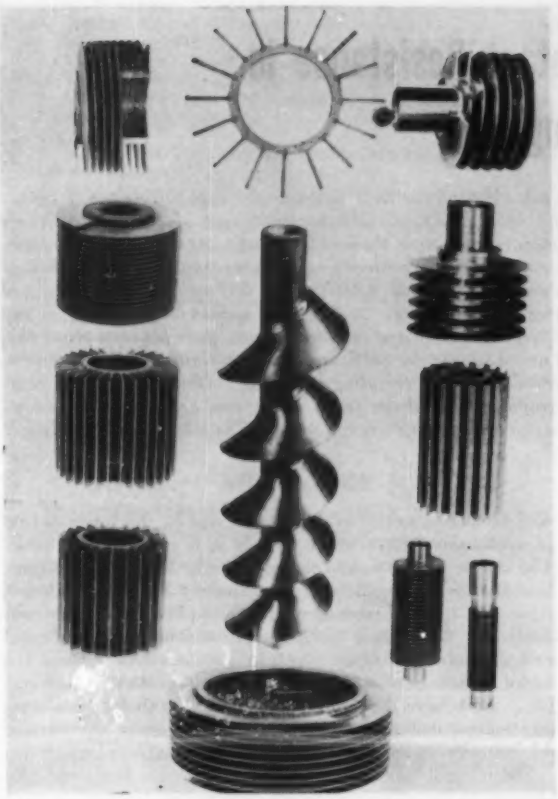

Fig. 1 Some typical forms of extended-surface tubing

its own field of application. The boundaries are quite well defined from the standpoint of ability of the materials to withstand the pressure, temperature, or corrosive nature of the fluids involved. They are ill defined, however, from the standpoint of the maximum tolerable operating temperature level beyond which fin-to-tube contact pressure is completely relaxed, and from the standpoint of the penalty in loss of heat-transfer capacity which must be paid for trespass of this bound.

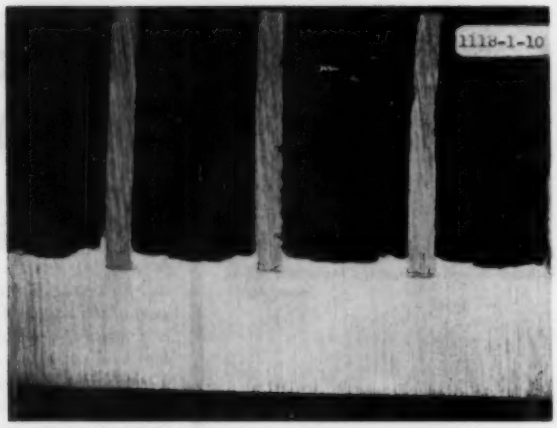

Fig. 2 Magnified cross section of embedded type of fin-tube attachment in a sample taken from Unit A

It is the object of this paper to evaluate, in as general a way as possible, the thermal-bond (or gap) resistance between fins and tubes in terms of known properties of the extended surface, and of the process conditions to which it is subjected.

Literature Survey

The thermal-contact resistance between abutting metal surfaces has been investigated by many authors for almost as many purposes. Effects of contact pressure, surface roughness, nature and pressure of entrapped fluid, and nature of materials have all received attention. Brunot and Buckland [2] were interested in the influence on temperature rating of electrical equipment with laminated metal components. Weills and Ryder [3] were interested in the heat dissipation from aircraft-engine cylinders. Kouwenhoven and Potter [4] measured contact resistance between artificially roughened steel surfaces over a wide range of contact pressures. Cetinkale and Fishenden [5] combined experimental work similar to that of Weills and Ryder with a fairly elaborate theory of contact resistance. Barzelay, Tong, and Holloway [6, 7] were concerned with the ability of aircraft structures to compensate for local aerodynamic heating by conduction to less adversely affected areas.

Estimation of the over-all heat-transfer coefficient from liquid

Nomenclature

r_i = inside fluid film, plus dirt, plus tube-wall resistance, (Btu/hr/sq ft/deg F)$^{-1}$
r_i' = inside fluid film, plus dirt resistance, (Btu/hr/sq ft/deg F)$^{-1}$
r_o = outside fluid film, plus dirt resistance, (Btu/hr/sq ft/deg F)$^{-1}$
r_w = tube-wall-metal resistance, (Btu/hr/sq ft/deg F)$^{-1}$
R = over-all heat-transfer resistance, (Btu/hr/sq ft/deg F)$^{-1}$
R^* = over-all heat-transfer resistance in absence of any gap resistance, (Btu/hr/sq ft/deg F)$^{-1}$
t = tube-wall thickness, in.
t_f = fin-base thickness, in.
T = fin-metal temperature at radius r, deg F
T_o = fin and tube temperature as fabricated, deg F
T_a = ambient fluid bulk temperature, deg F
T_b = fin-base temperature, deg F
T_h = heating medium temperature, deg F
T_w = tube-wall temperature, deg F
u_f = radial displacement at radius r, in.
$u_{f,b}$ = radial displacement of fin base, in.
$u_{t,b}$ = radial displacement of tube OD, in.
U_o = over-all heat-transfer coefficient, Btu/hr/sq ft/deg F
α_f = thermal expansion coefficient of fin material, (deg F)$^{-1}$
α_t = thermal expansion coefficient of tube material, (deg F)$^{-1}$
Δt_m = mean temperature difference between heating medium and ambient fluid, deg F
Δu_f = radial displacement of fin base with respect to initial displacement, in.
Δu_t = radial displacement of tube OD with respect to initial displacement, in.
μ = constant defined by equation (20), (psi)$^{-1}$
ν_f = Poisson ratio of fin material
ν_t = Poisson ratio of tube material
ρ = resistance parameter defined by equation (23), (Btu/hr/sq ft/deg F)$^{-1}$
σ_{fr} = radial stress in fin, psi
σ_{ft} = tangential stress in fin, psi
ϕ = fin efficiency

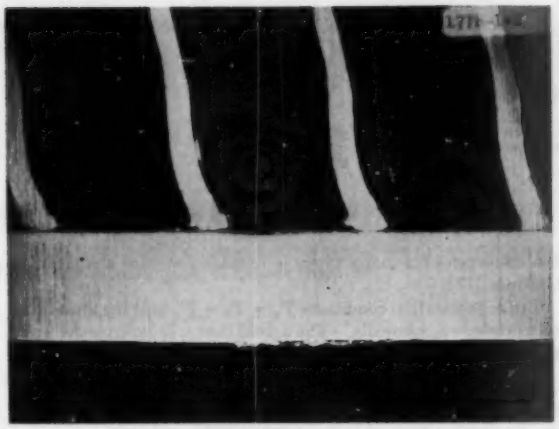

Fig. 3 Magnified cross section of tension-wound type of fin-tube attachment in a sample taken from Unit B

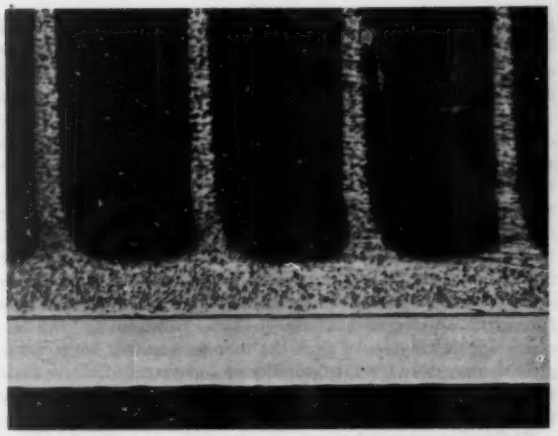

Fig. 5 Magnified cross section of muff type of finned tubing in a sample taken from Unit D

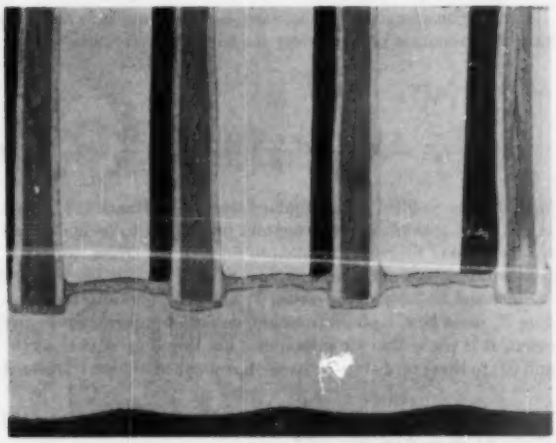

Fig. 4 Magnified cross section of an embedded brazed fin with copper core and stainless-steel cladding

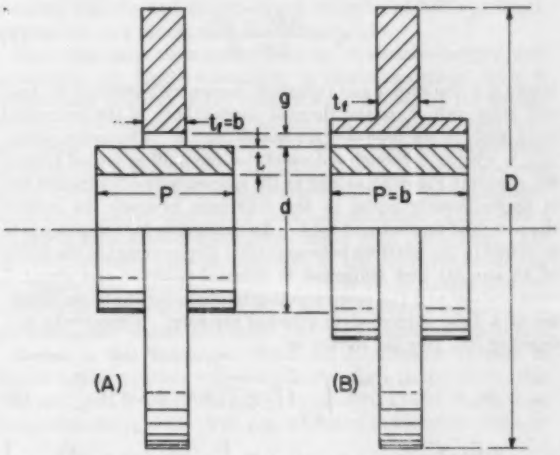

Fig. 6 Idealized interference-fit fin-to-tube junction of (A) the tension wound and (B) the muff type

sodium to boiling water through contacting duplex tubes in an interleakage-proof apparatus described by Boni [8] led to theoretical studies by Mehringer [9], and experimental work by King and Andrews [10]. The over-all coefficients were determined and estimates of the bond resistance were made.

Young, et al. [11] reported on apparatus suitable for quality-control testing of the contact resistance in bimetal muff-type finned tubing. Values of the resistance were given for various metal combinations at low temperatures (180 to 220 F). Using the same apparatus [11] and testing temperatures, Young and Katz [12] studied the effect of thermal cycling to temperatures of 350 and 600 F on the subsequent low-temperature bond resistance of bimetal finned tubing.

Wheeler [13], while this paper was under preparation, reported on an investigation of the thermal-contact resistance between nuclear-reactor fuel elements and their cladding; six additional foreign references on this aspect of the problem were cited.

The foregoing review is somewhat cursory simply because the work done, while of great merit for the purposes prompting it, has relatively little bearing on the subject of the present paper. In all cases, the metal surfaces remained in reasonably intimate contact and, except at very low contact pressures, the bond resistances between smooth surfaces were so low as to be negligible by comparison to the other heat-transfer resistances normally encountered in finned-tube applications. Furthermore, temperature and contact pressure, in those cases where both were investigated, were treated as independent variables.

It is the condition of effectively complete loss of intermetallic contact as a result of thermal relaxation of contact pressure that the authors discuss herein. The resultant gap resistance and its effect on over-all heat-transfer coefficients are the object of study. The only published work on this subject of which the authors have knowledge came about more or less by accident in London, Kays, and Johnson's studies on compact heat-exchanger surfaces [14, 15]. The observed contact resistance in a bimetal finned tube was treated, although inconclusively, in the discussion and closure of the latter reference.

Theoretical Attack

The mechanism of introduction of a thermal gap resistance between fins and tubes of the types illustrated in Figs. 3 and 5, and idealized in Fig. 6, is qualitatively simple. In the first place the tubing as fabricated at or near room temperature has a high contact pressure, of the order of 5000 psi if properly made. The fins are normally made of aluminum, and the tube of steel or admi-

ralty metal so, as the operating temperature is increased, the fins tend to expand away from the tube wall because of their higher expansion coefficient. The tube wall, being in a state of radial compression, follows this expansion and maintains metal-to-metal contact although at decreasing pressure. In general, no significant contact resistance is introduced in this phase; it is present, and increasing, but negligible in comparison with the other resistances in the heat-transfer path. With further increase in tube-metal temperature, however, a point is reached where the contact pressure and intermetallic contacts are so reduced that heat flow must henceforth be through the entrapped fluid. Still further temperature increases open up the gap between fin base and tube wall with consequent increase of heat-flow-path length through the entrapped fluid; on the other hand, the fin then becomes appreciably cooler than the tube wall and so tends, for a given temperature level, to stabilize at a gap somewhat less than would be computed on the basis of a common tube-wall-and-fin temperature.

The quantitative solution is also basically very simple. The gap resistance for the idealized junction shown in Fig. 6(*a*), referred to the fin surface, is given by

$$r_g = \frac{g(D^2 - d^2)}{24k_g\, db} \tag{1}$$

where g is the radial gap (assumed concentric) between fin base and tube wall, k_g is the thermal conductivity of the entrapped fluid, and b is the base contact length per fin. This same expression is adequate, though not exact, for the muff or footed type of fin, shown in Fig. 6(*b*), as long as the spacing between adjacent fins is approximately equal to the difference between the outside diameters of fin foot and tube. An expression for the gap g is to be found in the relations between radial displacement of the inside of an annular disk subjected to internal pressure and elevated temperature and the corresponding relations for the outer diameter of a tube subjected to external pressure. Timoshenko and Goodier [16] give the former as

$$u_f = \frac{(1 + \nu_f)\alpha_f}{r}\int_{d/2}^{r}(T - T_o)r\,dr + C_1 r + \frac{C_2}{r} \tag{2}$$

$$\sigma_{fr} = \frac{\alpha_f E_f}{r^2}\int_{d/2}^{r}(T - T_o)r\,dr - E_f\left[\frac{C_1}{(1-\nu_f)} - \frac{C_2}{(1+\nu_f)r^2}\right] \tag{3}$$

$$\sigma_{ft} = \frac{-\alpha_f E_f}{r^2}\int_{d/2}^{r}(T - T_o)r\,dr - E_f\left[\frac{C_1}{(1-\nu_f)} + \frac{C_2}{(1+\nu_f)r^2}\right] + \alpha_f E_f(T - T_o) \tag{4}$$

where the equations give radial displacement, radial stress, and tangential stress at radius r, and C_1 and C_2 are integration constants. Stresses are considered positive if compressive, and displacement positive if directed away from the tube axis. The equations are valid only when the fin deformations are elastic.

Since the radial stress vanishes at the fin edge ($r = D/2$), and equals the contact pressure p_o at the fin base, the constants may be eliminated with the result that, for the fin base

$$u_{f,b} = \frac{d}{2}\left\{\frac{p_o}{E_f}\left[\frac{D^2 + d^2}{D^2 - d^2} + \nu_f\right] + \frac{8\alpha_f}{(D^2 - d^2)}\int_{d/2}^{D/2}(T - T_o)r\,dr\right\} \tag{5}$$

The integral in equation (5) may be put in more familiar terms by noting that the fin efficiency is defined by

$$\phi = \frac{8}{(D^2 - d^2)(T_b - T_o)}\int_{d/2}^{D/2}(T - T_o)r\,dr \tag{6}$$

It follows that

$$u_{f,b} = \frac{d}{2}\left\{\frac{p_o}{E_f}\left[\frac{D^2 + d^2}{D^2 - d^2} + \nu_f\right] + \alpha_f\left[(T_o - T_o) + \phi\,(T_b - T_o)\right]\right\} \tag{7}$$

Fin efficiencies for many types of extended surface are given by Gardner [17].

Under fabrication conditions $T_o = T_b = T_w$, and the initial contact pressure p_{co} prevails. The actual *change* in fin-base deformation referred to fabrication conditions as a datum thus becomes

$$\Delta u_f = \frac{d}{2}\left\{\alpha_f[(T_o - T_o) + \phi(T_b - T_o)] + \frac{(p_o - p_{co})}{E_f}\left[\frac{D^2 + d^2}{D^2 - d^2} + \nu_f\right]\right\} \tag{8}$$

Similar consideration on the tube, assuming uniform distribution of the contact pressure over the tube wall,[2] result in

$$\Delta u_t = \frac{d}{2}\left\{\alpha_t(T_w - T_o) - \frac{(p_o - p_{co})}{E_t}\frac{t_f}{P}\left[\frac{d^2 + (d - 2t)^2}{d^2 - (d - 2t)^2} - \nu_t\right]\right\} \tag{9}$$

This may be verified from standard texts, e.g., Roark [18], bearing in mind that the fin-base contact pressure is to be multiplied by the ratio of fin-base thickness to fin pitch to obtain the effective uniform external pressure.

Since the fin-base temperature T_b and the tube-wall temperature T_w must be computed from known fluid temperatures in any event, it is preferable for subsequent use to reduce equations (8) and (9) to these terms. The over-all resistance to heat transfer is

$$R = \frac{1}{U_o} = R^* + r_g \tag{10}$$

where

$$R^* = \frac{r_o}{\phi} + r_o^* + r_i \tag{11}$$

R^* is thus the over-all resistance which obtains under conditions where there is no observable gap resistance. The resistances r_o and r_i contain not only the outside and inside fluid-film resistances but also the appropriate fouling resistances and, in the case of r_i, the core-tube-metal resistance, all referred to the total outside surface. The term r_o^* is the *bond* resistance whose effect, in the reduction of most heat-transfer tests, cannot be segregated from that of r_o. It is listed separately merely to call attention to the fact that the *gap* resistance r_g subsequently computed from equation (10) is low by the small uncertain value of r_o^*.

Since the fin efficiency is normally high in finned-tube systems, an observation by Dusinberre [19] may be utilized to simplify equation (11) further. For fin efficiencies of the order of 0.8 or higher a very good approximation is given by

$$\phi = \frac{1}{\left[1 + \frac{K(D - d)^2}{24k_f l_f r_o}\right]} \tag{12}$$

[2] This assumption is strictly valid only when the tube diameter, tube thickness, and fin spacing are so related that $P < 0.43\sqrt{t(d - t)}$, in which case the variation in radial displacement along the tube between fins is negligible.

where K is a constant depending only on the fin dimensions. Thus letting

$$r_f = \frac{K(D-d)^2}{24k_f t_f} \qquad (13)$$

$$\frac{r_o}{\phi} = (r_o + r_f),$$

and

$$R^* = (r_o + r_o^* + r_f + r_i) \qquad (14)$$

Since the potential drops in a series circuit are directly proportional to the resistances, it follows that

$$(T_w - T_o) = (T_b - T_o) - \frac{r_i}{(R^* + r_g)}(T_b - T_o) \qquad (15)$$

and

$$\phi(T_b - T_o) = \frac{r_o}{(R^* + r_g)}(T_b - T_o) \qquad (16)$$

With these substitutions, equations (8) and (9) become

$$\Delta u_f = \frac{d}{2}\left\{\alpha_f\left[(T_b - T_o) - \left(1 - \frac{r_o}{R^* + r_g}\right)(T_b - T_o)\right] + \frac{(p_o - p_{oo})}{E_f}\left[\frac{D^2 + d^2}{D^2 - d^2} + \nu_f\right]\right\} \qquad (17)$$

$$\Delta u_i = \frac{d}{2}\left\{\alpha_i\left[(T_b - T_o) - \left(\frac{r_i}{R^* + r_g}\right)(T_b - T_o)\right] - \frac{(p_o - p_{oo})}{E_i}\frac{t_f}{P}\left[\frac{d^2 + (d-2t)^2}{d^2 - (d-2t)^2} - \nu_i\right]\right\} \qquad (18)$$

and their difference,

$$(\Delta u_f - \Delta u_i) = \frac{d}{2}\left\{(\alpha_f - \alpha_i)(T_b - T_o) - \left[\alpha_f\left(1 - \frac{r_o}{R^* + r_g}\right) - \alpha_i\left(\frac{r_i}{R^* + r_g}\right)\right](T_b - T_o) + \mu(p_o - p_{oo})\right\} \qquad (19)$$

where

$$\mu = \left\{\frac{1}{E_f}\left[\frac{D^2 + d^2}{D^2 - d^2} + \nu_f\right] + \frac{1}{E_i}\frac{t_f}{P}\left[\frac{d^2 + (d-2t)^2}{d^2 - (d-2t)^2} - \nu_i\right]\right\} \qquad (20)$$

a constant dependent only on fin and tube properties. Negative values of $(\Delta u_f - \Delta u_i)$ are of course not permissible; only zero or positive values have significance.

Contact Pressures and Radial Stresses. When $(\Delta u_f - \Delta u_i) = 0$, fins and tubes are in contact and the contact resistance is either negligibly small, or inextricably associated with r_o. Equation (19) may then be rearranged to give

$$p_o = p_{oo} - \frac{1}{\mu}\left\{(\alpha_f - \alpha_i)(T_b - T_o) - \left[\alpha_f\left(1 - \frac{r_o}{R^*}\right) - \alpha_i\frac{r_i}{R^*}\right](T_b - T_o)\right\} \qquad (21)$$

Negative values of p_o do have significance for the integral, embedded, and bonded types of fin attachment. They represent the radial tensile stress in the fin base and in the bonding material and thus provide a quantitative measure of the ability of the bond to withstand the operating conditions. Negative values of p_o for the interference-fit types of fin attachment mean only that a gap has opened between fin base and tube wall.

Positive values of p_o represent true contact pressures in all types of fin attachment. Values exceeding p_{oo} (as may be brought about by certain temperature conditions) should be viewed with suspicion, however, since they may take the fin base or tube wall into a partially plastic condition. Equation (21), based on *elastic* theory, would therefore not apply.

Nadai [20] shows, for an ideally plastic material, that incipient plasticity at the inner circumference of an annular disk is just reached when the internal pressure is 0.577 σ_{yf}, where σ_{yf} is the yield stress observed in a simple tensile test, and that a maximum pressure of 1.155 σ_{yf} is reached when a plastic zone is created out to 1.75d. It seems unlikely that a zone of such extent could be created, or maintained, in the thin high fins of commercial extended-surface tubing. The maximum possible initial contact pressure, if fin-limited, is probably of the order of 0.67 σ_{yf}, which corresponds to a plastic zone boundary at 1.1d.

Since the most commonly used fin materials—copper and aluminum—are highly susceptible to strain-hardening, there is considerable doubt as to the value of σ_{yf} produced by the finning process. There is *no* doubt, however, that no initial contact pressure higher than that computed for the dead soft annealed material can be relied upon if aluminum fins of nonheat-treatable alloys are subjected to temperatures over 400 F for appreciable lengths of time, or over 600 F even momentarily. These alloys revert to their annealed condition under such conditions. For the commercially used fin materials in the annealed condition, σ_{yf} ranges from 5000 to 6000 psi. If there is any danger of overtemperature, however transient, it would therefore be unwise to assume p_{oo} any higher than about 3500 psi for interference-fit fins.

Contact or Gap Resistance. With the interference-fit type of finned tubing, positive values of $(\Delta u_f - \Delta u_i)$ given by equation (19) are equal to the radial gap g of equation (1) and, under these circumstances $p_o = 0$. The gap resistance is therefore given by

$$r_g = \rho\left\{(\alpha_f - \alpha_i)(T_b - T_o) - \mu p_{oo} - \left[\alpha_f\left(1 - \frac{r_o}{R^* + r_g}\right) - \alpha_i\left(\frac{r_i}{R^* + r_g}\right)\right](T_b - T_o)\right\} \qquad (22)$$

where

$$\rho = \frac{(D^2 - d^2)}{48bk_e} \qquad (23)$$

The exact solution for r_g would involve a quadratic equation. In any practical application of finned tubing, however, r_g must be a reasonably small fraction of R^*. Equation (22) may then be linearized by writing

$$\frac{1}{(R^* + r_g)} = \frac{1}{R^*}\left(1 - \frac{r_g}{R^*}\right)$$

which involves a maximum error of only 6 per cent in those terms containing $(R^* + r_g)$ for values of r_g/R^* as high as 0.25. With this simplification,

$$r_g = R^*\left\{\frac{[(\alpha_f - \alpha_i)(T_b - T_o) - \mu p_{oo}] - \left[\alpha_f\left(1 - \frac{r_o}{R^*}\right) - \alpha_i\frac{r_i}{R^*}\right](T_b - T_o)}{\frac{R^*}{\rho} + \left[\alpha_f\frac{r_o}{R^*} + \alpha_i\frac{r_i}{R^*}\right](T_b - T_o)}\right\} \qquad (22a)$$

It should be emphasized at this point that equations (22) and (22*a*) are based upon an idealized model in which:

1 The tube fluid temperature is constant.
2 The fin-side fluid temperature is constant.
3 The fin base and tube wall are concentric.
4 The contacting length per fin b is perfectly smooth and parallel to the tube wall.
5 The influence of the fluid pressures is negligible as far as tube-wall deformations are concerned.

None of these conditions is strictly true in practice, although each may be closely approximated.

The first condition limits application of equation (22*a*) to increments of tube length in which the change in tube fluid temperature is small. This might be the entire tube length in condensers, or only a few feet in liquid or gas coolers with long cooling ranges.

The second condition is reasonably well met, for a single tube layer in which gap resistance exists, by defining $(T_h - T_o)$ as the logarithmic mean value for that layer. With condensers where T_h is constant over all tube layers and high enough to produce a gap resistance in all of them, the logarithmic mean temperature difference for the exchanger as a whole may be used for $(T_h - T_o)$. An attempt was made to estimate the effective mean $(T_h - T_o)$ value when the local value is large enough at the ambient-fluid inlet to suppress any gap resistance in the inlet layers, but is reduced in subsequent layers to a level where such resistance may be introduced. Promising preliminary results were obtained, but not soon enough, or specific enough, for use in this paper. Little error seems to be involved, with condensers at least, in assuming that *all* rows are affected and that the over-all logarithmic mean temperature difference may be used. This does not necessarily hold for *coolers*, in which the outlet layers (downstream) are presented with coolant from progressively hotter layers.

The third (concentricity) condition is shown in the Appendix to be of relatively little consequence. The tendency to reduce the value of ρ and hence, to a lesser extent, of r_g amounts only to a few per cent when averaged over all possible values of the eccentricity.

It is also shown in the Appendix that the fourth condition—unevenness over the contact length—may have a very drastic effect on the gap resistance.

The fifth condition—influence of tube and ambient fluid pressures—may be dealt with to a good approximation by adding $0.85[1 - 1.6(t/d)](P/t_f)p_i$ to the initial contact pressure in equations (22) and (22*a*), et seq. It is likely that this is a refinement beyond the accuracy of the equations, however.

Finally, for the sake of completeness, a case is treated which is forsworn by all manufacturers but which may come about through abuse of an initially satisfactory product; namely, the case in which the initial *contact pressure* is completely lost and replaced instead by an initial *gap resistance*. The equations analogous to equations (22) and (22*a*) become

$$r_g = r_{go} + \rho \left\{ (\alpha_f - \alpha_t)(T_h - T_o) - \left[\alpha_f \left(1 - \frac{r_o}{R^* + r_g} \right) - \alpha_t \left(\frac{r_i}{R^* + r_g} \right) \right] (T_h - T_o) \right\} \quad (24)$$

and

$$r_g = R^* \left\{ \frac{\left[(\alpha_f - \alpha_t)(T_h - T_o) + \frac{r_{go}}{\rho} \right] - \left[\alpha_f \left(1 - \frac{r_o}{R^*} \right) - \alpha_t \frac{r_i}{R^*} \right] (T_h - T_o)}{\frac{R^*}{\rho} + \left[\alpha_f \frac{r_o}{R^*} + \alpha_t \frac{r_i}{R^*} \right] (T_h - T_o)} \right\} \quad (24a)$$

It can be seen, by comparison of terms in equations (22*a*) and (24*a*), that (r_{go}/ρ) is directly comparable to $(-\mu p_{eo})$, and vice versa.

Experimental Apparatus and Procedure

The apparatus used to provide heat-transfer data for this study is shown in Fig. 7. A centrifugal blower forced atmospheric air through a heater section, a calming duct section, the test unit, and finally through an ASME long radius-low ratio nozzle. Condensing steam was used as the heating medium inside the tubes. The steam entered the top of the unit shown, condensed on the inside of the finned tubes, and was subcooled prior to weighing. A seal pot was interposed between the test unit and the subcooler. The entire test circuit was insulated thoroughly on both steam and air sides.

One typical test unit is shown in Fig. 8. Five such units were tested in the course of this investigation. In all cases the test core consisted of four layers of finned tubes in the direction of air flow, with tubes staggered in alternate layers, and with a square face area 21 in. to the side. Significant dimensions of the test cores are listed in Table 1. Air stops were used in the open end of each layer to minimize edge effects. Materials were carbon steel for the tubes and aluminum for the fins. A sample of each type of finned tube was chosen at random to secure magnified cross sections of the fin-to-tube attachment, as shown in Figs. 2, 3, 5, 9, and 10.

All of the units investigated were tested under as nearly identical conditions as possible. The first group of runs was made with five air-mass velocities ranging from 0.6 to 3.0 lb/sec/sq ft while maintaining the steam temperature constant at 225 F and the inlet air at approximately 110 F. The second, third, and fourth groups were run in the same manner except that the steam temperatures were held at 260, 315, and 380 F, respectively. It should be noted that the air-outlet temperature (and hence the average) decreased with increasing air velocity in these runs. The fifth group of runs was made holding the steam temperature constant at 380 F as in the fourth group, but with the air-outlet temperature held at 330 F. Under these conditions, of course, the average air temperature *increased* with increasing air velocity.

Data were recorded at five minute intervals for a minimum of three readings after steady state was achieved. For purposes of these tests the criterion of "steady state" was considered to be absence of any variations exceeding 1 deg F in any of the terminal temperatures for a period of ten minutes. No data leading to heat-balance discrepancies greater than 5 per cent were considered worth further analysis.

The over-all heat-transfer coefficients were calculated from

$$U_o = Q/A_o \Delta t_m$$

where the subscript o indicates the total outside surface as the reference surface. Although equation (14) lumps tube-fluid film and tube-wall resistances together for simplicity in presentation, the data must be analyzed on the basis of the following relation:

$$R = \frac{A_o \Delta t_m}{Q} = (r_o + r_o^* + r_g) + r_f + r_i' + r_w \quad (25)$$

in which r_i' and r_w are the aforesaid fluid and wall resistances, both referred to the total outside surface.

The condensing steam film resistance r_i' was evaluated in

Table 1 Test unit characteristics

	Unit[a]				
	A	B	C	D	E
Tube pitch in layer, in.	2.375	2.375	2.375	2.125	2.625
Spacing between layers, in.	2.406	2.406	2.406	2.094	2.344
Fin pitch, P, in.	0.125	0.125	0.125	0.111	0.111
Fin OD, D, in.	2.236	2.264	2.255	1.979	2.296
Muff OD, in.	[b]	[c]	1.094	1.087	1.094
Tube OD, d, in.	1.001	1.001	1.003	1.001	1.002
Tube ID, $d - 2t$, in.	0.828	0.825	0.834	0.892	0.905
Fin-tip thickness, in.	0.016	0.009	0.012	0.011	0.013
Fin-base thickness, t_f, in.	0.016	0.017	0.025	0.023	0.030
Number of tubes	30	30	30	36	30
Face area, sq ft	2.78	2.79	2.79	3.07	3.07
Minimum free-flow area, sq ft	1.34	1.38	1.23	1.26	1.33
Total outside surface, sq ft	231.7	237.5	227.1	218.5	264.6
Characteristic $\mu \times 10^6$ (Eq. 20)	[b]	0.203	0.214	0.260	0.266
Characteristic ρ @ 375 F (Eq. 23).[d]	[b]	254	35	28	41

[a] Finned tubing was obtained from the following sources:
Units A, B—The Griscom-Russell Company, Massillon, Ohio.
Unit C—The Hudson Engineering Corp., Houston, Tex.
Units D, E—Wolverine Tube, Division of Calumet and Hecla, Inc., Detroit, Mich. The tubing for Unit E was in a developmental stage at the time it was obtained.

[b] Mechanically embedded fins.

[c] Tension-wound fins.

[d] The value of ρ varies inversely as the thermal conductivity of the entrapped fluid at the fin base temperature so these values apply only to runs of groups 4 and 5.

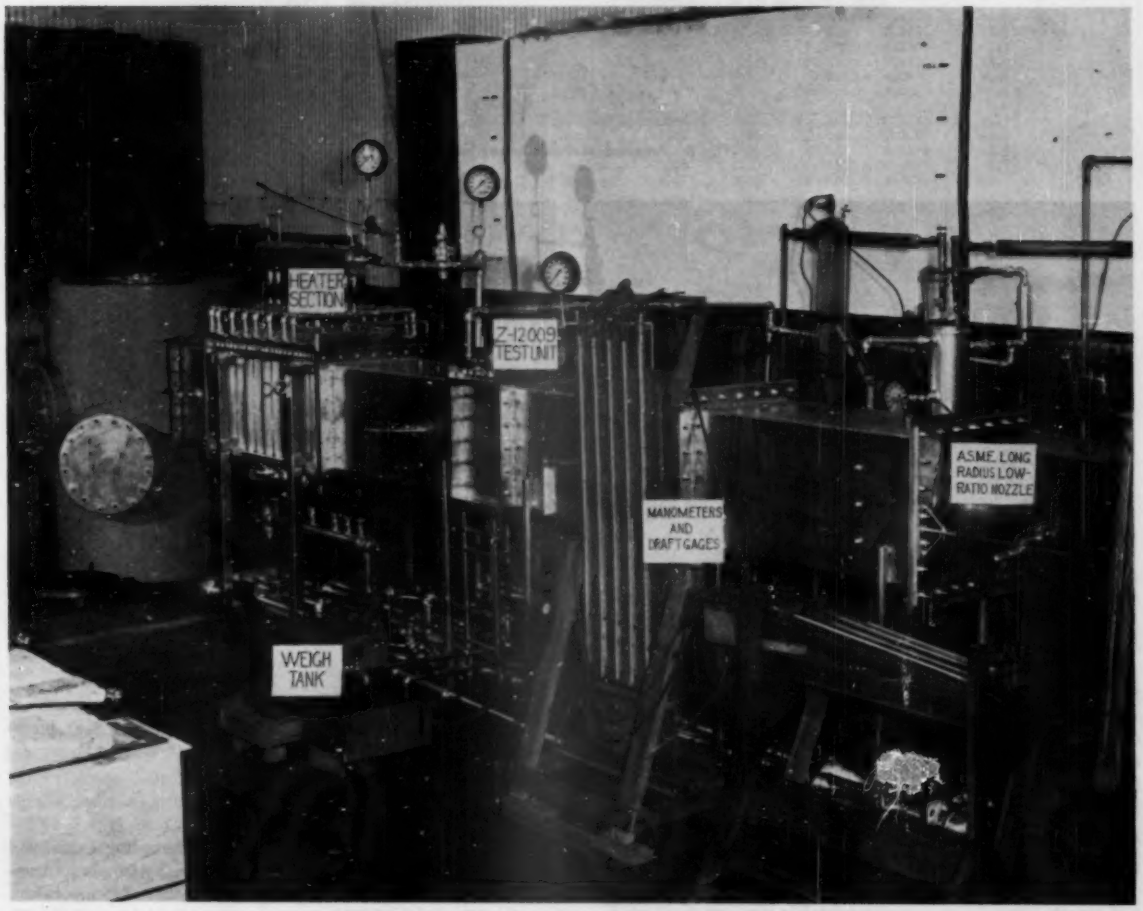

Fig. 7 View of test apparatus used in this investigation

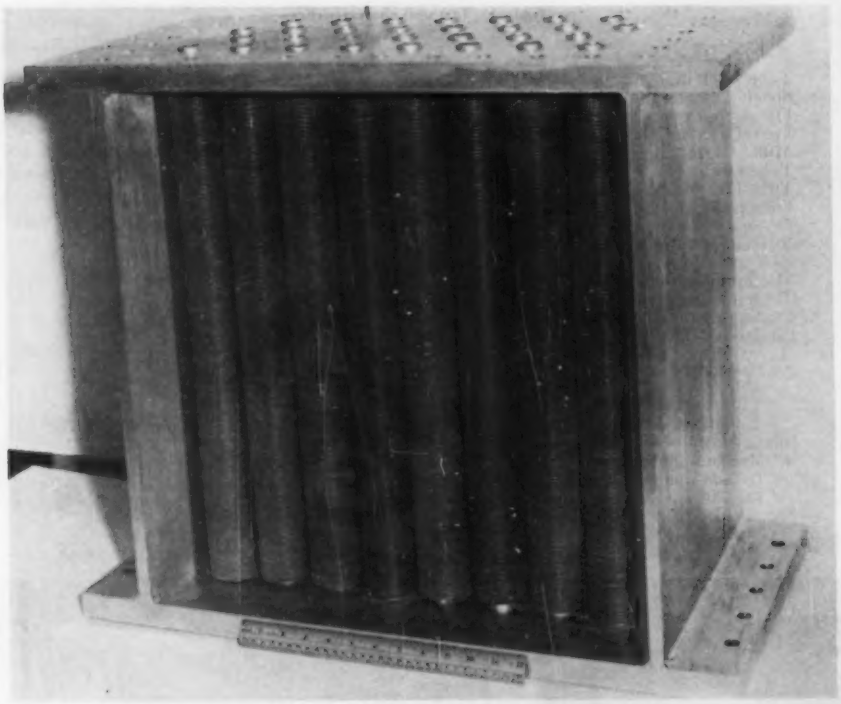

Fig. 8 A typical test unit finned-tube core

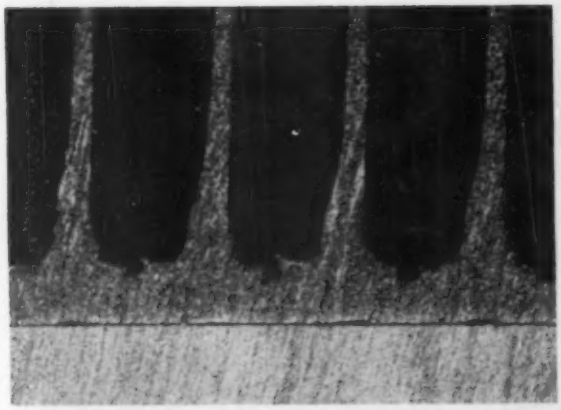

Fig. 9 Magnified cross section of a fin-tube junction sample taken from Unit C

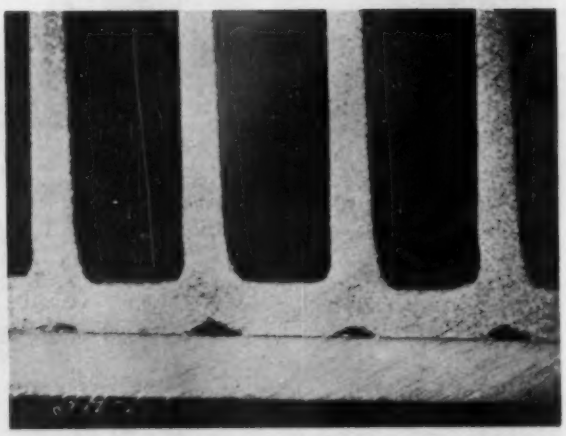

Fig. 10 Magnified cross section of a fin-tube junction sample taken from Unit E

accordance with the Nusselt type equation recommended by McAdams [21]. No fouling resistance was included.

The tube-wall resistance r_w was calculated as for a bare tube and then multiplied by the ratio of total outside surface to bare-tube surface to make it applicable to the same reference surface as the other resistances.

The fin resistance r_f was evaluated from equation (13), using a K-value appropriate to the fin type under consideration; this value ranged from 0.5 to 0.67.

The thermal conductivities used in the two foregoing resistances were 25 for carbon steel and 120 for aluminum.

With R, r_i', r_w, and r_f known, the sum of the terms within parentheses in equation (25) was obtained by difference. The resultant sum of air film, gap, and/or bond resistances is shown as a function of air-mass velocity by the symbols in Figs. 11(a–e), inclusive, for test units identified as Units A, B, C, D, and E, respectively, in Table 1.

Discussion of Results

The experimental results described in the foregoing section are susceptible to analysis for the gap resistance r_g by simple subtraction of the values of $(r_o + r_o^*)$ obtained for the low-temperature runs (i.e., those in which there was no trend to higher values with increasing temperature) from the values of $(r_o + r_o^* + r_g)$ obtained from the high-temperature runs at the same air-side

Table 2 Experimental and derived data on thermal-contact resistance

Unit & Group	Steam Temp deg F	Inlet Air Temp deg F	Outlet Air Temp deg F	Air Mass Velocity lbs/sec/ft²	Exptl Value $(r_o+r_c+r_g)$	Film & Bond Resist (r_o+r_c)	Exptl Gap Resist r_g	Initial Contact Press p_{co}	Calcd Gap Resist r_g	Calcd Value $(r_o+r_c+r_g)$	% Error Calcd $(r_o+r_c+r_g)$
	1	2	3	4	5	6	7	8	9	10	11
B3	315.7	106.5	261.0	0.638	0.1847	0.1669	0.0178	6348	0.0187	0.1856	+0.5
	315.7	111.9	249.2	0.908	0.1503	0.1369	0.0134	6197	0.0117	0.1486	-1.1
	315.7	112.1	237.1	1.254	0.1201	0.1140	0.0061	6227	0.0051	0.1191	-0.8
	315.7	114.1	216.6	2.154	0.0874	0.0842	0.0032	(5734)	0.0000	0.0842	-3.7
	315.7	115.5	207.2	2.812	0.0745	0.0724	0.0021	(5458)	0.0000	0.0724	-3.1
B4	381.8	118.2	301.0	0.636	0.2086	0.1647	0.0439	6682	0.0453	0.2100	+0.7
	380.3	114.3	283.0	0.905	0.1681	0.1350	0.0331	6522	0.0315	0.1665	-1.0
	379.6	101.5	265.4	1.231	0.1378	0.1142	0.0236	6319	0.0208	0.1350	-2.0
	380.6	118.3	244.4	2.169	0.0950	0.0829	0.0121	6286	0.0115	0.0944	-0.6
	380.5	117.4	232.0	2.789	0.0806	0.0718	0.0088	6030	0.0060	0.0778	-3.5
B5	380.0	241.1	327.9	0.627	0.2546	0.1604	0.0942	6185	0.0926[a]	0.2520[a]	-1.0
	381.5	269.3	328.8	0.874	0.2334	0.1322	0.1012	6061	0.0952[a]	0.2274[a]	-2.6
	380.7	281.0	326.1	1.219	0.2071	0.1089	0.0982	6063	0.0928[a]	0.2018[a]	-2.6
	381.1	298.0	325.6	2.018	0.1755	0.0812	0.0943	6216	0.0937[a]	0.1749[a]	-0.3
	381.5	305.5	327.9	2.569	0.1645	0.0704	0.0941	6210	0.0932[a]	0.1636[a]	-0.6
C4	381.9	128.7	314.0	0.705	0.1795	0.1617	0.0178	6000	0.0170	0.1787	-0.4
	381.5	126.9	302.1	0.999	0.1438	0.1320	0.0118	6644	0.0147	0.1467	+2.0
	380.3	125.0	289.2	1.334	0.1191	0.1121	0.0070	7120	0.0124	0.1245	+4.5
	381.1	125.6	260.8	2.345	0.0850	0.0814	0.0036	7061	0.0082	0.0896	+5.5
	380.7	129.4	250.4	3.013	0.0723	0.0705	0.0018	7134	0.0066	0.0771	+6.6
C5	381.5	196.0	335.8	0.680	0.1792	0.1617	0.0175	6470	0.0197	0.1814	+1.2
	382.1	215.7	329.5	0.971	0.1515	0.1309	0.0206	5831	0.0187	0.1496	-1.5
	381.0	252.4	330.2	1.313	0.1360	0.1089	0.0271	4814	0.0187	0.1276	-6.2
	382.7	281.8	330.1	2.211	0.1079	0.0801	0.0278	4656	0.0182	0.0983	-8.9
	382.5	290.6	330.1	2.873	0.0969	0.0688	0.0281	4980	0.0178	0.0866	-10.6
D4	382.2	123.6	322.6	0.667	0.1672	0.1591	0.0081	6371	0.0139	0.1730	+3.5
	380.4	126.1	307.6	0.958	0.1380	0.1284	0.0096	5760	0.0119	0.1403	+1.7
	381.7	125.7	293.8	1.306	0.1141	0.1066	0.0075	5955	0.0106	0.1172	+2.7
	379.9	122.1	264.3	2.326	0.0820	0.0754	0.0066	5455	0.0072	0.0826	+0.7
	380.8	120.6	253.1	2.927	0.0710	0.0657	0.0053	5526	0.0060	0.0717	+1.0
D5	380.4	134.4	327.7	0.663	0.1660	0.1595	0.0065	6608	0.0140	0.1735	+4.5
	380.9	184.4	325.1	0.946	0.1441	0.1272	0.0169	4795	0.0136	0.1408	-2.3
	382.0	227.4	326.4	1.313	0.1217	0.1033	0.0184	4601	0.0137	0.1170	-3.9
	382.3	266.3	328.8	2.215	0.0950	0.0744	0.0206	4203	0.0133	0.0877	-7.7
	381.9	278.6	328.4	2.817	0.0858	0.0641	0.0217	3965	0.0130	0.0771	-10.2
E3	315.7	125.8	270.3	0.863	0.1433	0.1293	0.0140	4215	0.0173	0.1466	+2.3
	315.7	127.3	260.0	1.237	0.1181	0.1043	0.0138	3933	0.0134	0.1177	-0.3
	315.6	124.7	249.6	1.657	0.0989	0.0875	0.0114	3947	0.0111	0.0986	-0.3
	315.6	120.6	242.2	1.987	0.0873	0.0786	0.0087	4077	0.0096	0.0882	+1.0
	315.7	120.1	230.1	2.765	0.0710	0.0645	0.0065	4041	0.0071	0.0715	+0.7
E4	380.8	123.3	316.6	0.887	0.1472	0.1257	0.0215	4439	0.0245	0.1502	+2.0
	380.6	122.8	300.4	1.210	0.1276	0.1044	0.0232	3838	0.0212	0.1256	-1.6
	379.8	125.3	287.4	1.631	0.1046	0.0875	0.0171	4234	0.0182	0.1057	+1.1
	381.8	126.9	280.9	1.925	0.0939	0.0792	0.0147	4368	0.0168	0.0960	+2.2
	379.8	130.3	263.7	2.769	0.0759	0.0637	0.0122	4212	0.0132	0.0769	+1.3
E5	381.7	194.0	329.2	0.915	0.1532	0.1215	0.0317	3647	0.0280	0.1495	-2.4
	381.3	227.5	329.2	1.188	0.1372	0.1027	0.0345	3346	0.0260	0.1307	-4.7
	381.5	248.5	329.2	1.560	0.1199	0.0868	0.0331	3500	0.0276	0.1144	-4.6
	381.5	256.5	327.5	1.872	0.1089	0.0775	0.0314	3627	0.0269	0.1044	-4.1
	381.7	278.1	329.0	2.639	0.0932	0.0615	0.0317	3582	0.0266	0.0881	-5.5

[a] Values computed from true quadratic solution of equation 22, not linear approximation of equation 22A.

mass velocity, making the appropriate correction for air thermal conductivity. For this latter purpose, all low-temperature data for a given test unit were given a least-mean-square fit to an equation of the form

$$(r_o + r_c^*) = \frac{a}{G^n k^{1-n}} \tag{26}$$

The value of $(r_o + r_c^*)$ for the actual mass velocity and thermal conductivity of each high-temperature test point was calculated from this equation, and r_g obtained by difference. Values of r_g thus computed are shown in column 7 in Table 2.

The simple form of equation (26) is justified by the fact that both specific heat and Prandtl number of air are essentially constant throughout the temperature range investigated. Maximum deviations were small, ranging from +1.1 and −1.8 per cent for Unit E to +3.9 and −4.5 per cent for Unit D. The absence of any significant temperature-dependent bond resistance in these basic values is thus confirmed.

Bond Resistance. In view of the higher resistances observed in Units B and C as compared to Unit A, even in the low-temperature runs, it is tempting to conclude that the difference represents the bond resistance r_c^* inherent in the tension-wound and muff types of finned-tube construction. (Units D and E were not sufficiently similar in geometry to Unit A to warrant any such conclusion.) Values of approximately 0.01 for tension-wound and 0.015 for muff-type fins would thus be indicated; referred to the surfaces at which they occur, rather than the outside surface, these resistances would be 0.00008 and 0.0009, respectively. There are sufficient differences in detail, however—surface roughness, straightness of fins, and so on—to suggest that it would be unwise to ascribe all of the observed difference to bond resistance; some of it is no doubt due to slight variances in air-film resistance.

With the actual gap resistances known, it is possible to apply a rather severe test to the theoretical equation. The solution of equation (22) for the initial contact pressure is

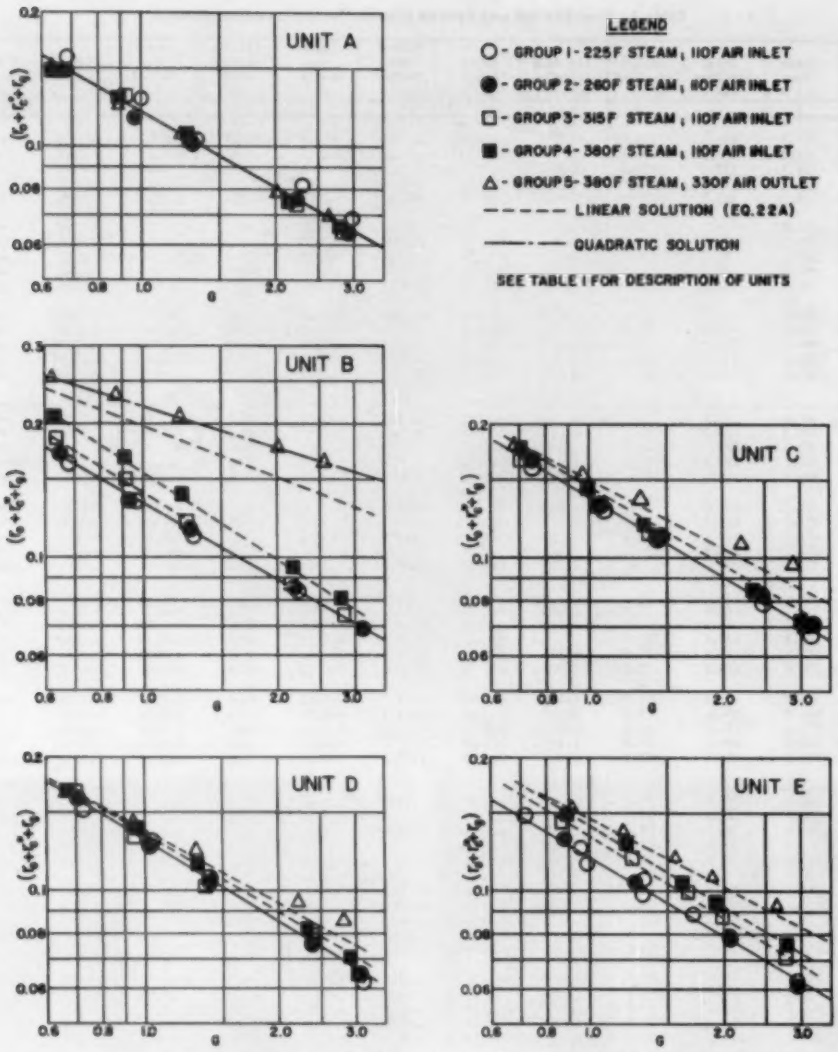
UNIT A
UNIT B
UNIT C
UNIT D
UNIT E
LEGEND
○ - GROUP 1 - 225F STEAM, 110F AIR INLET
● - GROUP 2 - 260F STEAM, 80F AIR INLET
□ - GROUP 3 - 315F STEAM, 110F AIR INLET
■ - GROUP 4 - 380F STEAM, 110F AIR INLET
△ - GROUP 5 - 380F STEAM, 330F AIR OUTLET
LINEAR SOLUTION (EQ. 22A)
QUADRATIC SOLUTION
SEE TABLE I FOR DESCRIPTION OF UNITS

Fig. 11 Experimental results taken on Units, A, B, C, D, and E compared with theoretical prediction of the sum of film, bond, and gap resistances

$$p_{co} = \frac{1}{\mu}\left\{(\alpha_f - \alpha_t)(T_h - T_o) - \left[\alpha_f\left(1 - \frac{r_o}{R^* + r_g}\right) - \alpha_t\left(\frac{r_i}{R^* + r_g}\right)\right](T_h - T_a) - \frac{r_g}{\rho}\right\} \quad (27)$$

Obviously, neither T_o nor p_{co} should be influenced by the test conditions since they depend only on fabrication conditions. Therefore, *regardless of the conditions under which the tests were run*, the value of the initial contact pressure from equation (27) should be the same for a given tube bundle. (This statement must be qualified if $T_h > 400$ F, in view of possible annealing, or if the tube-side pressure is large enough to contribute appreciably to the computed contact pressure.) Since T_h, r_o, r_g, and T_a all varied considerably in the tests, the constancy of p_{co} should be a sensitive indication of the validity of the equations derived in the theoretical section.

Contact Pressure. Computed values of the initial contact pressure are shown in column 8 in Table 2. These were all based on an expansion coefficient of 6.7×10^{-6} for steel and 13.5×10^{-6} for aluminum and, in the same order, elastic moduli of 29.5×10^6 and 10.1×10^6. No correction for tube-side pressure was applied; if it had been, the pressures would all tend to be lower by about 200 psi for the runs of group 3, and about 500 psi for groups 4 and 5.

Quite satisfactory constancy is shown for Units B and E, although group E5 differs somewhat from groups E3 and E4; the variation within each group is slight, except for group B3 in which it is thought the last two runs had only partial gap resistance. Units C and D, however, exhibit systematic trends within each group of runs which indicate that either the theoretical equations, or the data put into them, leave something to be desired. In view of the satisfactory results obtained on Unit B, whose tension-wound fins closely approach the idealized attachment in Fig. 6(*a*), the authors believe these trends may be due to neglect of the contribution of the basic muff wall to the initial

contact pressure for Units C, D, and E. As can be seen from Fig. 10, Unit E had rather incomplete contact between muff and tube wall; this may account for the fact that it behaved more like Unit B than the other two finned-muff units; the manufacturers of this tubing advise that this particular size was in a developmental stage at the time it was obtained.

Gap Resistance. The fact that there is less than perfect agreement with theory, as far as the constancy of p_{ec} is concerned, detracts little from the utility of the basic equations. Using the arithmetic average of all the p_{ec}-values given in column 8 in Table 2 for each unit, r_g was calculated for each run from equation (22*a*). The results are tabulated in column 9 and may be compared to the experimental values in column 7. Some of the discrepancy, particularly at large r_g, is attributable to the error in the linear approximation to a quadratic solution inherent in equation (22*a*); this equation is not accurate when r_g is of the same order of magnitude as r_c.

Combined Resistances. The quantity of chief interest to the designer of finned-tube heat exchangers is the sum $(r_o + r_c^* + r_g)$—the accuracy of any component of this sum is of academic interest, but the accuracy of the sum itself is of primary importance to reliable rating. Column 10 in Table 2 shows the calculated values of this quantity as obtained by adding the computed gap resistance of column 9 to the values of $(r_o + r_c^*)$ from column 6. These are to be compared to the observed quantities in column 5. The percentage error in the calculated values of $(r_o + r_c^* + r_g)$ is given in the last column in Table 2. The comparison of actual data with semitheoretical prediction is also shown graphically in Figs. 11(*b*–*e*), where the dashed lines represent the locus of computed points from Table 2. ("Semitheoretical" is used because the applicable initial contact pressure is itself determined from the heat-transfer tests. However, any one reliable data point could have provided this value, or it could have been determined by nonheat-transfer methods.)

In general the agreement between theory and observation is good. One feature in Figs. 11(*b*) and 11(*e*) which may be puzzling at first glance is the difference in slope of the data points of group 5, as compared to those of groups 3 and 4. The explanation is, as mentioned before, that the average air temperature is decreasing with increasing air velocity in groups 3 and 4; the fin temperatures therefore decrease from left to right and the gap between fin and tube closes. With the group 5 runs, on the other hand, the average air temperature *increases* with increasing air velocity and the tendency is for the gap to open. The theoretical equations predict this behavior quite satisfactorily. The chain-dashed line in Fig. 11(*b*) represents the true quadratic solution to equation (22) for the group 5 runs, thus providing for these extreme conditions a measure of the error in the linear approximation, which is shown by the dashed lines.

Better agreement with the group 5 data points might have been achieved by selecting the initial contact pressure derived from them alone as the actual value; predictions for other groups of runs would then have been somewhat conservative. It seems fair to conclude, then, that the prediction of the heat-transfer behavior of finned tubing need not involve as extensive testing as that carried out by the authors. Two series of runs, one at low heating-medium temperature to establish a base line, the other at artificially high average air temperatures, should be sufficient to predict with considerable accuracy the effect of gap resistance for all other conditions by means of equation (22*a*).

Summary

The so-called "bond resistance" of interference-fit finned tubes is of a relatively small order of magnitude in air-cooled heat-transfer equipment, although its measurement may have value as a quality-control device. The gap resistance of such tubes, however, may become a significant part of the total resistance to heat transfer when the service temperature is sufficiently high to cause complete relaxation of any initial contact pressure by differential thermal expansion between fin and tube. Quantitative methods of calculating this initial contact pressure are suggested, equation (27), and from it, methods of computing the gap resistance as a function of the operating temperatures, materials, and dimensional characteristics of the finned tubing, equation (22*a*). Supporting data on five finned-tube bundles—one embedded, one tension wound, and three muff type—show reasonable agreement with the proposed equations, Fig. 11 and Table 2. Certain systematic discrepancies in the muff type require further explanation, however.

Acknowledgment

The authors appreciate the willingness of The Griscom-Russell Company to publish test data of a nature normally considered proprietary. Particular thanks are due Messrs. K. B. Ris and O. W. Heimberger, President and Vice-President—Engineering, respectively. Further acknowledgment is due a respected competitor, Wolverine Tube, Division of Calumet and Hecla, Inc., who, with full knowledge that it was to be used for laboratory testing, provided the tubing for Units D and E reported herein.

References

1 C. B. Jackson, "Liquid Metals Handbook. Sodium-NaK Supplement," section by K. A. Gardner and R. M. Gould, Atomic Energy Commission and Bureau of Ships, Department of the Navy, Washington, D. C., 1955, pp. 371–381.

2 A. W. Brunot and F. F. Buckland, "Thermal Contact Resistance of Laminated and Machined Joints," TRANS. ASME, vol. 71, 1949, pp. 253–257.

3 N. D. Weills and E. A. Ryder, "Thermal Resistance Measurements of Joints Formed Between Stationary Metal Surfaces," TRANS. ASME, vol. 71, 1949, pp. 259–267.

4 W. B. Kouwenhoven and J. H. Potter, "Thermal Resistance of Metal Contacts," *The Welding Journal* (Research Supplement), vol. 27, 1948, pp. 515-s–520-s.

5 T. N. Cetinkale and M. Fishenden, "Thermal Conductance of Metal Surfaces in Contact," Proceedings of the General Discussion on Heat Transfer, The Institution of Mechanical Engineers and ASME, 1951, pp. 271–275.

6 M. E. Barzelay, K. N. Tong, and G. F. Holloway, "Thermal Conductance of Contacts in Aircraft Joints," NACA TN 3167, 1954.

7 M. E. Barzelay, K. N. Tong, and G. F. Holloway, "Effect of Pressure on Thermal Conductance of Contact Joints," NACA TN 3295, 1955.

8 F. Boni, "The Design of a Liquid Metal Heated Bayonet Tube Steam Generator," *Journal of the American Society of Naval Engineers*, vol. 70, 1958, pp. 231–243.

9 F. J. Mehringer, "Design, Fabrication, and Performance of the Duplex Heat Transfer Tube," U. S. Atomic Energy Commission Research Report KAPL-1797, 1957.

10 E. C. King and R. C. Andrews, "The Generation of Steam From Liquid Metal at High Heat Fluxes," American Institute of Chemical Engineers Heat Transfer Symposium, Preprint No. 5, 1953 Annual Meeting.

11 E. H. Young, et al., "Development of an Apparatus for the Measurement of Low Bond Resistances in Finned and Bare Duplex Tubes," Engineering Research Institute, University of Michigan, Report No. 48, Project 1592, 1957.

12 E. H. Young and M. L. Katz, "The Effect of Thermal Cycling to 350°F and 600°F on the Heat Transfer Performance of Integral Finned Tubes," AIChE Symposium Series, vol. 24, 1959, also, American Documentation Institute No. ADI 5859.

13 R. G. Wheeler, "Thermal Contact Conductance of Fuel Element Materials," presented at the Fifth Nuclear Congress, Cleveland, Ohio, April 7, 1959.

14 D. W. Johnson, "The Performance of Finned-Circular-Tube Heat Exchanger Surfaces," Technical Report No. 12, Navy Contract N6-ONR-251 Task Order VI, Department of Mechanical Engineering, Stanford University, 1951.

15 A. L. London, W. M. Kays, and D. W. Johnson, "Heat-Transfer and Flow-Friction Characteristics of Some Compact Heat-Exchanger Surfaces—Part 3," TRANS. ASME, vol. 72, 1952, pp. 1167–1178.

16 S. Timoshenko and J. N. Goodier, "Theory of Elasticity," second edition, McGraw-Hill Book Company, Inc., New York, N. Y., 1951, pp. 406–407.
17 K. A. Gardner, "Efficiency of Extended Surface," TRANS. ASME, vol. 67, 1945, pp. 621–631.
18 R. J. Roark, "Formulas for Stress and Strain," third edition, McGraw-Hill Book Company, Inc., New York, N. Y., 1954, Table XIII, case no. 28.
19 G. M. Dusinberre, "Fin Efficiency," *Mechanical Engineering*, vol. 78, 1956, p. 570.
20 A. Nadai, "Theory of Flow and Fracture of Solids," second edition, McGraw-Hill Book Company, Inc., New York, N. Y., 1950, p. 479.
21 W. H. McAdams, "Heat Transmission," third edition, McGraw-Hill Book Company, Inc., New York, N. Y., 1954, p. 337.

APPENDIX

The gap g between tube OD and fin base has been assumed uniform. It is actually given circumferentially by

$$g_\theta = g - \epsilon \cos\theta \tag{28}$$

where the symbols are as defined in Fig. 12(*a*). The local gap resistance is therefore

$$r_{g\theta} = r_g\left(1 - \frac{\epsilon}{g}\cos\theta\right) \tag{29}$$

The heat transfer per unit tube length thus becomes

$$Q = \frac{(T_h - T_a)d}{12}\int_0^\pi \frac{d\theta}{\left[R^* + r_g\left(1 - \frac{\epsilon}{g}\cos\theta\right)\right]}$$

or

$$Q = \frac{\pi(T_h - T_a)d}{12(R^* + r_g)\left[1 - \left(\frac{\epsilon}{g}\right)^2\left(\frac{r_g}{R^* + r_g}\right)^2\right]^{1/2}} \tag{30}$$

Assuming that all values of ϵ/g from 0 to 1 are equally probable,

$$Q_{avg} = \frac{\pi(T_h - T_a)d}{12(R^* + r_g)}\int_0^1 \frac{d(\epsilon/g)}{\left[1 - \left(\frac{\epsilon}{g}\right)^2\left(\frac{r_g}{R^* + r_g}\right)^2\right]^{1/2}}$$

$$= \frac{\pi(T_h - T_a)d}{12r_g}\sin^{-1}\left(\frac{r_g}{R^* + r_g}\right) \tag{31}$$

Also,

$$Q_{avg} = \frac{\pi(T_h - T_a)d}{12(R^* + r_g)_{avg}} \tag{32}$$

$$\therefore r_{g,avg} = \frac{r_g}{\sin^{-1}\left(\frac{r_g}{R^* + r_g}\right)} - R^* \tag{33}$$

As long as $r_g < R^*$, this is well represented by

$$r_{g,avg} = r_g\left[1 - \frac{1}{6}\left(\frac{r_g}{R^* + r_g}\right)\right] \tag{34}$$

But, since r_g should normally be held to less than 20 per cent of R^*, the error in assuming concentricity is less than 3 per cent in r_g, or 0.4 per cent in $(R^* + r_g)$.

When the gap g varies longitudinally of the tube it may take many forms. For purposes of example, let

$$g_x = g + \frac{\Delta g}{2}\left(1 - \cos\frac{2\pi x}{fb}\right) \tag{35}$$

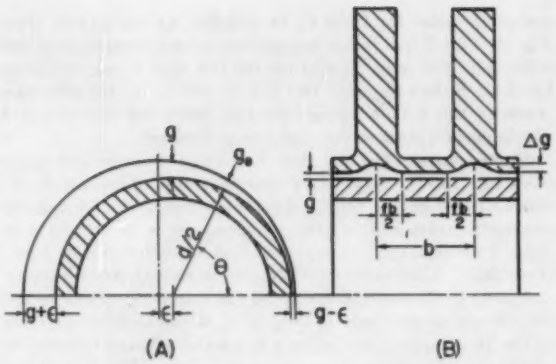

Fig. 12 Definition sketch showing types of nonuniformity in fin-to-tube junction

over a fraction f of the base contact length and $g_x = g$ over the remainder, as shown in Fig. 12(*b*). Then the heat transfer per base contact surface is

$$Q_{avg} = \frac{\pi d}{6}\left\{\int_0^{(1-f)/2}\frac{d(x/b)}{(R^* + r_g)} + \int_0^{f/2}\frac{d(x/b)}{\left[(R^* + r_g) + r_g\frac{\Delta g}{2g}\left(1 - \cos\frac{2\pi x}{fb}\right)\right]}\right\}$$

or

$$Q_{avg} = \frac{\pi d}{12(R^* + r_g)}\left\{(1 - f) + \frac{f}{\left[1 + \frac{\Delta g}{g}\left(\frac{r_g}{R^* + r_g}\right)\right]^{1/2}}\right\} \tag{36}$$

By comparison with equation (32), then,

$$(R^* + r_g)_{avg} = \frac{(R^* + r_g)}{\left\{(1 - f) + \frac{f}{\left[1 + \frac{\Delta g}{g}\left(\frac{r_g}{R^* + r_g}\right)\right]^{1/2}}\right\}} \tag{37}$$

The effective over-all heat-transfer coefficient may therefore be considerably less than the ideal value, depending on the extent of nominal contact length which is actually in initial contact. The effect of incomplete contact on the gap resistance itself is, of course, much more drastic.

DISCUSSION

D. Q. Kern[3]

The authors have contributed a paper which contains the excellent type of derivation we have come to expect of them. If the tubes they describe and the products in which they are assembled are to find an expanding market, an improvement of design procedures is required. By starting with the tube itself they have included timeliness as well.

There should be little objection to the models employed by the authors in their derivations. While they are greatly simplified, it is important that they be committed to print so that refinements will follow as the need becomes apparent. The physical

[3] D. Q. Kern Associates, Cleveland, Ohio. Mem. ASME.

differences between tension-wound fins and what are termed "muff-type" fins in the paper suggest an additional resolution of the models and I am certain the authors have already given consideration to it.

The authors describe a method for interpreting tube tests and the results of such tests are not necessarily identical with generalizations relative to the various methods of manufacturing tubes. The matter of cost has not been included. The poorest tube might easily represent the greatest value depending upon its cost per square foot of effective surface. The paper does not qualify the tubes nor indicate when they were produced and whether any were pretested. Any manufacturing improvement, even a minor one it seems to me, could readily reverse the scorings of all of the bimetallic tubes.

Tubes manufactured by any method when tools and dies were in a worn phase of their maintenance cycle might show up quite poorly since any absolute concept of uniformity appears impractical in an industrial operation. It is not stated in the paper whether any of the units have statistical significance; that is, were the tubes assembled by random sampling from many production runs? We have no idea whatever of the history of the tubes obtained from the other manufacturers.

It is noted that the authors did not indicate that any of the tubes had been manufactured to a particular preconceived level of bond resistance and so tested so that the experimental results possessed a basis for comparison. The different types of tubes, it seems to me, principally provided an opportunity to test the theoretical procedures for the purpose of changing the hypothetical model on which the derivation is based.

My comments have been solicited by the authors and I want to felicitate them on what they have accomplished. I hope no one, and least of all the authors, will think my discussion of the limitations of the experimental study exposes anything other than a few of the questions I find unanswered after several readings.

Ennis C. Smith[4]

The paper discussed herein is represented by its authors to be a general theoretical approach to the determination of "the thermal bond (or gap) resistance between fins and tubes in terms of known properties of the extended surface, *and of the process conditions to which it is subjected.*" However, due to the multitude of unsupported statements in the paper, and to the procedure for selection of test samples, the purpose of this paper appears more to be a subtle effort toward an evaluation of tubes of a specific manufacturer and of one other competitive type of tubing. In consideration of these commercial aspects it seems improper to submit this paper before a reputable technical society.

If complete objectivity of the tests, evaluation, and sample selection could be assumed, what then is the significance of the results upon selection of tubing for air-cooled heat exchangers for actual operating process conditions? Referring to Fig. 11 of the discussed paper, the tension-wound fins in Unit B failed under fairly moderate conditions, and the tubes of Unit E were excused by the authors as being in the development stage. This reduces the scope of the paper to a comparison of tubes in Unit A, which are sponsored by the authors, with those in Units C and D, which are competitive products. Note that the tubes in Unit C *through the Group 4 tests* indicated no appreciable depreciation of bond, in fact, showed less deviation from a single line representing all the Group 1 through 4 tests than the tubes in Unit A. The inlet air temperature in Groups 1 through 4 was 110 F, which is reasonable, although higher than average for actual exchanger operating conditions. The authors found it necessary to artificially elevate the temperature of the inlet air to 300 F before appreciable bond deterioration resulted. Such an inlet air temperature is completely unrealistic. The Group 5 tests, therefore, bear no resemblance to a typical, or even a high temperature operating industrial air-cooled exchanger.

In Fig. 13 of this discussion is a tabulation of 100 typical operating exchangers in refinery and chemical plant installations as a function of the inlet fluid temperature. Air and fin metal temperatures are always lower than inlet fluid temperatures. Note that 52 per cent of the services have inlet fluid temperatures be-

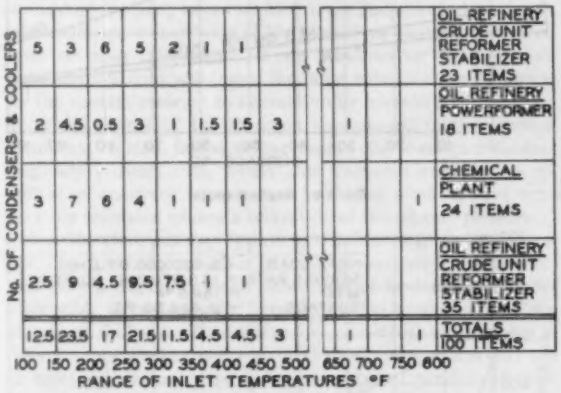
No. OF CONDENSERS & COOLERS
5 3 6 5 2 1 1
OIL REFINERY CRUDE UNIT REFORMER STABILIZER 23 ITEMS
2 4.5 0.5 3 1 1.5 1.5 3 1
OIL REFINERY POWERFORMER 18 ITEMS
3 7 6 4 1 1 1 1
CHEMICAL PLANT 24 ITEMS
2.5 9 4.5 9.5 7.5 1 1
OIL REFINERY CRUDE UNIT REFORMER STABILIZER 35 ITEMS
12.5 23.5 17 21.5 11.5 4.5 4.5 3 1 1
TOTALS 100 ITEMS
100 150 200 250 300 350 400 450 500 650 700 750 800
RANGE OF INLET TEMPERATURES °F

Fig. 13 Frequency of operating inlet temperatures to air-cooled exchangers for typical oil refineries and chemical plants

low 250 F, 86 per cent are below 350 F, and 95 per cent are below 450 F. If typical natural gasoline and pipeline compressor station services had been included in this tabulation, the average inlet fluid temperature of the group would have been considerably less. It is significant that the five services above 450 F had over-all heat-transfer rates averaging less than 20 Btu/hr/sq ft of bare surface/deg F. This would be expected, since most high temperature services are for cooling viscous fluids or low pressure gases. Performance of these units would show no effect of stress damage on a well-bonded tube, even if such damage occurred.

It is most important that fin metal temperature is just as much a function of air temperature, air film coefficient, and hot fluid film coefficient as of the inlet fluid temperature. Fin metal temperature is also dependent upon resistance of the metals and upon fouling. The effect of these variables is illustrated by Figs 14 through 17, which are plots of temperature versus the percentage of heat exchanger surface affected. Temperatures are given for hot fluid, liner tube outer surface, and air. Aluminum fin temperature will fall between air temperature and liner outer wall temperature. This paper showed that there was no appreciable deterioration of bond in Unit C through the Group 4 tests, and that the average fin temperature in this group was up to 290 F. Examination of Figs. 14, 15, and 16 given herein, which are typical for high temperature applications with inlet fluid temperatures up to 650 F, shows that an average fin temperature of 290 F was never reached. Compare these exchangers to the plot of the Group 5 tests of Unit C, in Fig. 17, where the fin metal exceeded 345 F. This high fin metal temperature, as compared to the other tests, resulted from the unnatural heating of the inlet air, producing a completely unrealistic operating condition.

It can therefore be concluded that in only a negligibly small percentage of air-cooled heat-exchanger applications, are fin metal temperatures reached which would result in stress deterioration of the bond of a properly fabricated extruded finned tube. Even in those cases, only a negligible portion of the exchanger surface is affected.

This conclusion is corroborated by the paper, "Design, Fabri-

[4] Manager, Cooling Equipment Division, Hudson Engineering Corporation, Houston, Texas.

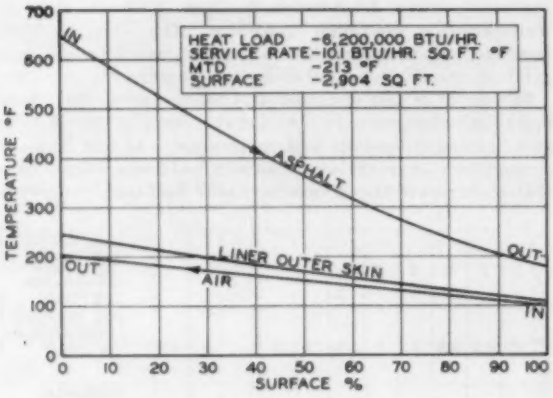

Fig. 14 Asphalt cooler

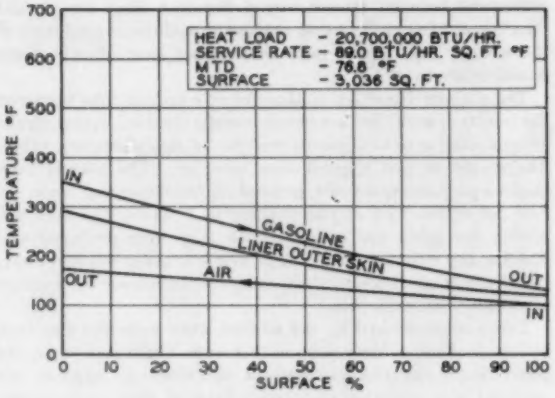

Fig. 15 Gasoline condenser

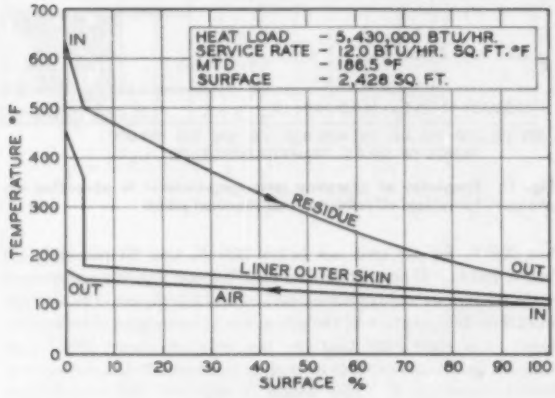

Fig. 16 Residue cooler

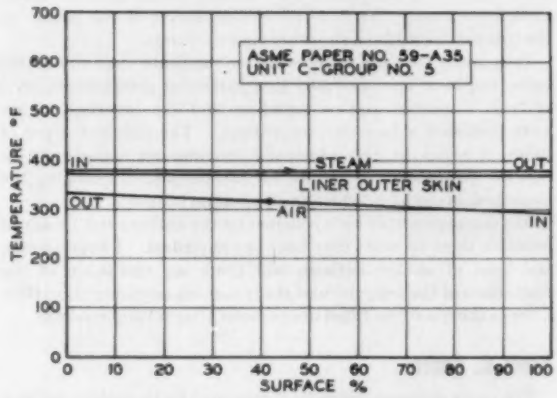

Fig. 17 Steam condenser

cation, and Performance of the Duplex Heat Transfer Tube," by F. J. Mehringer, U. S. Atomic Commission Research Report KAPL-1797 (1957), which is reference [9] in the discussed paper. This reference study, although conducted upon bare duplex tubing having less difference in coefficient of expansion between inner and outer tubes than is typical for aluminum finned tubes having steel liners, was made on an evaporator having molten metal with an inlet temperature of approximately 900 F on the inside of the tubes and boiling water at approximately 460 F on outside. Operating flux varied from 100,000 to 150,000, which was due both to high temperature difference between the fluids and high over-all heat-transfer rates. Bond resistance at the bimetallic interface would therefore have a very damaging effect upon this type of service. Quoting directly from this article as follows:

"The high stresses exist only for a small part of the duplex tube length. Any resultant yield of the duplex tube can only affect the thermal contact or gap resistance between the two tubes in this short length. The original gap resistance is less than $^1/_3$ of the over-all thermal resistance of a well-fabricated duplex tube. It is therefore expected that even if yielding occurs in the duplex tubes, that effect on the over-all heat-transfer performance of the evaporator will be negligible."

We advocate further comparative tests on various representative finned tube samples. The tests should include a measure of bond resistance after accelerated weathering of the tubes, to show the prolonged effects of moisture, salt water spray, and corrosive atmospheres on tube heat-transfer capability. The tests should also include a measure of strength and sturdiness of the fins, to determine their durability when subjected to rough handling and severe operating conditions.

Authors' Closure

Both discussers have called attention to certain limitations in scope or range of applicability of the authors' data and its analysis. Although no claims were made in the paper that these particular areas were under investigation, it is well to have it clearly understood that they were not.

Dr. Kern raises several points that are well taken. The authors claim no statistical significance for their data, except to the extent that the minor variations in local quality encountered in any production run are averaged out over approximately forty feet of tubing in each test unit. It is quite true that manufacturing changes, whether process improvement or tool deterioration, might have produced different results. The authors prefer, however, not to consider such differences as changes in the "scorings" of the various tubes. The object of the paper was primarily to find whether the theoretical approach was adequate to explain observed phenomena, regardless of the source of tubes tested which, as Dr. Kern says, merely "provided an opportunity to test the theoretical procedures. . . . ."

Mr. Smith also makes one point that is well taken among several that are not. It was pointed out in the paper, following equation (22), that the analysis applied only to local conditions and that temperature variation throughout an actual unit would

necessitate integration of these local values over all the surface. Mr. Smith's Figs. 13 through 17, and the discussion pertaining to them, provide valuable amplification of this point as applied to air-cooled heat exchangers.

As to "the multitude of unsupported statements in the paper," careful rereading by the authors discovers no basis for such a remark, unless possibly a survey should have been conducted to support the statement that finned tubes with an initial *gap resistance* instead of an initial *contact pressure* are "forsworn by all manufacturers." All other statements appear to have been suitably documented or qualified.

The authors do not concur that "the tension-wound fins of Unit B *failed* under fairly moderate conditions," that any other unit *failed* at *any* condition, nor that the scope of the paper is reduced to a comparison of any two types of tubing. The point is that although *all* units, under extreme operating conditions, suffer a loss in their heat-transfer capability, the extent of this loss is predictable and may be used with considerable confidence in design. Any impropriety involved in testing an engineering theory on commercial equipment obtained from a variety of sources, and objectively reporting the results, is not apparent to the authors. The suggestion that there is any such impropriety is impertinent, in both senses of the word.

Much of Mr. Smith's discussion appears to be from the rather parochial viewpoint of finned tubing with the hot fluid inside the tubes and atmospheric air as coolant. It is true that the temperature conditions of the Group 5 runs "bear no resemblance to a typical, or even a high temperature operating industrial air-cooled exchanger"; neither do they resemble typical refrigerant condensers, flue gas heated economizers, or many others that might be mentioned. This is not odd, however, since the paper is not *about* any of these things; it is about the gap resistance in interference fit finned tubing, whereever it may occur, and does not profess otherwise.

Although Mehringer's work [9] may be apropos as a reference to the local nature of gap resistance in a sensible heat exchanging unit, it is *not* pertinent from the standpoint of the magnitude of such resistance, as Mr. Smith appears to suggest. Both tubes of the duplex tubing tested by Mehringer had identical expansion coefficients since they were of low chromium molybdenum steel, with the inner tube expanded into the outer for tight contact. Since the hot fluid was inside the inner tube, the tendency was for the contact pressure to *increase* under operating conditions—quite the reverse of the situation encountered in the authors' aluminum on steel finned tubing tests. Any contact resistance originally present, then, would have *decreased* unless stress relieving at operating temperature or during some upward temperature excursion caused a relaxation of the contact pressure.

It is therefore not appropriate to cite Mehringer in corroboration of a conclusion which is in itself unwarranted, to the effect that only a negligibly small percentage of heat exchangers are susceptible to heat-transfer impairment due to annealing of the aluminum fin base. To consider any unit which is incapable of delivering specified capacity as "negligible" because it is only one of many satisfactory ones, is to take a rather carefree attitude toward the obligations of the design engineer.

E. M. SPARROW
At present, Professor of Mechanical Engineering, University of Minnesota. Formerly, NASA Lewis Research Center. Assoc. Mem. ASME

J. L. GREGG
NASA, Lewis Research Center, Cleveland, Ohio. Assoc. Mem. ASME

Mass Transfer, Flow, and Heat Transfer About a Rotating Disk

The effects of mass injection or removal at the surface of a rotating disk on heat transfer and on the flow field about the disk are studied. Consideration is given to gaseous systems which are composed of either one or two component gases. Solutions of the equations which govern the hydrodynamics, energy transfer, and mass diffusion have been obtained over the entire range from large suction velocities to large blowing velocities. Results are given for the velocity, temperature, and mass-fraction distributions, as well as for the heat-transfer, mass-transfer, and torque requirements. The effects of the mass transfer are discussed in detail. It is shown that fluid injection sharply decreases the heat transfer at the surface.

Introduction

THE PIONEERING STUDY of fluid flows in which there is mass addition or mass removal at a bounding surface was carried out by Prandtl in 1904. His attention was directed toward control of the boundary layer on aerodynamic bodies, an end which can be achieved by sucking fluid away through slots in the surface. Investigation of the problem of boundary-layer suction has continued up to the present. Results of these suction studies may also be applied when the mass removal comes about due to freezing (i.e., icing) at the surface.

In recent years, considerable interest has also been shown in mass addition to boundary-layer flows, especially in connection with the cooling of the turbine blades and the skins of high-speed aero-vehicles. Such a cooling process, frequently termed transpiration, might utilize a porous surface through which a coolant, either a gas or liquid, is forced. In the case of a liquid coolant, evaporation would take place due to the hot boundary-layer gases, and the latent heat of vaporization would thus be utilized. In an alternate technique of transpiration cooling, the surface of the vehicle would be fabricated of a material which would evaporate and hence cool the boundary layer (ablation cooling).

From this discussion, it is clear that an attack on the problem of fluid injection or removal involves consideration of the flow velocities, the heat transfer, and the mass transfer. For boundary-layer flows, a fundamental study of this type has been made by Hartnett and Eckert [1].[1] As a logical first step, they examined the laminar boundary-layer equations for the case of an incompressible, two-component gas where the properties of the diffusing gas were identical to those of the free-stream fluid. The results of such an analysis can be applied to two-component systems in which the properties of the separate components are not too different (and, of course, to one-component systems). But an even greater utility of such an analysis is that it indicates basic trends and behavior patterns.

Fig. 1 Physical model and co-ordinates

In the present investigation, we turn to an altogether different physical configuration. The system to be studied, shown schematically in Fig. 1, is a rotating disk immersed in a large body of otherwise quiescent fluid. Motions are induced within the fluid by the rotation of the disk. Mass transfer to, or from, the fluid may take place at the surface of the disk, either by direct injection or suction, or else by phase change. The rate of mass addition or removal is uniform at all points on the disk surface. Heat transfer may also take place due to a difference in temperature between the ambient fluid and the surface of the disk. As a first step, we study this problem by using the same assumptions about fluid properties as has been mentioned in connection with reference [1]. The solutions and results thus obtained constitute a fundamental body of information which provides insight into behavior patterns and may also be of direct application to single-

[1] Numbers in brackets designate References at end of paper.

Contributed by the Heat Transfer Division and presented at the Annual Meeting, Atlantic City, N. J., November 29–December 4, 1959, of THE AMERICAN SOCIETY OF MECHANICAL ENGINEERS.

NOTE: Statements and opinions advanced in papers are to be understood as individual expressions of their authors and not those of the Society. Manuscript received at ASME Headquarters, August 13, 1959. Paper No. 59—A-107.

Nomenclature

c_p = specific heat at constant pressure
D = coefficient of diffusion
F, G, H = dimensionless velocity variables defined in equation (9b)
h = heat-transfer coefficient, $q/(T_w - T_\infty)$
k = thermal conductivity
M = torque
m = rate of mass flow
Nu = Nusselt number, $h\left(\frac{\nu}{\omega}\right)^{1/2}\Big/k$
P = dimensionless pressure defined by equation (9b)
Pr = Prandtl number, $\nu/\alpha = c_p\mu/k$
p = static pressure
q = heat-transfer rate per unit area
r = radial co-ordinate
Sc = Schmidt number, ν/D
T = static temperature
V_r, V_φ, V_z = convective velocity components
v_r, v_φ, v_z = diffusive velocity components
W_i = mass fraction, ρ_i/ρ
z = co-ordinate measuring distance normal to disk surface
α = thermal diffusivity
δ = thickness of viscous or thermal layers (see subscripts)
η = dimensionless independent co-ordinate, $(\omega/\nu)^{1/2}z$
θ = dimensionless temperature, $(T - T_\infty)/(T_w - T_\infty)$
μ = absolute viscosity

(Continued on next page)

component or to two-component gases. Consideration will be given here to the entire range of mass transfers, extending from large suction through small suction and injection to large injection.

A modest beginning on this problem has been made by Stuart [2]. He confined his attentions to the effects of suction on the velocity distribution; heat and mass transfer were not considered. Most of his work was directed to large suctions, with only a single case of moderate suction reported. No consideration was given to fluid injection. Other analytical work on the problem of laminar flow about a rotating disk, which may be of background interest, may be found in references [3–7].

Analysis

The Governing Equations. The velocity, temperature, and diffusion fields around a rotating disk are governed by the basic conservation principles: Momentum, energy, and mass; and it is these which form the starting point of our study. The momentum principle is represented by the three Navier-Stokes' equations, one for each co-ordinate direction; while energy conservation provides a fourth equation. For a multicomponent gas, conservation of mass must be satisfied by the separate components. When there are two components, as is the case in the present analysis, mass conservation is fully expressed by a continuity equation for the mixture and a diffusion equation for one component.[1]

The mathematical statement of the conservation laws appropriate to an incompressible, constant-property, nondissipative flow may be written in cylindrical co-ordinates as follows:

Momentum conservation

$$\rho\left(\frac{dV_r}{dt} - \frac{V_\varphi^2}{r}\right) = -\frac{\partial p}{\partial r} + \mu\left(\nabla^2 V_r - \frac{2}{r^2}\frac{\partial V_\varphi}{\partial \varphi} - \frac{V_r}{r^2}\right) \quad (1)$$

$$\rho\left(\frac{dV_\varphi}{dt} + \frac{V_r V_\varphi}{r}\right) = -\frac{1}{r}\frac{\partial p}{\partial \varphi} + \mu\left(\nabla^2 V_\varphi + \frac{2}{r^2}\frac{\partial V_r}{\partial \varphi} - \frac{V_\varphi}{r^2}\right) \quad (2)$$

$$\rho\frac{dV_z}{dt} = -\frac{\partial p}{\partial z} + \mu\nabla^2 V_z \quad (3)$$

Energy conservation

$$\frac{dT}{dt} = \alpha\nabla^2 T \quad (4)$$

Mass conservation

$$\frac{1}{r}\frac{\partial}{\partial r}(rV_r) + \frac{1}{r}\frac{\partial V_\varphi}{\partial \varphi} + \frac{\partial V_z}{\partial z} = 0 \quad (5)$$

$$\frac{dW_1}{dt} = D\nabla^2 W_1 \quad (6)$$

[1] This will guarantee that mass conservation is satisfied for the second component.

where

$$\frac{d}{dt} = V_r\frac{\partial}{\partial r} + \frac{V_\varphi}{r}\frac{\partial}{\partial \varphi} + V_z\frac{\partial}{\partial z}$$

and

$$\nabla^2 = \frac{\partial^2}{\partial r^2} + \frac{1}{r}\frac{\partial}{\partial r} + \frac{\partial^2}{\partial z^2} + \frac{1}{r^2}\frac{\partial^2}{\partial \varphi^2}$$

The symbols V_r, V_φ, and V_z represent the usual convective velocity components. So, the first five equations remain the same whether or not the gas diffusing out of (or into) the wall is the same as the main-stream component. So, within the framework of the constant-property analysis, the velocity and temperature distributions are independent of the concentration field. Equation (6) is called the diffusion equation. It governs the distribution of the weight fraction W_1, which is defined as the ratio of the partial density of component 1 to the total density. A similar definition applies to W_2. Using the Gibbs-Dalton law, it follows that

$$\rho_1 + \rho_2 = \rho \quad \text{or} \quad W_1 + W_2 = 1 \quad (7)$$

In the derivation of equation (6), it has been assumed that the diffusion velocities are given by Fick's law [1]; e.g.,

$$(v_z)_1 = -\frac{D}{W_1}\frac{\partial W_1}{\partial z}, \quad (v_z)_2 = -\frac{D}{W_2}\frac{\partial W_2}{\partial z}, \text{ etc.} \quad (8)$$

In this analysis, we will assign the subscript 1 to identify the component diffusing through the wall, while 2 will represent the other component (which would most likely be air).

The solution of the partial differential equations (1) through (6) would appear, at first glance, a too formidable task. Fortunately, we can draw on the experience of von Karman [3], who successfully solved the velocity problem for an impermeable disk rotating in a single-component, incompressible fluid. Karman used a similarity transform to reduce the partial differential equations of his problem to ordinary differential equations, which are easier to solve. Utilizing his idea, we introduce the following new variables:

(*a*) New independent variable

$$\eta = z\left(\frac{\omega}{\nu}\right)^{1/2} \quad (9a)$$

(*b*) New dependent variables

$$F(\eta) = \frac{V_r}{r\omega}, \quad G(\eta) = \frac{V_\varphi}{r\omega}, \quad H(\eta) = \frac{V_z}{(\omega\nu)^{1/2}}, \quad P(\eta) = \frac{p}{\mu\omega}, \quad \theta(\eta) = \frac{T - T_\infty}{T_w - T_\infty}, \quad \Phi(\eta) = \frac{W_1 - W_{1\infty}}{W_{1w} - W_{1\infty}} \quad (9b)$$

The similarity aspects of the transformation are linked to the supposition that (except for a simple stretching of V_r and V_φ) the velocity, temperature, and concentration profiles do not change *shape* at different values of r. Also, the idea of angular symmetry has been invoked; i.e., $\partial/\partial\varphi \equiv 0$.

Nomenclature

ν = kinematic viscosity
ρ = density
τ_φ, τ_r = shear-stress components at the disk surface
Φ = dimensionless mass fraction, $(W_1 - W_{1\infty})/(W_{1w} - W_{1\infty})$
φ = angular co-ordinate
ω = angular velocity

Subscripts

1 = component 1, diffusing gas
2 = component 2, main stream gas
∞ = ambient conditions ($z \to \infty$)
c = convective
d = diffusive
dis = displacement
e = refers to entering temperature of coolant
m = momentum
t = thermal
w = conditions at surface ($z = 0$)

Under the transformation, the conservation equations (1) through (6) become

$$F'' = HF' + F^2 - G^2 \tag{1a}$$

$$G'' = HG' + 2FG \tag{2a}$$

$$P' = H'' - HH' \tag{3a}$$

$$\theta'' = (\mathrm{Pr})H\theta' \tag{4a}$$

$$H' = -2F \tag{5a}$$

$$\Phi'' = (\mathrm{Sc})H\Phi' \tag{6a}$$

where Pr and Sc, respectively, represent the Prandtl and Schmidt numbers. The primes denote differentiation with respect to η. It may be worth noting that it has not been necessary to invoke the boundary-layer assumptions in deriving equations (1*a*) through (6*a*). Although the transformation has provided a set of ordinary differential equations, a closed-form solution is still not within our grasp, and numerical techniques must be used. For computational convenience, it is desirable to eliminate F from equations (1*a*), (2*a*), and (5*a*), giving

$$H''' = HH'' - (H')^2/2 + 2G^2 \tag{10}$$

$$G'' = HG' - H'G \tag{11}$$

Simultaneous solution of these will yield H and G. Then, with a solution for H at our disposal, equations (4*a*) and (6*a*) may be attacked. If Pr = Sc and if the boundary conditions coincide, then equations (4*a*) and (6*a*) have identical solutions. The pressure distribution is somewhat incidental to the problem and no further attention will be given to equation (3*a*).

Boundary Conditions. The conservation equations give, within the framework of the simplifying assumptions, a complete description of the physical occurrences within the fluid. But, to complete the statement of the problem, it still remains to specify the boundary conditions.

For the velocity problem, it will be supposed that the no-slip condition of viscous flow continues to apply at the surface of the disk. Further, the convective velocity V_{zw} normal to the disk surface specifies the mass injection or withdrawal. Far from the disk surface, all fluid velocities must vanish aside from the induced axial component.

For the energy and diffusion equations, the temperature and weight fraction must, by continuity considerations, respectively, equal T_w and W_{1w} at the disk surface. At large distances from the disk, $T \to T_\infty$ and $W_1 \to W_{1\infty}$. A formal statement of these conditions is:

$$\left.\begin{aligned} V_r &= 0 \\ V_\varphi &= r\omega \\ V_z &= V_{zw} \\ T &= T_w \\ W &= W_{1w} \end{aligned}\right\} z = 0 \qquad \left.\begin{aligned} V_r &\to 0 \\ V_\varphi &\to 0 \\ T &\to T_\infty \\ W_1 &\to W_{1\infty} \end{aligned}\right\} z \to \infty \tag{12a}$$

In terms of the transformed variables, equation (12*a*) becomes

$$\left.\begin{aligned} H &= H_w \\ H' &= 0 \\ G &= 1 \\ \theta &= 1 \\ \Phi &= 1 \end{aligned}\right\} \eta = 0 \qquad \left.\begin{aligned} H' &\to 0 \\ G &\to 0 \\ \theta &\to 0 \\ \Phi &\to 0 \end{aligned}\right\} \eta \to \infty \tag{12b}$$

where H_w represents the dimensionless velocity normal to the disk surface. Positive values of H_w denote fluid injection, while negative values denote suction; i.e., mass withdrawal.

Up to this point, we have been at liberty to assign whatever values we please to V_{zw}, W_{1w}, $W_{1\infty}$, and so on. Solutions of the conservation equations can be obtained for any choices of these parameters. However, as pointed out in reference [1], there are a number of important situations where there is an added physical constraint which provides a relationship between V_{zw} and the boundary values of W_1. The temperature boundary values may also be interrelated through an additional physical constraint. Illustrations of these constraints and relationships will be given when the heat-transfer and mass-transfer results are discussed.

Solutions. The velocity problem is governed by the differential equations (10) and (11) subject to the boundary conditions (12*b*). By inspection of these conditions, it is seen that solutions cannot be obtained until numerical values of the dimensionless mass-transfer velocity H_w are prescribed. For a large number of values of H_w ranging from -4 to $+5$ as listed in Table 1, solutions of equations (10) and (11) have been carried out on an IBM 653 electronic computer utilizing the numerical techniques of reference [8]. The method is a forward integration procedure and the critical quantities which define a solution are the derivatives $H''(0)$ and $G'(0)$ which are needed to start the numerical computation. A listing of these starting values is given in Table 1. Later it will be shown that the $H''(0)$ and $G'(0)$ are also of direct application in shear-stress computations. For large positive values of H_w, the limitations of a computing machine which uses eight significant figures were keenly felt. The information listed in Table 1 for $H_w = 4$ and 5 is believed to be correct to at least the number of places given, but the corresponding solutions do not accurately satisfy the boundary conditions at large η.

Turning to the temperature and diffusion equations, (4*a*) and (6*a*), respectively, solutions were carried out for Pr = Sc = 0.7. There was, thus, no mathematical distinction between the equations. The needed input data for $H(\eta)$ was supplied by the previously mentioned solutions of equations (10) and (11). Since $H(\eta)$ is a function of H_w, so too are $\theta(\eta)$ and $\Phi(\eta)$. The values of $\theta'(0) = \Phi'(0)$ obtained from these solutions are listed in Table 1.[3] These are the starting values in our forward integration procedure and, as will be shown later, are directly related to the heat and mass-transfer coefficients.

For large suction velocities (large negative values of H_w), certain simple asymptotic solutions can be obtained. These will be discussed in a later section where their motivation is clear.

Results

Velocity Distributions. Insight into the physical occurrences within the flow field can be obtained by study of the velocity profiles. Inasmuch as space limitations preclude presentation of velocity data for all the cases listed in Table 1, we must content ourselves here with graphing the results for representative situations.

We turn our attention first to the distribution of the axial velocity V_z. Positive values indicate an outflow toward the free stream; while negative values represent an inflow from the free stream toward the disk. The distribution of V_z plotted as a function of distance normal to the disk is presented in Fig. 2 for representative values of the dimensionless injection (or suction) velocity H_w. Consider first the case of the impermeable surface, $H_w = 0$. The rotating disk acts like a fan, drawing fluid axially inward from the surroundings toward the disk surface. However, because the surface is solid, the inflowing fluid finds its path blocked, and it must reroute into a radial direction where there is no obstruction. So, in Fig. 2 we see that the negative velocity of inflow, starting from its largest value at large z, decreases steadily as we approach the disk (decreasing z) due to fluid escape into the

[3] Solutions of the θ-equation were not attempted for $H_w = 4$ and 5 because the available values of $H(\eta)$ were not sufficiently accurate to serve as input data.

Table 1 Some important properties of the solutions

H_w	$-H''(0)$	$-G'(0)$	$-\theta'(0) = -\phi'(0)$	$\frac{\delta_{dis}}{(\nu/\omega)^{1/2}}$	$\frac{\delta_m}{(\nu/\omega)^{1/2}}$	$\frac{\delta_t}{(\nu/\omega)^{1/2}}$	$-\frac{V_{z\infty}}{(\nu\omega)^{1/2}}$
-4	0.2495	4.005	2.802	0.2496	0.1248	0.3566	4.008
-3	.3312	3.012	2.106	.3315	.1657	.4741	3.018
-2.5	.3947	2.521	1.759	.3957	.1977	.5663	2.531
-2	.4848	2.039	1.418	.4875	.2434	.6995	2.058
-1.5	.6136	1.580	1.087	.6226	.3100	.8999	1.620
-1.2	.7104	1.328	.8998	.7300	.3622	1.066	1.391
-.8	.8463	1.036	.6730	.9000	.4423	1.348	1.150
-.4	.9576	.8016	.4798	1.085	.5240	1.698	.9872
-.2	.9956	.7033	.3969	1.178	.5625	1.895	.9298
-.08	1.012	.6497	.3515	1.234	.5846	2.020	.9014
0	1.020	.6159	.3231	1.271	.5989	2.106	.8845
.06	1.025	.5916	.3028	1.299	.6094	2.170	.8728
.1	1.028	.5758	.2897	1.318	.6163	2.214	.8654
.3	1.034	.5022	.2295	1.412	.6496	2.448	.8331
.5	1.029	.4364	.1782	1.506	.6811	2.685	.8070
.6	1.023	.4063	.1557	1.554	.6962	2.814	.7960
.7	1.015	.3779	.1353	1.602	.7111	2.941	.7859
.8	1.004	.3511	.1167	1.650	.7255	3.076	.7766
1	.9790	.3022	.08539	1.749	.7536	3.345	.7605
1.6	.8758	.1885	.02806	2.061	.8338	4.187	.7251
2	.7979	.1360	.01140	2.286	.8853	4.765	.7065
3	.6183	.06029	.0006204	2.902	1.017	6.214	.6707
4	.486	.0289					
5	.395	.0155					

radial direction. Now, consider the application of a suction at the disk surface; i.e., $H_w < 0$. Then, besides the fanlike pumping of the rotating disk, there is the additional pumping due to the suction. So, the quantity of fluid drawn in from the surroundings increases; or in terms of Fig. 2, the magnitude of $V_{z\infty}$ increases. Now, the inflowing fluid has two possible paths. It may continue its inflow through the suction holes of the disk, or, it may reroute into radial direction. The path chosen will, of course, be that of least resistance. As the wall suction increases, escape through the wall becomes easier and easier. So, with H_w becoming increasingly negative, more and more of the inflow goes directly into the porous disk. As a consequence, V_r tends to become almost constant with z. Next, consider the case of blowing (injection) at the disk surface. In this instance, the fluid drawn in by the fan action of the disk finds itself *actively* retarded by the outflowing stream of injected fluid. The greater the blowing velocity, the more strongly is the inflow opposed. The result is a decrease in the magnitude of $V_{z\infty}$ with increasing H_w. There is, in a real sense, a battle between the two streams; and as H_w increases, the outflow penetrates to greater distances from the disk surface. As a consequence, the crossover point between positive and negative V_r is pushed farther outward.

These events are reflected by the radial velocity distribution. Representative profiles are given in Fig. 3. Since the radial velocity is zero both at the disk surface and in the ambient fluid, there must be a maximum value somewhere between. The maximum is positive since the radial flow is always outward along the disk. For the impermeable disk ($H_w = 0$), all the axial inflow is ultimately diverted into radial flow. With increasing suction, more and more of the inflowing fluid passes directly into the

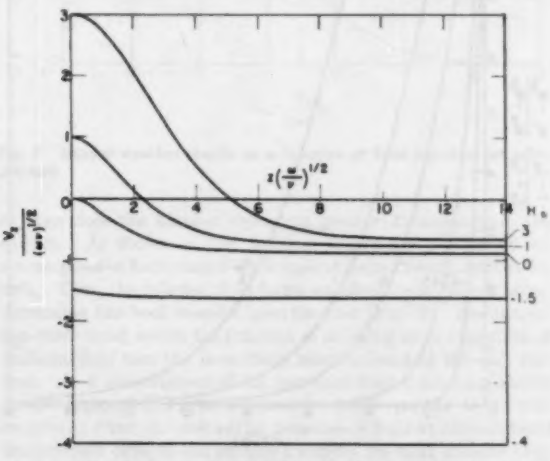

Fig. 2 Representative axial-velocity distributions

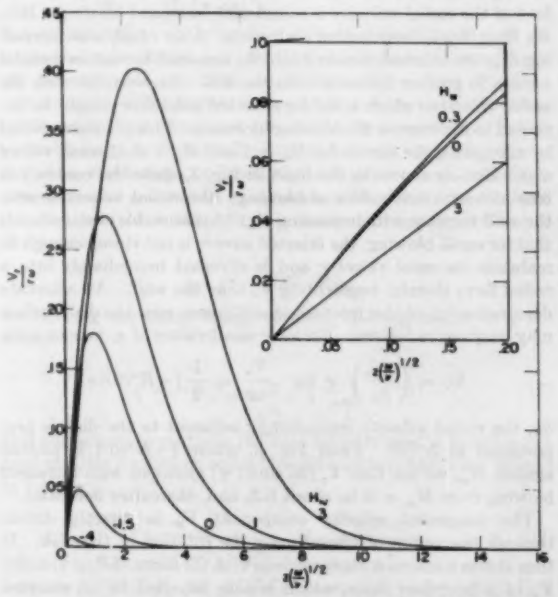

Fig. 3 Representative radial-velocity distributions

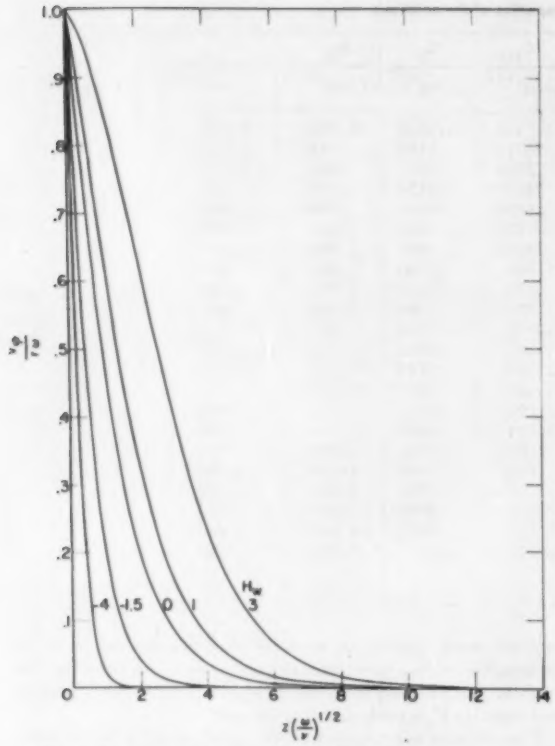

Fig. 4 Representative tangential-velocity distributions

porous wall; so, the radial velocities decrease as H_w becomes more negative. Further, since less fluid makes the turn from axial to radial flow, it can be accomplished closer to the surface, and hence $(V_r)_{max}$ occurs at smaller z. When blowing is applied ($H_w > 0$), the radial velocity must carry away not only the incoming axial flow, but also the injected fluid. So, the general *level* of the radial velocity is raised with increased blowing. But, the finer details bear further discussion. First of all, with increasing H_w, the injected stream might be expected to sustain its axial motion to greater distances from the wall. So, near the wall, the radial velocity (which is fed by diverted axial flow) might be expected to decrease as the blowing increases. This is substantiated by comparing the curves for $H_w = 1$ and $H_w = 3$ at small values of z. But, as shown in the inset in Fig. 3, quite the contrary is true at very *small* values of blowing; the radial velocities near the wall increase with increasing H_w. A reasonable explanation is that for small blowing, the injected stream is not strong enough to maintain its axial velocity and is diverted immediately into a radial flow, thereby augmenting V_r near the wall. An alternate demonstration of this interesting occurrence near the disk surface may be given as follows: For very small values of z, we can write

$$V_r = \left(\frac{\partial V_r}{\partial z}\right)_w z \quad \text{or} \quad \frac{V_r}{r\omega} = \frac{1}{2}\left[-H''(0)\right]\eta$$

So, the radial velocity immediately adjacent to the disk is proportional to $H''(0)$. From Fig. 6, where $[-H''(0)]$ is plotted against H_w, we see that V_r (at small η) increases with increased blowing from $H_w = 0$ to about 0.3, and, thereafter decreases.

The tangential velocity component V_φ is directly driven through the action of viscosity by the rotation of the disk. It thus shares a common characteristic with the forward-flow velocity V_z in a boundary layer, which is also impelled by an external driver—the free stream. The effect of fluid injection or withdrawal on the tangential component V_φ is remarkably similar to the well-established effects on V_z. Fig. 4 shows[4] the distribution of V_φ as a function of distance normal to the disk for representative values of the mass-transfer velocity H_w. It is easily seen that fluid injection ($H_w > 0$) gives rise to the familar S-shaped (inflection point) profiles, the effect becoming more pronounced with increased blowing. Since the presence of an inflection point is known to destabilize a laminar boundary layer, it would be expected that transition to turbulence would occur at lower Reynolds numbers as the blowing becomes stronger. The velocity profile becomes progressively flatter near the wall, suggesting the possibility of a "blow-off" phenomenon in which the viscous layer is lifted off the surface. Blow-off is characterized by the condition

$$(dV_\varphi/d\eta)_w = 0 \quad \text{or} \quad G'(0) = 0$$

In the plot of $G'(0)$ against the blowing parameter, Fig. 6, it is seen that $G'(0)$ appears to be approaching zero with increasing H_w, but we were unable to find the exact blow-off point because of the limitation of an eight-place computer. It remains an open question whether in this problem, where the full Navier-Stokes' equations are being used, the blow-off condition will be characterized by a finite or an infinite value of H_w. Returning to Fig. 4, it may be observed that suction ($H_w < 0$) has its usual effect of thinning the viscous layer, thereby increasing the stability of the laminar flow.

Temperature and Concentration Distribution. The distribution of the dimensionless temperature and concentration as a function of distance from the disk is given in Fig. 5 for representative values of H_w. Since we have selected Pr = Sc, the same curves and a similar discussion applies for both θ and Φ; and for brevity's sake, we will only make reference to the temperature. The action of fluid injection ($H_w > 0$) is to fill the space immediately adjacent to the disk with fluid having nearly the same temperature as that of the disk. As the blowing becomes stronger,

[4] The similarity between V_φ and V_z is best seen by turning Fig. 4 top to bottom.

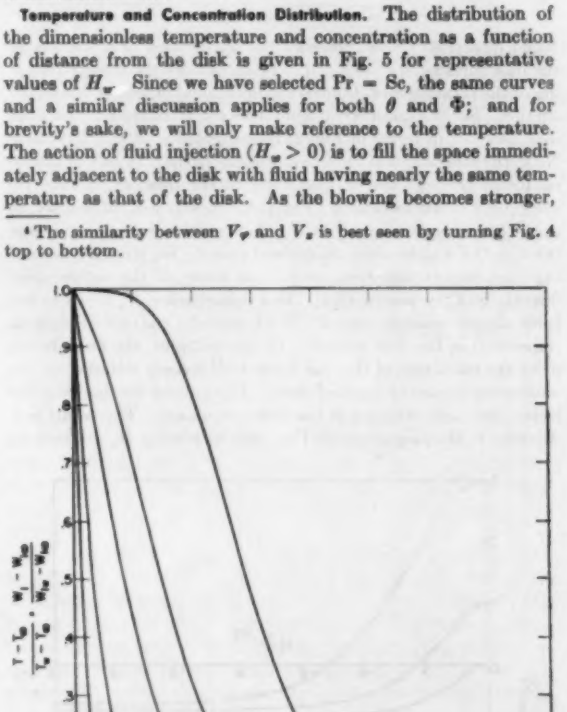

Fig. 5 Representative temperature and mass-fraction distributions

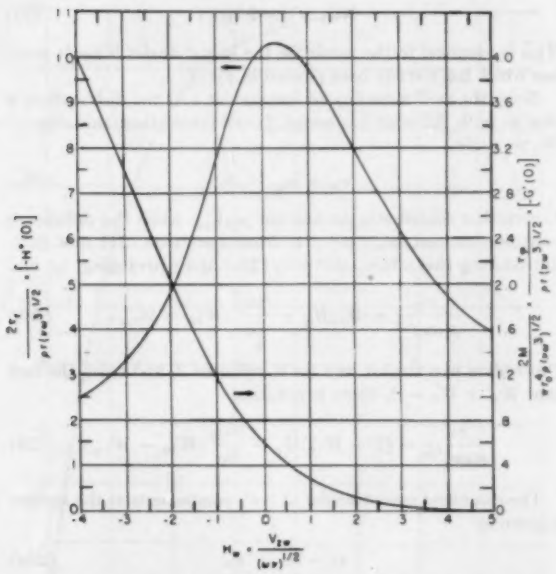

Fig. 6 Torque and shear-stress results as a function of fluid injection (or withdrawal)

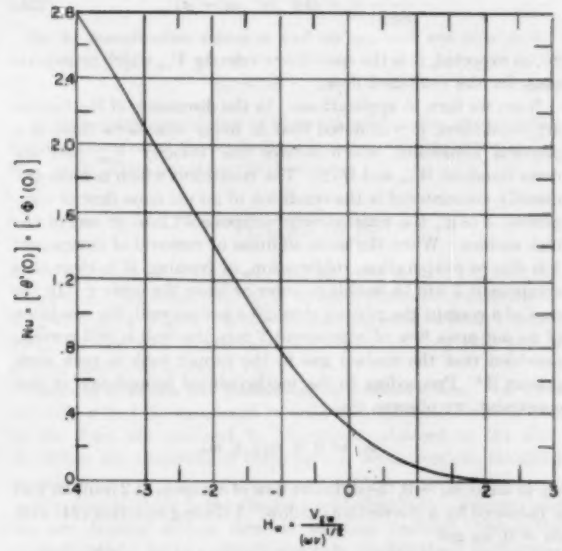

Fig. 7 Nusselt number results as a function of fluid injection (or withdrawal)

so then does the blanket extend to greater distances from the surface. As shown in Fig. 5, these effects are manifested by the progressive flattening of the temperature profile adjacent to the disk. Thus, the injected fluid forms an effective insulating layer, decreasing the heat transfer from the disk (Fig. 7). Suction, on the other hand, serves the function of bringing large quantities of ambient fluid into the immediate neighborhood of the disk surface. As a consequence of the increased heat-consuming ability of this augment flow, the temperature drops quickly as we proceed away from the disk. The presence of fluid at near-ambient temperature close to the surface increases the heat transfer (Fig. 7).

Shear Stress and Shaft Torque. The action of viscosity in the fluid adjacent to the disk tends to set up a tangential shear stress which opposes the rotation of the disk. As a consequence, it is necessary to provide torque at the shaft to maintain a steady rotation. To find the tangential stress τ_φ, we apply the Newtonian shear formula

$$\tau_\varphi = \mu \left(\frac{\partial V_\varphi}{\partial z} + \frac{1}{r} \frac{\partial V_z}{\partial \varphi} \right)_w \tag{13a}$$

In terms of the variables of the analysis, this expression becomes

$$\tau_\varphi / \rho r (\nu\omega^3)^{1/2} = G'(0) \tag{13b}$$

The shaft torque M required to overcome the shear on one side of a rotating disk is

$$M = -\int_0^{r_0} r \tau_\varphi 2\pi r \, dr \tag{14a}$$

where r_0 is the disk radius. Utilizing equation (13b), there is obtained

$$2M / \pi r_0^4 \rho (\nu\omega^3)^{1/2} = -G'(0) \tag{14b}$$

So, both the tangential shear τ_φ and the torque M are proportional to the slope $G'(0)$ of the tangential velocity profile which has been listed in Table 1. The torque and tangential shear results are plotted in Fig. 6 as a function of the mass-transfer velocity H_w. The effect of blowing is to decrease the tangential shear and the torque requirements. These quantities take on zero values at the blow-off point, but computing limitations prevented the determination of this condition. The effects of suction are opposite to those of blowing. These findings reflect the changes in tangential velocity profile as previously discussed and are qualitatively similar to the effects of mass transfer on the skin friction in a boundary-layer flow.

There is also a surface shear stress τ_r in the radial direction which, practically speaking, is of lesser importance than is the tangential stress. Again, using the Newton shear relations and then introducing the variables of the analysis, there is obtained

$$\tau_r = \mu \left(\frac{\partial V_r}{\partial z} + \frac{\partial V_z}{\partial r} \right)_w \quad \text{or} \quad \tau_r / \rho r (\nu\omega^3)^{1/2} = -\tfrac{1}{2} H'(0) \tag{15}$$

This dimensionless shear stress has been plotted in Fig. 6. A maximum value, which has already been discussed in relation to the velocity profiles, is achieved at about $H_w = 0.3$.

It would be of interest to compare the torque and shear-stress results with those computed for suction by Stuart [2]. Unfortunately, he gives numerical values only for the case $H_w = -1$, and these check quite satisfactorily with our more exact findings.

Heat Transfer and Surface Temperature. The heat transfer from the disk surface to the fluid is computed by application of Fourier's law

$$q = -k(\partial T / \partial z)_w$$

Introducing the transformed variables, the expression for q becomes

$$q = -k(T_w - T_\infty) \left(\frac{\omega}{\nu} \right)^{1/2} \theta'(0) \tag{16}$$

It is customary to rephrase the heat-transfer results in terms of a heat-transfer coefficient and a Nusselt number, which are defined as follows:

$$h \equiv \frac{q}{T_w - T_\infty}, \qquad \mathrm{Nu} = \frac{h(\nu/\omega)^{1/2}}{k} \tag{17}$$

where $(\nu/\omega)^{1/2}$ plays the role of a characteristic length. With this, equation (16) becomes

$$\mathrm{Nu} = -\theta'(0) \tag{18}$$

The Nusselt number results are presented in Fig. 7 as a function of the dimensionless mass-transfer velocity H_w. As has already been noted, the effect of fluid injection ($H_w > 0$) is to decrease the heat transfer significantly (and hence, the Nusselt number) by blanketing the surface with fluid whose temperature is close to T_w. Suction has an opposite effect on the heat transfer, since fluid at near-ambient temperature is brought to the neighborhood of the disk surface.

With these heat-transfer results at our disposal, we may proceed to make application to specific situations. Consider the situation of mass-transfer cooling by a gas. The coolant gas enters the porous disk (from a supply tank) at a temperature T_s and is heated in its course of flow through the wall. The flow passages are so arranged that the coolant emerges at a temperature T_w equal to that of the disk surface. It is of interest to determine how T_w is related to the other parameters of the problem. In the absence of heat losses by conduction and radiation, an energy balance on a control volume spanning the thickness of the porous wall yields

$$m_1 c_p (T_w - T_s) = h(T_\infty - T_w) \tag{19a}$$

The left-hand side is the energy absorbed by the coolant gas, while the right side is the heat transferred to the disk surface from the ambient fluid. Borrowing the result that $m_1 = \rho V_{sw}$ from equation (28) and introducing the definitions of the Nusselt and Prandtl numbers, equation (19a) may be rephrased as

$$\frac{T_w - T_s}{T_\infty - T_w} = \frac{\mathrm{Nu}}{\mathrm{Pr}\, H_w} \tag{19b}$$

Suppose that the entering coolant temperature T_s and the free-stream condition T_∞ are known. Further, when the blowing rate H_w is prescribed, the value of Nu may be read from Fig. 7. Hence equation (19b) permits the determination of the temperature T_w of the disk surface as follows:

$$T_w = \frac{T_\infty \left(\dfrac{\mathrm{Nu}}{\mathrm{Pr}\, H_w}\right) + T_s}{1 + \dfrac{\mathrm{Nu}}{\mathrm{Pr}\, H_w}} \tag{19c}$$

It is clear from equation (19c) that increased blowing causes the wall temperature T_w to approach more and more closely to T_s. As an alternative, equation (19b) can be solved to provide either the blowing velocity or the coolant temperature needed to maintain a given T_w.

Equation (19b) or (19c) illustrates the statement, made in discussing the boundary conditions, that there are important applications in which all of the boundary temperatures cannot be prescribed independently.

Additional examples showing the application of the Nusselt number results are given in reference [1].

Mass Transfer. The previous derivation of the heat-transfer coefficient and Nusselt number can be duplicated for diffusion. For component 1, the mass transfer at the disk surface *by diffusion alone* is given by Fick's law (8) as

$$m_{1d} = \rho_{1w}\left(-\frac{D}{W_1}\frac{\partial W_1}{\partial z}\right)_w = -\rho D\left(\frac{\partial W_1}{\partial z}\right)_w \tag{20}$$

Now, defining a diffusional transfer coefficient and diffusional Nusselt number as

$$h_d \equiv \frac{m_{1d}}{(W_{1w} - W_{1\infty})}, \qquad \mathrm{Nu}_d \equiv \frac{h_d (\nu/\omega)^{1/2}}{\rho D} \tag{21}$$

and introducing the variables of the analysis, there is obtained

$$\mathrm{Nu}_d = [-\Phi'(0)] \tag{22}$$

This is identical to the result for the heat-transfer Nusselt number which has already been plotted in Fig. 7.

Now, the *total* mass flow of component 1 at the disk surface is due to both diffusion (subscript d) and convection (subscript c). So, we write

$$m_1 = m_{1d} + m_{1c} \tag{23a}$$

Convection contributes an amount $\rho_{1w} V_{sw}$, while the diffusional contribution can be computed from equations (21) and (22). Introducing this information into (23a) and rearranging, we find

$$\frac{m_1}{\rho(\omega\nu)^{1/2}} = W_{1w} H_w + \frac{\mathrm{Nu}_d}{\mathrm{Sc}}(W_{1w} - W_{1\infty}) \tag{23b}$$

Proceeding in a similar way for component 2, and using the fact that $W_1 + W_2 = 1$, there is obtained

$$\frac{m_2}{\rho(\omega\nu)^{1/2}} = (1 - W_{1w}) H_w - \frac{\mathrm{Nu}_d}{\mathrm{Sc}}(W_{1w} - W_{1\infty}) \tag{24}$$

The combined mass transfer of both components at the surface is given by

$$m = m_1 + m_2 \tag{25a}$$

Adding equations (23b) and (24), we get

$$\frac{m}{\rho(\omega\nu)^{1/2}} = H_w \quad \text{or} \quad m = \rho V_{sw} \tag{25b}$$

So, as expected, it is the convective velocity V_{sw} which transports mass for the combined flow.

Now, we turn to applications. In the discussion of the boundary conditions, it was noted that in many situations there is a physical constraint which relates the velocity V_{sw} and the mass fractions W_{1w} and $W_{1\infty}$. The constraint which is most frequently encountered is the condition of no *net* mass flow of component 2 (e.g., the main stream component) into or out of the disk surface. When the mass addition or removal of component 1 is due to evaporation, sublimation, or freezing, it is clear that component 2 will be unable to enter or leave the surface. In the case of a coolant gas passing through a porous wall, the condition of no net mass flow of component 2 into the wall is still correct, provided that the coolant gas in the supply tank is pure component 2.[5] Proceeding to the mathematical formulation of this constraint, we observe that

$$m_2 = 0 = m_{2d} + m_{2c}$$

So, to make $m_2 = 0$, the diffusive flow of component 2 into the wall is balanced by a convective outflow. Utilizing equation (24) with $m_2 = 0$, we get

$$\frac{H_w(\mathrm{Sc})}{\mathrm{Nu}_d} = \frac{W_{1w} - W_{1\infty}}{1 - W_{1w}} \tag{26}$$

or, in terms of physical variables

$$V_{sw} = -\frac{D}{1 - W_{1w}}\left(\frac{\partial W_1}{\partial z}\right)_w \tag{27}$$

For a given H_w, Nu_d is known. So, equation (26) expresses the fact that for no net mass flow of component 2 into the wall, only two of the quantities W_{1w}, $W_{1\infty}$, and H_w may be selected independently. When $m_2 = 0$, it follows from equations (25a) and (25b) that

[5] Additional discussion will be found in reference [1].

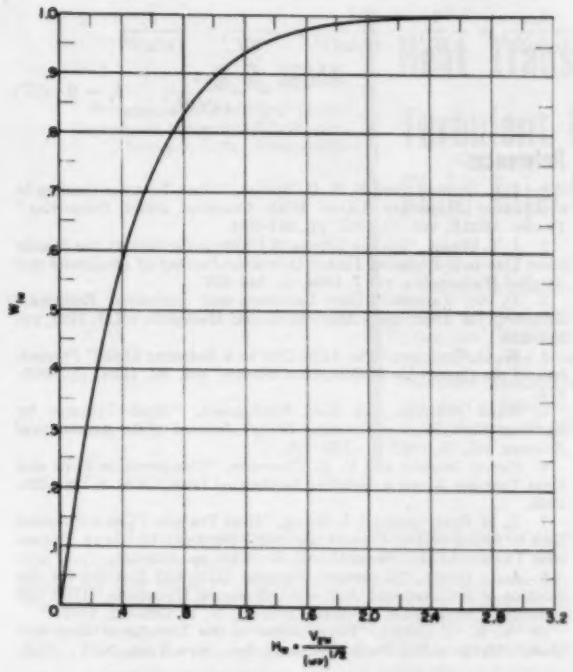

Fig. 8 Mass-fraction values at wall for $m_{1w} = 0$ and $W_{1\infty} = 0$

$$m_1 = m = \rho V_{rw} \tag{28}$$

An important special case of mass-transfer cooling occurs when the mass fraction of the coolant gas is zero in the free stream; i.e., $W_{1\infty} = 0$. Then equation (26) becomes

$$W_{1w} = \frac{1}{1 + \mathrm{Nu}_g/H_w(\mathrm{Sc})} \tag{29}$$

So, W_{1w} is fixed when H_w is specified and vice versa. Utilizing the Nusselt number results in Fig. 7, we have plotted the variation of W_{1w} with H_w in Fig. 8. It is seen that the coolant mass fraction (W_{1w}) at the wall increases rapidly with blowing rate and is greater than 0.95 for $H_w > 1.3$.

Thickness of Viscous and Thermal Layers; Ambient Inflow. Our solutions show that the significant velocity and temperature variations in the fluid are confined to the region adjacent to the disk. To define the thickness of these layers, we use certain standard measures.

The first of these is the displacement thickness. Inasmuch as we are dealing with a three-dimensional problem, the initial thought might be to evaluate separate displacement thicknesses for both the radial and tangential directions. However, since the radial flow is zero both at the disk surface and at infinity, a radial displacement thickness would have very little meaning. Then, for the tangential direction, we define a displacement thickness as

$$\delta_{d1a} = \int_0^\infty \frac{V_\varphi}{r\omega}\,dz \quad \text{or} \quad \delta_{d1a}/(\nu/\omega)^{1/2} = \int_0^\infty G\,d\eta \tag{30}$$

In physical terms, δ_{d1a} gives the thickness of a fictitious layer of fluid which is rotating at a uniform tangential velocity $r\omega$ and is carrying a tangential mass flow equal to that carried by the actual tangential velocity distribution. Values of the displacement thickness are given in Table 1. It is seen that suction appreciably reduces the thickness of the viscous layer, while blowing increases the thickness.

A momentum thickness for flow about a rotating disk has been defined by Stuart [2] as

$$\delta_m/(\nu/\omega)^{1/2} \equiv \int_0^\infty G(1 - G)dy \tag{31}$$

While this expression has a form similar to that for the boundary-layer momentum thickness, we are unable to give it a clear physical meaning. Values of δ_m are listed in Table 1 and show qualitative trends similar to those for δ_{d1a}.

As a measure of the extent of the thermal layer, we may introduce a thermal thickness based on the temperature excess $T - T_\infty$ above the ambient fluid. Then,

$$\delta_t \equiv \int_0^\infty \frac{T - T_\infty}{T_w - T_\infty}\,dz \quad \text{or} \quad \delta_t/(\nu/\omega)^{1/2} = \int_0^\infty \theta\,d\eta \tag{32}$$

Physically speaking, δ_t is the thickness of a fictitious fluid layer at temperature T_w whose integrated temperature excess over T_∞ is identical with that of the actual temperature distribution. Numerical values of the thermal thickness are listed in Table 1 as a function of the mass-transfer velocity H_w. With blowing, the thermal thickness increases; while with suction, it decreases.

The extent of the thermal layer is sometimes characterized by a convection thickness.[6] In reference [9], the definition of such a thickness was motivated by the results of an over-all energy balance. Setting up such a balance for the present problem, we find

$$\frac{\mathrm{Nu}}{\mathrm{Pr}} = -H_w - \int_0^\infty H'\theta\,d\eta \tag{33}$$

The integral represents the convection of energy in the radial direction. So, in analogy to previous work, we define

$$\delta_c/(\nu/\omega)^{1/2} \equiv -\int_0^\infty H'\theta d\eta = \frac{\mathrm{Nu}}{\mathrm{Pr}} + H_w \tag{34}$$

The convective thickness can be evaluated using Fig. 7 or Table 1, since $\mathrm{Nu} = -\theta'(0)$. It may easily be verified that δ_c increases with blowing and decreases with suction.

It may also be of interest to know the quantity of ambient fluid which is drawn inward toward the rotating disk. The inflow velocity of the ambient fluid is $V_{z\infty}$ and its dimensionless counterpart is H_∞. A listing of H_∞-values is given in Table 1. As expected on the basis of previous discussion, H_∞ increases with suction and decreases with blowing. The information given in Table 1 may also be to compute the radial flow. Imagine a cylindrical control surface of radius r extending from the disk surface to the ambient fluid. Then the flow passing through this cylindrical surface is

$$\text{Radial flow} = \rho\pi r^2[V_{rw} - V_{z\infty}] = \rho\pi r^2(\omega\nu)^{1/2}[H_w - H_\infty]$$

For large suction, Table 1 shows that $H_w - H_\infty$ is very small, indicating a small radial flow. The effect of blowing is to increase the radial flow.

Asymptotic Solutions

For large suction (i.e., large negative values of H_w), it is possible to find simple asymptotic solutions of the governing equations. The key to the simplification is the fact, graphically displayed in Fig. 2, that the axial velocity V_z is essentially constant throughout the flow when the suction is strong. In terms of the dimensionless variables of the analysis, this means that H is essentially independent of η for a fixed value of H_w. With this, equations (4a) and (6a) become

[6] Reference [9], pp. 118–119.

$$\theta'' = (\mathrm{Pr})H_w\theta' \quad \text{and} \quad \Phi'' = (\mathrm{Sc})H_w\Phi' \tag{34a}$$

A solution satisfying the boundary conditions is

$$\theta = e^{(\mathrm{Pr})H_w\eta}, \qquad \Phi = e^{(\mathrm{Sc})H_w\eta} \tag{34b}$$

from which it follows that

$$\theta'(0) = (\mathrm{Pr})H_w \qquad \Phi'(0) = (\mathrm{Sc})H_w \tag{34c}$$

For $\mathrm{Pr} = \mathrm{Sc} = 0.7$ and $H_w = -4.0$, equation (34*c*) predicts that $\theta'(0) = \Phi'(0) = -2.8$. This is in excellent agreement with the value -2.802 which appears in Table 1. Proceeding in the same manner, it is easy to show that solution of equation (11) for G is

$$G = e^{H_w\eta}, \qquad G'(0) = H_w \tag{35}$$

The $G'(0)$ prediction of equation (35) for $H_w = -4$ is very close to the value 4.005 given in Table 1.

Continuing, we may use equation (10) to predict values of $H''(0)$. Noting that $(H')^2/2$ is smaller than the other terms, we integrate between limits of $\eta = 0$ and $\eta = \infty$ and get

$$H''(0) = \frac{1}{H_w} \tag{36}$$

For $H_w = -4$, equation (36) gives $H''(0) = -0.25$, which is in excellent agreement with the value of -0.2495 in Table 1.

With these results, it is easy to derive that the thickness parameters take the following form for large negative values of H_w:

$$\frac{\delta_{d1*}}{(\nu/\omega)^{1/2}} = -\frac{1}{H_w}, \qquad \frac{\delta_m}{(\nu/\omega)^{1/2}} = -\frac{1}{2H_w}, \qquad \frac{\delta_t}{(\nu/\omega)^{1/2}} = -\frac{1}{(\mathrm{Pr})H_w}, \qquad \delta_e = 0 \tag{37}$$

References

1 J. P. Hartnett and E. R. G. Eckert, "Mass-Transfer Cooling in a Laminar Boundary Layer With Constant Fluid Properties," TRANS. ASME, vol. 79, 1957, pp. 247–254.

2 J. T. Stuart, "On the Effects of Uniform Suction on the Steady Flow Due to a Rotating Disk," *Quarterly Journal of Mechanics and Applied Mathematics*, vol. 7, 1954, pp. 446–457.

3 T. von Karman, "Über Laminare und Turbulent Reibung," *Zeitschrift für Angewandte Mathematik und Mechanik*, vol. 1, 1921, pp. 233–235.

4 W. G. Cochran, "The Flow Due to a Rotating Disk," *Proceedings of the Cambridge Philosophical Society*, vol. 30, 1934, pp. 365–375.

5 Knox Millsaps and Karl Pohlhausen, "Heat Transfer by Laminar Flow From a Rotating Disk," *Journal of the Aeronautical Sciences*, vol. 19, 1952, pp. 120–126.

6 Simon Ostrach and P. R. Thornton, "Compressible Flow and Heat Transfer About a Rotating Isothermal Disk," NACA TN 4320, 1958.

7 E. M. Sparrow and J. L. Gregg, "Heat Transfer From a Rotating Disk to Fluids of Any Prandtl Number," JOURNAL OF HEAT TRANSFER, TRANS. ASME, Series C, vol. 81, 1959, pp. 249–251.

8 J. L. Gregg, "A General Purpose IBM 653 Routine for the Solution of Simultaneous Ordinary Differential Equations," IBM 650 Scientific Computation Seminar, Endicott, N. Y., October, 1957.

9 E. R. G. Eckert, "Introduction to the Transfer of Heat and Mass," McGraw-Hill Book Company, Inc., New York, N. Y., 1949.

R. A. SEBAN

Professor, Mechanical Engineering Department, University of California, Berkeley, Calif. Mem. ASME

Heat Transfer and Effectiveness for a Turbulent Boundary Layer With Tangential Fluid Injection

Experimental results are presented for the effectiveness and for the heat-transfer coefficient for a film cooling system in which air was used both for the film and for the free-stream fluids. Injection occurred at a single tangential slot near the leading edge of the plate and the slot size was varied. All flows were turbulent and the injection velocities covered a range from much less to much greater than the free-stream velocity. Correlations are realized for both the effectiveness and for the heat-transfer coefficient and, as in the past experience with such systems, separate specifications are needed for injection velocities greater and less than the free-stream velocity.

This is a presentation of experimental results on a film cooling system using air both as the free stream and "film" fluids, the flow being two dimensional, turbulent, and subsonic. The system examined was a flat plate with a slot located at its upstream edge and the film air emerged from this slot tangentially. In such an arrangement the injected air serves to shield the plate from the main stream, and so inhibits the heat transfer between the main stream and the plate. When the plate is insulated, the effect of the injection can be characterized completely in terms of the ratio of the excess of plate over free-stream temperature to the excess of the injected air over the free-stream air temperature. This ratio is called the effectiveness. If there is a heat flux at the plate surface, it is necessary to know in addition the local heat-transfer coefficient in order to evaluate the flux. Both the effectiveness and the heat-transfer coefficient were determined in the experiments here described.

It is the general nature of the problem that first efforts were directed to the determination of the effectiveness. The pioneer investigation of Wieghardt [1][1] produced such values for a slot in which nearly tangential injection was achieved, and that research first indicated that a maximum existed in the effectiveness when the velocities of the free stream and injected air were of the same order. Chin [2] has recently noted these and other results, in connection with the presentation of experimental values of the effectiveness which embraced a large range of variables, including significant variations in density and of the boundary-layer thickness just upstream of the tangential injection slot. Correlation of all these results was achieved empirically by the use of an expression made complicated by the many variables involved.

Analysis has not yet borne significantly on this problem because of the complicated nature of the flow, affected as it is by the geometry of the slot and the relative values of the velocities of the free stream and injected flows. Only for very low or very high injection rates are there any indications from theory. For the low rates, Klein and Tribus [3] considered that the entire flow was so dominated by the free-stream flow that only the thermal effect of the injection might be significant, and for heated injection this might be considered to have the same effect as a line source of heat at the leading edge of the plate. If the source strength, Q, is taken to be the energy rate of the injected flow $\rho_s u_s c_p s t_s$, then the result for such a case is:

$$\frac{t_a}{t_s} = 5.77 \left(\frac{\nu}{\alpha}\right)^{1/3} \left(\frac{u_s \rho}{\nu}\right) \left(\frac{u_1 x}{\nu}\right)^{-0.5} \qquad (1)$$

This expression was shown to predict the order of magnitude of the results of Wieghardt but it fails to predict the results given by Chin.

When the injection-flow velocity exceeds that of the free stream, the injection flow itself is the dominant influence on the nature of the flow in a region that extends far downstream of the slot. The extreme situation is, of course, presented in the absence of a free-stream flow, in which case the flow has been aptly

[1] Numbers in brackets designate References at end of paper.

Contributed by the Heat Transfer Division and presented at the Annual Meeting, Atlantic City, N. J., November 29–December 4, 1959, of THE AMERICAN SOCIETY OF MECHANICAL ENGINEERS.

NOTE: Statements and opinions advanced in papers are to be understood as individual expressions of their authors and not those of the Society. Manuscript received at ASME Headquarters, September 3, 1959. Paper No. 59—A.-177.

Nomenclature

A, B, C = variables defined in Equations (6), (10), (12)

c_p = specific heat at constant pressure

h = local heat-transfer coefficient

k = thermal conductivity

q = heat flux

s = injection slot height

t = temperature above free-stream temperature, deg F; t_s injection air, t_1 free stream, t_o wall temperature, t_a adiabatic wall temperature

T = absolute temperature, deg R

u = velocity; u_s injection air, u_1 free stream

x = distance downstream of the slot

α = thermal diffusivity

μ = absolute viscosity

ν = kinematic viscosity

ρ = density

Subscripts

s = injection air

1 = free stream

o = wall

a = adiabatic wall

named the "wall jet" by Glauert [4], who predicted analytically the nature of the velocity profiles for it, showing that similarity does not exist but is approached closely for limited ranges of Reynolds numbers. The development of the flow along the plate is specified less clearly, making difficult the evaluation of the temperature distribution or the heat flux at the wall from that solution of the hydrodynamic problem. Experimental evidence related to these quantities for the wall jet has, however, been provided by Jakob [5].

The results reported here are directed toward a further clarification of the nature of the effectiveness and the heat-transfer coefficient with particular reference to the effect of changing the slot size. Results have been obtained for three slot sizes with ratios of injection to free stream velocity both less and greater than one, in the latter case attaining values that approach wall jet conditions.

Apparatus and Procedure

The test surface was a bakelite plate, 12 in. wide, 18 in. long, and $^1/_2$ in. thick, the plate being the top wall of the $4^1/_2$ by 12-in. rectangular test section of a small, once-through, wind tunnel. Air from the test section passed through a diffuser, centrifugal blower, throttle, and back into the room. This air was drawn from the room into the test section through a nozzle.

The injection slot was located at the upstream edge of the plate, immediately downstream of the nozzle, and it spanned completely the 12-in. width of the plate. Fig. 1(*a*) indicates a section through the slot unit and shows the manner of adjustment of the slot size, involving the movement of the downstream part of the slot block and of the entire test plate that was attached to it. In this way the tangential injection was preserved when the slot size was changed. Air entered the slot from a flow system containing a positive-displacement blower, surge tank, flowmeter, and a heater and cooler for the adjustment of the temperature. This temperature was measured by five iron-constantan thermocouples spanning the slot block, with the center thermocouple on the center line.

The test plate contained on its surface five nichrome ribbons, each 1 in. wide and 0.002 in. thick, placed longitudinally with the center ribbon on the plate center line. Heating was produced by the passage of alternating electric current through the ribbons in series. Iron-constantan thermocouples were placed immediately below the ribbon, in small slots in the plate surface, with the primary set of junctions under the center ribbon. Pressure taps were located in $^1/_{16}$-in. spaces between the three center ribbons and the outer ribbons, with successive taps on alternate sides. The back, exterior surface of the plate was insulated, and additional thermocouples were located at this surface.

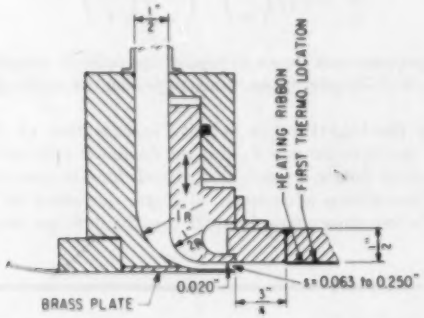

(a) Adjustable slot used to obtain the results of the paper

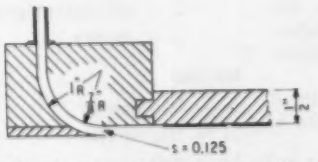

(b) Detail of an older slot unit, certain results from which are shown in Fig. 3

Fig. 1 Section through the injection slot

Certain problems existed in the realization of uniformity in the temperature and velocity of the air emerging across the span of the injection slot. There was a small variation in velocity due to the relatively small plenum chamber located just upstream of the slot block and partly also to nonuniformity in the slot height. This velocity change was not very great, being less than 2 per cent over the central 11 in. of the slot width. The slot height itself varied by ± 0.002 in. due to irregularities at the edges, and the settings were made so that the quoted openings were average values. Variations in the temperature of as much as 6 per cent of the excess of injection over free-stream temperature occurred, particularly near the outer edges of the slot, though the temperature excess in the central six inches was generally constant to within 2 per cent. This variation was due to heat transfer from the injection system, particularly in the plenum chamber upstream of the slot, and this was consequently more severe at the lower injection rates. Reduction of this heat transfer would have required a reduction in size of the upstream flow assembly, with a consequent increase in the nonuniformity of the flow.

When the system was operated with heated injection and without heating of the plate, adiabatic conditions on the plate surface were approximated well in most cases, and the observed surface temperature t_o was taken as equal to the adiabatic surface temperature t_a. Here these temperatures, and temperature of the injection air t_s are all taken with free-stream temperature as datum. Then the effectiveness was evaluated directly from the experimental results as

$$t_a/t_s = t_o/t_s \tag{2}$$

All the results are presented on this basis, despite the error involved in taking the wall temperature as the adiabatic wall temperature and despite the error in the precise value of the injection temperature t_s. The former error was always less than $1^1/_2$ per cent and the latter less than 2 per cent except insofar as is concerned the larger disparity near the outer edges of the slot. This was serious only with low injection rates, and its effects would have been significant only far downstream. Under those circumstances and in that location, the effectiveness is very low and the accuracy of the determination there is dominated by errors in temperature indication. When the effectiveness was less than 0.10 this error may have been as much as 10 per cent.

When the plate is heated, the excess of plate over free-stream temperature depends upon the injection temperature as well as upon the parameters associated with the flow. For constant properties, this case may be considered to be the superposition of the adiabatic-wall jet, with heated injection, and the case of a heated plate, with injection at the free-stream temperature. This consideration indicates that the effective temperature difference is that between the plate-surface temperature and the adiabatic wall temperature corresponding to the existing flow conditions and injection temperature. Then the heat-transfer coefficient is specified as

$$h = q/(t_o - t_a) \tag{3}$$

In its evaluation, the heat flux q was obtained on the assumption that all the heat generated in the ribbon was transferred to the air stream, thus ignoring the very small radiative transfer and the larger effects of heat conduction. The largest possible error that could have been introduced in this way would have

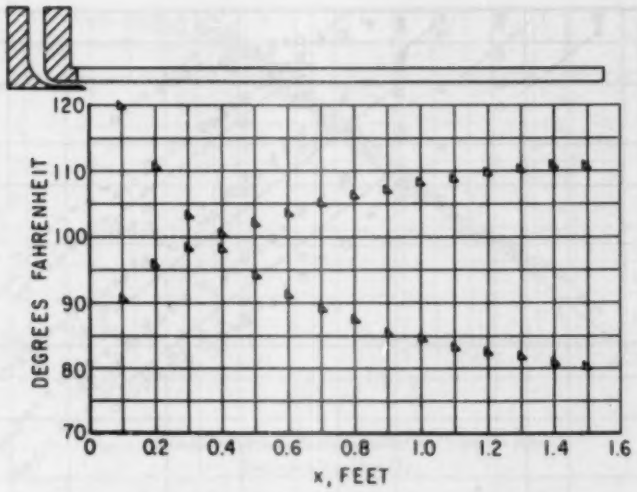

Fig. 2 Typical wall temperatures with adiabatic and with heated operation
Runs 129 and 130 are shown, the former being the adiabatic case

been 4 per cent; generally it was much less. With this operation the injection air temperature was set close to the free-stream temperature, so that the adiabatic wall temperature, obtained from the effectiveness results, was also very close to free-stream temperature. Temperature differences were of the order of 25 F and the error in this determination together with the error in the flux contributed to an estimated maximum error of 5 per cent in the heat-transfer coefficient.

In operation, temperatures in the free stream were between 50 F and 70 F and injection temperatures were between 0 F and 70 F above the free-stream temperature, with practically all effectiveness determinations being made with the 70 F excess temperature. Free-stream velocities ranged from 50 to 150 fps, and injection velocities from 50 to 250 fps. Three slot heights were used, 0.250, 0.125, and 0.063-in.

Fig. 2 shows typical results for adiabatic wall and for heated wall operation, and by its distance scale also defines the location of the thermocouples along the plate. Only here are temperatures indicated in the usual Fahrenheit scale; in all subsequent presentations the temperatures are given in degrees Fahrenheit with free-stream temperature as datum.

For presentation the results are divided, with those for mass velocity ratios less and greater than one being considered separately. Tables 1 and 2 summarize some of the experimental conditions and serve to identify the points used in the figures.

Table 1 Mass-velocity ratios less than unity

		ADIABATIC WALL					HEAT TRANSFER				
		Fig. 3, 4, 5, 6, 7					Fig. 8				
Symbol	s, in.	Run	$\frac{\rho_1 u_1}{\rho_\infty u_\infty}$	$\frac{u_1}{u_\infty}$	$\frac{\rho_1}{\rho_\infty}$	$\frac{\mu_1}{\mu_\infty} \times 10^{-3}$	Run	$\frac{\rho_1 u_1}{\rho_\infty u_\infty}$	$\frac{u_1}{u_\infty}$	$\frac{\rho_1}{\rho_\infty}$	$\frac{\mu_1}{\mu_\infty} \times 10^{-3}$
□	.125	103	.88	130	122	5.22	105	.89	107	121	6.88
△	.125	105	.58	79	120	3.97	106	.60	72	120	4.65
◇	.125	107	.39	54	121	2.72	108	.39	57	120	3.00
○	.125	109	.17	24	121	1.21	110	.18	28	120	1.44
■	.125	111	.60	59	97	3.05					
▽	.125	113	.26	36	97	1.32					
◆	.250	117	.88	64	63	6.45	118	.87	55	64	7.06
▼	.250	119	.59	43	96	6.35	120	.59	55	95	7.05
⊙	.250	121	.38	25	96	2.52	122	.36	21	59	2.73
◀	.250	123	.18	23	118	2.42	124	.18	21	118	2.73
●	.250	125	.06	24	82	2.42					
◣	.063	127	.60	81	124	2.16	130	.60	72	123	2.38
◺	.063	131	.39	56	122	1.38					
⊕	.063	133	.27	39	123	.93	134	.27	33	123	1.06
⊖	.063	135	.18	25	123	.62					
⊗	.063	137	.76	105	122	2.49					

Adiabatic Wall Temperatures With Low Injection Velocities

Results for the adiabatic wall temperature, such as shown in Fig. 2, are presented in Fig. 3 in terms of the effectiveness, and are shown there in terms of the number of slot heights downstream of the injection slot. Effectiveness values are given for the three slot heights, for nearly equal ratios of injection to free-stream mass velocities, with a maximum ratio of 0.88. Since in all these runs the density ratio was substantially invariable at $\rho_1/\rho_\infty = 1.14$, the mass-velocity ratio indicates the velocity ratio also. A salient feature of the representation is the approximate dependence, particularly at low velocity ratios, on the value of (x/s). This is obviously at variance with the indication of Equation (1) and, as will be seen, with other proposed correlations. Typical of all the runs is an initially almost constant value of the effectiveness which extends downstream an increasing distance as the mass-velocity ratio increases. This is followed by a transition to an approximate power-law dependence on distance. Consistent behavior is evident in the power-law regime, particularly for mass-velocity ratios of 0.60 and less, to indicate a proportionality to (x/s) to the 0.80 power. Lines showing such an approximation are indicated in Fig. 3.

It is obviously possible to achieve a correlation of the results in the power-law regime by alternating the abscissa of Fig. 3. This is done by specifying the distance indicated by the extrapolation of the lines in that figure to indicate the distance, $(x/s)_1$, at which they indicate an effectiveness of unity. These distances are shown in Fig. 4 and a power law is indicated for their representation. In so far as a final correlation is concerned, the location of this line is critical and the one indicated is actually the one giving the best final representation of the results. It is:

$$\left(\frac{x}{s}\right)_1 = 56\left(\frac{\rho_2 u_2}{\rho_1 u_1}\right)^{1.8} \tag{4}$$

If this distance is made the basis of measurement of distance downstream, then the effectiveness can be expressed as

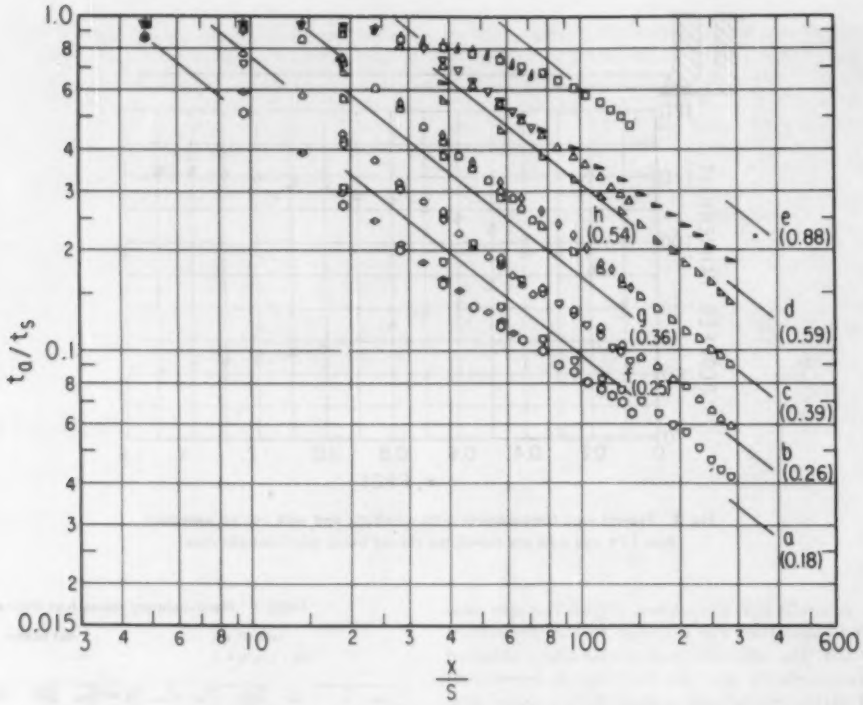

Fig. 3 Effectiveness for mass-velocity ratios less than unity

The points are identified in Table 1. Lines a, b, c, d, and e are the best fit for the mass-velocity ratios indicated. Lines f, g, h are similar best fit lines indicating results that were obtained with the slot shown in Fig. 1(b).

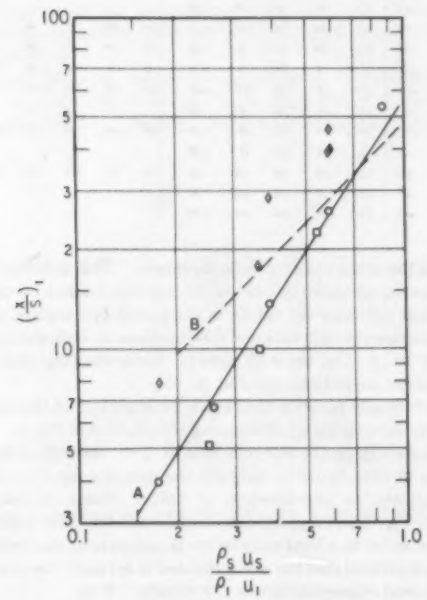

Fig. 4 Initial distance for the power laws

The distance $(x/s)_1$ is that at which curves a, b, c, d, e of Fig. 3 indicate an effectiveness of unity. Line A is the best fit to points a, b, c, d. Points f, g, h refer similarly to the same curves in Fig. 3. The diamond points refer to Fig. 8 and indicate values of 1.10 or 0.90 in that figure. Line B is that given by Wieghardt's results.

$$\frac{t_0}{t_s} = \left(\frac{x}{s}\right)^{-0.8} \left(\frac{x}{s}\right)_1^{0.8}$$

or

$$\frac{t_0}{t_s} = 25 \left(\frac{\rho_s u_s}{\rho_1 u_1}\right)^{1.2} \left(\frac{x}{s}\right)^{-0.8} \tag{5}$$

Fig. 5 shows the correlation of the results that is achieved on this basis and this representation is best for the consideration of the effect of the various system parameters. For instance, the best slot height for a given injection mass flow is the smallest slot, for at constant x and fixed flow, $\rho_s u_s s$, the effectiveness in the power law region varies as $s^{-0.4}$. The maximum effectiveness wall, of course, is obtained with $\rho_s u_s \approx 0.9\, \rho_1 u_1$.

Fig. 3 also contains lines which indicate experimental results that were obtained from a different, though similar, system incorporating the slot shown in Fig. 1(*b*). With this unit only an $^1/_8$-in. slot was available, which differed essentially from the unit shown in Fig. 1(*a*) in its curved approach section. This yielded an emerging flow similar to that expected for flow in a curved channel, at a turbulence level that must have been considerably higher than that emerging from an adjustable slot. The results for the effectiveness are, however, only slightly different, and that possibly due to other causes. The dependence on distance is essentially confirmed, though the corresponding points in Fig. 4 are slightly below Equation (4). Within this margin, the nature of the injection slot does not affect the results.

Wieghardt [1] interpreted his results in a similar way and if those results are appraised in the manner used in Fig. 4, they define a different power law for the point $(x/s)_1$. Since the slope of that relation is unity, he was able to represent his results in

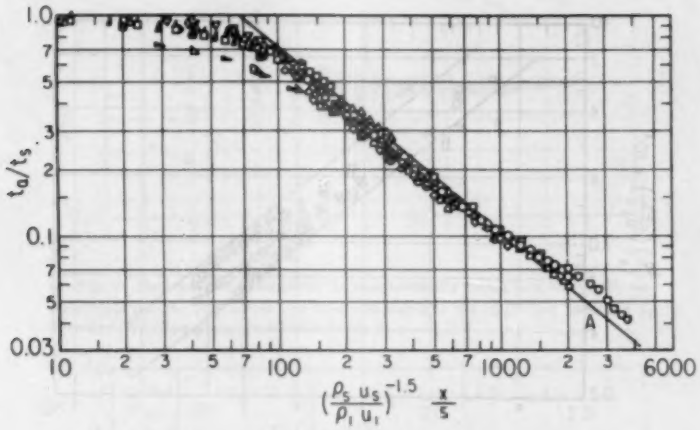

Fig. 5 Correlation of the effectiveness for low injection rates
Curve A is Equation (5)

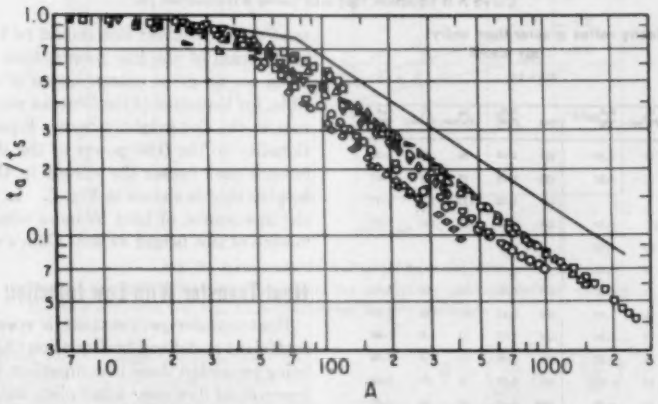

Fig. 6 The effectiveness presented according to Chin
The points are those of Fig. 3 and the curves are Chin's correlation

terms of the single group $(\rho_s u_s s/\rho_1 u_1 x)$. It is evident that while the present results are of the same magnitude and have the same dependence on x/s, the effect of the mass-velocity ratio is different.

Chin [2] has presented similar results for a system incorporating a 0.106-in. slot similar to the one shown in Fig. 1(*b*). The initial boundary-layer thicknesses were greater and were varied, and there were in those results greater changes in the density ratio. For the region of final power-law behavior, similar to that defined by Equation (5), Chin correlated the values of the effectiveness by

$$\frac{t_a}{t_s} = 12.7\, A^{-0.8}$$

where

$$A = \left(\frac{\rho_1}{\rho_s}\right)^{1.5} \left(\frac{u_1}{u_s}\right)^{1.0} \left(\frac{u_s s}{\nu_s}\right)^{-0.2} \left(\frac{u_1 L}{\nu_1}\right)^{0.13} \left(\frac{x}{s}\right) \qquad (6)$$

or, approximately, by taking the viscosity as proportional to the temperature

$$A = \left(\frac{\rho_1 u_1}{\rho_s u_s}\right)^{1.30} \left(\frac{\nu_1}{u_1 L}\right)^{0.11} \left(\frac{T_s}{T_1}\right)^{0.80} \left(\frac{L}{s}\right)^{0.30} \left(\frac{x}{s}\right) \qquad (7)$$

The present results are represented on this basis in Fig. 6 and that representation emphasizes the lower magnitude of the present results, which is largely due to the 0.8 rather than the 0.65 power dependence. The results for the individual slot heights are fairly well aligned, since in group A the mass-velocity ratio enters to a power not too different from that indicated by Equation (4). In the representation of Fig. 6, the distance L was taken as 2.5 in., based on the results of boundary-layer traverses made just upstream of the slot.

Important also in a comparison of Equations (5) and (6) is the absence in Equation (5) of a separate temperature dependence such as indicated in the form of the group as it is given by Equation (7). Such an effect was not easily established in the present experiments, in which the temperature ratio could be changed only in the range $1.14 > T_s/T_1 > 1.06$, the lower limit being enforced by acceptable accuracy in the results. Within this range, no separate temperature effect was detected when the mass-velocity ratio was held constant, but the change in effectiveness according to Equation (6) would have been only 4 per cent.

It is appropriate also to examine the values of the effectiveness in relation to Equation (1), which is a prediction for a line source at the leading edge of a plate. This is done in Fig. 7, where there are shown results only for the lowest mass-velocity ratios, which might be expected to provide the best correspondence with the theory. Since slot and free-stream Reynolds numbers are used in the figure, Equation (1) is taken in the form

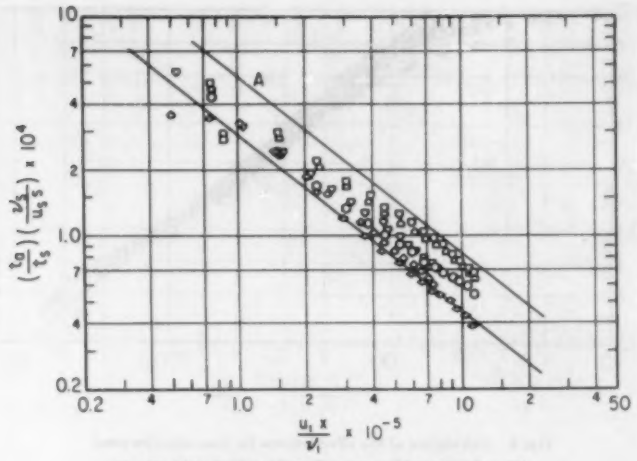

Fig. 7 Effectiveness values compared to Equation (1)
Curve A is Equation 1(a) and Curve B is Equation (8)

Table 2 Mass-velocity ratios greater than unity

		ADIABATIC WALL FIG - 10, 11					HEAT TRANSFER FIG - 12				
Symbol	$\frac{s}{l_0}$	Run	$\frac{\rho_1 u_1}{\rho_s u_s}$	$\frac{u_1}{u_s}$ sec	$\frac{u_1}{u_s}$ sec	$\frac{u_s s}{\nu_s} \times 10^{-3}$	Run	$\frac{\rho_1 u_1}{\rho_s u_s}$	$\frac{u_1}{u_s}$ sec	$\frac{u_1}{u_s}$ sec	$\frac{u_s s}{\nu_s} \times 10^{-3}$
▽	.125	101	1.08	105	97	5.37	102	1.08	96	88	6.00
○	.250	135	1.07	64	59	6.60	116	1.05	55	53	7.07
●	.063						128	1.12	133	123	4.37
○	.063	111	2.14	253	101	6.10	152	2.25	215	100	7.03
⊙	.063	143	3.12	362	69	6.05					
⊙	.063	145	5.13	362	42	6.05					
▽	.063	147	20.75	237	10	6.19	110	0.44	212	25	6.80
◢	.063	149	9.06	133	14	3.53	150	0.93	120	14	3.92
△	.063	151	5.96	67	7	1.29	152	7.85	43	6	1.30
□	.250	159	1.90	68	36	5.57	160	3.30	52	16	6.96
○	.250	161	3.57	56	15	6.60	162	2.02	54	26	6.93
▯	.250	163	4.62	56	11	6.96	162a	5.28	56	11	7.00
○	.250	165	4.59	30	6	3.90	168a	5.15	30	6	3.95
⊙	.250						170		0	122	0
▽	.250						172		0	63	0
◇	.125	173	6.68	119	17	6.68	174	6.68	133	17	7.09
⊙	.125	175	6.69	65	9	3.80	176	7.57	61	9	3.89
⊙	.125	177	4.67	23	5	1.38	178	3.89	125	32	7.95

$$\frac{l_a}{l_s} = 5.77(0.70)^{3/8} \frac{\mu_s}{\mu_1} \left(\frac{u_s s}{\nu_s}\right) \left(\frac{u_1 x}{\nu_1}\right)^{-0.8} \qquad (1a)$$

with the factor μ_s/μ_1 taken as 1.14, typical of most of the operating conditions. There is shown also in the figure a prediction made from a Lighthill-type analysis based on the $^1/_7$-power-law velocity profile and a Prandtl number of one. The result is somewhat different than Equation (1), just as the unheated starting-length correction produced by such an analysis is different from the Rubesin result for an unheated starting length that is the genesis of Equation (1). While this difference is relatively small, that for the line source of heat is large. The result, with a factor of (μ_s/μ_1) inserted arbitrarily, is

$$\frac{l_a}{l_s} = 3.1(0.70)^{3/8} \left(\frac{\mu_s}{\mu_1}\right) \left(\frac{u_s s}{\nu_s}\right) \left(\frac{u_1 x}{\nu_1}\right)^{-0.8} \qquad (8)$$

As shown in Fig. 7, the factor μ_s/μ_1 is taken as 1.14.

In the figure, the results for the three slot heights are bracketed by the two equations, with those for the $^1/_{16}$-in slot being closest to Equation 1(a). If it is implied that the results pertinent to the smallest slot should be those that approach best the assumption of the line source, then Klein's analysis is favored. Even so, no great extrapolation of such correspondence is possible, for Equation (1) indicates a proportionality of the effectiveness to the slot height, whereas Equation (5) indicates a proportionality to the 0.80 power of the slot height and it is the difference that causes the spread in the results for the three slot heights that is shown in Fig. 7. In this sense the prediction for the line source of heat includes almost the same additional influence of slot height as does Chin's correlation.

Heat Transfer With Low Injection Velocities

Heat-transfer performance is specified according to the local coefficient as defined by Equation (3), and this is shown in Fig. 8, being presented there in comparison to the local coefficient for the free-stream flow over a flat plate that is specified by the Colburn equation:

$$\frac{h_0}{\rho_1 u_1 c_p} = 0.037 \left(\frac{u_1 x}{\nu_1}\right)^{-0.2} \qquad (9)$$

Fig. 8 shows that such values are attained within about 70 slot heights, with the local coefficients approaching this value in a way dependent upon the magnitude of the injection velocity. An appraisal of the rapidity of the approach is possible by defining the distance downstream needed to attain an arbitrary departure from Equation (9), and a 10 per cent departure was selected. Because the nature of the individual dependence of the coefficients on the downstream distance, the 10 per cent point is not easy to specify accurately and there is a consequent scatter in these points as they are shown in Fig. 4. There the points do show a trend similar to those points, obtained from the results for the effectiveness, that were used to establish Equation (4), and they thereby support the inference that after an initial flow regime that is controlled by the mixing flow there exists a downstream region dependent only on the nature of the free-stream flow.

In the region immediately downstream of the slot there exists a complicated behavior in which, as is indicated in Fig. 8, the heat-transfer coefficient depends on the ratio of the mass velocities, as well as on the free-stream conditions. Besides this influence there is also that of flow separation at the slot when the injection velocity is low. If it is zero, the separated flow reattaches at about six slot heights downstream, to give a maximum coefficient at that point. Moving downstream of this point, it is known that the heat-transfer coefficient rapidly attains a value characteristic

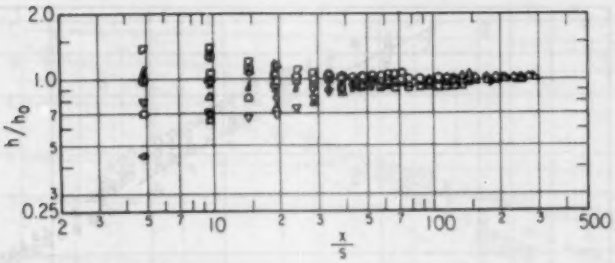

Fig. 8 Heat-transfer coefficients for mass-velocity ratios less than unity
Local heat-transfer coefficients are here compared to the coefficient specified by Equation (9). Points are identified in Table 1.

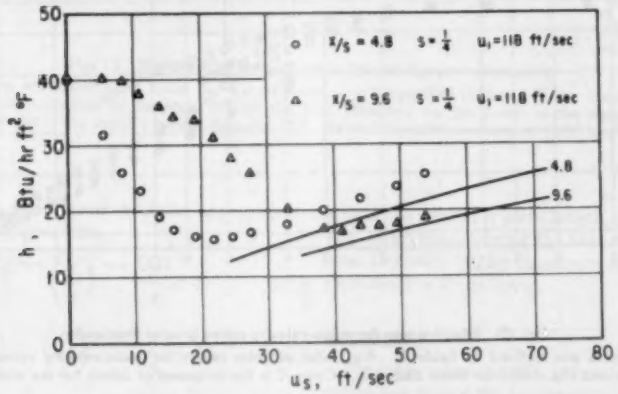

Fig. 9 Heat-transfer coefficient near the slot
There is exhibited the dependence of the coefficient on the injection velocity. Curves B are curve B of Fig. 12 evaluated for the two positions.

of flow over a flat plate. With flow through the slot, the maximum heat transfer is reduced as the flow pattern is changed, and Fig. 9 illustrates this effect for the first two positions downstream of the slot, at $x/s = 4.8$ and 9.6, for the 0.250 in. slot and a free-stream velocity of 118 fps. As the injection flow is increased, there is first a rapid reduction in the coefficient, followed by an increase. This increase, particularly for the second position, turns out to be almost completely predictable from the correlation of the heat-transfer coefficient for high injection velocities that is presented later.

Effectiveness With High Injection Velocities

The increase of the effectiveness with increasing mass-velocity ratio that is portrayed in Fig. 3 terminates at a mass-velocity ratio of the order of 0.90. At higher ratios the effectiveness is practically constant until a ratio of about 1.1 is attained, then the effectiveness begins to diminish. This reduction is much less sensitive to the velocity ratio, and is accompanied by an increased influence of other system parameters. This behavior is generally revealed by the results as shown in Fig. 10, where the representation is the same as that of Fig. 3. No correlation or indication thereof is provided in this way, and to realize some clarity the presentation is separated for mass-velocity ratios less than three and greater than three. Fig. 10(*b*), for the higher ratios, does indicate that in the limit the effectiveness is still of the order of what is attained at mass-velocity ratios of 0.60.

Chin [2] presented a few results at velocity ratios greater than unity and correlated them, for $1.21 < \frac{u_s}{u_1} < 1.65$, on the basis of the group

$$B = \left(\frac{\rho_1}{\rho_s}\right)^{1.8} \left(\frac{u_s s}{\nu_s}\right)^{-0.2} \left(\frac{u_1 L}{\nu_1}\right)^{0.18} \left(\frac{x}{s}\right)$$

For $B > 60$ the effectiveness is given by

$$\frac{t_s}{t_s} = 3.93\, B^{-0.40} \tag{10}$$

One result, for $u_s/u_1 = 2.85$, was about 20 per cent below this line.

If this group is used for the results shown in Fig. 10 then correlation is achieved within ±5 per cent for those results for a mass-velocity ratio greater than 2.5. In the final power-law region the relation specifying the effectiveness is

$$\frac{t_s}{t_s} = 3.63\, B^{-0.44} \qquad B > 20 \tag{11}$$

To account for those results in which the mass-velocity ratio was between 1.08 and 2.5, an account must be made for the difference between the injection and free-stream velocities. In this change, the free-stream Reynolds number ($u_1 L/\nu_1$) was removed, for its contributions were small in the correlation of Equation (11) and its retention leads to ambiguity as the free-stream velocity approaches zero in the limit. Thus a new group was chosen:

$$C = \left(\frac{\rho_1}{\rho_s}\right)^{1.8} \left(\frac{u_s - u_1}{u_s}\right)^{0.2} \left(\frac{u_s s}{\nu_s}\right)^{-0.2} \left(\frac{x}{s}\right)$$

Fig. 11 presents on this basis all the results that are shown in Fig. 10, to show a correlation which includes even the run for a mass-velocity ratio of 1.08 and which at the same time is ostensibly valid for the wall-jet case. For the final power-law region, the effectiveness can be expressed as:

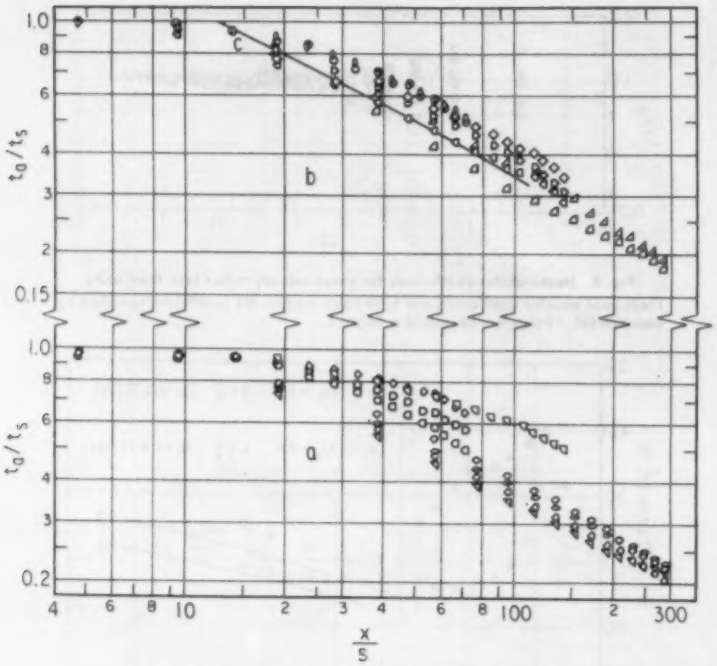

Fig. 10 Effectiveness for mass-velocity ratios greater than unity

The points are defined in Table 2. Fig. 10(*a*) contains results for mass-velocity ratios less than 3 and Fig. 10(*b*) for those above 3. Curve C is the proposal of Jakob for the wall jet.

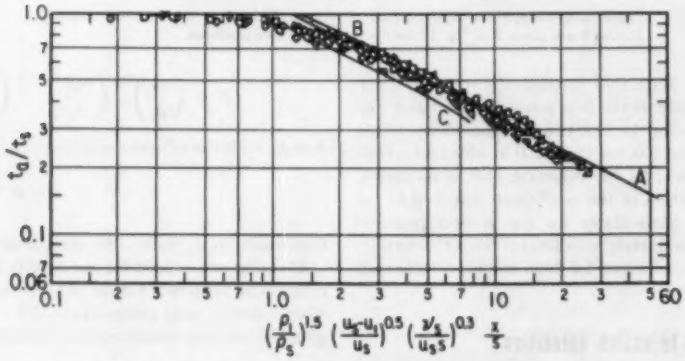

Fig. 11 Correlation of the effectiveness for high injection rates

Curve A is Equation (12), curves B and C correspond to Curve C of Fig. 10, for slot Reynolds numbers of 4340 and 17,400, respectively

$$\frac{t_a}{t_s} = 1.09\ C^{-0.8} \tag{12}$$

Jakob, in examining a wall jet, evaluated an effectiveness based on the maximum temperature in the boundary layer rather than on the adiabatic wall temperature. With an adiabatic wall these would be the same; but with heat transfer, as did exist in Jakob's experiment, they might be different, and the difference would depend on the relative magnitude of the heat transfer. This difference is not easy to appraise, though Jakob's results infer that the heat transfer was small enough to make the effectiveness values comparable. Within this uncertainty, and in recognition of the differences in injection-slot geometry, Jakob's result is shown in Fig. 10(*b*). There it is of the order of the present results for the highest mass-velocity ratios. It is shown in a different way in Fig. 11, where the curve of Fig. 10(*b*) is plotted for the highest and lowest-slot Reynolds numbers used in Jakob's experiments. Again there is adequate correspondence with the present results to indicate their probable applicability even in the limiting case of the wall jet.

Heat Transfer With High Injection Velocities

As indicated in Table 2, determinations of the heat-transfer coefficient were made for the same range of conditions as those for which the effectiveness was determined. These coefficients are presented in Fig. 12, being contained there in a Stanton number, as a function of the slot Reynolds number and the relative down-

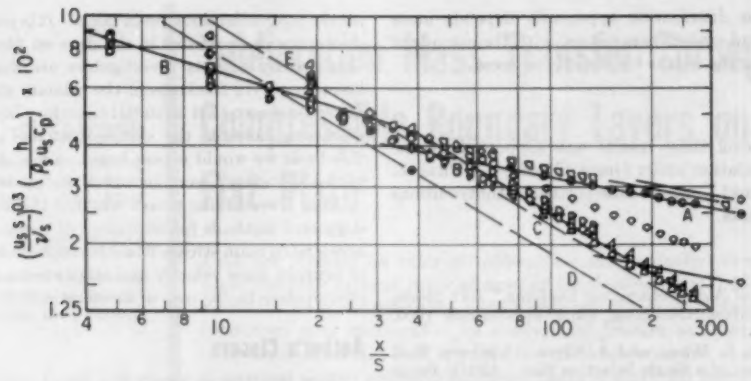

Fig. 12 Heat transfer for mass-velocity ratios greater than unity

The points are identified in Table 2. Curves B and C are Equations (13) and (14). Curves A are predictions according to Equation (9) for the Runs identified by the points in the right margin. Curves D and E are Jakob's results, Equation (15), for slot Reynolds numbers of 1000 and 7000.

stream distance. Correlation is achieved, and the appropriate functions can be stated as two power laws.

$$\frac{h}{\rho_s u_s c_p} = 0.10 \left(\frac{u_s \delta}{\nu_s}\right)^{-0.2} \left(\frac{x}{\delta}\right)^{-0.2} \qquad \frac{x}{\delta} < 40 \tag{13}$$

$$\frac{h}{\rho_s u_s c_p} = 0.41 \left(\frac{u_s \delta}{\nu_s}\right)^{-0.2} \left(\frac{x}{\delta}\right)^{-0.8} \qquad \frac{x}{\delta} > 40 \tag{14}$$

These are a convenience for the representation of the results but the uncertainty in the dimension x may contribute to the existence of the two equations. An increase in the effective value of x, such as to account for an effective origin of the flow upstream of the slot, would so shift the results that a single equation, with an 0.60-power dependence on x, would fairly represent many of the results. The entire situation is not clear enough for such an adjustment and it is significant also that Zerbe [6] obtained a -0.4 power dependence for results in which the distance was adjusted for an effective origin upstream of the slot. Jakob [5], on the other hand, made no adjustment and correlated his results in the form

$$\frac{h}{\rho_s u_s c_p} = 0.15 \left(\frac{u_s \delta}{\nu_s}\right)^{-0.2} \left(\frac{x}{\delta}\right)^{-0.4} \tag{15}$$

Here the heat-transfer coefficient is defined in terms of the difference between the wall temperature and the maximum temperature in the boundary layer, and is subject to the same question as noted previously in connection with the associated effectiveness as defined in terms of that maximum temperature. There is a fair correspondence with the present results as demonstrated in Fig. 12 by curves showing the indication of Equation (15) for the maximum and minimum slot Reynolds numbers of the present experiments. This supports the idea that the correlation indicated by Equations (13) and (14) implies a "slot-controlled" flow that is almost independent of free-stream influence and is therefore practically the same as that of the wall jet.

When the ratio of mass flows is of the order of unity, the influence of the free-stream flow is ultimately evident in a departure of the heat-transfer coefficient from the indication of Equation (14). At a ratio of unity there is an almost immediate transition to values typical of flat-plate flow, but this simple behavior is not continued for a ratio of two. In this latter case the heat-transfer coefficients remain significantly above the "flat-plate" value, and although tending toward it, that value was not attained within the available plate length. This behavior is exhibited in Fig. 12 by lines showing the heat-transfer coefficient as predicted from Equation (9) for those runs identified by the symbols in the right margin of the figure.

Conclusion

For mass-velocity ratios of less than unity, and particularly for ratios less than 0.90, the present results for the effectiveness indicate the existence of a power-law dependence on the ratio of distance to slot height, downstream of a point that depends on the ratio of the mass velocities. Consequently, a correlation in terms of these two quantities can be specified for this power-law region. It is, however, different in nature from the previous proposals of Wieghardt [1] and Chin [2], and it predicts results that are nearer the former and definitely less than the latter. Consequently, the status of this problem remains uncertain to some degree despite its considerable experimental history.

In this same flow regime, the measured heat-transfer coefficients, new in this presentation, turn out to be practically the same as those for turbulent flow on a flat plate at distances downstream greater than about 70 slot heights. In the region nearer the slot the behavior of the coefficient is complicated, but there are indications that in part of the region the coefficient depends only on the flow from the slot.

When the mass velocity of the injected flow exceeds that of the free stream, the effectiveness depends less critically on the important flow parameters. Thus, while the effectiveness is reduced as the injection flow increases, even for very high injection rates the effectiveness remains greater than that for a mass velocity of 0.60. Correlation of these results is possible on a basis similar to that used by Chin.

In this regime the heat-transfer coefficient is again capable of correlation, yielding a Stanton number that can be expressed in terms of the slot Reynolds number and the relative downstream distance, the relation being of such nature that the heat-transfer coefficient is completely determined by the slot flow for considerable distances downstream of the slot, even when the velocities of free stream and slot flow are nearly equal. This simple behavior of the heat-transfer coefficient arises from its dependence in the flow immediately adjacent to the wall, and this depends primarily on the flow from the slot. Contrasted to this, the effectiveness is related to the velocity distribution in the external part of the boundary layer, between the velocity maximum and the free-

stream value, and this distribution apparently depends more critically on the flow and system parameters, with the attendant difficulty in generalizing the results for the effectiveness.

Acknowledgment

The research producing these results was supported by the National Science Foundation under Grant G 4631. J. Pitts, Z. Rosztoczy, K. Dailey, and L. Back made particular contributions toward the present results.

References

1 K. Wieghardt, "Hot Air Discharge for De-Icing," ATI 24536, original in Deutsche Luftfahrtforsching, Forschungsbericht, 1900, 1943.

2 J. Chin, S. Skirvin, L. Hayes, and A. Silver, "Adiabatic Wall Temperature Downstream of a Single Injection Slot," ASME Paper No. 58—A-104.

3 J. Klein and M. Tribus, "Forced Convection From Non-Isothermal Surfaces," Heat Transfer, A Symposium, University of Michigan Press, Ann Arbor, Mich., 1953.

4 M. B. Glauert, "The Wall Jet," *Journal of Fluid Mechanics*, vol. 1, 1956, p. 525.

5 M. Jakob, R. Rose, and M. Spielman, "Heat Transfer From an Air Jet to a Plane Plate With Entrainment of Water Vapor From the Environment," TRANS. ASME, vol. 72, 1950, pp. 859–867.

6 J. Zerbe and J. Selna, "An Empirical Equation for the Coefficient of Heat Transfer to a Flat Surface From a Plane Heated Air Jet Directed Tangentially to the Surface," NACA TN 1070, 1946.

DISCUSSION

H. E. Weber[2]

I wish to commend the author on a well-designed experiment. He has taken care to insure a thin primary boundary layer at the beginning of the slot, a uniform primary stream velocity, and a purely tangential slot stream inlet. It is possible that some of the discrepancies or scatter in the data on film cooling effectiveness obtained by various investigators are due to the variation in boundary layer thickness of the primary stream at the slot inlet. It can be shown that an initial boundary layer will reduce the rate of mixing between the slot coolant and primary streams. On this basis we would expect lower values of effectiveness for thin initial boundary layers for which the mixing rates are high.

Also, I would like to ask whether the author has any data or suggested methods for treatment of single slot film cooling with accelerated main stream flow. Is it possible to use the local value of primary mass velocity and other stream properties to evaluate effectiveness in the case of acceleration?

[2] Supervisor, Thermodynamics, Flight Propulsion Laboratory Department, General Electric Company, Danville, Calif.

Author's Closure

Since the time at which this paper was prepared, the system has been operated with greater initial boundary-layer thicknesses, obtained by extending the test section upstream and by using grit roughness at the end of the nozzle section. With this modification the initial boundary layer was about ten times as thick as it was for the operation reported here. Substantial changes in the effectiveness were found only for the 0.125 and 0.063 in. slots, as a relatively small decrease in effectiveness at larger distances downstream. This evidence, which it is hoped will appear later as a Brief Note in this Journal[3], does not substantiate Mr. Weber's inference that the effectiveness with a thin initial boundary layer might be less than with a thicker one.

The small amount of evidence now at hand for the effect of main-stream acceleration on the effectiveness does not enable an appraisal of how that might be accounted for. There is some indication that, at low ratios of injection to free-stream flow, the effectiveness is but little altered by strong accelerations occurring relatively far downstream from the slot.

[3] Appearing in this issue, pp. 392-393.

Sublimation Mass Transfer Through Compressible Boundary Layers on a Flat Plate

T. K. SHERWOOD
Professor of Chemical Engineering, Massachusetts Institute of Technology, Cambridge, Mass. Mem. ASME

OLEV TRÄSS
Assistant Professor of Chemical Engineering, University of Toronto, Toronto, Ont., Canada

Data are reported on rates of sublimation mass transfer from an adiabatic, sharp-edged flat plate exposed to air streams at Mach numbers of 0.43, 2.0, and 3.5. Thickness decrease of the subliming naphthalene coating, plate surface temperature, and flow conditions were measured. An analysis of friction and heat transfer in turbulent compressible flow has been extended to mass transfer at low rates. Agreement between theory and data is good over the entire range of Reynolds numbers from 3×10^4 to 9×10^6. The effect of compressibility on mass transfer is found to be slightly greater than on friction. The measurement of the sublimation rate of thin coatings of solids provides a powerful technique of obtaining local friction coefficients, being simpler and of a wider applicability than the method involving force measurements on small floating surface elements.

RECENT advances in the design of high-speed aircraft and missiles emphasize the need for exact knowledge of skin friction and heat transfer under extreme flow conditions. Both theoretical and experimental studies of the effect of gas compressibility on friction and heat transfer have related these two processes. Very little work on mass transfer at high speeds has been reported, though the experimental study of mass transfer is potentially simpler than heat-transfer or skin-friction measurements. The experimental methods currently available for measuring local friction coefficients are either complex or inaccurate, whereas local mass transfer by sublimation from a solid body can be measured quite accurately without great difficulty. When the relationships between heat, mass, and momentum transfer are established for supersonic flow, such mass-transfer data can be used to determine friction and heat transfer under similar conditions.

This paper reports data on rates of naphthalene sublimation from an adiabatic, sharp-edged flat plate exposed to subsonic and supersonic air streams in parallel flow with negligible pressure gradients. To permit correlation and extrapolation of the data, a theoretical analysis of heat transfer and friction by Deissler and Loeffler [1][1] has been extended to mass transfer.

[1] Numbers in brackets designate References at end of paper.

Contributed by the Heat Transfer Division and presented at the Annual Meeting, Atlantic City, N. J., November 29–December 4, 1959, of THE AMERICAN SOCIETY OF MECHANICAL ENGINEERS.

Note: Statements and opinions advanced in papers are to be understood as individual expressions of their authors and not those of the Society. Manuscript received at ASME Headquarters, August 21, 1959. Paper No. 59—A-137.

Equipment and Procedure

Local rates of mass transfer from a flat plate to an air stream were obtained by measuring the rate of decrease of thickness of a thin coating of naphthalene on the exposed surface of the plate. The temperature at various points on the surface and the flow conditions of the air stream were measured also. Local mass-transfer coefficients and dimensionless Stanton numbers were calculated from the data obtained.

Two series of experiments, series A and B, were made in the continuous-type, supersonic wind tunnel at the Naval Supersonic Laboratory of the Massachusetts Institute of Technology. The test section of this wind tunnel was 18 in. wide and 18 or 24 in. high, depending on the Mach number. The temperature and pressure of the air stream could be controlled accurately, and it was possible to maintain steady flow over extended periods of time. Apparatus was available for taking Schlieren pictures of the test section. Table 1 summarizes test schedules and operating conditions.

Two flat-plate models were constructed. They were both 33 in. long and 18 in. wide, spanning the test section of the wind tunnel. Each was of a sandwich-type construction with a stainless-steel skin insulated from the steel supporting plate by a $^1/_2$-in-thick layer of Rubatex blown-rubber insulation. Temperatures were measured by stainless-steel-constantan thermocouples embedded in the stainless-steel skin. In the first model, used in series A experiments, there were 33 thermocouples. Twenty-five of them were spaced along the center line of the plate, and eight were used to measure the spanwise temperature distribution. In the second model, used for series B experiments, there were 72 thermocouples, 46 of which were spaced along two

Nomenclature*

c_f = local friction coefficient
c_F = average friction coefficient
c_p = heat capacity at constant pressure
D = molecular diffusivity of mass
h = heat-transfer coefficient
J = mechanical equivalent of heat
k = thermal conductivity
m = exponent in viscosity-temperature relation
M = Mach number in free stream
n = constant
N = flux of mass across plane parallel to transfer surface
P = vapor pressure, mm Hg
q = flux of heat across plane parallel to transfer surface
r = temperature recovery factor
R = universal gas constant
t = distance from origin of turbulence
$t^{+\prime}$ = temperature parameter, Equation (16)

* Consistent absolute units except where specifically indicated.

(Continued on next page)

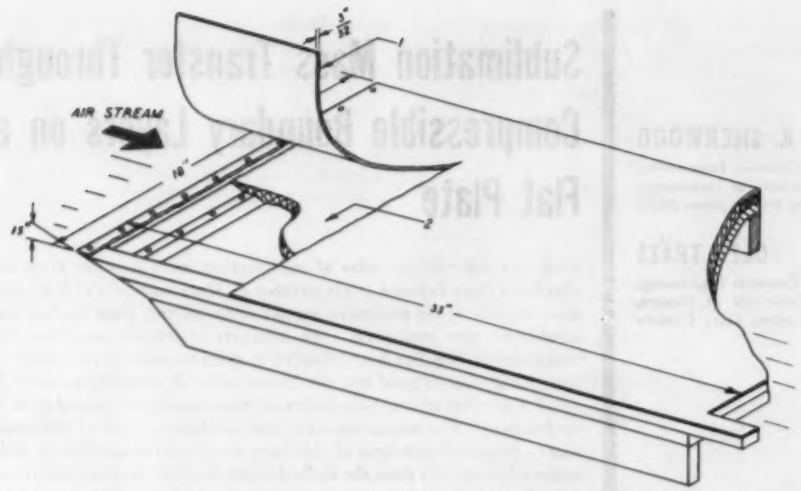

Fig. 1 Adiabatic flat plate (1) stainless-steel skin (2) insulation (second model; the skin of the first was $^1/_{32}$ in.)

Table 1 Test schedules and operating conditions

Test no.	Length of test, min, sec	Mach no.	Stagnation pressure (P stagn), psia	Stagnation temp (T stagn), deg F	Re × 10^{-6} per ft	Data obtained: Region	Data obtained: No. of traces
A-1	16–0	3.50	24.0	102.0	2.74	laminar	1
						turbulent	1
A-2	13–20	3.50	24.0	125.0	2.56	laminar	1
A-3	23–0	3.50	24.0	90.7	2.82	laminar	2
						turbulent	2
A-4	30–35	3.50	24.0	90.4	2.82	laminar	2
						turbulent	1[a]
A-5	19–10	1.99	9.0	91.0	2.26	laminar	1
						turbulent	2
A-6	30–15	1.99	9.0	91.0	2.26	laminar	1
B-1	46–0	0.43	20.0	86.2	3.60	turbulent	2
B-2	30–45	1.99	15.0	91.0	3.78	turbulent	2
B-4	38–30	1.99	15.0	88.8	3.78	turbulent	2

[a] 1 point.

lines 1 in. on either side of the plate center line. Plate construction is shown in Fig. 1. The second plate was flat essentially to within 0.005 in., the first one being slightly more wavy. Both plates had nearly razor-sharp edges widening into 15-deg half wedges.

Smooth naphthalene coatings, about 10 to 20 mils thick, were applied to the plate surface, covering a strip about 12 in. wide along the center of the plate. Molten naphthalene was applied by the use of a traveling brass box 12 × 3 × $1^1/_2$ in. having a slot along the center of the long, narrow bottom surface. On the slot there were movable jaws with which the slot width could be varied. Generally, slot widths of the order of 1 to 2 mils were used. Immediately behind the slot, looking from the direction in which the distributor was moved, there was a smooth half cylinder attached to one jaw extending over its whole length. Small teflon legs supported the distributor so that the half cylin-

Nomenclature

T = absolute temperature
u = velocity in x-direction, parallel to plate surface
u^+ = velocity parameter, Equation (15)
x = distance from plate leading edge
y = distance normal to surface
y^+ = distance parameter, Equation (14)
w = weight fraction naphthalene in air
w^+ = concentration parameter, Equation (17)

Subscripts

i = incompressible value
w = wall conditions
δ = outer edge of boundary layer; free-stream conditions
1 = outer edge of region near wall

Greek Symbols

α = frictional heating parameter, Equation (16)
γ = heat-capacity ratio
ϵ = eddy diffusivity
$\epsilon_{d,h,v}$ = eddy diffusivity of mass, heat, momentum
κ = constant
μ = viscosity
ν = kinematic viscosity
ρ = density
τ = shear stress

Dimensionless Groups

Pr = Prandtl number, $c_p\mu/k$
Re_t = Reynolds number for turbulent flow, $tu\rho/\mu$
Re_x = Reynolds number, $x\mu\rho/\mu$
Sc = Schmidt number, $\mu/\rho D$
St_h = heat-transfer Stanton number, $h/c_p\rho u$
St_m = mass-transfer Stanton number, Equation (1)

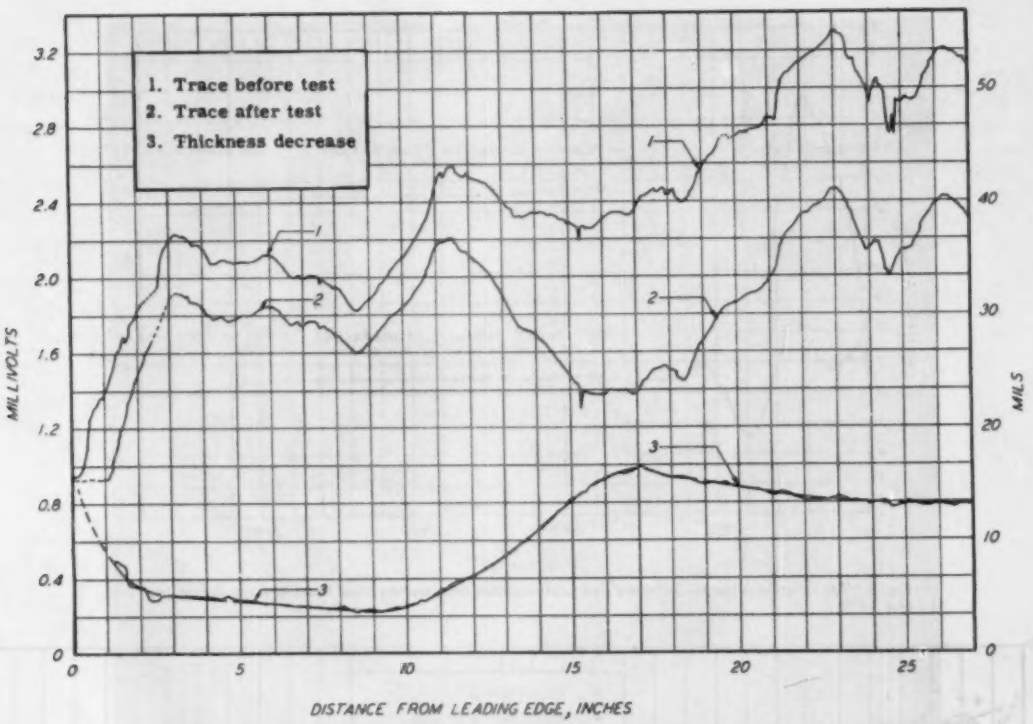

Fig. 2 Surface thickness traces before and after test A-1, and profile of naphthalene thickness decrease

der was 10 to 20 mils above the plate surface. The distributor was wound with heating wire and insulated.

To apply a coating, the distributor was filled with molten naphthalene and placed at either end of the plate with the slot downward. Pressure was then applied to force the melt out, and the distributor was moved by hand along the plate at about 1 fps. The narrow slot distributed the molten naphthalene uniformly along its length, the melt was squeezed under the cylindrical hump, and a flat, smooth surface formed which solidified about a second later. Before each test the leading edge of the coating was smoothed into a beveled shape with a razor blade and rubbed with a cloth dampened in acetone.

Records of the naphthalene surface profile on two lines along the plate were obtained by use of sensitive strain gages (Statham Instrument Company strain gages No. G7A) equipped with pick-up needles touching the surface. The strain gages were mounted on a movable bridge supported at the edges of the plate. Their output was fed to two Bristol recorders, the drives of which were synchronized with the motor pulling the strain-gage bridge along the plate toward the rear. The output of a strain gage was proportional to the position of the pick-up needle and thus indicative of the coating thickness.

A continuous trace of the naphthalene surface profile along the plate was made before and after each test, following exactly the same line on the plate. The thickness decrease of the naphthalene coating was then related to the amount sublimed during the test. Fig. 2 shows the surface traces made before and after run A-1 together with the resulting profile of naphthalene thickness decrease. In this test the boundary layer was laminar for the first 10 in., resulting in a low sublimation rate, and in the last 10 in. the flow was turbulent, giving a much higher rate of transfer. The location of the transition zone is evident. In series B experiments surface profile traces and temperature measurements were obtained along the same lines, parallel to air flow.

In series A thermocouple readings relative to an ice reference junction were recorded manually from a Brown self-balancing potentiometer. In this way about one reading was obtained every 3 min from each thermocouple, and temperature data during the unsteady tunnel start-up and shutdown periods were incomplete. In series B the output voltages from the 72 thermocouples were fed six at a time to six Brown potentiometers. These in turn were connected to an IBM card punch, and a record of six thermocouple readings could be obtained in about 10 sec. The complete and reliable temperature data obtained from this setup were used to estimate the unsteady period temperatures for the experiments of series A. The tunnel stagnation temperature was measured by 12 copper-constantan thermocouples in the tunnel stilling section. Fig. 3 shows the variation of the tunnel stagnation temperature and the plate surface temperature during run B-4 as recorded by one thermocouple near the leading edge. Fig. 4 shows the time-average temperature as measured by the 46 thermocouples during the 39-min duration of the same run.

The installation of the plate model in the wind tunnel was time-consuming, and so the naphthalene coatings were applied to the plate in position in the tunnel. All surface profile measurements were also made with the plate in place. During each run all relevant flow conditions were recorded, and Schlieren pictures were taken. A typical Schlieren picture is shown in Fig. 5, where the plate is shown exposed to an air stream approaching at a Mach number of 2.

The following raw data were obtained: Tunnel stagnation pressure and temperature, approach Mach number, thickness decrease versus distance along one or two lines on the plate, and temperature versus distance along the plate.

Analysis of Data

Mass-transfer data are conveniently presented as mass-transfer

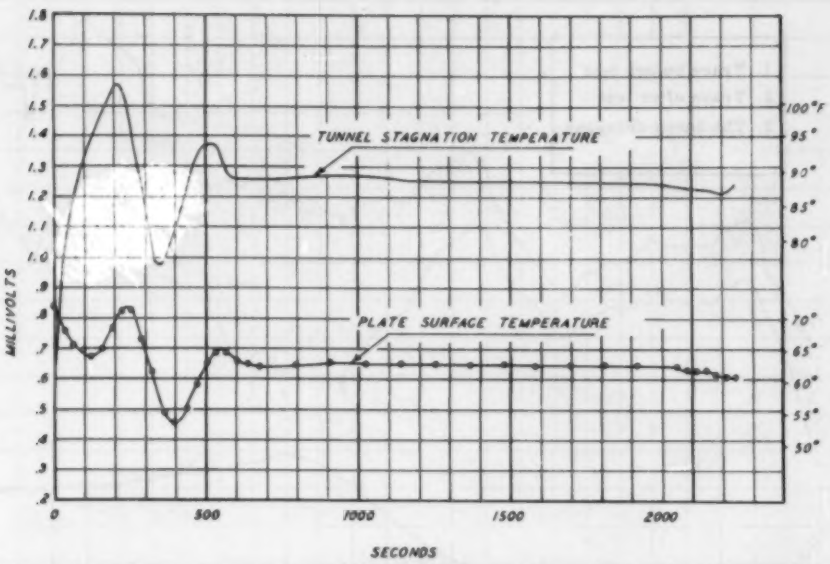

Fig. 3 Tunnel stagnation temperature and plate-surface temperature near leading edge during test B-4 (M = 2)

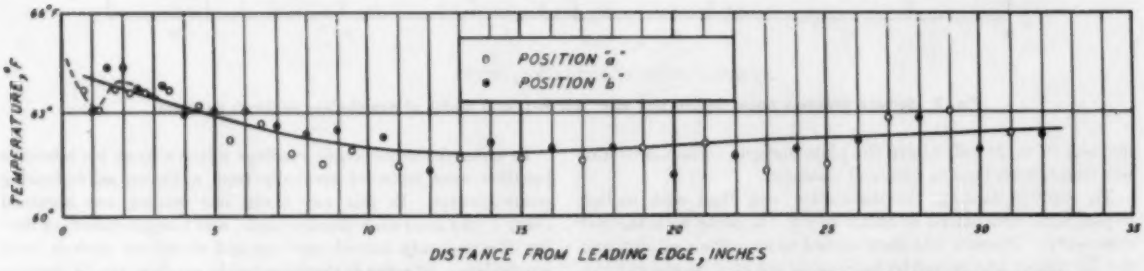

Fig. 4 Surface temperatures along plate during test B-4 (M = 2). Positions (a) and (b) 1 in. on either side of the plate center line.

coefficients and mass-transfer Stanton numbers. The former is the mass flux divided by the over-all concentration difference. The latter is properly thought of as the ratio of the mass flux to the rate of transfer needed to increase the free-stream flow (per unit area of the free-stream cross section) to the same weight fraction of diffusing substance as exists at the wall. The Stanton number based on free-stream conditions is then defined by:

$$\mathrm{St}_m = \frac{N_w}{(w_w - w_\delta)\rho_\delta u_\delta} \tag{1}$$

where N_w is the mass flux, w represents weight fraction, and the subscript δ refers to free-stream conditions.

Mass flux was calculated from the measured decrease in thickness of the surface coating and the known exposure time, using measured values of the density of the naphthalene coating. The concentration at the plate surface was that of air saturated with naphthalene at the surface temperature, calculated from the vapor-pressure data given in the Appendix. The concentration in the free stream was zero. Both thickness decrease and temperature data were smoothed with position on the plate before the Stanton numbers were calculated (as functions of position or distance from the plate leading edge). Local values of St_m can be related to friction coefficients and to Stanton numbers for heat transfer.

For purposes of presenting and correlating the data, it is desirable to relate the position on the plate to a length Reynolds number Re_x. For the laminar region Re_x was defined in terms of the free-stream velocity, density, viscosity, and distance from the leading edge of the plate. For the turbulent region free-stream properties were again used, but the distance term was related to an "origin of turbulence" arbitrarily defined.

The difficulty is illustrated in Fig. 6, which shows the nature of the variation of momentum thickness, local friction coefficient, and surface temperature through the transition zone. Seiff [2] defines the origin of turbulence such that the total momentum loss in the laminar and transition zones is equal to that of a hypothetical turbulent region extrapolated forward from the actual region of turbulence (point *a*, Fig. 6). Coles [3] and Hakkinen [4] obtained good correlations of their data by using the point of maximum shear stress (point *b*, Fig. 6). A third possibility is the middle of the transition zone corresponding approximately to the maximum surface temperature (point *c*, Fig. 6). This last gave the best correlation of the present data and is used here in defining the length Reynolds number for turbulent flow denoted by Re_t. Except in the tests of series A at Mach 3.5 transition was abrupt and the origin of turbulence was indicated to be essentially the same by all three methods.

Transfer Relations for Incompressible Flow

For laminar incompressible boundary-layer flow along a flat plate, the Blasius exact solution of the boundary-layer equations gives the local friction coefficient c_f as

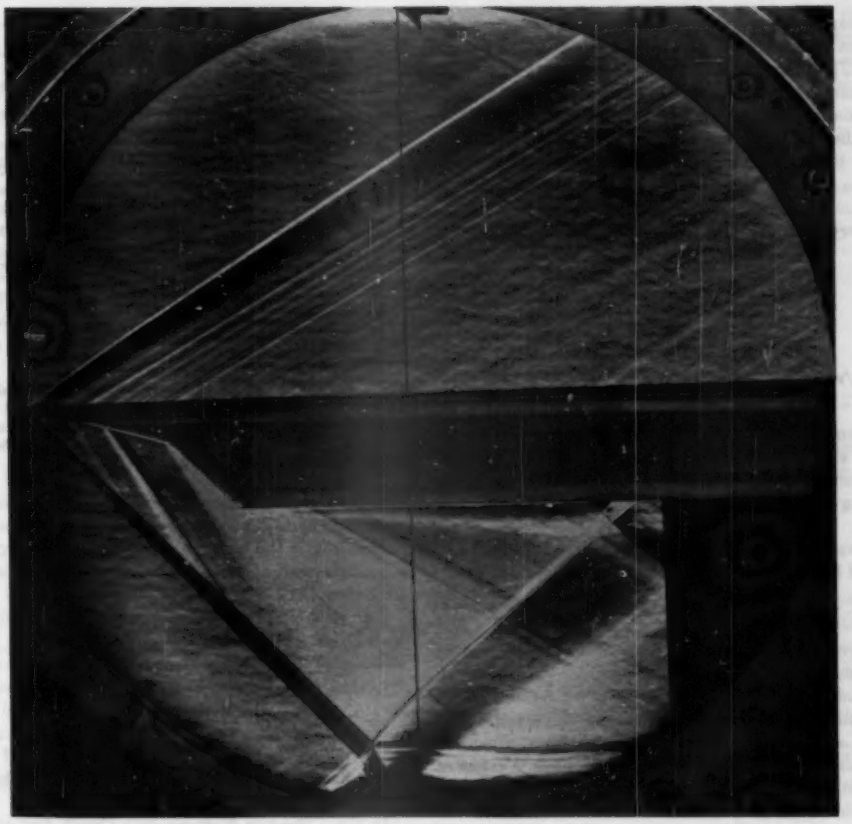

Fig. 5 Schlieren picture of model in wind tunnel. Test B-4 ($M = 2$).

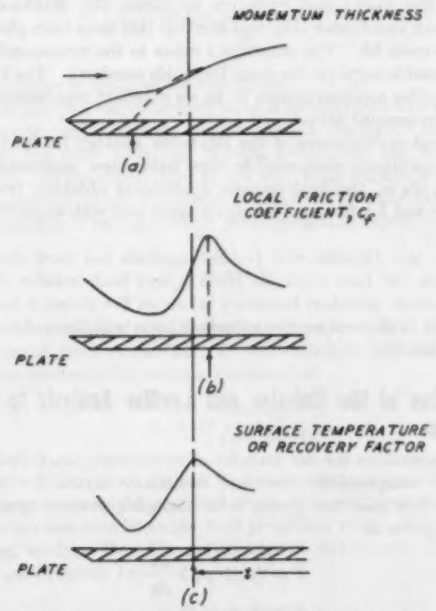

Fig. 6 Three methods of specifying the origin of turbulence

$$c_f = 0.664\,(\mathrm{Re}_x)^{-1/2} \tag{2}$$

Pohlhausen's exact solution for heat transfer is also applicable to mass transfer if the Prandtl number is replaced by the Schmidt number. This solution can be represented accurately in the Schmidt or Prandtl number range of 0.4 to 6 by

$$\mathrm{St}_h(\mathrm{Pr})^{2/3} = \mathrm{St}_m(\mathrm{Sc})^{2/3} = \frac{c_f}{2} = 0.332\,(\mathrm{Re}_x)^{-1/2} \tag{3}$$

For turbulent boundary-layer flow numerous semiempirical relations have been suggested. These include the Prandtl-Schlichting friction formulas and the von Karman-Schoenherr skin-friction law. The latter gives the local friction coefficient as

$$(c_f)^{-1/2} = 1.7 + 4.15\,\log_{10}(\mathrm{Re}_x c_f) \tag{4}$$

The various relations have been presented and compared by Schlichting [5]. An analysis by Deissler and Loeffler [1], to be discussed later, also gives an incompressible skin-friction law in good agreement with the others.

The Reynolds' analogy relating friction and heat transfer takes into account the similarity of the mechanisms of heat and momentum transfer by turbulent eddies but makes no allowance for molecular motion; i.e., it neglects the presence of a region near the wall where transfer occurs predominantly by molecular motion. Later modifications, following that of von Karman [6], have assumed molecular and eddy transport to occur in parallel and introduced various assumptions as to the nature of variation

of eddy diffusivity ϵ with distance from the wall. These developments have recently been reviewed and compared by one of the authors [7]. For values of Pr or Sc greater than 1.0, the three most important analyses are those of Lin, Moulton, and Putnam [8], Deissler [9], and Deissler and Loeffler [1].

When the Schmidt number is large, a very small amount of turbulence near the wall can increase the mass transfer considerably and must be taken into account. Lin, Moulton, and Putnam [8] introduced an empirical allowance for eddy diffusivity in the region very near the wall by the following assumed relations:

$$\epsilon/\nu = \left(\frac{y^+}{14.5}\right)^3; \quad 0 < y^+ < 5 \tag{5}$$

$$\epsilon/\nu = \frac{y^+}{5} - 0.949; \quad 5 < y^+ < 33 \tag{6}$$

where the dimensionless distance parameter y^+ is defined by Equation (14), ϵ is the eddy diffusivity, and ν the kinematic viscosity. Beyond $y^+ = 33$ the Reynolds' analogy was employed, assuming the heat or mass flux proportional to the shear stress.

Deissler [9] assumed that near the wall (to $y^+ = 26$) the eddy diffusivity could be represented by

$$\epsilon/\nu = n^2u^+y^+(1 - e^{-n^2u^+y^+}) \tag{7}$$

where the dimensionless velocity parameter u^+ is defined by Equation (15) and the empirical constant n has the value of 0.124. In the region away from the wall, i.e., beyond $y^+ = 26$, the von Karman logarithmic velocity distribution was employed. Calculated values of the Stanton number have been presented graphically in Reference [9] for pipe flow and a limited range of Reynolds numbers.

The analysis by Deissler and Loeffler to be discussed in the next section was developed primarily for compressible flow, but with constant fluid properties it is nearly identical to the Deissler analysis, only neglecting the effect of kinematic viscosity on eddy motion [the term in parentheses in Equation (7) is omitted and n is taken as 0.109].

For flow over a flat plate at $Re_l = 10^6$, c_f is approximately 0.0036, and the Reynolds' analogy gives $St_\infty = c_f/2 = 0.00180$. For Sc = 2.5 (naphthalene-air) the various allowances for molecular transport and variation of ϵ across the stream give smaller values of St_∞, the extreme being 0.00098 predicted by Chilton and Colburn [10]. The Lin, Moulton, and Putnam value is 0.00123, the Deissler result 0.00124, and that of Deissler and Loeffler, 0.00129.

Transfer Relations for Compressible Flow

In low-speed flow, fluid properties are usually assumed constant and so the velocity profile is independent of temperature variations. In compressible flow, however, steep temperature gradients caused by frictional heating, exist in the boundary layer. Therefore variation of fluid properties with temperature must be accounted for and the velocity and temperature profiles must be considered jointly, since one affects the other.

Skin friction under compressible-flow conditions has been studied extensively. For laminar-boundary-layer flow various theoretical and empirical equations are available for predicting the effect of compressibility on the friction coefficient [11, 12]. Due to the small effect on c_f, e.g., 11 per cent reduction at $M = 3.5$, these analyses are in reasonably good agreement within themselves and with experimental data.

For turbulent-boundary-layer flow von Karman suggested, as a first approximation, the use of his incompressible friction law,

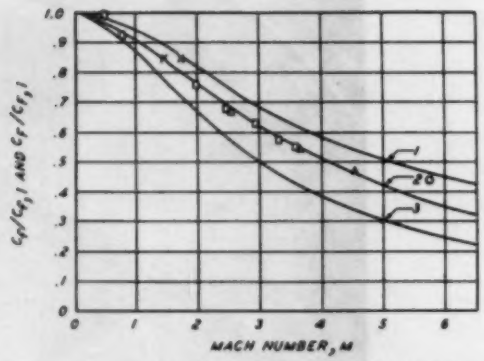

Fig. 7 Effect of compressibility on friction. × Hakkinen [4], $c_f/c_{f,i}$, $Re_l = 10^6$; △ Coles [3], $c_f/c_{f,i}$, $6.6 < Re_l \times 10^{-6} < 8.9$; ○ Korkegi [16], $c_f/c_{f,i}$, $Re_l = 5.5 \times 10^6$; □ Chapman and Kester, $c_F/c_{F,i}$, $6 < Re_l \times 10^{-6} < 16$; 1, Van Driest [14], $Re_l = 10^7$; 2, Deissler-Loeffler, [1], $Re_l = 10^7$; 3, von Karman, $Re_l = 10^7$.

Equation (4), with density and viscosity evaluated at the wall temperature rather than at free-stream conditions. This method overestimates the effect of compressibility; some weighted average of the wall and free-stream temperatures, such as suggested by Eckert [11], is more appropriate.

Analyses proposed subsequently often deviate widely [13]. Van Driest [14] performed an analysis which yielded compressible friction and heat-transfer coefficients. An analysis for an insulated plate by Frankl and Voishel, extended by Rubesin, et al. [15] gives, partly due to internal cancellation of errors, friction coefficients which agree very well with experimental data. Adiabatic friction coefficients from the Deissler and Loeffler analysis to be discussed next, are almost identical to those from the extended Frankl and Voishel analysis.

In Fig. 7 the von Karman, Van Driest, and Deissler and Loeffler compressible-friction relations are compared with experimental data. Data from direct friction measurements on sharp-edged flat plates and cylinders by Coles [3], Hakkinen [4], Chapman and Kester [13], and Korkegi [16] have been plotted as $c_f/c_{f,i}$ versus M. The subscript i refers to the corresponding incompressible value (at the same Reynolds number). The Deissler and Loeffler analysis is seen to be an excellent representation of the experimental data.

Several modifications of the Reynolds' analogy for heat transfer in turbulent compressible flow have been suggested [17]. Among these, the heat-transfer coefficients obtained from the Deissler and Loeffler analysis again agree well with available data [1, 18].

Since the Deissler and Loeffler analysis has been shown to represent the best available friction and heat-transfer data in compressible turbulent boundary layers on flat plates, it has been extended in the next section to include mass transfer under similar conditions.

Extension of the Deissler and Loeffler Analysis to Mass Transfer

The equations for the transfer of momentum, heat, and mass through compressible turbulent boundary layers for steady, parallel flow past flat plates, with negligible pressure gradients, may be given as

$$\tau = (\mu + \rho\epsilon_*)\frac{du}{dy} \tag{8}$$

$$q = -(k + \rho c_p\epsilon_h)\frac{dT}{dy} - u\,(\mu + \rho\epsilon_*)\frac{du}{dy} \tag{9}$$

$$N = -(\rho D + \rho\epsilon_d)\frac{dw}{dy} \tag{10}$$

where τ is the shear stress at the plane parallel to and at a distance y from the wall, and q and N represent the flux of heat and mass across that plane. The eddy diffusivities are denoted by ϵ_v, ϵ_h, and ϵ_d, corresponding to the molecular transport properties μ/ρ, $k/\rho c_p$, and D. u, T, and w, which appear differentiated with respect to the distance y, are the time mean velocity, temperature, and weight fraction of the diffusing component. These equations are identical to those used when fluid properties are constant, except for the inclusion of the last term in the heat-transfer equation to account for the conversion of mechanical energy into heat.

In dimensionless form Equations (8), (9), and (10) become, for the case of an adiabatic wall ($q = 0$):

$$\frac{\tau}{\tau_w} = \left(\frac{\mu}{\mu_w} + \frac{\rho}{\rho_w}\frac{\epsilon_v}{\mu_w/\rho_w}\right)\frac{du^+}{dy^+} \tag{11}$$

$$\frac{q}{q_w} = 0 = \left(\frac{k}{k_w}\frac{1}{\mathrm{Pr}_w} + \frac{\rho}{\rho_w}\frac{\epsilon_h}{\mu_w/\rho_w}\right)\frac{dt^{+\prime}}{dy^+} - 2u^+\left(\frac{\mu}{\mu_w} + \frac{\rho}{\rho_w}\frac{\epsilon_v}{\mu_w/\rho_w}\right)\frac{du^+}{dy^+} \tag{12}$$

$$\frac{N}{N_w} = \left(\frac{\rho D}{\rho_w D_w}\frac{1}{\mathrm{Sc}_w} + \frac{\rho}{\rho_w}\frac{\epsilon_d}{\mu_w/\rho_w}\right)\frac{dw^+}{dy^+} \tag{13}$$

The dimensionless parameters are defined by:

$$y^+ = y\frac{(\tau_w/\rho_w)^{1/2}}{\mu_w/\rho_w} \tag{14}$$

$$u^+ = \frac{u}{(\tau_w/\rho_w)^{1/2}} \tag{15}$$

$$t^{+\prime} = \frac{2(T_w - T)c_p\rho_w}{\tau_w} = \frac{1 - (T/T_w)}{\alpha} \tag{16}$$

$$w^+ = \frac{(w_w - w)\rho_w(\tau_w/\rho_w)^{1/2}}{N_w} \tag{17}$$

The subscript w refers to wall conditions.

In the analysis the boundary layer is divided into two regions, the predominantly laminar "region close to the wall," for $y^+ \leq 26$, and the fully turbulent "region away from the wall," for $y^+ > 26$. In the region close to the wall, eddy motion is allowed for in addition to the molecular transfer. The eddy diffusivity of momentum is represented by the empirical relation:

$$\frac{\epsilon_v}{\nu} = n^2u^+y^+ \tag{18}$$

where the constant $n = 0.109$ has been determined from pipe data at constant fluid properties. In the turbulent region the von Karman similarity hypothesis, expressed as

$$\epsilon_v = \kappa^2\frac{(du/dy)^3}{(d^2u/dy^2)^2} \tag{19}$$

with $\kappa = 0.36$ is used. It has thus been assumed that the eddy-diffusivity expressions obtained from flow with constant fluid properties also hold when the fluid properties vary. For the subsequent analysis the eddy diffusivities of momentum, heat, and mass are equated; i.e.,

$$\epsilon_v = \epsilon_h = \epsilon_d = \epsilon \tag{20}$$

The viscosity of air is assumed to vary as the 0.68 power of the absolute temperature. The Prandtl number and the specific heat are assumed to be constant. For mass transfer the Schmidt number is also assumed to be independent of temperature, though for naphthalene in air it is estimated to vary as $T^{-0.138}$ (Appendix).

With the preceding assumptions, the property ratios in Equations (11), (12), and (13) can be written as:

$$\frac{\mu}{\mu_w} = \frac{k}{k_w} = \left(\frac{T}{T_w}\right)^m = \left(\frac{T}{T_w}\right)^{0.68} \tag{21}$$

$$\frac{\rho}{\rho_w} = \frac{1}{T/T_w} \tag{22}$$

$$\frac{D}{D_w} = \left(\frac{T}{T_w}\right)^{1+m} = \left(\frac{T}{T_w}\right)^{1.68} \tag{23}$$

Introducing Equation (16), it is evident that all property ratios are given in terms of α and $t^{+\prime}$.

In solving Equations (11) to (13) the variations of the shear stress and the heat and mass fluxes across the boundary layer have been assumed identical and negligible:

$$\frac{\tau}{\tau_w} = \frac{q}{q_w} = \frac{N}{N_w} = 1 \tag{24}$$

The validity of this and other assumptions, as pertaining to heat and momentum transfer, has been tested and discussed in Reference [1]. It should be permissible to make corresponding assumptions for mass transfer, at least when Sc is between 1 and 2.5, provided that the transfer rate is so low as not to affect the velocity and temperature profiles in the boundary layer. This was the case in the present sublimation study.

For the region near the wall ($y^+ < 26$), substitution of the property ratios into Equations (11) to (13) gives, in integral form:

$$u^+ = \int_0^{y^+}\frac{dy^+}{(1 - \alpha t^{+\prime})^m + \dfrac{n^2u^+y^+}{1 - \alpha t^{+\prime}}} \tag{25}$$

$$t^{+\prime} = \int_0^{y^+}\frac{2u^+dy^+}{\dfrac{(1 - \alpha t^{+\prime})^m}{\mathrm{Pr}} + \dfrac{n^2u^+y^+}{1 - \alpha t^{+\prime}}} \tag{26}$$

$$w^+ = \int_0^{y^+}\frac{dy^+}{\dfrac{(1 - \alpha t^{+\prime})^m}{\mathrm{Sc}} + \dfrac{n^2u^+y^+}{1 - \alpha t^{+\prime}}} \tag{27}$$

In the region away from the wall the molecular transfer terms are neglected. Equations (11), (12), and (13), with condition (20), and integration from $y_1^+ = 26$ to y^+ gives:

$$t^{+\prime} - t_1^{+\prime} = (u^+)^2 - (u_1^+)^2 \tag{28}$$

$$w^+ - w_1^+ = u^+ - u_1^+ \tag{29}$$

where the subscript 1 refers to the value at $y^+ = 26$.

Equations (25) and (26) have been solved simultaneously by Deissler and Loeffler [1] by iterative numerical integrations. With u^+ and $t^{+\prime}$ given, w^+ at $y^+ \leq 26$ can be obtained from Equation (27) for any desired value of Sc by simple graphical integration. For the region away from the wall ($y^+ > 26$), substitution of Equation (28) and the von Karman similarity hypothesis, Equation (19) into Equation (11), gives a relation between u^+ and y^+, with α as parameter. The $t^{+\prime}$ and w^+ profiles can then be obtained by use of Equations (28) and (29).

The dimensionless velocity and temperature profiles through

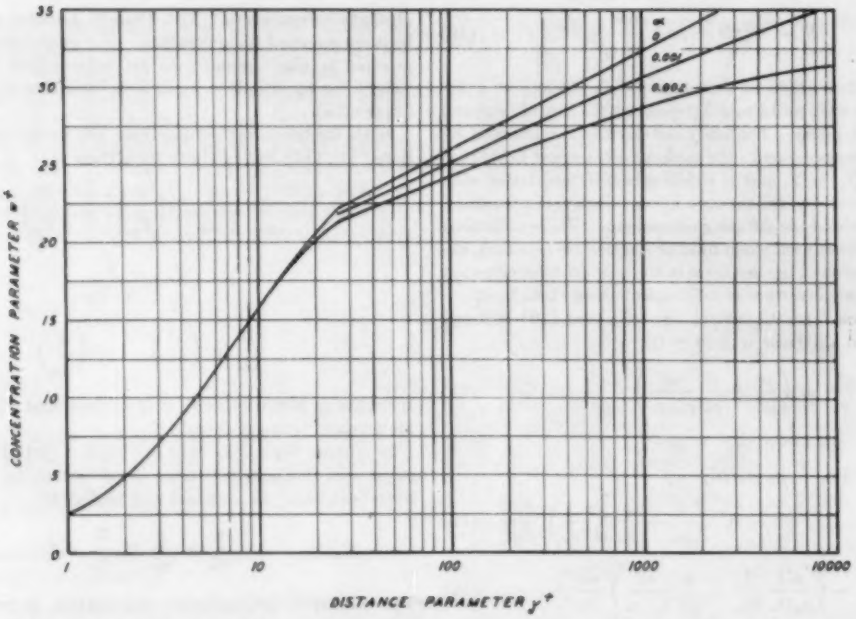

Fig. 8 Dimensionless concentration profiles. Insulated flat plate, Pr = 0.73, Sc = 2.5.

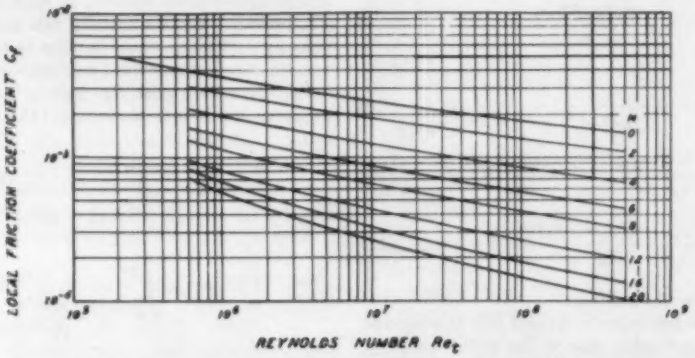

Fig. 9 Variation of local friction coefficients with Reynolds and Mach numbers as predicted by Deissler and Loeffler. Insulated flat plate, Pr = 0.73.

the boundary layer are given in Reference [1]. Fig. 8 gives the dimensionless concentration profile for a value of Sc of 2.50 calculated from Equations (27) and (29) by the procedure described. The curve for the frictional heating parameter α of zero corresponds to incompressible flow; those for $\alpha = 0.001$ and 0.002 correspond to increased frictional heating of the flat-plate surface.

In the terms of this analysis the local friction coefficient c_f is given by

$$c_f = \frac{2\tau_w}{\rho_\delta u_\delta^2} = \frac{2(1-\alpha)}{(u_\delta^+)^2} \tag{30}$$

where the subscript δ refers to the outer edge of the boundary layer. The mass-transfer Stanton number St_m, defined by Equation (1), becomes

$$St_m = \frac{N_w}{(w_w - w_\delta)\rho_\delta u_\delta} = \frac{1 - \alpha t_\delta^{+\prime}}{u_\delta^+ w_\delta^+} = \frac{c_f}{2}\frac{u_\delta^+}{w_\delta^+} \tag{31}$$

which illustrates the correction to the Reynolds' analogy.

To calculate St_m at any desired Reynolds and Mach number, the dimensionless parameters must be evaluated. The integrations necessary for relating these parameters to Re_t and M can be avoided by use of Fig. 9, which gives the corresponding local friction coefficients from [1]. The procedure used for calculating the theoretical St_m curves shown in Fig. 12 was as follows:

1 Obtain c_f from Fig. 9 at the selected M and Re_t.
2 Obtain T_w from the selected T_δ and the equation

$$T_w = T_\delta\left(1 - r\frac{\gamma - 1}{2}\mathrm{M}^2\right) \tag{32}$$

where the theoretical recovery factor r is obtained from Figs. 16 and 18 of Reference [1], and γ is the heat-capacity ratio (1.4 for air).

3 Calculate α, u_δ^+, and $t_\delta^{+\prime}$ from Equations (16) and (30) and the Mach number relation:

$$\mathrm{M} = u_\delta^+\left[\frac{2\alpha}{(\gamma-1)(1-\alpha t_\delta^{+\prime})}\right]^{1/2} \tag{33}$$

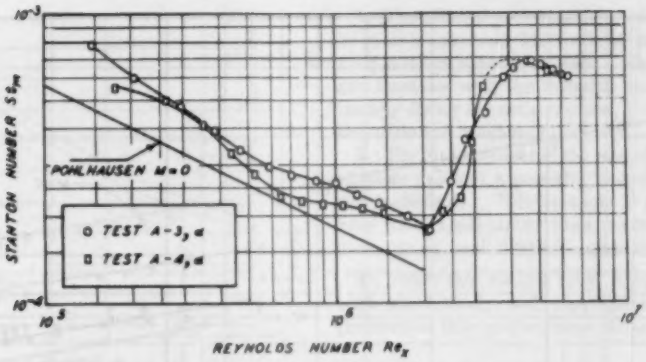

Fig. 10 Mass-transfer Stanton number versus Reynolds number Re_x (based on distance from leading edge). Tests A-3 and A-4, position (a), M = 3.5.

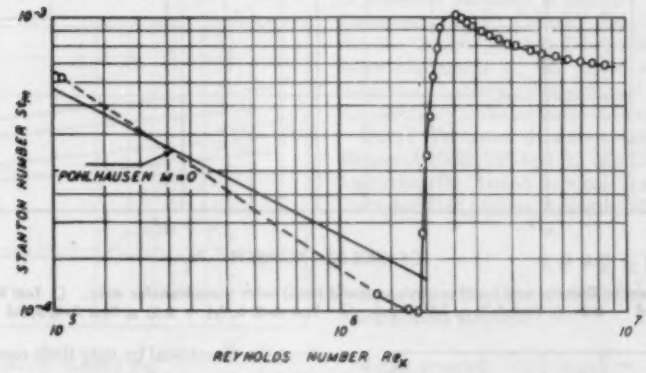

Fig. 11 Mass-transfer Stanton number versus Reynolds number Re_x (based on distance from leading edge). Test B-2, position (a), M = 2.

4 Obtain y_δ^+ from Fig. 4 (u^+ versus y^+, α for adiabatic plate) or Fig. 6 ($t^{+\prime}$ versus y^+, α) of Reference [1]. The two values should agree.

5 Obtain w_δ^+ from Fig. 8.

6 Calculate St_m by the use of Equation (31).

Discussion of Results

Representative data at Mach 2.0 and 3.5 are shown in Figs. 10 and 11 as St_m versus Re_x. Natural transition occurred in the tests plotted in Fig. 10; in the test shown in Fig. 11 transition was sharply induced by a disturbance near the end of the laminar region. In both these, and most other tests, continuous data are available through the transition zone, but no attempt has been made to correlate them.

Since sublimation rates in the laminar-flow region are considerably lower than those in the turbulent region, the accuracy in the measurement of the small thickness decreases was poor. Reliable data could be obtained if an experiment were devoted exclusively to laminar mass transfer, but not in conjunction with turbulent measurements. Therefore these data have not been analyzed in detail, but are compared to the Pohlhausen incompressible laminar heat-transfer solution, Equation (3), represented by the solid lines in Figs. 10 and 11.

Subsonic Results

Fig. 12 shows the experimental mass-transfer Stanton numbers at Mach numbers of 0.43, 2.0, and 3.5, plotted versus the turbulent-length Reynolds number Re_t. The figure also shows the calculated results of the extended Deissler and Loeffler analysis for Mach numbers of 0, 2, 3.5, 4, and 6. This is analogous to the c_f plot in Fig. 9.

Data at M = 0.43 represent the average from two position traces. The maximum deviation from the average was 2 per cent occurring at the highest Reynolds number (lowest transfer rate).

According to the analysis St_m at M = 0.43 should be about 3 per cent below the incompressible value. The subsonic data points in Fig. 12 fall about 2 to 5 per cent below the M = 0 curve. This indicated agreement is better than would be expected, since the experimental error was 3 to 4 per cent.

With such excellent agreement over the range of Reynolds numbers from $Re_t = 3 \times 10^4$ to 9×10^6, both theory and these subsonic data provide a reliable basis for the evaluation of subsequent supersonic results, and thus for a study of compressibility effects. One of the major uncertainties present in such investigations has thereby been eliminated.

Supersonic Results

Turbulent Mach 3.5 data were obtained in four series A tests. Data from one position of runs A-3 and A-4 are most reliable because of good surface traces and acceptable temperature measurements. The experimental errors, largely arising from uncertain and inadequate temperature measurements, may be 5 to 10 per cent of the St_m values. These data are plotted in Fig. 12 versus Re_t, the Reynolds number based on the distance from the origin of turbulence. Their average falls 3 per cent above the theoretical curve with the most reliable data just below it.

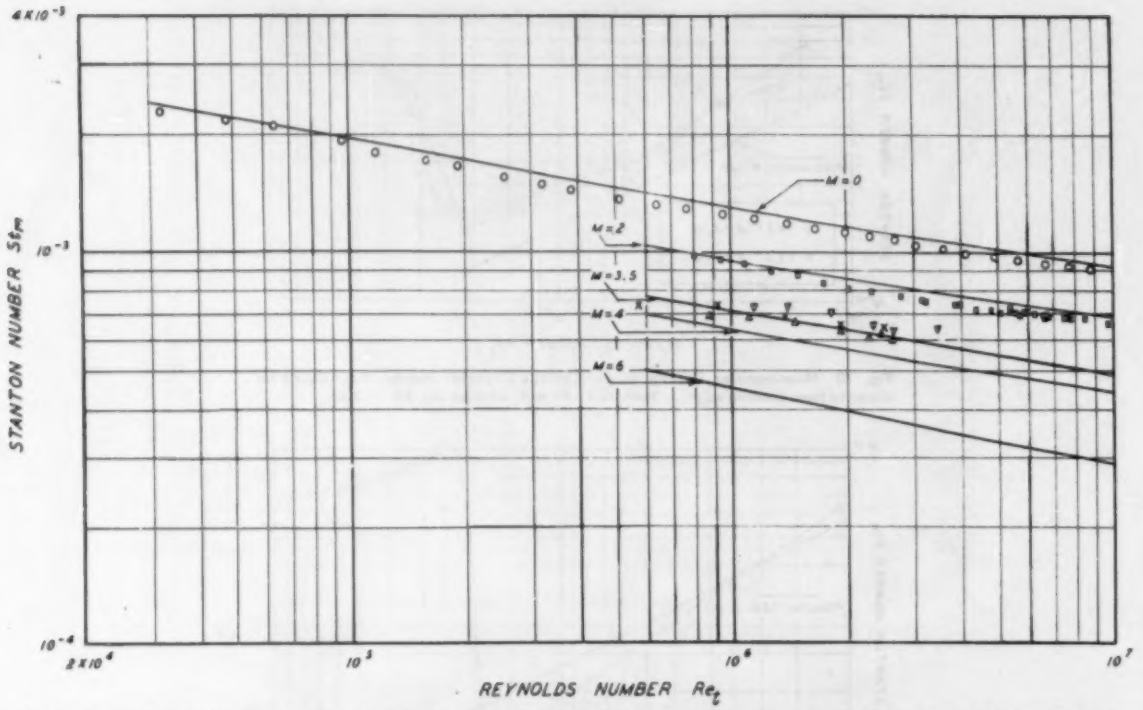

Fig. 12 Comparison of the extended Deissler and Loeffler analogy (solid lines) with mass-transfer data. ○ Test B-1, M = 0.43; □ Tests B-2, B-4, M = 1.99; x Test A-1, M = 3.5; △ Test A-3, a, M = 3.5; ▽ Test A-3, b, M = 3.5; ▲ Test A-4, a, M = 3.5 (all for Sc = 2.5).

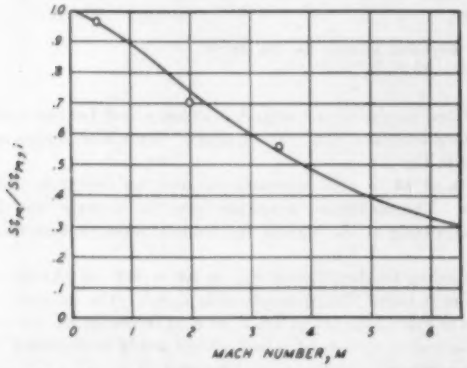

Fig. 13 Effect of compressibility on mass transfer. Experimental data compared with extended Deissler and Loeffler analysis. $Re_t = 3 \times 10^6$, Sc = 2.5.

Some turbulent Mach 2 data were obtained in run A-5, but they were plagued by several uncertainties, including an unusual transition in two stages which made their correlation difficult. Results from runs B-2 and B-4, with two separate traces from each, have been plotted in Fig. 12. The estimated error in St_m is about 3 per cent.

These data agree well with the theoretical curve at $Re_t = 10^6$ but fall some 5 per cent below it at higher Reynolds numbers. They are remarkably consistent within themselves. Transition in these runs was "induced" by disturbances and not natural; this may have affected the subsequent mass transfer, but it is difficult to assess any such effect, and it could hardly be great. The excellent internal consistency of the data may be fortuitous, but it does establish a very definite experimental value, deviating from the theoretical by very little more than the probable experimental error.

The Stanton numbers at $Re_t = 3 \times 10^6$ have been divided by their incompressible theoretical value at the same Reynolds number ($St_{m,i} = 1.096 \times 10^{-3}$) and plotted versus the Mach number in Fig. 13. This is analogous to the treatment of friction coefficients in Fig. 7. Agreement with the theoretical curve is good. The Mach 0.43 point falls on the curve, the Mach 2 point falls 3.4 per cent below, and the Mach 3.5 point 1.4 per cent above the theoretical curve, the percentages being based on the incompressible value.

Evaluation of Theory

A comparison between the experimental mass-transfer data and the Deissler and Loeffler analysis, extended to mass transfer, has been presented. The data support the theoretical results in both incompressible and compressible flow. Similar good agreement has been shown between theory and local skin-friction data obtained experimentally by direct force measurements. Comparisons with heat-transfer measurements have been made elsewhere [1, 18], also with favorable results.

It must be concluded that this analysis predicts all three transfer processes in incompressible as well as compressible flow to a reasonable accuracy. The mass-transfer extension holds at least for Schmidt numbers between 1 and 2.5. If much higher Schmidt numbers were considered, the extended theory would have to be modified to include the damping effect of kinematic viscosity on eddy properties in the region near the wall.

A comparison of the effect of compressibility on momentum, heat, and mass transfer, as predicted by the Deissler and Loeffler analysis and its extension at $Re_t = 3 \times 10^6$, is given in Fig. 14. The effect on heat transfer and friction is about the same, whereas with Sc = 2.5, the reduction in St_m is about 10 per cent larger.

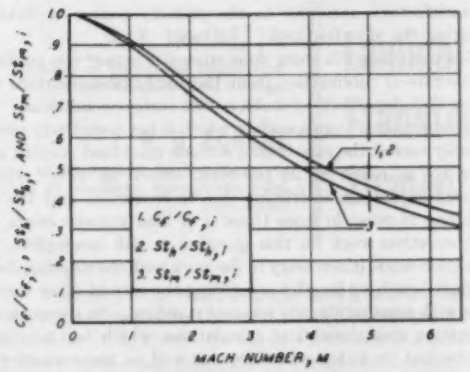

Fig. 14 Effect of compressibility on heat, mass, and momentum transfer, as predicted by the extended Deissler and Loeffler analysis

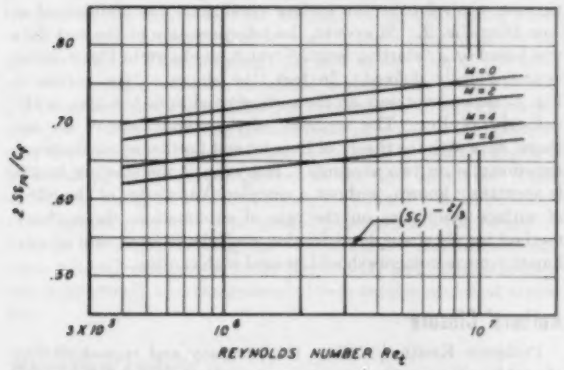

Fig. 15 Variation of the Reynolds' analogy factor with Reynolds and Mach numbers. Upper curves are for Deissler and Loeffler theory; lowest is Chilton-Colburn analogy (Sc = 2.5).

This difference is a function of the Schmidt number, as can be deduced from the theory.

The ratio $2\ St_m/c_f$ for Sc = 2.50 has been plotted in Fig. 15 as a function of the Reynolds number, with the Mach number as parameter. This indicates the same trend with respect to the Mach number. The Chilton-Colburn analogy factor, $Sc^{-2/3}$, has been included for comparison; by the Reynolds' analogy the ordinate is unity.

Conclusion

Sublimation mass transfer through compressible boundary layers on a flat plate has been measured. The results have been related to a theoretical analysis of turbulent heat, mass, and momentum transfer. The following conclusions are drawn:

1 The technique used to determine sublimation mass transfer by measurement of the thickness decrease of the subliming solid layer and of model surface temperature can yield accurate mass-transfer data under both subsonic and supersonic flow conditions.

2 An analysis of skin friction and heat transfer in turbulent compressible flow by Deissler and Loeffler has been extended to mass transfer at low rates, with Sc = 2.5. Agreement between theory and the measured data at Mach numbers of 0.43, 2.0, and 3.5 is good over the experimental range of Reynolds numbers.

3 An analogy between heat, mass, and momentum transfer on a flat plate with zero inclination in turbulent compressible flow has been established. The substantiation is limited to low values of Sc or Pr.

4 The effect of compressibility on skin friction and heat transfer in air is essentially identical, whereas for mass transfer at Sc = 2.5 it is about 10 per cent larger. This difference is zero at Sc = 1 and increases with the Schmidt number. Thus the Reynolds' analogy factor for mass transfer, $2\ St_m/c_f$, is a function of both Reynolds and Mach numbers.

5 The measurement of the rate of sublimation of thin coatings of solids provides a powerful technique for obtaining local friction coefficients. This technique is simpler and would appear to have wider applicability than the method involving force measurements on small floating surface elements.

To utilize this method fully, it will be necessary to determine both theoretically and experimentally, the effect of pressure gradients in flow over surfaces of various shapes.

Acknowledgment

The work described was supported in large part by the Office of Scientific Research of the Air Research and Development Command (USAF), Contract No. AF 49(638)-234. Thanks are due the General Electric Educational and Charitable Fund for fellowship grants to the junior author. The M.I.T. Naval Supersonic Laboratory contributed wind-tunnel time and valuable assistance in the course of the experimental work.

NOTE: Tabulated data are available in Reference [18] and in Report AFOSR TR-58-131, ASTIA AD-203-713, obtainable on loan from the Armed Services Technical Information Agency, Arlington Hall Station, Arlington 12, Virginia.

APPENDIX

Some physical properties of naphthalene (purified by recrystallization from alcohol):

Vapor pressure [19]: $\log_{10}P = -\frac{3765}{T} + 11.55$ where P is expressed in mm Hg and T in deg K

Density: Pycnometer measurement [20] = 1.145 g/cm³ at 20 C

Cast material [18] = 1.078 ± 0.012 g/cm³ at 20 C

Coefficient of volumetric expansion = 0.00028/ deg C

Diffusivity in air = 0.0611 cm²/sec at 25 C and 1 atm

Schmidt number in air = $\mu/(\rho D) = 7 \times T^{-0.328}$; T = deg K (100 to 500 K), Sc = 2.50 at 265 K

The two density values in the "International Critical Tables" [20], at 17 and 20 C were presumably taken with a pycnometer and represent the density of naphthalene with no air enclosed in the pores. The coatings, however, were crystalline and somewhat porous. Therefore the density of the naphthalene coatings as used was measured, the foregoing figure representing the average of 17 measurements, with the ± value at 95 per cent confidence level. Since the temperature coefficient extrapolated from [20] was abnormally high, it was measured with a dilatometer.

Diffusivity and Schmidt number were calculated according to the procedure recommended in [21]. Since the calculated diffusivity (D = 0.0620 or 0.0614) agreed well with the experimental value (0.0611), the foregoing calculated Schmidt number relation is believed to give the most reliable published values for the naphthalene-in-air system.

References

1 R. G. Deissler and A. L. Loeffler, Jr., "Analysis of Turbulent Flow and Heat Transfer on a Flat Plate at High Mach Numbers With Variable Fluid Properties," NACA TN 4262, 1958.

2 Alvin Seiff, "Examination of the Existing Data on the Heat Transfer of Turbulent Boundary Layers at Supersonic Speeds From the Point of View of the Reynolds' Analogy," NACA TN 3284, 1954.

3 D. Coles, "Measurement of Turbulent Friction on a Smooth Flat Plate in Supersonic Flow," *Journal of the Aeronautical Sciences*, vol. 21, 1954, pp. 433–438.
4 R. J. Hakkinen, "Measurements of Turbulent Skin Friction on a Flat Plate at Transonic Speeds," NACA TN 3486, 1955.
5 H. Schlichting, "Boundary Layer Theory," McGraw-Hill Book Company, Inc., New York, N. Y., 1955.
6 Theodore von Karman, "The Analogy Between Fluid Friction and Heat Transfer," TRANS. ASME, vol. 61, 1939, pp. 705–710.
7 T. K. Sherwood, Chemical Engineering Progress, Symposium Series, no 25, vol. 55, 1959, pp. 71–85.
8 C. S. Lin, R. W. Moulton, and G. L. Putnam, "Mass Transfer Between a Solid Wall and Fluid Streams," *Industrial and Engineering Chemistry*, vol. 45, 1953, pp. 636–640.
9 R. G. Deissler, "Analysis of Turbulent Heat Transfer, Mass Transfer, and Friction in Smooth Tubes at High Prandtl and Schmidt Numbers," NACA Report 1210, 1955.
10 T. H. Chilton and A. P. Colburn, "Mass Transfer (Absorption) Coefficients," *Industrial and Engineering Chemistry*, vol. 26, 1934, pp. 1183–1187.
11 E. R. G. Eckert, "Engineering Relations for Heat Transfer and Friction in High-Velocity Laminar and Turbulent Boundary-Layer Flow Over Surfaces With Constant Pressure and Temperature," TRANS. ASME, vol. 78, 1956, pp. 1273–1283.
12 M. W. Rubesin and H. A. Johnson, "A Critical Review of Skin-Friction and Heat-Transfer Solutions of the Laminar Boundary Layer on a Flat Plate," TRANS. ASME, vol. 71, 1949, pp. 383–388.
13 D. R. Chapman and R. H. Kester, "Turbulent Boundary Layer and Skin Friction Measurements in Axial Flow Along Cylinders at Mach Numbers Between 0.5 and 3.6," NACA TN 3097, 1954.
14 E. R. Van Driest, "Turbulent Boundary Layer in Compressible Fluids," *Journal of the Aeronautical Sciences*, vol. 18, 1951, pp. 145–160.
15 M. W. Rubesin, R. C. Maydew, and S. A. Varga, "An Analytical and Experimental Investigation of the Skin Friction of the Turbulent Boundary Layer on a Flat Plate at Supersonic Speeds," NACA TN 2305, 1951.
16 R. H. Korkegi, "Transition Studies and Skin Friction Measurements on an Insulated Flat Plate at a Mach Number of 5.8," *Journal of the Aeronautical Sciences*, vol. 23, 1956, pp. 97–107.
17 M. W. Rubesin, "A Modified Reynolds Analogy for the Compressible Turbulent Boundary Layer on a Flat Plate," NACA TN 2917, 1953.
18 Olev Trass, "Sublimation Mass Transfer Through Compressible Boundary Layers on a Flat Plate," ScD thesis in Chemical Engineering, Massachusetts Institute of Technology, 1958.
19 T. K. Sherwood and H. S. Bryant, Jr., "Mass Transfer Through Compressible Turbulent Boundary Layers," *Canadian Journal of Chemical Engineering*, vol. 35, 1957, pp. 51–57.
20 "International Critical Tables," McGraw-Hill Book Company, Inc., New York, N. Y., 1928.
21 R. C. Reid and T. K. Sherwood, "The Properties of Gases and Liquids," McGraw-Hill Book Company, Inc., New York, N. Y., 1958.

DISCUSSION

Frank Kreith[2]

The authors have presented an interesting method of deducing skin friction coefficients from measurements of sublimation rates of naphthalene. The analogy between heat, mass, and momentum transfer has in the past usually been restricted to relating heat and mass transfer or to deduce heat or mass-transfer coefficients from known information on skin-friction coefficients. The reason given by the authors for reversing the procedure, i.e., predict the skin friction from mass-transfer rates, is that local skin-friction measurements are either more complex or less accurate than the measurements of local sublimation rates. This statement implies that the accuracy of their measurements has been evaluated and found to be satisfactory in all respects.

This discusser has over the past few years studied mass transfer from a naphthalene surface cast on a rotating plate. In the course of this work observations have been made which lead one to question the basic premise of the authors—namely, that the sublimation rates measured with the profilometer can be used with satisfactory accuracy as the primary source of data for calculating the skin friction.

It has been found in work done since our paper[3] was published that the rate of sublimation from the naphthalene surface of a rotating disk depends very much on the surface conditions. The rate of sublimation from a surface which is not completely smooth can easily exceed the rate from a surface machined smooth after casting by as much as 25 per cent. Since no direct relation between the increase in friction due to roughness and the corresponding increase in mass transfer or heat transfer exists, and since theoretical work on this question is still incomplete, this observation made it necessary in the work with the rotating disk to "calibrate" each surface by comparing the rate of mass transfer from it with some arbitrarily selected standard. In the work with the rotating disk theoretical calculations, which had previously been checked by independent heat as well as mass-transfer experiments, were used as the "standard."

In the experiments described in this paper, the sublimation rates from only a very few test surfaces were measured and no rigorous control over the surface conditions was maintained as seen from Fig. 2. Moreover, the interpretation of the test data was based on a "starting length" which, as shown in Fig. 6, is not unambiguously defined. In fact, the slopes of the curves in Fig. 12 depend not only on the surface conditions but also on the definition of Re_t. The accuracy of the comparison of the authors' data with the theory of Deissler and Loeffler seems therefore questionable on two accounts. But even if the starting length is accurately known, without a complete knowledge of the effect of surface conditions on the rate of sublimation, the authors' method for obtaining local friction coefficients from rate of sublimation measurements should be used with caution.

[2] Professor of Mechanical Engineering, University of Colorado, Boulder, Colo. Assoc. Mem. ASME.

Authors' Closure

Professor Kreith questions the accuracy and reproducibility of sublimation rate measurements. He also questions the comparison of data and theory because of the arbitrary definition of Re_t.

The precision attained in measuring the decrease in thickness of the naphthalene coating is suggested indirectly by the top two curves of Fig. 2. We believe that with the strain gages and instrumentation employed this decrease was measured to better than 3 per cent. It would appear to be more difficult to obtain similar precision by direct force measurements which are limited to flat surfaces in the measurement of skin friction. Actually, the principal source of error doubtless lay in the temperature measurements and not in the measurements of sublimation rate.

Properly prepared surfaces gave quite reproducible results. Preliminary studies emphasized the need for smooth surfaces which did not roughen during a test. Large crystals are formed if the naphthalene is cooled slowly, giving a coating which may be smoothed initially but which becomes rough before the test is complete. This condition was avoided in all tests reported. Small crystals formed by rapid solidification of the naphthalene gave surfaces which remained smooth and during a test attained a polished appearance, uniform in the longitudinal direction.

The problem of defining a starting length, or origin of turbulence, is encountered in most friction and heat-transfer studies. The manner in which Re_t is defined affects the correlation of the data but not the comparison of transfer coefficients for heat, mass, and momentum.

[3] F. Kreith, J. H. Taylor, and J. P. Chong, "Heat and Mass Transfer From a Rotating Disk," JOURNAL OF HEAT TRANSFER, TRANS. ASME, Series C, vol. 81, 1959, pp. 95–105.

T. F. IRVINE, JR.
Professor of Mechanical Engineering, North Carolina State College, Raleigh, N. C.

E. R. G. ECKERT
Professor of Mechanical Engineering, University of Minnesota, Minneapolis, Minn. Mem. ASME

Laminar Skin Friction and Heat Transfer on Flat Plates With Wedge-Shaped Grooves in Flow Direction

THE FLOW of fluids in ducts having noncircular cross sections has been studied by the authors and reported in a number of publications [1, 2, 3, 4].[1] In one of the cross sections investigated, that of an isosceles triangle with a height to base ratio of 10, it was observed that the flow in the narrow apex region behaved in a very peculiar manner in the neighborhood of the transition point. It was shown by flow-visualization techniques and velocity-field measurements that the influence of the converging walls in corner regions was such as to exert a stabilizing influence on the flow field. Thus, although the flow in the core of the fluid near the triangle base was turbulent, a significant portion of the fluid near the apex was laminar and remained so at high Reynolds numbers. This stabilizing phenomenon gave rise to the speculation that in external flow it might be possible to delay transition by installing wedge-shaped grooves in the flow direction. Thus an interest was generated in studying the boundary-layer development in such grooves. The present paper reports the results of such an investigation using the von Karman-Pohlhausen-Kroujiline integral equations to study the velocity and thermal boundary-layer growth and the associated skin friction and heat transfer.

Momentum Analysis

When fluid flows along a plane surface with grooves such as illustrated in Fig. 1, boundary layers will build up next to the solid walls of the surface. A constant-pressure main stream such as that over a flat plate can be expected to exist beyond the boundary layers. These boundary layers, which at first occur only in the immediate vicinity of the solid walls, will increase in thickness in the downstream direction and eventually overflow from the grooves.

By proposing appropriate velocity and temperature distributions within the boundary layers and through the use of momentum and energy integral equations, it is possible to calculate the rate of boundary-layer growth in the flow direction and thus to determine the related skin friction and heat transfer. In this analysis a rectangular co-ordinate system, such as shown in Fig. 2, will be used. As illustrated in the figure, the x-axis is taken along, and the y-axis perpendicular to, one wall of the groove. The z-axis is in the direction of the flow. The angle between the walls of the groove is 2α.

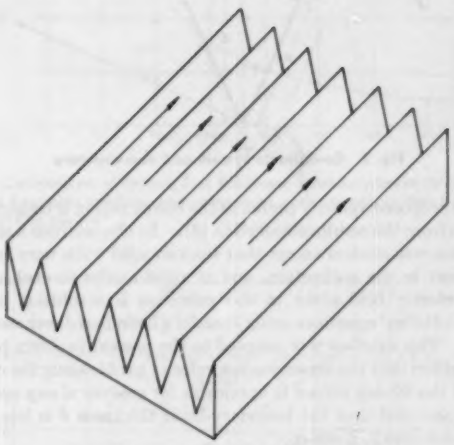

Fig. 1 Flow over a grooved flat plate

To simplify the investigation it is only necessary because of symmetry to consider half of the flow area between the grooves. The boundary layer is designated as the region between the dotted lines and the solid wall in Fig. 2. The dotted lines, which denote the outer edges of the boundary layer, are drawn parallel to the solid walls and are described as meeting at a sharp angle at the center line.

The boundary-layer thickness is denoted by δ along the center line of the groove in Fig. 2. The distance along the wall corresponding to δ is designated by R. It will be specified that a boundary layer with a flat-plate velocity profile exists along the wall of the groove beyond $x = R$ and that the velocity field in the corner of the groove joins smoothly to the flat-plate profile at $x = R$.

[1] Numbers in brackets designate References at end of paper.

Contributed by the Heat Transfer Division and presented at the Annual Meeting, Atlantic City, N. J., November 29–December 4, 1959, of THE AMERICAN SOCIETY OF MECHANICAL ENGINEERS.

NOTE: Statements and opinions advanced in papers are to be understood as individual expressions of their authors and not those of the Society. Manuscript received at ASME Headquarters, August 17, 1959. Paper No. 59—A-143.

Nomenclature

c_p = specific heat at constant pressure
F = drag force based on total groove-surface area
h = heat-transfer coefficient $= \dfrac{-k(\partial T/\partial y)_{y=0}}{T_s - T_w}$
k = thermal conductivity
L = length of groove wall, Fig. 2
q = specific heat flux, Btu/hr-sq ft
Q = heat flux, Btu/hr
R = projection of boundary-layer thickness on x-axis, Fig. 2
T = local temperature
u = velocity in z-direction
W = distance across top of groove, Fig. 2
x = co-ordinate
y = co-ordinate
z = co-ordinate
α = groove half angle, Fig. 2
δ = boundary-layer thickness, Fig. 2
$\Delta T = T_s - T_w$
ξ = ratio of boundary-layer thickness
ρ = mass density
μ = dynamic viscosity

Subscripts

fp = flat-plate conditions

(Continued on next page)

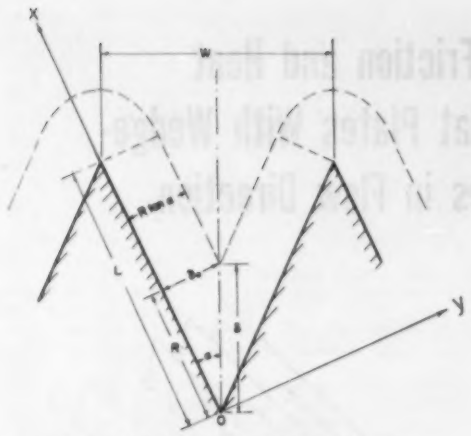

Fig. 2 Co-ordinate system and nomenclature

The proposed velocity profile in the corner region is constructed in part from the results obtained in [5]. In this analysis a similar situation was studied except that the two solid walls were infinite in extent in the x-direction, and at right angles to each other. The velocity field given in this reference is a solution of the Navier-Stokes' equations using Prandtl's boundary-layer assumptions. This solution was adapted to the present problem by the supposition that the dimensionless velocity profile along the center line of the 90-deg corner is applicable for grooves of any opening angle provided that the boundary-layer thickness δ is less than the notch depth, $L \cos \alpha$.

With the specifications just discussed, there are now three conditions which may be applied to the velocity field within the grooves. The first is that, at $x = R$, the corner velocity profile must be identical with that for the boundary layer along a flat plate and that the corner and side boundary layers should join smoothly. Second, the center-line velocity profile is taken as matching the one given in [5]. Third, the velocity should vanish at all solid surfaces.

For laminar boundary layers along a flat plate, the velocity profile is given according to [6] as:

$$\frac{u}{u_s} = {}^3/_2\left(\frac{y}{\delta_0}\right) - {}^1/_2\left(\frac{y}{\delta_0}\right)^3 \tag{1}$$

where u_s is the free-stream velocity taken as a constant and δ_0, the flat-plate boundary-layer thickness, is a function of s or the flow direction. The Nomenclature may be consulted for the meaning of other symbols. Since it has been specified that the thickness of the boundary layer existing at $x = R$ is a constant for each s-location at a given free-stream Reynolds number, the velocity profile in Equation (1) may be written as:

$$\frac{u}{u_s} = {}^3/_2\left(\frac{y}{R\tan\alpha}\right) - {}^1/_2\left(\frac{y}{R\tan\alpha}\right)^3 \tag{2}$$

Thus Equation (2) specifies the velocity distribution in the region $R < x < L$ and $0 < y < R \tan \alpha$. It is therefore taken that the velocity component in the x-direction is negligibly small in this region.

Also from the considerations just discussed, the velocity distribution given subsequently may be specified in the corner region $0 < x < R$ and $0 < y < x \tan \alpha$

$$\frac{u}{u_s} = \left[{}^{35}/_{12}\left(\frac{x}{R}\right) - {}^{35}/_{8}\left(\frac{x}{R}\right)^2 + {}^{17}/_{12}\left(\frac{x}{R}\right)^3\right]\left[3\left(\frac{y}{R\tan\alpha}\right) - \left(\frac{y}{R\tan\alpha}\right)^3\right] \tag{3}$$

The derivation of Equation (3) is given in detail in Appendix 1.

The velocity distributions given in Equations (2) and (3) may now be used in the integral momentum boundary-layer equation to determine the rate of boundary-layer growth. For the co-ordinate system described in Fig. 2, and for a control volume consisting of the groove walls, the outer edge of the boundary layer and two planes parallel to the x-y-plane and a distance of dz apart, the two-dimensional integral equation is written as:

$$-\frac{d}{dz}\left[\int_0^R\int_0^{x\tan\alpha} \rho u^2 dy\,dx + \int_R^L\int_0^{R\tan\alpha} \rho u^2 dy\,dx\right] + u_s\frac{d}{dz}\left[\int_0^R\int_0^{x\tan\alpha} \rho u\,dy\,dx + \int_0^L\int_0^{R\tan\alpha} \rho u\,dy\,dx\right] = \int_0^L \mu\left(\frac{\partial u}{\partial y}\right)_{y=0} dx \tag{4}$$

The first term on the left-hand side of Equation (4) represents the difference between momentum entering and leaving the two planes, the second term represents the momentum exchange rate with the free stream and the right-hand side equals the shear stresses acting on the fluid at the walls. When Equation (4) is written for constant properties in dimensionless form it reduces to

$$\frac{\rho u_s}{\mu}\tan^3\alpha\,\frac{d}{dz}\left[R^3\int_0^1\int_0^{z/R}\frac{u}{u_s}\left(1-\frac{u}{u_s}\right)d\left(\frac{y}{R\tan\alpha}\right)d\left(\frac{x}{R}\right)\right] + \frac{d}{dz}R^3\left[\int_0^{L/R}\int_0^1\frac{u}{u_s}\left(1-\frac{u}{u_s}\right)d\left(\frac{y}{R\tan\alpha}\right)d\left(\frac{x}{R}\right)\right] = \int_0^{L/R}\left[\frac{\partial\left(\frac{u}{u_s}\right)}{\partial\left(\frac{y}{R\tan\alpha}\right)}\right]_{y=0} d\left(\frac{x}{R}\right) \tag{5}$$

If the velocity expressions from Equations (2) and (3) are now inserted in Equation (5) and the appropriate integrations performed, the following first-order linear differential equation results:

$$\frac{d}{dz}\left[b_1\left(\frac{R}{L}\right) - b_2\left(\frac{R}{L}\right)^2\right] = \left[b_3\left(\frac{L}{R}\right) - b_4\right]\frac{\mu}{\rho u_s\tan^3\alpha} \tag{6}$$

with

$b_1 = 0.13928572$ $\quad b_2 = 1.50000000$
$b_3 = 0.05986989$ $\quad b_4 = 0.14583334$

Nomenclature

o = boundary layer on side of groove, Fig. 2
s = free-stream conditions
t = thermal boundary layer
w = wall conditions
x = x-co-ordinate
z = flow direction or z-co-ordinate

Dimensionless Groups

f = local friction factor $= \dfrac{\mu\left(\dfrac{\partial u}{\partial y}\right)_{y=0}}{\rho u_s^2/2}$

Nu = Nusselt number $= hZ/k$

Pr = Prandtl number

Re = Reynolds number $\left(\mathrm{Re}_s = \dfrac{\rho u_s Z}{\mu}\right)$

z^* = dimensionless z-co-ordinate, $z^* = \left[\dfrac{Z}{L\tan\alpha}\,\dfrac{1}{\mathrm{Re}_{L\tan\alpha}}\right]$

Integration of Equation (6) then gives the relation between boundary-layer thickness, in this case R/L, and the z-location

$$d_1\left(\frac{R}{L}\right) + d_2\left(\frac{R}{L}\right)^3 + d_3 \ln\left[1 - d_4\left(\frac{R}{L}\right)\right] = \left(\frac{z}{L \tan \alpha}\right)^2 \frac{1}{\mathrm{Re}_z} \tag{7}$$

with

$$d_1 = 7.49021839 \qquad d_3 = 77.04224279$$
$$d_2 = 0.41053637 \qquad d_4 = 0.09722223$$

Before proceeding to a discussion of the skin friction, the rate of boundary-layer growth in the corner regions will be examined. Not only is this growth related to wall friction in external flow, but it is of interest in connection with the prediction of hydrodynamic entrance lengths in noncircular ducts in internal flows.

Equation (7) indicates that the dimensionless boundary-layer thickness δ/L is a function of Re_z, z/L, and α. This suggests a comparison, at the same Re_z, between the growth of the boundary layer in the z-direction on a flat plate and in grooves of various values of α. Such a comparison will be made for the situation when $\delta = L \cos \alpha$; i.e., where the groove is filled. Then the z-distance for the groove may be easily obtained from Equation (7). The ratio δ/δ_{fp} is calculated from Equation (7) and from the well-known flat-plate solution.

$$\delta_{fp} = \frac{4.64\, z}{\sqrt{\mathrm{Re}_z}} \tag{8}$$

into which the foregoing value of z is inserted.

Such a comparison is shown in Fig. 3 where

$$(\delta/\delta_{fp})_{\delta = L \cos \alpha}$$

is plotted against the wedge angle 2α.

The figure indicates that, at small wedge angles, the rate of boundary-layer growth in the groove is very much greater than for a flat plate. Only at angles greater than 140 deg are the two boundary-layer growths very nearly the same. At an angle of 20 deg, for example, when the boundary layer has filled the groove, at the same z-distance and free-stream conditions, the flat-plate boundary layer is less than one tenth as thick.

A general representation of the results for any boundary-layer thickness is given in Fig. 4. The abscissa of this figure is a dimensionless co-ordinate in the flow direction which contains a Reynolds number based on the groove dimension and which for convenience is referred to as z^*. On the left-hand ordinate is the dimensionless boundary-layer thickness R/L, which is equal to $\delta \cos \alpha/L$. From Fig. 2 this is also seen to be equal to $\delta_0/L \tan \alpha$ and thus the left ordinate shows the growth of both the boundary layer in the corner δ, and along the side δ_0, when the curve marked wedge is used as the connection from z^*. On the right-hand ordinate is shown for reference the dimensionless boundary-layer thickness for a flat plate $\delta_{fp}/L \tan \alpha$. The connection between this ordinate and z^* is the curve marked flat plate. The upper curve in Fig. 4 is obtained from Equation (7) and the lower curve from a rearrangement of Equation (8) after the insertion of the reference length $L \tan \alpha$.

It is of interest to note from Fig. 4 that the rate of growth of a normal flat-plate boundary is less than the rate of growth of the boundary layer on the side of the groove whose thickness is δ_0. This is so because the rate of growth of δ_0 is controlled in part by the boundary-layer processes in the corner region. It also may be seen that the differences between δ_0 and δ_{fp} becomes less where the boundary layers in the groove are thin.

Figs. 5 and 6 show the local characteristics of the velocity field within the groove. In Fig. 5, lines of constant u/u_e are plotted at a given value of R/L and for a wedge angle of 45 deg. Particu-

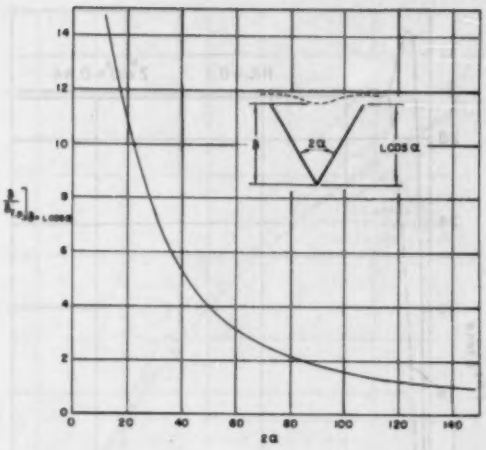

Fig. 3 Comparison of groove and flat-plate, boundary-layer thickness at equal Reynolds numbers and z-distances under condition that boundary layer fills groove

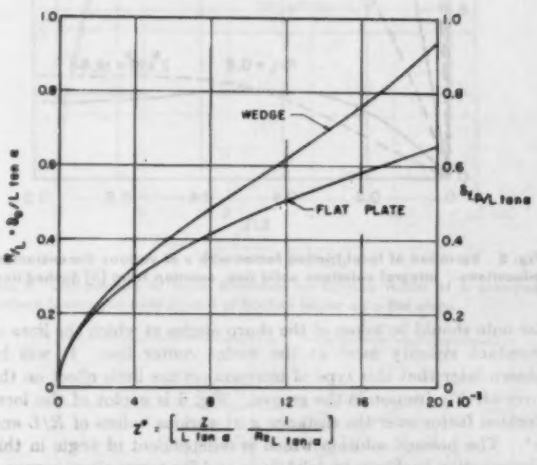

Fig. 4 Variation of dimensionless boundary-layer thickness in grooves and on flat plates with dimensionless z-co-ordinate

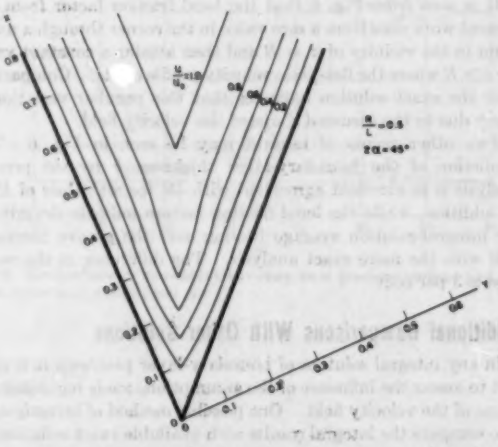

Fig. 5 Lines of constant velocity in groove, $2\alpha = 45$ deg

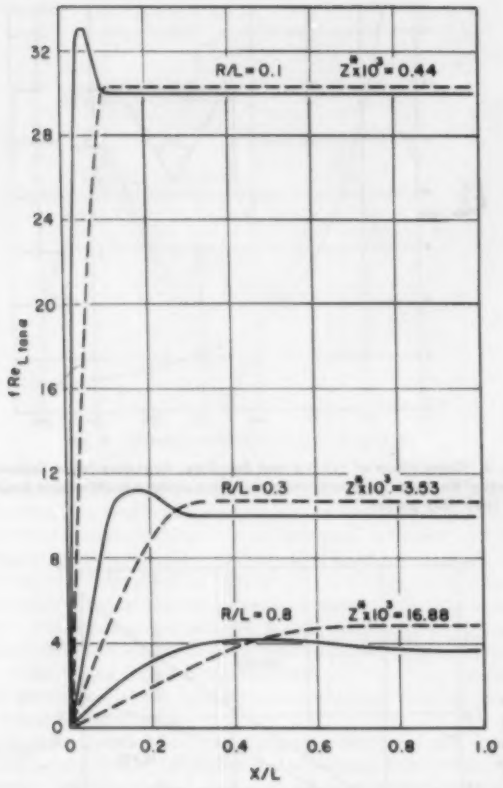

Fig. 6 Variation of local friction factor with x at various dimensionless z-locations. Integral solutions solid line, solution from [5] dashed line.

lar note should be taken of the sharp angles at which the lines of constant velocity meet at the wedge center line. It will be shown later that this type of intersection has little effect on the over-all skin friction in the groove. Fig. 6 is a plot of the local friction factor over the distance x at various values of R/L and z^*. The present solution which is independent of angle in this presentation is shown as solid lines and for comparison purposes the exact solution for the 90-deg infinite corner from [5] is shown by dashed lines.

It is seen from Fig. 6 that the local friction factor from the present work rises from a zero value in the corner through a maximum in the vicinity of $x = R$ and then attains a constant value for $x > R$ where the flat-plate velocity profile exists. Comparison with the exact solution indicates that this peculiar variation is likely due to the assumed shape of the velocity field.

Two other points of interest may be seen in Fig. 6. The prediction of the boundary-layer thickness δ by the present analysis is in excellent agreement with [5] for all values of R/L. In addition, while the local friction factors indicate deviations, the integral-solution average friction over the groove compares well with the more exact analysis. The difference in the worst case is 3 per cent.

Additional Comparisons With Other Solutions

In any integral solution of boundary-layer problems it is difficult to assess the influence of the assumptions made regarding the shape of the velocity field. One possible method of investigation is to compare the integral results with available exact solutions as was done in the foregoing. Another approach is to carry out

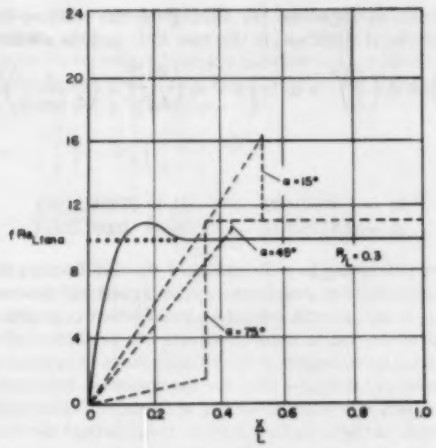

Fig. 7 Comparison of local friction factor at a given x-location for three solutions. Solution A (solid line), Solution B (dotted line), Solution C (dashed line).

solutions with different velocity assumptions and examine the final results. This will be done in the following paragraphs for three different assumed velocity distributions.

The three solutions which are available for comparison will be called Solutions A, B, and C. Solution A is the present analysis whose basic assumptions have already been discussed. Solution B has been obtained by specifying that a flat-plate velocity profile exists both in the corner and side regions of the groove. In other words, Equation (2) applies on the side walls in the region $R < x < L$, $0 < y < \delta_0$ and in the corner region $0 < x < R$, $0 < y < x \tan \alpha$. Solution C is presented in [7] and involves quite a different set of assumptions regarding the velocity field. In this reference the boundary layer near the peaks of the grooved-surface side is specified to have a flat-plate velocity profile which grows at the same rate as on a normal flat plate. The shape of the outer border of the boundary layer near the corner is taken as a hyperbola which fits smoothly into the outer border of the boundary layers near the peaks. In [7] a number of polynomials of different degrees were used to describe the shape of the velocity profile within the boundary layer. In the comparison to follow, the velocity profile in Solution C is a sixth-degree polynomial.

Three comparisons have been made among the three solutions and are shown in Figs. 7, 8, and 9. Fig. 7 has the local friction factor $f_{x,s}$ plotted against the dimensionless x-co-ordinate. Solution A has been discussed before. It is shown as a full line. Solution B (indicated by dots) shows, as would be expected from the single velocity profile assumed, a constant value of the local friction factor. Solution C has a friction-factor distribution which unlike the other solutions is angle dependent. Therefore it is presented for three angles. It is interesting to note that Solution C for small angles shows the same general characteristics as Solution A in that the local friction factor rises from a value zero in the corner, goes through a maximum, and then drops to the flat-plate value on the side of the wedge. The differences in flat-plate friction factors in Fig. 7 between Solutions A and C may be attributed to the different side boundary-layer growth rates discussed previously.

Fig. 8 shows the friction factor $\bar{f}$ averaged at a given z-location as it varies with the dimensionless distance z^* in flow direction. Once again, Solution C which is angle dependent in this representation is given for three angles. In addition, the flat-plate value is presented for comparison. In this figure, the differences between the three solutions, which were apparent in Fig. 7, are minimized because of the averaging process.

A final comparison between the three solutions is presented in Fig. 9. The dimensionless drag, which is equal to $\bar{f}_{z,1}\mathrm{Re}_z^{1/2}(L/z)$, at a fixed aspect ratio z/W and free-stream Reynolds number Re_z, is plotted over the angle α. Solution A is shown as solid points, Solution B as circles, and Solution C as hollow squares. Two main points of interest may be noted. First, it is remarkable that all three solutions agree very closely. Second, at small angles the total drag of the grooved surface is much larger than that of a flat plate with the same projected area. At groove angles of approximately 150 degrees, the drags are equal.

Energy Analysis

In a manner analogous to that used to solve for the skin friction in the groove, the heat transfer may be calculated also. If the law of conservation of energy is applied to the flow of a laminar, constant-property fluid through the same control volume as used previously, the following integral boundary-layer equation results:

$$\frac{d}{dz}\left[\delta c_p u_e T_e \int_0^{R_t}\int_0^{x\tan\alpha} \frac{u}{u_e}\left(1-\frac{T}{T_e}\right)dy\,dx\right] + \frac{d}{dz}\left[\rho c_p u_e T_e \int_{R_t}^{L}\int_0^{R_t\tan\alpha} \frac{u}{u_e}\left(1-\frac{T}{T_e}\right)dy\,dx\right] = k\int_0^L \left(\frac{\partial T}{\partial y}\right)_{y=0} dx \quad (9)$$

The specification will be made that the dimensionless temperature profile in the corner region, $0 < x < R_t$, $0 < y < x\tan\alpha$ is given by a relation similar to the velocity profile:

$$\frac{T-T_w}{T_e-T_w} = \left[{}^{30}/_{12}\left(\frac{x}{R_t}\right) - {}^{10}/_{2}\left(\frac{x}{R_t}\right)^2 + {}^{17}/_{12}\left(\frac{x}{R_t}\right)^3\right]\left[3\left(\frac{y}{R_t\tan\alpha}\right) - \left(\frac{y}{R_t\tan\alpha}\right)^3\right] \quad (10)$$

Note that the subscript t relates to the thermal boundary layer.

In a similar way, the temperature distribution on the groove side walls in the region $R_t < x < L$, $0 < y < R_t\tan\alpha$ is given by

$$\frac{T-T_w}{T_e-T_w} = {}^{3}/_{2}\left(\frac{y}{\delta_{0t}}\right) - {}^{1}/_{2}\left(\frac{y}{\delta_{0t}}\right)^3 \quad (11)$$

The wall temperature will be assumed locally constant.

A new dependent variable ξ is now defined which is equal to the ratio of thermal to velocity boundary-layer thickness.

$$\xi = \frac{\delta_t}{\delta} = \frac{R_t}{R}$$

If the temperature distributions given by Equations (10) and (11) are inserted in Equation (9) and the indicated differentiations and integrations are performed, the following nonlinear first-order differential equation may be obtained:

$$\frac{d\xi}{d\left(\frac{z}{L}\right)} = \left\{\frac{B_1 + B_2\left(\frac{R}{L}\right) + B_3\left[f'\left(\frac{R}{L}\right)\right]\left(\frac{R}{L}\right) + B_4\left[f'\left(\frac{R}{L}\right)\right]}{B_5\left(\frac{R}{L}\right)^3 + B_6\left(\frac{R}{L}\right)^2}\right\}\frac{\mu}{\rho u_e L\tan^2\alpha} \quad (12)$$

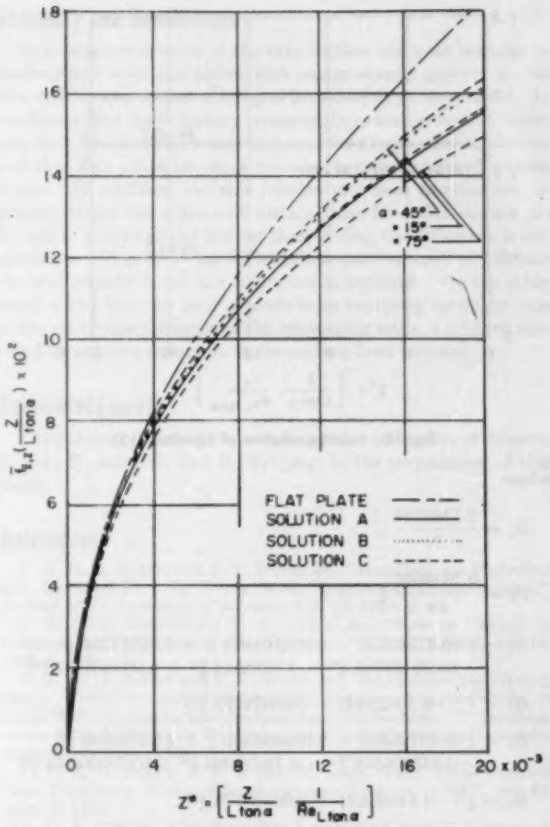

Fig. 8 Comparison of three solutions for friction factor of a grooved surface (averaged over x) and of friction factor on a flat plate

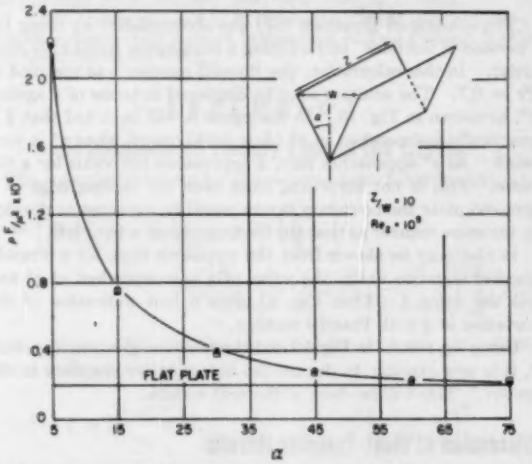

Fig. 9 Comparison of dimensionless drag on a grooved surface and on a flat surface of dimensions Wz

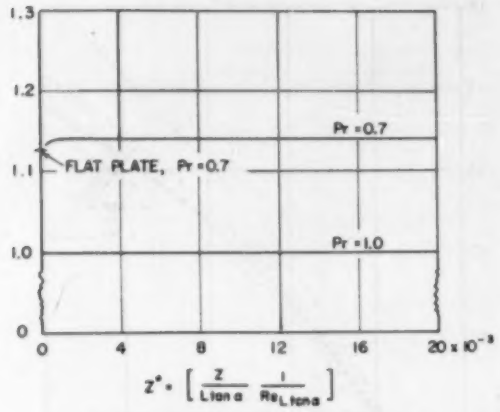

Fig. 10 Isocline solution of Equation (12)

where

$$B_1 = \frac{2.7243216}{\Pr}$$

$$B_2 = \frac{0.2648646}{\Pr}\,\xi$$

$$B_3 = \xi^4[0.27243216 - 0.474101638\,\xi + 0.46757256\,\xi^2 - 0.139167765\,\xi^3 - 0.0278544\,\xi^4 + 0.009855597\,\xi^5]$$

$$B_4 = \xi^3[-0.13621608 + 0.00972972\,\xi^2]$$

$$B_5 = \xi^3[0.81729648 - 1.896406552\,\xi + 2.33786280\,\xi^2 - 0.835006536\,\xi^3 - 0.19498080\,\xi^4 + 0.078844776\,\xi^5]$$

$$B_6 = \xi^3[-0.54486432 + 0.07783776\,\xi^3]$$

$$f'[(R/L)] = \frac{1.5000000 - 0.14583334(R/L)}{0.06964286 - 0.05986989(R/L)}$$

The solution of Equation (12) was accomplished by using the "method of isoclines" and utilizing a Remington Rand 1103 computer. In this calculation, the Prandtl number was specified as $\Pr = 0.7$. The solution may be displayed in terms of ξ against z^*, as shown in Fig. 10. In the figure it will be noted that ξ is practically independent of z^* ($\xi = 1.14$) except when z^* is very small. As z^* approaches zero, ξ approaches the value for a flat plate. This is not surprising since near the leading edge of a grooved plate the boundary layers would be expected to develop in the same manner as near the leading edge of a flat plate.

It also may be shown from the equations that, for a Prandtl number equal to unity, the value of ξ is independent of z^* and has the value 1. Thus Fig. 10 gives a first indication of the variation of ξ with Prandtl number.

Using the results in Fig. 10 and the relations given in Appendix 2, it is now possible to discuss the heat-transfer situation in the groove. This will be done in the next section.

Discussion of Heat-Transfer Results

In Fig. 11, the distribution of the local Nusselt number over the length x is shown for four z^*-locations, for a Prandtl number of 0.7, and for four values of R/L. A comparison with Fig. 6 indicates that the local Nusselt number and friction factor vary in a similar manner. The Nusselt number rises from a value zero in the corner, goes through a maximum, and approaches the fixed value at the side of the groove from above. This, again, is obviously determined by the assumed shape of the temperature field.

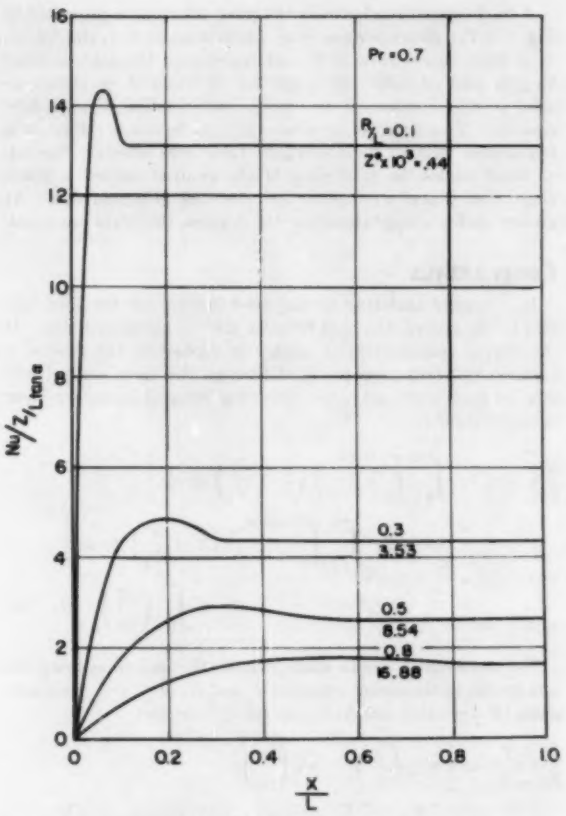

Fig. 11 Variation of local Nusselt number with x at various dimensionless z-locations

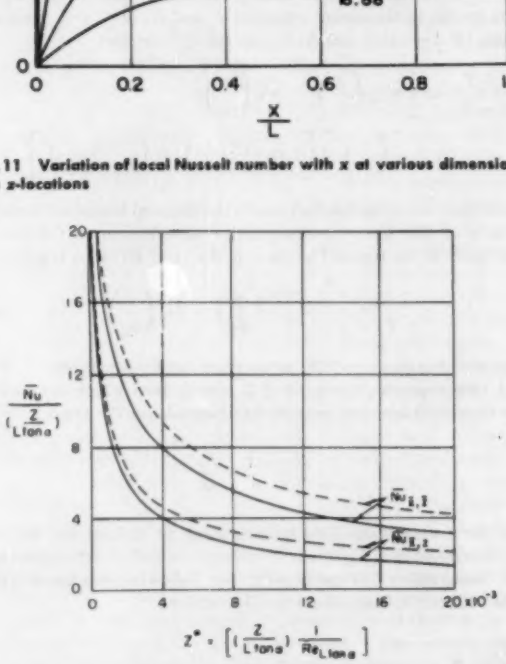

Fig. 12 Variation of average Nusselt numbers in dimensionless z-direction (dashed lines for grooved surface, solid lines for flat plate)

Fig. 12 shows as dashed lines the variation of the groove Nusselt numbers averaged over x only and over both x and z against the dimensionless distance z^*. This figure determines the heat-transfer performance of a grooved surface with length z for a Prandtl number of 0.7 once the Reynolds number $\mathrm{Re}_{L\tan\alpha}$, the groove angle, and side length L are specified. Also shown for

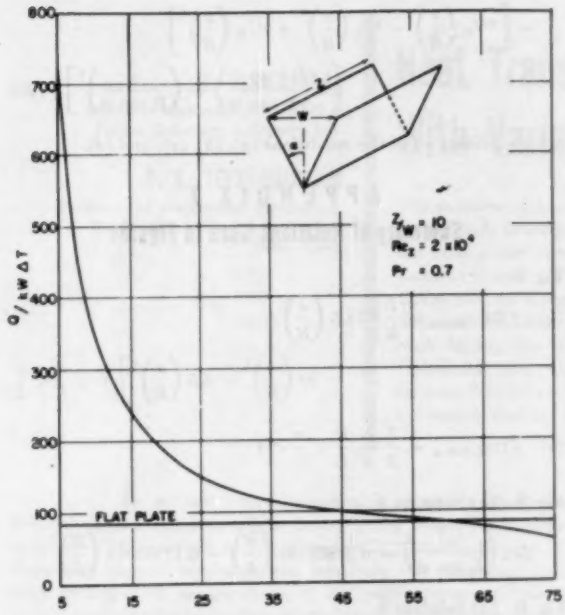

Fig. 13 Comparison of heat transferred from a grooved surface to that transferred from a flat surface of dimensions Wz

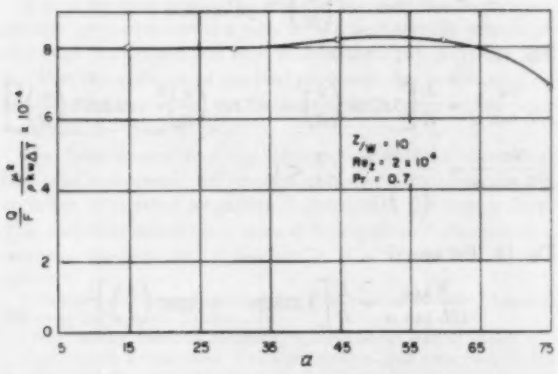

Fig. 14 Ratio of heat flux to drag for grooved surfaces of various groove angles

comparison, as solid lines, are the relations for the local and average Nusselt number on a flat plate.

Fig. 13 shows a dimensionless heat-flux parameter transferred from a grooved surface at particular values of Prandtl number, Reynolds number Re_z, and aspect ratio z/W. The heat-flux parameter which is identical with an average Nusselt number $\bar{h}z/k$ is plotted over the groove half angle α. For comparison purposes, the heat flux transferred from a flat plate of area zW is also shown. The heat transferred from the grooved surface is larger than that from the flat plate at groove half angles less than approximately 55 deg.

Of interest in possible applications of grooved surfaces is the variation with groove angle of the ratio of the heat flux to the drag. This ratio is shown in Fig. 14 for the same values of Prandtl number, Reynolds number Re_z, and aspect ratio z/W. It may be seen that, under the prescribed conditions, the ratio of heat flux to drag is essentially independent of the groove angle.

Summary and Conclusions

An analysis was made of the skin friction and heat transfer in laminar flow over flat plates with wedge-shaped grooves in the flow direction by means of integral boundary-layer equations. It was found that the boundary layers in the groove grow at a faster rate than flat-plate boundary layers under comparable conditions and that this effect becomes more pronounced at small groove angles. In addition, the skin friction and heat transfer are, in general, larger for a grooved surface than for a flat surface although at groove angles greater than 90 deg, the difference is not excessive. Thus grooving of a surface may be used to increase the heat transfer if the flow is laminar in any case. On the other hand, if the flow can be prevented from becoming turbulent due to the stabilizing influence of the converging walls, a grooved surface may cause a reduction in the surface heat transfer.

Acknowledgments

The authors gratefully acknowledge the assistance of Messrs. J. Yen, R. Schmidt, and R. Sampson in the preparation of this paper.

References

1 E. R. G. Eckert and T. F. Irvine, Jr., "Simultaneous Turbulent and Laminar Flow in Ducts With Noncircular Cross Sections," *Journal of the Aeronautical Sciences*, vol. 22, 1955, p. 65.

2 E. R. G. Eckert and T. F. Irvine, Jr., "Flow in Corners of Passages With Noncircular Cross Sections," TRANS. ASME, vol. 78, 1956, p. 709.

3 E. R. G. Eckert and T. F. Irvine, Jr., "Incompressible Friction Factor, Transition and Hydrodynamic Entrance Length Studies of Ducts With Triangular and Rectangular Cross Sections," Proceedings of the Fifth Midwestern Conference on Fluid Mechanics, University of Michigan Press, 1957.

4 E. R. G. Eckert, T. F. Irvine, Jr., and J. Yen, "Local Laminar Heat Transfer in Wedge-Shaped Passages," TRANS. ASME, vol. 80, 1958, p. 1433.

5 G. F. Carrier, "The Boundary Layer in a Corner," *Quarterly of Applied Mathematics*, vol. 4, 1947, p. 367.

6 E. R. G. Eckert and R. M. Drake, "Heat and Mass Transfer," McGraw-Hill Book Company, Inc., New York, N.Y., 1959.

7 L. G. Loitsianskii and V. P. Bolshakov, "On Motion of Fluid in Boundary Layer Near Line of Intersection of Two Planes," NACA TM 1308, November, 1951.

APPENDIX 1

Development of Velocity Field in the Groove

The equation proposed for the velocity field, Equation (3), is

$$\frac{u}{u_e} = \left[C_1\left(\frac{x}{R}\right) + C_2\left(\frac{x}{R}\right)^2 + C_3\left(\frac{x}{R}\right)^3\right] \left[C_4\left(\frac{y}{R\tan\alpha}\right) + C_5\left(\frac{y}{R\tan\alpha}\right)^3\right] \quad (13)$$

As discussed in the text, the conditions for evaluating the coefficients in Equation (13) are:

(*a*) at $x = R$, $\frac{u}{u_e} = \frac{3}{2}\left(\frac{y}{R\tan\alpha}\right) - \frac{1}{2}\left(\frac{y}{R\tan\alpha}\right)^3$

(*b*) at $x = R$, $\frac{\partial u}{\partial x} = 0$

(*c*) at $y = 0$, $\frac{u}{u_e} = 0$

(*d*) at $p = x\tan\alpha$ and $x < R$, $\frac{u}{u_e}$ agrees with reference [5]

To satisfy the conditions (*a*), (*b*), and (*c*)

$$C_4(C_1 + C_2 + C_3) = {}^9/_2 \tag{14}$$

$$C_5(C_1 + C_2 + C_3) = -{}^1/_2 \tag{15}$$

$$(C_1 + C_2 + C_3) = 0 \tag{16}$$

or from the foregoing

$$C_4 = -3C_5 \tag{17}$$

In order to satisfy condition (*d*), the center-line profile is taken as

$$\frac{u}{u_s} = A_2\left(\frac{x}{R}\right)^2 + A_3\left(\frac{x}{R}\right)^3 + A_4\left(\frac{x}{R}\right)^4 + A_5\left(\frac{x}{R}\right)^5 + A_6\left(\frac{x}{R}\right)^6$$

By comparing this with Equation (13) along the center line, $y = x \tan \alpha$, the following relations are seen to hold:

$$\begin{aligned} A_2 &= C_1C_4 \\ A_3 &= C_2C_4 \\ A_4 &= C_1C_5 + C_3C_4 \\ A_5 &= C_2C_5 \\ A_6 &= C_3C_5 \end{aligned} \tag{18}$$

Introducing (14), (15), (16), (17) into (18) then yields the following:

$$\begin{aligned} A_2 + {}^1/_2\,A_3 &= {}^9/_4 \\ {}^1/_2\,A_3 + A_4 &= -{}^3/_2 \\ A_4 - A_5 &= -{}^3/_2 \\ A_5 + 2A_6 &= {}^1/_2 \end{aligned} \tag{19}$$

Since there are now five unknowns, A_2 to A_6, and only four equations, one of the five A's may be additionally specified. This is done so as to obtain the best agreement between the center-line profile of [5]. An investigation showed that a selection of $A_3 = 29/4$ satisfied this condition very closely. Thus from Equation (19)

$$A_3 = -10,\ A_4 = 11/6,\ A_5 = 10/3,\ A_6 = -17/12$$

Using the relations (18), the velocity field in the groove is then given by

$$\frac{u}{u_s} = \left[{}^{29}/_{12}\left(\frac{x}{R}\right) - {}^{10}/_3\left(\frac{x}{R}\right)^2 + {}^{17}/_{12}\left(\frac{x}{R}\right)^3\right]\left[3\left(\frac{y}{R\tan\alpha}\right) - \left(\frac{y}{R\tan\alpha}\right)^3\right] \tag{20}$$

which satisfies all of the conditions (*a*), (*b*), (*c*), and (*d*).

APPENDIX 2
Summary of Relations Used in Figures

Fig. 6

(*a*) $f\,\mathrm{Re}_{L\tan\alpha} = \frac{L}{R}\left[14.5\left(\frac{x}{R}\right) - 20\left(\frac{x}{R}\right)^2 + 8.5\left(\frac{x}{R}\right)^3\right], 0 < \frac{x}{L} < \frac{R}{L}$

(*b*) $f\,\mathrm{Re}_{L\tan\alpha} = \frac{3}{2}\frac{L}{R}, \frac{R}{L} < \frac{x}{L} < 1$

Fig. 8 (*a*) Solution A

$$f_{z,x}\left(\frac{z}{L\tan\alpha}\right) = 0.27857144\left(\frac{R}{L}\right) - 0.11973978\left(\frac{R}{L}\right)^2$$

Fig. 9 (*a*) Solution A

$$\frac{\rho F}{\mu^2} = \frac{(\mathrm{Re}_s)^2\left[0.1393\left(\frac{R}{L}\right) - 0.0599\left(\frac{R}{L}\right)^2\right]}{\left(\frac{z}{W}\right)^2 4\sin\alpha\cos\alpha}$$

Fig. 11

$$\frac{\mathrm{Nu}}{z/L\tan\alpha} = \frac{L}{R}\left[5.5786\left(\frac{x}{R}\right) - 6.7499\left(\frac{x}{R}\right)^2 + 2.5263\left(\frac{x}{R}\right)^3\right]$$

$$\frac{\mathrm{Nu}}{z/L\tan\alpha} = \frac{1.3158}{\left(\frac{R}{L}\right)}, \frac{R}{L} < \frac{x}{L} < 1$$

Fig. 12 For groove

$$\frac{\overline{\mathrm{Nu}}_{z,s}}{z/L\tan\alpha} = \frac{L}{R}\left[1.31578 - 0.14583\left(\frac{R}{L}\right)\right]$$

R. VISKANTA[1]
School of Mechanical Engineering,
Purdue University, Lafayette, Ind.

Y. S. TOULOUKIAN
Professor of Mechanical Engineering,
Purdue University, Lafayette, Ind.
Mem. ASME

Heat Transfer to Liquid Metals With Variable Properties

The problem of heat transfer to liquid metals with variable physical properties for the case of fully developed turbulent flow in cylindrical tubes of constant diameter is studied, the fluid under consideration being heated or cooled by a constant and uniform heat flux at the wall. The similarity theory between momentum and heat transfer is used. Using the von Karman universal velocity profile the differential equations for turbulent flow with heat transfer are solved for the Prandtl number and the kinematic viscosity, each having five different sets of temperature-dependent exponents of a_1 and a_2. Calculated temperature distributions, mixing-cup temperatures, as well as relations between Nusselt versus Peclet numbers are presented for the cases of heat addition, heat extraction, and the nonvariable-property case.

In recent years considerable attention has been focused on the liquid metals as heat-transfer media for nuclear reactors. This interest in liquid metals is primarily because of their high thermal conductivities, relatively low viscosities, and high boiling-point temperatures at low vapor pressures. As a result, under similar hydrodynamic and thermal conditions, higher temperature differences and higher heat fluxes can be attained with liquid metals as compared to conventional heat-transfer media.

A need for determining the effect of the variation of thermophysical properties across a tube on the heat-transfer process at very high heat fluxes and high temperatures is indicated. The fact that the variation of physical properties due to temperature variation has an effect on the heat-transfer process has been recognized by Nusselt [17].[2]

The disagreement between the experimental and theoretical results in heat-transfer parameters is due, in part at least, to the variation of physical properties of fluids with the temperature. This variation necessitates more or less arbitrary selection of a reference temperature. Therefore it is of interest to inquire analytically, at least, into the effect of temperature variation and heat flux upon the magnitude of convective heat transfer in fully developed turbulent flow of liquid metals. The case of constant and uniform heat addition or extraction is postulated in this work.

Since the development of differential equations for temperature distribution involves the inclusion of physical properties as power functions of temperature, it is also of interest to inquire into the dependence of the predicted heat-transfer correlation on the values determined for the exponents of kinematic viscosity, Prandtl number, density, and specific heat. The variation of thermal conductivity with temperature is accounted for in the Prandtl number. It is shown later in this paper that, of the four quantities listed in the foregoing, the viscosity and the Prandtl number are the only major quantities involved, while the temperature dependence of density and specific heat constitutes only a second-order effect. The present paper is written with the hope that it will shed some light on the over-all question of temperature dependence of thermophysical properties in heat-transfer calculations in liquid metals.

The material presented in this paper is a continuation of the work at Purdue University and is a combination of the analyses given in references [3, 11, 14]. Temperature profiles along the radius of the tube and mixing-cup temperatures are calculated and Nusselt numbers are predicted.

Basic Equations

It can be shown [10] that the three Navier-Stokes' equations of motion, the energy equation, and the continuity equation for incompressible flow reduce to

[1] On leave of absence from Reactor Engineering Division, Argonne National Laboratory, Lemont, Ill.

[2] Numbers in brackets designate References at end of paper.

Contributed by the Heat Transfer Division and presented at the Annual Meeting, Atlantic City, N. J., November 29–December 4, 1959, of The American Society of Mechanical Engineers.

Note: Statements and opinions advanced in papers are to be understood as individual expressions of their authors and not those of the Society. Manuscript received at ASME Headquarters, August 17, 1959. Paper No. 59—A-148.

Nomenclature

A = area, sq ft
a_1 = exponent in equation (5) for variation of Prandtl number with temperature
a_2 = exponent in equation (6) for variation of kinematic viscosity with temperature
c_p = specific heat at constant pressure, Btu lb^{-1} deg F^{-1}
D = diameter of pipe, ft
h = convective film heat-transfer coefficient between pipe wall and fluid, Btu hr^{-1} ft^{-2} deg F^{-1}
K = coefficient defined as $K = [N_{Pr}/(N_{Pr})_w]^{1/4}$
k = thermal conductivity, Btu hr^{-1} ft^{-1} deg F^{-1}
N_{Nu} = Nusselt number, $N_{Nu} = hD/k$
N_{Pe} = Peclet number, $N_{Pe} = N_{Pr}N_{Re}$
N_{Pr} = Prandtl number, $N_{Pr} = c_p\mu/k$
N_{Re} = Reynolds number, $N_{Re} = u_mD/\nu$
q = rate of heat flow, Btu/hr
r = distance from center line of tube, ft
r_0 = radius of tube, ft
r_0^* = dimensionless tube radius, $r_0^* = (\tau_w/\rho_w)^{1/2}[r_0/\nu_w]$
T = dimensionless temperature ratio, $T = (t_w - t)/(t_w - t_c)$
t = mean local temperature, deg F
t_m^* = mixing-cup temperature defined by equation (13)
t^* = dimensionless temperature parameter, $t^* = (t_w - t)c_{pw}\tau_wA/q_w(\tau_w/\rho_w)^{1/2} = 1/\beta(1 - t/t_w)$
u = mean local velocity in x-direction, fps

(Continued on next page)

$$\frac{\tau_w}{\rho}\left(1-\frac{y}{r_0}\right)=(\epsilon_M+\nu)\frac{du}{dy} \tag{1}$$

$$\frac{q_w}{c_p\rho A_w}\left(1-\frac{y}{r_0}\right)=-(\epsilon_H+\alpha)\frac{dt}{dy} \tag{2}$$

if the following assumptions are made:

1 The flow is fully developed and steady.
2 All parameters are independent of the angular co-ordinate.
3 The temperature gradient $\partial t/\partial x$ is independent of x, r, ϕ.
4 Boussinesq's concept of "eddy diffusivity" for momentum and heat transfer is valid.
5 It is assumed that $q_r/q_w=(A_r/A_w)(r/r_0)$.

The quantities ϵ_M and ϵ_H are known as eddy diffusivities for momentum and heat transfer, respectively, the values of which are dependent upon the amount and kind of turbulent mixing existing at a point in the flowing fluid.

When written in dimensionless form, equations (1) and (2) become

$$\left(1-\frac{y^*}{r_0^*}\right)\left(\frac{\rho_w}{\rho}\right)=\frac{1}{\nu_w}(\nu+\epsilon_M)\frac{du^*}{dy^*} \tag{3}$$

$$\left(1-\frac{y^*}{r_0^*}\right)\left(\frac{\rho_w}{\rho}\right)\left(\frac{c_{pw}}{c_p}\right)=\frac{1}{\nu_w}\left(\frac{\nu}{N_{Pr}}+\epsilon_H\right)\frac{dt^*}{dy^*} \tag{4}$$

Physical Properties of Liquid Metals

Calculation of Nusselt numbers requires accurate knowledge of physical properties of liquid metals, particularly the specific heat at constant pressure c_p; the kinematic viscosity ν; the thermal conductivity k; the density ρ; and the derived quantity Prandtl number N_{Pr}.

In this paper the density and specific heat are considered constant with temperature variation.[3] The variation with temperature of c_p and ρ of liquid metals is of a much lower order of magnitude than the variation of ν and N_{Pr}. That is, the variation of physical properties for NaK, 56 per cent Na by weight, in the temperature range from 200 to 1300 F (based on 1300 F) is as follows: k varies by 11.4 per cent; ρ by 19.9 per cent; c_p by 8.4 per cent; ν by 200 per cent; and Prandtl number by 400 per cent. The variation with temperature of thermal conductivity will not be discussed separately because it does not appear as a separate parameter in the differential equations.

The variation with temperature of kinematic viscosity and Prandtl number of liquid metals can be shown to be adequately represented by equations of the form:

$$\frac{N_{Pr}}{(N_{Pr})_w}=\left(\frac{t}{t_w}\right)^{a_1}=(1-\beta t^*)^{a_1} \tag{5}$$

[3] The actual effect of this assumption is shown in the discussion of results by some spot-check calculations where the temperature variation of these quantities has been included.

$$\frac{\nu}{\nu_w}=\left(\frac{t}{t_w}\right)^{a_2}=(1-\beta t^*)^{a_2} \tag{6}$$

The Prandtl number and the kinematic viscosity of five commonly used liquid metals have been correlated by means of equations (5) and (6) and the values of the exponents a_1 and a_2 are tabulated in Table 1. These exponents represent the available data in general to within ±5 per cent or better with few isolated instances when the departures may reach a maximum of ±10 per cent. These departures are of the same order of magnitude or better than the accuracy assigned to the experimental data.

Table 1 Values of the exponents a_1 and a_2 in equations (5) and (6) giving temperature dependence of N_{Pr} and ν for five liquid metals

Fluid	Temp range, deg F	Ref.	Exponents in equations (5) and (6): Prandtl no., a_1	Kinematic viscosity, a_2
Mercury	100–600	[13]	−0.55	−0.35
Sodium	200–1300	[13]	−0.60	−0.60
NaK (eutectic)	400–1400	[5]	−0.70	−0.50
NaK (56% Na)	200–1300	[13]	−0.80	−0.65
Pb-Bi (eutectic)	300–1100	[6]	−1.15	−0.75

Temperature Profiles

Eddy Diffusivities. The coupling of equations for momentum and heat transfer is made possible through the ratio of eddy diffusivity of momentum and heat transfer. Reference [11] postulates a model for turbulent heat exchange and derives the following analytical expression for the ratio of eddy diffusivities:

$$\sigma=\frac{6}{\pi^2}\left[e^{-\frac{0.01}{N_{Pr}}}+{}^1\!/_4 e^{-\frac{0.04}{N_{Pr}}}+\ldots+\frac{1}{n^3}e^{-\frac{0.01\,n^2}{N_{Pr}}}\right] \tag{7}$$

Only the first two terms of the foregoing infinite series were used in temperature-profile calculations since preliminary estimates have shown that the maximum error introduced by neglecting higher-order terms in equation (7) was less than 2 per cent for Prandtl numbers smaller than 0.05.[4]

Velocity Profiles. In this work the well-known von Karman generalized velocity profile is used which is divided into three zones. Attempts to account for this in a rigorous manner are of doubtful value; the only soundly established conclusion is that a combination of dimensional analysis and mixing-length considerations lead to the hypothesis that $u^*=f(y^*)$. This velocity profile was chosen because of its simplicity, which makes the analytical treatment of the problem much easier. Furthermore, it has been shown [11] that for fluids with Prandtl numbers close to zero their temperature profiles should depend very little on the

[4] The prediction of σ and its agreement with the limited experimental data are also discussed in reference [7, 8, 9]. The empirical relations reported in these references do not contribute new insight over and above the considerations outlined in reference [11].

Nomenclature

u^* = generalized mean local velocity, $u^*=u(\tau_w/\rho_w)^{1/2}$
y = distance in radial direction measured from tube wall, ft
y^* = generalized perpendicular distance from wall, $y^*=[(\tau_w/\rho_w)^{1/2}/\nu_w]y$
z = dimensionless distance, $z=y/r_0=y^*/r_0^*$
α = thermal diffusivity, $\alpha=k/\rho c_p$, ft²/sec
β = dimensionless heat-transfer parameter, $\beta=q_w(\tau_w/\rho_w)^{1/2}/c_{pw}\tau_w t_w A_w$
ϵ_H = eddy diffusivity for heat transfer, ft²/sec
ϵ_M = eddy diffusivity for momentum transfer, ft²/sec
ν = kinematic viscosity, ft²/sec
ρ = mass density, lb sec²/ft⁴
σ = ratio of eddy diffusivities, $\sigma=\epsilon_H/\epsilon_M$
τ = fluid shear stress, psf
ϕ = angular cylindrical co-ordinate in radians

Subscripts

c = refers to center of pipe
m = refers to mixing-cup temperature
r = refers to r-direction
w = refers to wall of pipe

velocity profile and therefore uncertainties in the exactness of this profile are not important in the estimation of temperature profiles. However, it will be shown later in this paper that the form of the velocity profile has a marked effect on the mixing-cup temperature and therefore on the Nusselt number.

In the von Karman velocity profile the demarcation points between the laminar sublayer and buffer layer, and between the buffer layer and turbulent core, depend to some extent on individual judgment; the following values and the resulting formulas are those generally accepted as best representing the facts:

Laminar sublayer:	$u^* = y^*$	$0 \leqslant y^* \leqslant 5$
Buffer layer:	$u^* = -3.05 + 5 \ln y^*$,	$5 \leqslant y^* \leqslant 30$
Turbulent core:	$u^* = 5.5 + 2.5 \ln y^*$,	$30 \leqslant y^*$

Temperature Profiles. As stated earlier, the specific heat and density are assumed to be constant with temperature variation and since there is no turbulent mixing in the laminar sublayer, $\sigma = 0$. The differential equations for temperature distribution in the three regimes of flow were derived in reference [19] and are reproduced in the following:

Laminar sublayer

$$\frac{dt^*}{dy^*} = \left(1 - \frac{y^*}{r_0^*}\right)(N_{Pr})_w(1 - \beta t^*)^{a_1 - a_2} \tag{8}$$

Buffer layer

$$\frac{dt^*}{dy^*} = \frac{\left(1 - \dfrac{y^*}{r_0^*}\right)}{\sigma\left[\dfrac{(1 - \beta t^*)^{a_1 - a_2}}{\sigma(N_{Pr})_w} - (1 - \beta t^*)^{a_2} + 0.2y^*\left(1 - \dfrac{y^*}{r_0^*}\right)\right]} \tag{9}$$

Turbulent core:

$$\frac{dt^*}{dy^*} = \frac{\left(1 - \dfrac{y^*}{r_0^*}\right)}{\sigma\left[\dfrac{(1 - \beta t^*)^{a_1 - a_2}}{\sigma(N_{Pr})_w} - (1 - \beta t^*)^{a_2} + 0.4y^*\left(1 - \dfrac{y^*}{r_0^*}\right)\right]} \tag{10}$$

In equations (9) and (10), σ is a function of Prandtl number and therefore varies with temperature along the tube radius.

Determination of Heat-Transfer Parameters

The mean velocity of a fluid flowing in a pipe can be defined as

$$u_m = \frac{\int_0^{r_0} \rho u(r_0 - y)dy}{\int_0^{r_0} \rho(r_0 - y)dy} \tag{11}$$

Assuming that ρ is constant and writing equation (11) in dimensionless form one gets

$$u_m^* = \frac{\int_0^{r_0^*} u^*(r_0^* - y^*)dy^*}{\int_0^{r_0^*} (r_0^* - y^*)dy^*} \tag{12}$$

The mixing-cup temperature is defined as

$$t_m = \frac{\int_0^{r_0} tu\rho c_p(r_0 - y)dy}{\int_0^{r_0} u\rho c_p(r_0 - y)dy} \tag{13}$$

Writing in dimensionless form, equation (13) reduces to

$$t_m^* = \frac{\int_0^{r_0^*} t^*u^*(r_0^* - y^*)dy^*}{\int_0^{r_0^*} u^*(r_0^* - y^*)dy^*} \tag{14}$$

The Peclet number, with the fluid properties evaluated at the wall temperature, is defined as

$$(N_{Pe})_w = (N_{Re})_w(N_{Pr})_w = \left(\frac{u_m D}{\nu_w}\right)\left(\frac{\nu\rho c_p}{k}\right)_w = 2u_m^* r_0^*\left(\frac{\nu\rho c_p}{k}\right)_w \tag{15}$$

Using the dimensionless co-ordinates and introducing the kinematic viscosity and Prandtl number variation with temperature the Peclet number defined at the mixing cup temperature becomes

$$(N_{Pe})_m = 2u_m^* r_0^*(N_{Pr})_w(1 - \beta t_m^*)^{a_1 - a_2} \tag{16}$$

The Nusselt numbers calculated in this paper are based on the heat-transfer coefficient h, defined by Newton's law of cooling, in terms of the temperature difference between the wall temperature and the mixing-cup temperature; namely,

$$(N_{Nu})_m = \frac{q_w D}{k_m(t_w - t_m)A_w} \tag{17}$$

By the use of the definitions of u_m^*, t_m^*, the expression for Nusselt number can be written as

$$(N_{Nu})_m = \frac{2r_0^*(\rho c_p \nu)_w}{(kt^*)_m} = \frac{2r_0^*}{t_m^*}\left(\frac{\nu_w}{\nu_m}\right)\left(\frac{c_p\rho\nu}{k}\right)_m \tag{18}$$

$$= \frac{2r_0^*(N_{Pr})_w}{t_m^*}(1 - \beta t_m^*)^{a_1 - a_2} \tag{18a}$$

The differential equations (8), (9), and (10) for the temperature distribution were solved by the Runge-Kutta numerical method employing a Datatron digital computer. The increments of the independent variable y^*, ranged from 1 to 50 depending on the value of the dimensionless tube radius r_0^*. The integration of equations (12) and (14), for the mean velocity and mixing-cup temperature, was also performed on the digital computer using varying increments of the dimensionless distance y^*, between the limits of $y^* = 0$ and $y^* = r_0^*$.

The computations were performed for four different Prandtl numbers and five sets of values of the exponents a_1 and a_2. Nusselt number calculations included the nonvariable property $a_1 = a_2 = 0$; heat addition $\beta = 0.025$, and heat extraction $\beta = -0.025$.

Discussion of Results

In the earlier part of this paper it was stated that the results obtained in this work are based only on the consideration of variable ν and N_{Pr}. In order to ascertain the validity of the assumption that the temperature dependence of ρ and c_p has a negligible effect on the results, a number of calculations were performed to indicate the influence of variable ρ and c_p at extreme conditions. From these spot-check calculations, the results for the most extreme condition are given in Table 2.

In Table 2 the parameters t_m^* and $(N_{Pe})_w$ were chosen instead of T and N_{Re} for reasons of simplicity. The comparative results are equally valid and the foregoing presentation obviates the need for reproducing $T = f(z)$ and $N_{Re} = f(T)$ for various values of β. Of course $(N_{Re})_w$ is independent of β.

From the extremes of the figures seen in Table 2, it is felt that the simplifying assumption of considering ρ and c_p constant is

Table 2

$[(N_{Pr})_w = 0.02, (N_{Pe})_w = 100{,}000, (q_w D)/A = 8.75 \times 10^7 \text{ Btu hr}^{-1} \text{ ft}^{-1}]$

Dimensionless heat-transfer parameter	t_m^* All properties variable	t_m^* Only ν and N_{Pr} variable	t_m^* Per cent difference	N_{Nu} All properties variable	N_{Nu} Only ν and N_{Pr} variable	N_{Nu} Per cent difference
$a_1 = a_2 = 0$; $(\beta \equiv 0)$	33.20	33.20	0	104.32	104.32	0
$\beta = +0.025$	23.95	24.06	+0.54	134.14	133.67	−0.35
$\beta = -0.025$	39.69	39.92	−0.58	86.43	86.95	+0.60

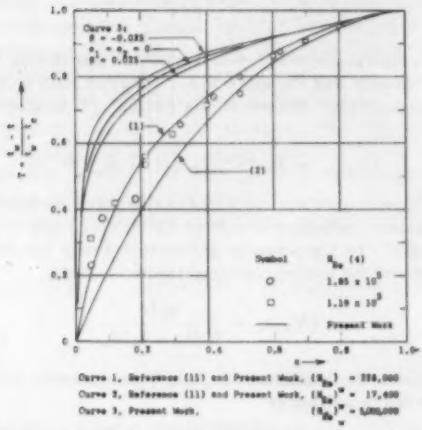

Fig. 1 Temperature distribution for different Reynolds numbers reported by Isakoff and Drew [4] compared with the present work for $(N_{Pr})_w = 0.02$ and the predictions of reference [11]

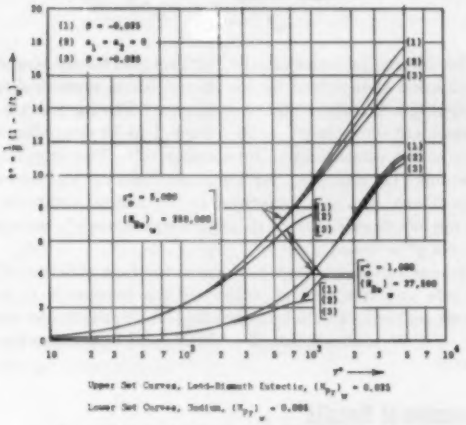

Fig. 2 Dimensionless temperature distribution

fully within the limits of uncertainty of both heat-transfer theory and data.

In Fig. 1, the predicted temperature profiles for $(N_{Pr})_w = 0.02$ are compared with the theoretical results of reference [11] and experimental data of Isakoff and Drew [4] for mercury, $N_{Pr} = 0.0239$. The calculated results of the present study exactly coincide with the theoretical predictions of reference [11] (curves 1 and 2), and are in good agreement with the data of Isakoff and Drew, except at $x < 0.2$ where considerable scatter of the experimental data exists. The temperature profiles for $\beta = \pm 0.025$ and $a_1 = a_2 = 0$ practically coincide with each other and cannot be distinguished in Fig. 1. Even curve 3 of this figure indicates that the influence of variable properties of N_{Re} of the order of 5×10^6 is no greater than 7 per cent.

From Fig. 2, it can be observed that for $r_0^* < 1000$ (Re ≈ 37,500), the temperature profiles are almost identical for the three cases indicated; namely, the nonvariable-property case $a_1 = a_2 = 0$,[5] heat addition to the fluid $\beta = 0.025$,[6] and heat extraction from the fluid $\beta = -0.025$. These results indicate that increasing the rate of heat addition, as evidenced by positive heat-transfer parameter β causes a slight decrease in the values of t^* for constant y^* as compared with those of nonvariable-property case, whereas an opposite effect is indicated for heat extraction.

Fig. 2 also indicates that at a constant y^* the difference between the temperature profiles for the nonvariable-property case and heat addition or heat extraction is small; however, as the Prandtl number is increased this difference becomes greater. This is due to the fact that as N_{Pr} is increased t^* increases and since N_{Pr} and ν are functions of t^* as given by equations (5) and (6), respectively, the difference between the temperature profiles for the nonvariable-property case and heat addition or heat extraction widens.

Additional calculations [19] of temperature profiles for two fluids having the same Prandtl number $(N_{Pr})_w = 0.01$, but different exponents a_1 and a_2[7] ($a_1 = -0.70$, $a_2 = -0.50$, and $a_1 = -0.80$, $a_2 = -0.65$) show that for the case of $\beta = \pm 0.025$ at $y^* = 5000$ the maximum difference between the values of t^* is of the order of 1 per cent, which indicates that the influence of the exponents on the temperature profile is rather small.

In Fig. 3, the predicted Nusselt numbers of this work are plotted against the Peclet numbers for mercury $(N_{Pr})_w = 0.02$, for the case $a_1 = a_2 = 0$. The results are compared with the empirical equations of Lyon [12], Deissler [2], Mikheyev, et al. [15] (for clean tubes), and the theoretical results of Lykoudis and Touloukian [11]. Nusselt numbers predicted by Lyon's equations for $\sigma = 1$ are too high. The curve representing the equation of Deissler, while predicting lower values of N_{Nu} than those of Lyon's, definitely distorts the function, $N_{Nu} = f(N_{Pe})$.

The predictions of reference [11] are, in general, good agreement with the present results for the case $a_1 = a_2 = 0$; however, there is a difference in N_{Nu} of about 12 per cent at $N_{Pe} = 100{,}000$. The discrepancy between the two results is seen to be primarily due to the difference in the velocity profiles selected. Since these two velocity profiles yielded temperature profiles which are in excellent agreement, Fig. 1, curves 1 and 2, the discrepancy in N_{Nu} lies in the difference in the mixing-cup temperatures and the mixing-cup velocities obtained from these two velocity profiles. These two mean quantities affect the N_{Nu} in different ways; namely, the lower t_m^* of the von Karman profile tends for higher N_{Nu} and the higher u_m^* of the von Karman profile tends to higher N_{Pe}; the net result being that the N_{Nu} versus N_{Pe}-function using the

[5] In reference [3] this case is called $\beta = 0$ or isothermal. One must note that this interpretation is physically meaningless since $\beta = 0$ means zero heat input which is not the case. In equation (18) the term $(1 - \beta t_m^*)^{a_1 - a_2}$ should be made equal to 1 by setting $a_1 = a_2 = 0$ 0 rather than $\beta = 0$. This reasoning is further supported by the fact that should β be allowed to become zero then the definition of t^* (see Nomenclature) breaks down since t^* becomes infinite.

[6] For lead-bismuth eutectic, $\beta = 0.025$ corresponds to heat flux of $(q/A)D = 3.12 \times 10^6$ Btu hr^{-1} ft^{-1}, for $N_{Pr} = 0.025$ at $N_{Re} = 230{,}000$. Similarly for $N_{Pr} = 0.020$ at $N_{Re} = 3.9 \times 10^6$ the heat flux of $(q/A)D = 8.75 \times 10^7$, Btu hr^{-1} ft^{-1}.

[7] This is the case of NaK eutectic and NaK, 56 per cent Na, as seen from Table 1.

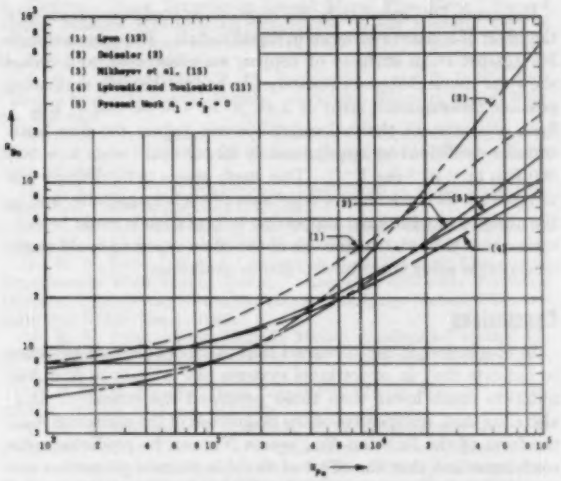

Fig. 3 Comparison of various predictions of Nusselt number variation with Peclet number for mercury $(N_{Pr})_w = 0.02$

von Karman velocity profile is in general higher than that resulting from the Lykoudis-Touloukian profile (Fig. 4).[8]

Similar to the case of the temperature profiles discussed earlier, calculations indicate [19] that for two fluids having the same Prandtl number $(N_{Pr})_w = 0.01$, $(N_{Re} = 228{,}000)$, but different sets of exponents a_1 and a_2 ($a_1 = -0.70$ and $a_2 = -0.50$, and $a_1 = -0.80$ and $a_2 = -0.65$) show that for the case of $\beta = \pm 0.025$ the difference in Nusselt numbers is of the order of 1.5 per cent. As expected, the results are identical for the case $a_1 = a_2 = 0$.

From Fig. 5 it can be seen that the agreement of the present work with the experimental data of Johnson, et al. [6], for $N_{Pr} = 0.025$ is good in trend. The magnitude is on the average about 12 per cent lower than the theoretical predictions for the nonvariable-property case. To the extent that the maximum value of the parameter β in the reported data was calculated to be 0.0054, its comparison with the case of $a_1 = a_2 = 0$ was considered more appropriate than the other two cases, $\beta = \pm 0.025$.

Finally, it can be seen from Fig. 5 that at $N_{Pe} = 5000$ $(N_{Re} = 2 \times 10^5)$ the effect of heat addition ($\beta = 0.025$) is to increase the Nusselt number by 13 per cent while heat extraction ($\beta = -0.025$) exhibits a decrease of 7 per cent. The corresponding maximum figures for mercury, Fig. 6, $N_{Pr} = 0.02$, $N_{Pe} = 100{,}000$ $(N_{Re} = 5 \times 10^6)$, are found to be about 26 and 17 per cent, respectively. On the basis of these findings it can be stated that for liquid metals the effect of the variation in properties as function of temperature is only moderate even for extremely high heat-flux conditions and Reynolds numbers.

At the time of its presentation, in August, 1957, reference [11] had attempted to compare the theoretical predictions with the then existing experimental data. Since that time there has been a noticeable increase in the Russian literature on liquid-metal heat transfer [1, 7, 8, 9, 16], which not only report new data but also review most of the past works and present both analytical and empirical correlations.

Mikheyev [15] reports the following empirical correlation equation which includes a correction factor for property temperature dependence:

$$N_{Nu} = (3.2 + 0.021 N_{Re}^{0.8} N_{Pr}^{n}) K \qquad (19)$$

[8] In this figure the independent parameter r_0^* was used in place of N_{Pe} in order to be able to separate the effect of the velocity profile on t_m^*. This would not be possible with the use of N_{Pe} since the latter depends on both the velocity profile and the mean temperature.

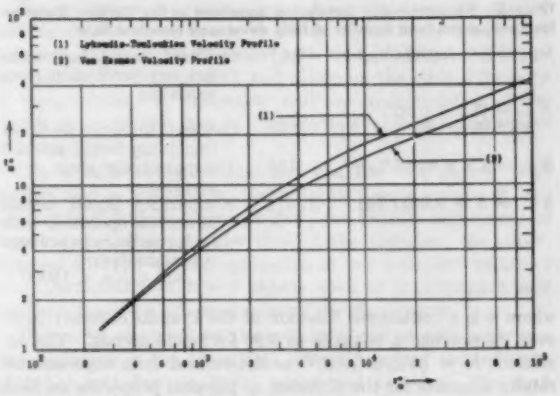

Fig. 4 Dependence of dimensionless mixing-cup temperature on dimensionless radius r_0^* for nonvariable-property case, $a_1 = a_2 = 0$, and $(N_{Pr})_w = 0.02$

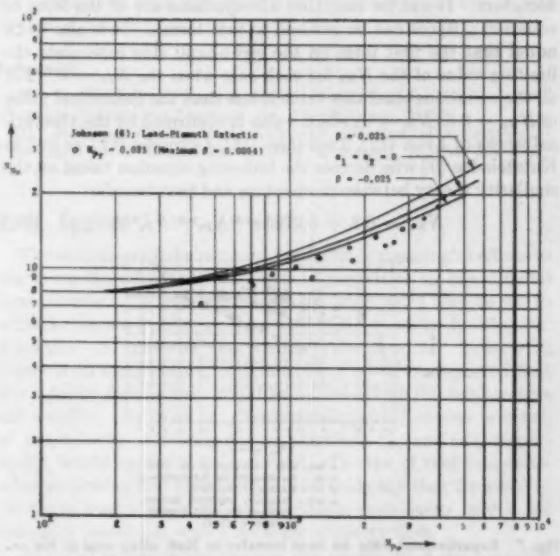

Fig. 5 Comparison of experimental data of Johnson, et al. [6], with present work

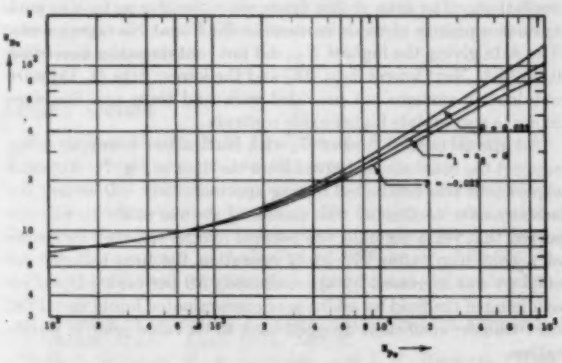

Fig. 6 Variation of Nusselt number with Peclet number for mercury $(N_{Pr})_w = 0.02$

Table 3 Recommended correlation equations in the Russian literature for liquid-metal heat transfer in fully developed turbulent flow

$N_{Nu} = 3.0 + 0.014N_{Pe}^{0.8}$	[15]	Oxidized steel tubes, without any precaution from oxidation
$N_{Nu} = [3.2 + 0.021 N_{Re}^{0.8}N_{Pr}^{n}]K$	[15]	Oxidized tubes for all fluids (including liquid metals)
$N_{Nu} = 4.5 \times 0.014N_{Pe}^{0.8}$	[15]	Comparatively clean tube surfaces
$N_{Nu} = 5 + 0.0021N_{Pe}$	[1, 7, 8]	Nonpurified liquid metals in normal operation with no special care to prevent contamination: $300 < N_{Pe} < 15000$

where n is a continuous function of the Prandtl number; however, in practice n is taken as 0.90 for liquid metals. The coefficient $K = [N_{Pr}/(N_{Pr})_w]^{1/4}$ as determined from experimental results accounts for the influence of physical properties on heat transfer. Equation (19) gives essentially the same temperature-dependence prediction as in the present work and confirms the general trend of variation in N_{Nu} versus N_{Re}. Table 3 gives a summary of correlating equations recommended in the Russian literature. It can be seen that all equations are of the form of equation (19) (or can be reduced to that form). It is also to be noted that the first term on the right-hand side represents the limiting value of the N_{Nu} for each case when the $N_{Pr} \to 0$. For all the equations cited this value is less than the theoretical value of $N_{Nu} = 6.8\ (N_{Pr} \to 0)$ which value is confirmed by the theoretical works of Lyon [12], Trefethen [18], Lykoudis [11], as well as Kutateladze [9] who derives the following equation based on the similarity theory between momentum and heat transfer:

$$N_{Nu} = 6.8 + 0.0765\sigma^{0.01}N_{Pr}^{0.001}N_{Pe}^{0.72} \qquad (20)$$

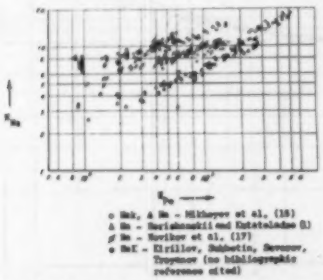
o NaK, Δ Na – Mikheyev et al. (16)
Δ Na – Borishanskii and Kutateladze 5)
β Na – Novikov et al. (17)
• NaK – Kirillov, Subbotin, Suvorov, Troyanov (no bibliographic reference cited)

Fig. 7 Experimental data on heat transfer to NaK alloy and to Na reproduced from reference [7]

Fig. 7 which is reproduced from reference [7] forcefully indicates the effect of oxide content of the fluid on the heat-transfer coefficient. The data of this figure show the change in N_{Nu} with various amounts of oxide content in NaK and Na experiments. The data giving the highest N_{Nu} did not contain oxides exceeding 0.003%.[9] Next lowest data [16] and the lowest data [1, 15] were obtained in systems not provided with cold traps and therefore likely to accumulate higher oxide contents.

Additional careful studies [7] with NaK alloys in copper tubes support the conclusions derived from the data in Fig. 7. A special experiment was conducted lasting approximately 450 hr and the heat-transfer coefficient was measured at intervals. It was observed that when the fluid was purified (oxides removed by means of a cold trap) after 275 hr of operation the heat-transfer coefficient was increased by approximately 20 per cent. Upon reoxidizing of the fluid by addition of contaminated liquid metal the heat-transfer coefficient dropped back to its value prior to purification.

[9] Data of Kirillov, Subbotin, Suvorov, Troyanov as reported in reference [7] with no direct reference to authors' work.

Reference [16] seems to be the only one to study systematically the effect of contact resistance in liquid metals. Experiments with Na against clean surfaces of copper, stainless steel, and nickel show the thermal-contact resistance to be less than the maximum possible measurement error of 2.44×10^{-6} hr ft^2 deg F Btu^{-1}. Such a maximum thermal resistance can reduce the film heat-transfer coefficient by approximately 20 per cent (when h = 10,000 Btu hr^{-1} ft^{-2} deg F^{-1}). This study seems to be the only one to report a thermal-contact resistance of such magnitude, and in the absence of additional supporting information it could be construed that the total magnitude of the effect reported could easily incorporate some contribution due to oxidation.

Conclusions

In conclusion, it can be stated that there is adequate evidence to indicate that in operational systems one is likely to find N_{Nu} numbers much lower than those predicted theoretically. It is also clear that, irrespective of the magnitude of the minimum N_{Nu}, the form of the function N_{Nu} versus N_{Pe} can be predicted with confidence and that the effect of variable thermal properties can be incorporated into analytical solutions by the application of correction coefficients of the form given by Mikheyev or the present work.

In the latter case the temperature-correction coefficient is obtained by multiplying and dividing the right-hand side of equation (18) by $(N_{Pr})_w$ and regrouping terms.

$$(N_{Nu})_m = (N_{Nu})_w \left(\frac{\nu_w}{\nu_m}\right) \frac{(N_{Pr})_m}{(N_{Pr})_w}$$

or

$$(N_{Nu})_m = (N_{Nu})_w \left(\frac{\alpha_w}{\alpha_m}\right) \qquad (21)$$

where (α_w/α_m) is the correction factor derived from the analytic expressions of this work. The correction factors proposed by Mikheyev and this work give the same trend of N_{Nu}; however, they vary from 0 up to 10 per cent (at N_{Pe} = 100,000), the direction of the deviation depending on the case of heat extraction or heat addition.

Acknowledgment

The senior author wishes to express his appreciation for the financial assistance provided by the Trane Company in the form of a fellowship while he was studying toward his Master's degree. The authors wish to acknowledge the interest shown by Dr. P. S. Lykoudis in this work and the helpful suggestions he has given.

References

1 V. M. Borishansky and S. S. Kutateladze, "Heat Transfer and Hydraulic Resistance in Liquid Metal Flowing in Circular Pipes," *Zhurnal Technicheskoi Fisiki*, vol. 28, 1958, pp. 836–847.

2 R. G. Deissler, "Analysis of Fully Developed Turbulent Heat Transfer at Low Peclet Numbers in Smooth Tubes With Application to Liquid Metals," NACA RM E52F05, 1952.

3 R. G. Deissler, "Heat Transfer and Fluid Friction for Fully Developed Turbulent Flow of Air and Supercritical Water With Variable Properties," TRANS. ASME, vol. 76, 1954, pp. 73–85.

4 S. E. Isakoff and T. B. Drew, "Heat and Momentum Transfer in Turbulent Flow of Mercury," Proceedings of the General Discussion on Heat Transfer, The Institution of Mechanical Engineers and ASME, 1951, pp. 405–409.

5 C. B. Jackson, editor, "Liquid Metals Handbook," Sodium (NaK) Supplement, Atomic Energy Commission, Department of the Navy, 1955.

6 H. A. Johnson, J. P. Hartnett, and W. J. Clabaugh, "Heat Transfer to Molten Lead-Bismuth Eutectic in Turbulent Pipe Flow," TRANS. ASME, vol. 75, 1953, pp. 1191–1198.

7 S. S. Kutateladze, V. J. Subbotin, V. M. Borishansky, and P.

L. Kirillov, "Heat Transfer in Liquid Metal Pipe Flow," Second United Nations International Conference on the Peaceful Uses of Atomic Energy, Paper No. A/CONF 15/P/2210, Geneva, Switzerland, September, 1958.

8 S. S. Kutateladze, V. M. Borishansky, and I. I. Novikov, "Heat Transfer to Liquid Metals," *Atomnaya Energiya*, vol. 4, 1958, pp. 422–436.

9 S. S. Kutateladze, "Heat Transfer in Liquid Metal Flow in Pipes and Over Flat Plates," *Zhurnal Technicheskoi Fiziki*, vol. 28, 1958, pp. 848–854.

10 J. Laufer, "The Structure of Turbulence in Fully Developed Pipe Flow," NACA Report 1174, 1954.

11 P. S. Lykoudis and Y. S. Touloukian, "Heat Transfer in Liquid Metals," TRANS. ASME, vol. 80, 1958, pp. 653–667.

12 R. N. Lyon, "Forced Convection Heat Transfer Theory and Experiments With Liquid Metals," Report ORNL-361, Technical Division, Engineering Research Station, Oak Ridge National Laboratory, Oak Ridge, Tenn., 1949.

13 R. N. Lyon, editor, "Liquid Metals Handbook," second edition, Atomic Energy Commission and Department of the Navy, 1952.

14 R. C. Martinelli, "Heat Transfer to Molten Metals," TRANS. ASME, vol. 69, 1947, pp. 947–959.

15 M. A. Mikheyev, V. A. Baum, K. D. Voskresensky, and O. S. Fedynsky, "Heat Transfer to Liquid Metals," Proceedings of the International Conference on the Peaceful Uses of Atomic Energy, vol. 9, Reactor Engineering and Chemical Processing, United Nations, New York, N. Y., 1956, pp. 285–289.

16 I. I. Novikov, A. N. Solovyev, E. M. Khabakhasheva, V. A. Grusdev, A. I. Pridantsev, and M. Y. Vasenina, "Heat Transfer Performance and Physical Properties of Molten Alkali Metals," *Atomnaya Energiya*, vol. 1, 1956, pp. 92–106.

17 W. Nusselt, "Der Einfluss der Gastemperatur auf den Warmeubergang im Rohr," *Technische Mechanik und Thermodynamik*, vol. 1, 1930, pp. 227–290.

18 L. McG. Trefethen, "Heat Transfer Properties of Liquid Metals," Report NP-1788, U. S. Atomic Energy Commission, Technical Information Service, Oak Ridge, Tenn., 1950.

19 R. Viskanta, "Heat Transfer to Liquid Metals With Variable Properties," MS thesis, School of Mechanical Engineering, Purdue University, Lafayette, Ind., 1956.

20 T. von Karman, "The Analogy Between Fluid Friction and Heat Transfer," TRANS. ASME, vol. 61, 1939, pp. 705–710.

DISCUSSION

Richard N. Lyon[10]

It has been pointed out in reference [12] and in a subsequent paper [21][11] that if σ is independent of the distance from the wall but not equal to unity, the approximate equation referred to in those references should be written:

$$N_{Nu} = 7 + 0.025\,(\sigma N_{Pe})^{0.8} \tag{22}$$

When this equation is plotted as N_{Nu} versus σN_{Pe}, it is found, as expected, that it is in substantial agreement with similar plots of the results of this paper for $\beta = 0$ and those of Lykoudis and Touloukian [11]. Since the last two agree well with many experimental data, Equation (22) does too.

In 1955, Lubarsky and Kaufman [22] proposed a purely empirical relationship which appeared to generalize a large fraction of the liquid metal heat-transfer data available at that time:

$$N_{Nu} = 0.625\,(N_{Pe})^{0.4} \tag{23}$$

It is interesting to note that when equation (23) is plotted as $\log N_{Nu}$ versus $\log (\sigma N_{Pe})$ for the approximate limits in N_{Pr} for most liquid metals, $N_{Pr} = 0.005$ or $\sigma = 0.08$ and $N_{Pr} = 0.025$ or $\sigma = 0.43$, the two lines straddle the curves representing the results of this paper, the results of Lykoudis and Touloukian, and equation (22). It appears then that the straight line predicted by Lubarsky and Kaufman is partly the result of a fortuitous increase in N_{Pr}, and hence in σ, when experimenters obtained data at the higher values of N_{Pe}.

[10] Oak Ridge National Laboratory, Oak Ridge, Tenn.

[11] Numbers [21] and [22] designate References at end of this discussion.

The authors of the present paper are to be congratulated for settling another uncertainty in the theory of liquid metal heat transfer. Their work, together with that of Deissler [2], Lykoudis and Touloukian [11], and others on the eddy diffusivity of heat, rounds out reasonably well our understanding of the case of constant heat flow in liquid metals far from the entrance of a round tube.

One notable exception remains: the low N_{Pe} region. The models used in the current theory do not permit a value of N_{Nu} below about 6.75 in turbulent flow, yet reliable experimenters report such values. In the view of the discusser, the superimposed effect of natural convection at low turbulent values of N_{Re}, particularly in heavy liquids such as lead-bismuth and mercury, may be a principal cause of the discrepancy.

The model employed by the authors of the present paper is a fine beginning in the theoretical determination of the influence of radial heat flow on liquid metal heat transfer. The next logical phase appears to be a study of the distortion of the velocity and temperature distribution as a result of superimposed natural convection, and a determination of the influence such distortions have on an average heat-transfer coefficient defined in terms which are compatible with the conditions of the experiments at low values of N_{Re}.

References

21 R. N. Lyon, "Liquid Metal Heat Transfer Coefficients," *Chemical Engineering Progress*, vol. 47, 1951, pp. 75–79.

22 B. Lubarsky and S. J. Kaufman, "Review of Experimental Investigations of Liquid Metal Heat Transfer," NACA TN 3336, March, 1955.

E. M. Sparrow[12]

The authors are to be commended on their meaningful efforts in clarifying the effects of variable fluid properties on liquid metal heat transfer. In connection with the analysis, it may be worth while to discuss briefly some aspects of the velocity distribution. Equation (3) governs the velocity distribution. Since ν/ν_w depends on temperature, equation (6), it would be expected that the velocity distribution would be influenced by the temperature distribution. In such a circumstance, simultaneous solution of the velocity and temperature equations (3) and (4), respectively, would appear to be indicated. In view of this, it is somewhat surprising that equation (3) is set aside and that the velocity profile is evaluated from von Karman's expressions, which are normally associated with a constant property flow.

As noted in the paper, the velocity profile can have a marked effect on the Nusselt number results. It would therefore be appreciated if the authors would explain more fully their treatment of the velocity distribution and, if possible, estimate the changes in their Nusselt numbers which could result if the velocity were obtained by simultaneous solution of the governing conservation equations.

Authors' Closure

The authors wish to thank Dr. Lyon and Professor Sparrow for their interest and comments on this paper.

The point Dr. Lyon raises in regards to the superimposed effect of natural convection at low Reynolds numbers is well taken. One should be able to observe this effect experimentally by directing the flow upward and downward. However, Johnson, et al.,[13] who performed experiments on mercury at Reynolds num-

[12] Professor of Mechanical Engineering, University of Minnesota, Minneapolis, Minn. Assoc. Mem. ASME.

[13] H. A. Johnson, W. J. Clabaugh, and J. P. Hartnett, "Heat Transfer to Mercury in Turbulent Pipe Flow," TRANS. ASME, vol. 76, 1954, pp. 505–511.

bers as low as 11,000, found no noticeable effect on the heat transfer with the direction of flow. Even though such studies are of limited scope, the authors are of the opinion that the superimposed effect of natural convection is not the principal cause of discrepancy between the theory and reliable experiments at low Peclet numbers.

Concerning the discussion of Professor Sparrow, the authors agree that the velocity distribution would be influenced by the temperature distribution, through ν/ν_w. For that matter, the temperature gradient also could play an important role as seen from equation (24). Coupling the equations of momentum and energy through the ratio of eddy diffusivities of momentum and heat transfer, we obtain

$$\frac{du^*}{dy^*} = \frac{\left(1 - \frac{y^*}{r_0^*}\right)\left(\frac{\rho_w}{\rho}\right)}{\left\{\left(\frac{\nu}{\nu_w}\right) + \frac{1}{\sigma}\left[\frac{\left(1 - \frac{y^*}{r_0^*}\right)\left(\frac{\rho_w}{\rho}\right)\left(\frac{c_{pw}}{c_p}\right)}{\frac{dt^*}{dy^*}} - \frac{1}{N_{Pr}}\left(\frac{\nu}{\nu_w}\right)\right]\right\}} \quad (24)$$

and

$$\frac{dt^*}{dy^*} = \frac{\left(1 - \frac{y^*}{r_0^*}\right)\left(\frac{\rho_w}{\rho}\right)\left(\frac{c_{pw}}{c_p}\right)}{\left\{\frac{1}{N_{Pr}}\left(\frac{\nu}{\nu_w}\right) + \sigma\left[\frac{\left(1 - \frac{y^*}{r_0^*}\right)\left(\frac{\rho_w}{\rho}\right)}{\frac{du^*}{dy^*}} - \left(\frac{\nu}{\nu_w}\right)\right]\right\}} \quad (25)$$

Attempts were made to solve equations (24) and (25) simultaneously, but had to be abandoned because of the difficulty inherent in these equations. Since at the wall $\sigma = 0$, the velocity gradient becomes 1 and the temperature gradient is equal to N_{Pr}. Using these values as the starting point and proceeding with the numerical integrations, one finds unreasonable values of the velocity gradient. The reason for this is that the terms $\left[\left(1 - \frac{y^*}{r_0^*}\right)\left(\frac{\rho_w}{\rho}\right)\left(\frac{c_{p_w}}{c_p}\right)\Big/\frac{dt^*}{dy^*}\right]$ and $\frac{1}{N_{Pr}}\left(\frac{\nu}{\nu_w}\right)$ in the denominator of equation (24) are of the same order of magnitude. Attempts to rearrange the equations as well as using smaller increments of integration were of no avail and it was impossible to obtain results of reasonable accuracy for the velocity distribution. Therefore the authors felt that it was justifiable to use a velocity profile which has been substantiated experimentally, even though only for the nonvariable property case, than to calculate one.

W. C. REYNOLDS[1]
W. M. KAYS[2]
S. J. KLINE[3]

A Summary of Experiments on Turbulent Heat Transfer From a Nonisothermal Flat Plate

The results of an extensive experimental investigation of heat transfer to a turbulent incompressible boundary layer from a nonisothermal flat plate are summarized. Data presented extend the range of low-Mach-number confirmation of the von Karman analogy to Reynolds numbers of 4×10^6 for an isothermal plate. Data for a step wall-temperature distribution confirm experimentally the preferable expression for this important superposition kernel case. Data from a variety of other examples confirm the use of the superposition theories to predict heat transfer from nonisothermal surfaces.

It is well known that the heat flux from a point on a heated surface depends upon three things: (*a*) The flow conditions; (*b*) the local wall-to-fluid temperature difference; and (*c*) the wall-temperature distribution upstream of the point in question. The influence of these effects upon the convection conductance has been the subject of numerous investigations. However, because of the infinitely many ways in which the surface temperature can vary, most studies have been restricted to relatively simple temperature distributions, with the bulk of all data being gathered for the special case of an isothermal surface. It has been pointed out by several authors [1, 2][4] that for incompressible flow over a flat plate the linearity of the boundary-layer energy equation allows the use of superposition techniques. The necessary kernel function, or superposition base, is given by the heat-transfer conditions which prevail when the front portion of the plate is unheated, i.e., held isothermal at the free-stream fluid temperature, and the remainder of the plate is heated such as to be maintained at a different temperature. For turbulent flow, a number of analyses for this *step wall-temperature*-distribution case have been made [2–6], and some experimental studies have been conducted [3, 6, 7]. For the special case under consideration (turbulent incompressible flow in zero pressure gradient), the various analyses lead to one of two forms. The earliest analysis, due to Rubesin, indicated that the local heat-transfer conductance downstream from the unheated starting length is given by

$$\mathrm{St}/\mathrm{St}_T = [1 - (l/x)^{9/8}]^{-1/9} \qquad (1a)$$

Independent analyses due to Seban [3], Sibulkin [4], Ferrari [5], and the present authors [6] yielded essentially identical results, and indicated that the local coefficients are given by

$$\mathrm{St}/\mathrm{St}_T = [1 - (l/x)^{9/10}]^{-1/9} \qquad (1b)$$

Here St_T denotes the Stanton number which would obtain if the plate were isothermal over its full length. Either of these two results may be used in superposition to predict heat flux for arbitrary wall-temperature cases, but the results of such predictions often differ substantially. An extensive experimental study of this problem was begun at Stanford University in 1954 under the sponsorship of the NACA. This work is described in detail elsewhere [6, 8, 9, 11]; the present paper is intended as a summary of the results and conclusions of these experiments.

Description of Apparatus and Techniques

The plate used in this investigation had an active flow length of 60.5 in. and was tested in the 7.5-ft-diameter free-jet wind tunnel at the Guggenheim Aeronautical Laboratory of Stanford University. Reynolds numbers up to 3.5×10^6 could be obtained with air velocities up to 130 fps.

[1] Assistant Professor, Department of Mechanical Engineering, Stanford University, Stanford, Calif. Mem. ASME.
[2] Professor, Department of Mechanical Engineering, Stanford University, Stanford, Calif. Mem. ASME.
[3] Associate Professor, Department of Mechanical Engineering, Stanford University, Stanford, Calif. Mem. ASME.
[4] Numbers in brackets designate References at end of paper.
Contributed by the Heat Transfer Division and presented at the Annual Meeting, Atlantic City, N. J., November 29–December 4, 1959, of The American Society of Mechanical Engineers.
Note: Statements and opinions advanced in papers are to be understood as individual expressions of their authors and not those of the Society. Manuscript received at ASME Headquarters, August 12, 1959. Paper No. 59—A-157.

Nomenclature

c_p = specific heat at constant pressure, Btu/lb deg F
G = mass velocity, $G = \rho u_\infty$, lb/(hr sq ft)
h = local convective heat-transfer coefficient, $h = q''/\Delta t$, Btu/(hr sq ft deg F)
l = unheated starting length, ft
Pr = Prandtl number, $\mathrm{Pr} = \mu c_p/k$
q'' = convective heat flux from wall, Btu/(hr sq ft)
Re_l = Reynolds number based on l, $\mathrm{Re}_l = Gl/\mu$
Re_x = Reynolds number based on x, $\mathrm{Re}_x = Gx/\mu$
St = local Stanton number, $\mathrm{St} = h/(Gc_p)$
St_T = local Stanton number for conditions of constant wall temperature
T_w = wall temperature, deg R
T_∞ = free-stream temperature, deg R
Δt = local temperature difference ($T_w - T_\infty$), deg F
u_∞ = free-stream velocity, fps
x = distance from leading edge, ft
ρ = density, pcf
μ = viscosity, lb/(hr ft)
ξ = variable of integration, ft

The active surface of the plate, shown in Fig. 1, was built up of 24 individually heated copper strips thermally insulated from each other. Electric-strip heaters were soldered to the back side of each of the copper strips. Each heater was separately controlled so that the temperature or heat flux from each of the copper strips could be varied independently. The surface was varnished and rubbed down several times to give a hydraulically smooth surface. The inactive side of the plate was well insulated so that the "back leak" was minimized. Heat meters were installed at several places on both the inactive side and at the ends of the heated strips to measure the back leak and end leak (2–5 per cent of power input). The emissivity of the heated surface was measured in order that radiation from this surface could be determined (5 per cent of power input). The insulation between the various strips provided a heat meter for evaluation of conduction between strips (very small, except at discontinuities).

Iron-constantan thermocouples were located near the surface at the center of each strip and at several other points in the plate. The thermocouples were referenced to a small copper plate mounted to one side of the heated surface; the reference plate in turn was referenced to distilled-water ice. This arrangement provided for a direct measurement of the surface-to-air temperature difference. Pressure taps located at several points on the active surface allowed measurement of static pressure on the flat plate, and a pitot tube was used to measure free-stream velocity. A watt meter was used to determine the power dissipated by each heater.

Because of the plate configuration, the strip-center temperatures were somewhat higher than their average temperatures. An analysis for the mean surface temperature in terms of the center temperature was made. The analysis (approximately a 13 per cent correction) was checked by measurement of the transverse temperature distribution, which was then integrated to give the mean temperature difference. Good agreement with the analysis was obtained.

Fig. 1 shows the plate prior to installation in the wind tunnel. Note that the heated strips are wider near the front than near the rear; this is to minimize contamination of the hot boundary layer by sidewise mixing with the cold boundary layers on the unheated portions. Fig. 2 shows the plate installed in the wind tunnel (looking upstream). The thermocouple, power, and pressure leads can be seen coming from the sides of the plate.

Prior to testing, the attitude of the plate was adjusted to approximate closely a uniform pressure distribution. Over the turbulent portion of the plate, the maximum static-pressure variation was less than 2 per cent of the dynamic pressure. Because of the presence of a large flow straightener upstream of the test section, the free-stream turbulence intensity over the plate was of the order of 2 per cent.[5] However, in view of the results of a recent study [10], it is felt that the influence of the free-stream turbulence is negligible compared to the nonisothermal effects investigated. Transition was stimulated artificially near the leading edge of the plate by a strip of scotch tape, and the boundary layer was fully turbulent over all but the first few strips. A study of the effect of transition-point location [11] indicated that the virtual origin of the boundary layer was essentially coincident with the leading edge of the plate, and all Reynolds numbers were computed using the length from the leading edge to the centers of the strips. Temperature differences not exceeding 50 deg F were employed, so that the effects of fluid-properties variations would be minor.

An analysis of the experimental uncertainty in the data indicates that the probable error in the local Stanton and Reynolds numbers are ±3 and ±1 per cent, respectively. These values are in agreement with the standard deviation of the data from the line of best fit.

Experimental Results

Isothermal Plate. An initial series of data was obtained for an isothermal plate [8]. Surprisingly, there are few experimental heat-transfer data in the literature for the turbulent flat-plate boundary layer, except at comparatively low Reynolds numbers where transition effects are uncertain, or at high Mach numbers where compressibility and large temperature-difference effects have considerable influence. The present data, Fig. 3, extend the range of available low Mach-number, heat-transfer data to Reynolds numbers up to 4,000,000. The local Stanton numbers, corrected for fluid-properties variations by the factor $(T_w/T_\infty)^{0.4}$ (see [8], this correction amounts to only 3–4 per cent) are plotted versus the local Reynolds numbers. The data compare very well with the von Karman analogy[6] when the data of Schultz-Grunow

[5] Determined by hot-wire measurements.

[6] Based on similarity of heat flux and shear distribution in turbulent core, equal eddy diffusivities, using three region universal velocity profile.

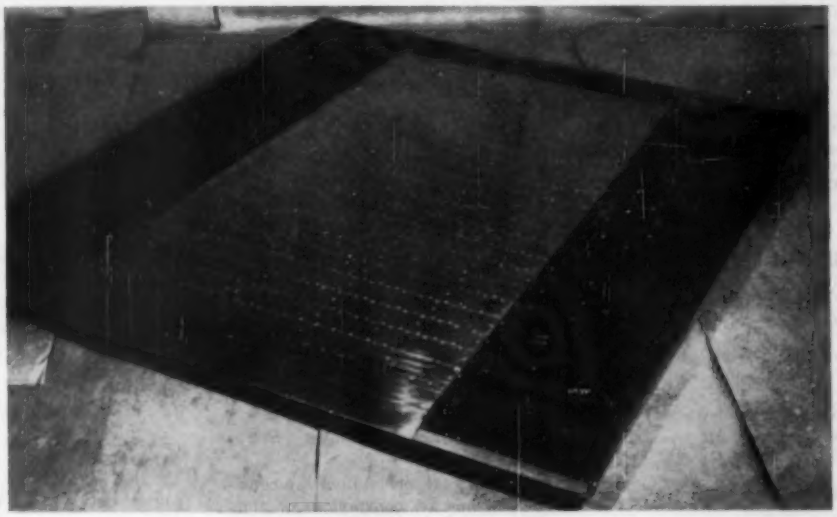

Fig. 1 Flat plate before mounting

are used to evaluate the local friction factors [8]. Over the Reynolds number range of interest, both the analogy and the data are represented very well by the simple expression

$$St_T Pr^{0.4}(T_w/T_\infty)^{0.4} = 0.0296\ Re_x^{-0.2} \qquad (2)$$

Again the subscript T is used to denote the Stanton numbers for the isothermal plate.

It is interesting to note that Equation (2) is similar to the familiar Colburn equation, except that the exponent to the Prandtl number is 0.4 rather than 2/3. For a Prandtl number of 0.7, the Colburn equation will overpredict the Stanton number by 10 per cent. The 0.4 exponent was chosen on the basis of Prandtl number effect in the von Karman analogy in the range $0.6 < Pr < 1$. It is further worth noting that the von Karman analogy is based on equality of momentum and thermal diffusivities, and the experimental data would indicate that either this assumption is adequate for Prandtl numbers near unity, or else there are other compensating effects.

Step Wall-Temperature Distribution. The local Stanton numbers for the step wall-temperature-distribution runs are shown in Fig. 4. Note that the data differ markedly from the isothermal correlation discussed previously. Near the temperature step, the departure from the isothermal Stanton-number line is quite large, with the heat transfer being of the order of 50 per cent higher than predicted using the isothermal conductance from Equation (2). Downstream from the step, the heat transfer gradually approaches that which would be predicted from (2); this is fully as expected, for the boundary layer eventually "forgets" that it ever had an unheated starting length.

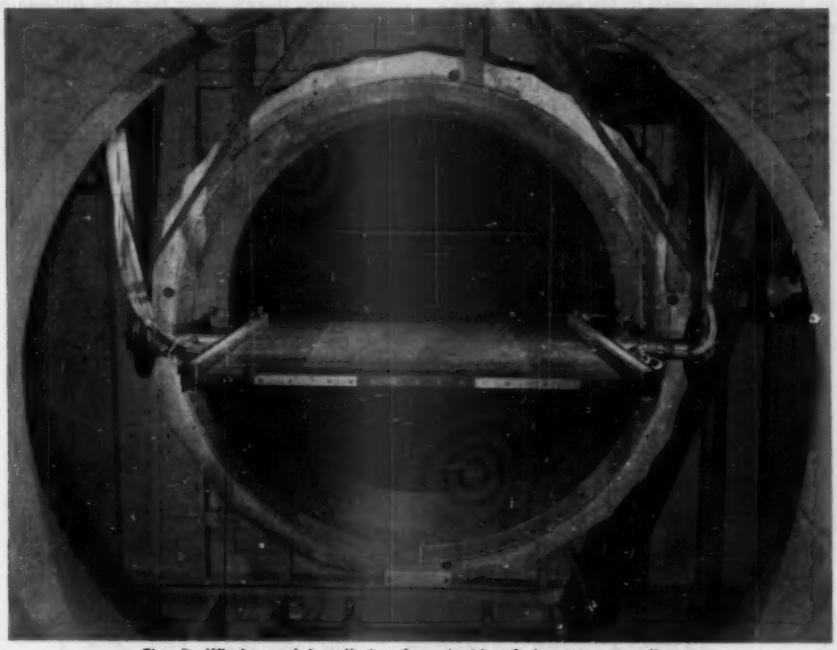

Fig. 2 Wind-tunnel installation from inside of downstream collector

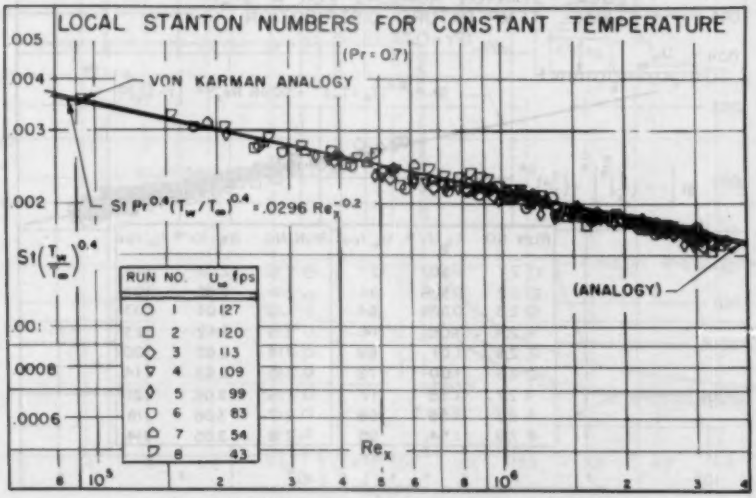

Fig. 3 Local Stanton numbers for an isothermal plate

As shown in reference [6], the step-function data are in best agreement with the correction given by Equation (1*b*). The earlier Rubesin correction, (1*a*), predicts heat fluxes which are too high. The Rubesin correction has been used extensively for some time, but the data show that Equation (1*b*) is definitely better. This will be demonstrated by comparisons of nonisothermal data and predictions. The correlation of the step-function data by Equation (1*b*) is shown in Fig. 5 and is seen to be excellent.

Before any conclusion is drawn regarding the preferability of (1*b*) over (1*a*), some discussion of other data is warranted. An experimental study by Scesa [3] was used as the basis for Rubesin's semiempirical analysis. Scesa's data were obtained on a relatively small plate, and as a result he was not able to obtain data as close to the step as could be obtained with the apparatus used in the present study. The difference between the two corrections, (1*a*) and (1*b*), is relatively small in the region of Scesa's data, and therefore his data are not too useful in distinguishing between the two suggested corrections. However, some recent data reported by Eichhorn, Eckert, and Anderson [7] also favor the latter correction, and are in good agreement with the data from the present study.

In the light of all available evidence, the authors conclude that the best available step-function correction is that given by Equation (1*b*), which will henceforth be referred to as the Seban correction.

Nonisothermal Examples. A number of tests with nonuniform wall temperature were performed [9]. Some of the more interesting data are shown in Figs. 6 to 9. An excellent description of the superposition methods is presented by Eckert and Drake [14].

Fig. 6 shows a case in which the wall temperature increased linearly after a step at the leading edge. The measured heat fluxes are compared with the predictions of nonisothermal superposition theory, using both the Rubesin and Seban kernel functions. In addition, the heat fluxes predicted from the iso-

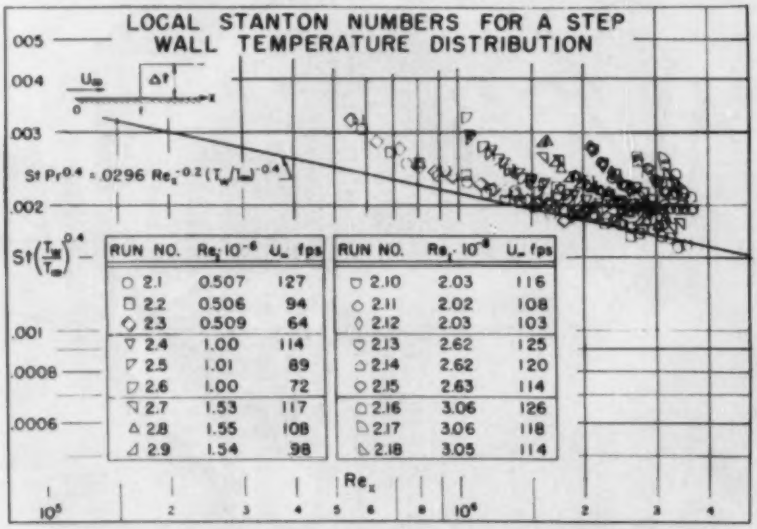

Fig. 4 Local Stanton numbers for a step wall-temperature distribution

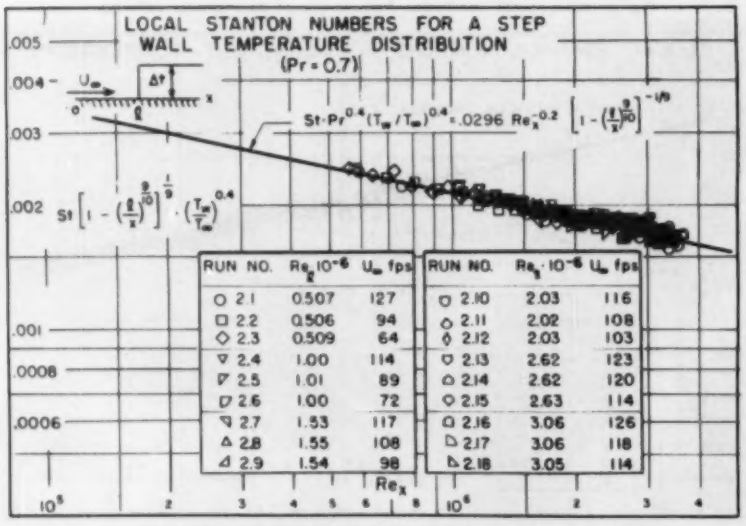

Fig. 5 Correlated local Stanton numbers for a step wall-temperature distribution

thermal Equation (2), using the local temperature differences, are shown. Note that the Rubesin prediction is slightly high, the isothermal prediction slightly low, and the Seban prediction quite satisfactory.

Fig. 7 shows a case for which the isothermal equation is completely inadequate; namely, that of an insulated surface downstream of an isothermal surface. The measured temperatures along the adiabatic portion of the plate are compared with the two predictions. With the exception of the first point on the insulated portion, the agreement with the Seban prediction is quite satisfactory, and the Rubesin prediction is high. The poor agreement of the first point is due to the fact that the first unheated strip receives some heat by conduction from the last heated strip, and therefore has a higher temperature than if it were truly adiabatic. Note that the isothermal conductance given in Equation (2) would predict an instantaneous decay of the wall temperature and a zero temperature difference downstream on all of the adiabatic portion.

Fig. 8 shows an example in which the heat flux was specified, rather than the wall temperature. Here the superposition theory allows prediction of the wall-temperature variation. The heat-flux distribution was essentially a double pulse, as shown in Fig. 8. The temperatures predicted by the Seban kernel are in good agreement with the measured temperatures. Again the predictions using the isothermal conductance are inadequate, with a zero temperature difference being predicted between the pulses.

Fig. 9 shows an example in which the plate was heated in an arbitrary manner. The temperature distribution was approximated by a series of steps and ramps, as shown, and the corresponding heat-flux distribution computed using the Seban kernel.

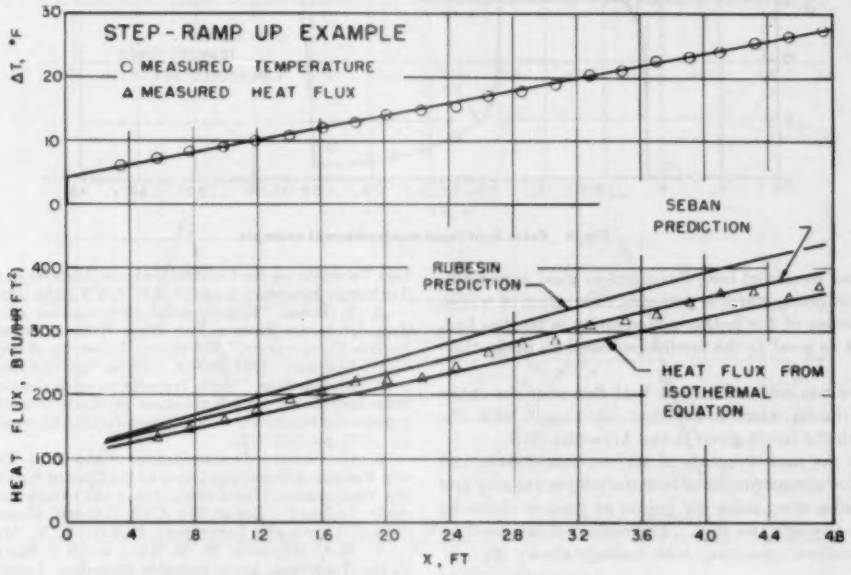

Fig. 6 Step-ramp up nonisothermal example

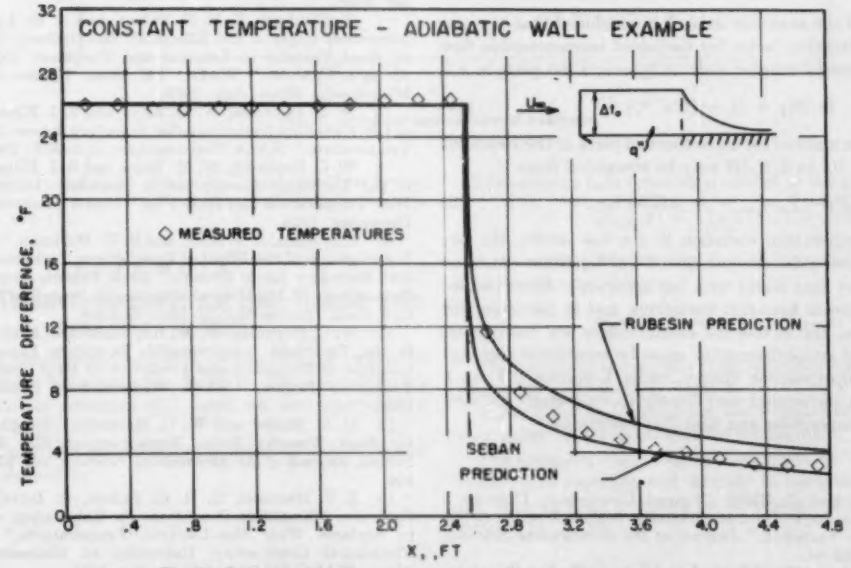

Fig. 7 Constant temperature-adiabatic wall nonisothermal example

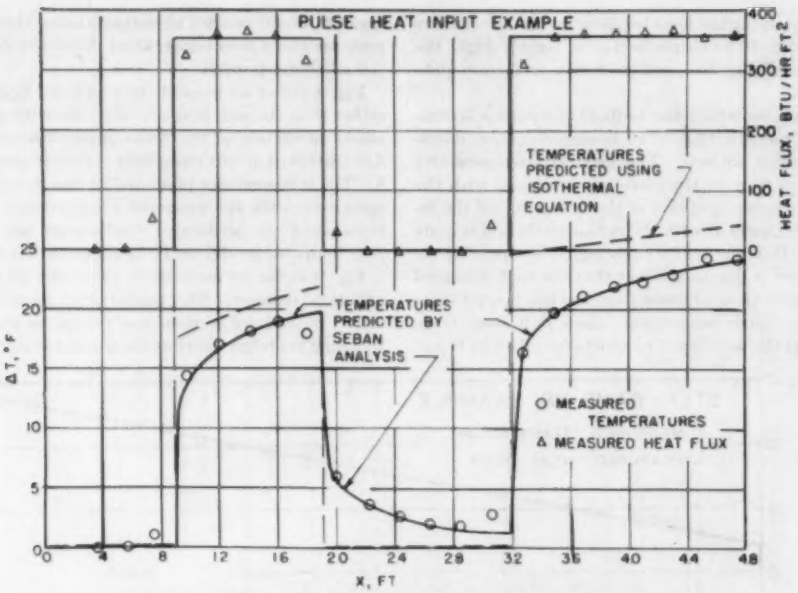

Fig. 8 Pulse heat-input nonisothermal example

The predicted and measured heat fluxes are in good agreement, except for the first point, which is probably in a region of transition. The prediction of the isothermal equation is not too bad, but certainly not as good as the prediction based on nonisothermal theory.

Tests also were run with a constant heat flux over the entire plate, and the results were in excellent agreement with the theory; e.g., with the result given in the Appendix [9].

In addition to the measurements of surface temperature and heat flux, extensive measurements of boundary-layer velocity and temperature profiles were made for points at various distances behind a surface temperature step. The measured temperature profiles are in excellent agreement with analogy theory [6].

Conclusions

On the basis of the available data, it is concluded that the best step-function correction factor for turbulent incompressible flow for fluids with Prandtl number near unity over a flat plate is

$$St/St_T = [1 - (l/x^{9/8})]^{-1/9} \qquad (1b)$$

The local Stanton number for an isothermal plate in the Reynolds number range of 10^6 to 4×10^6 may be computed from

$$St_T Pr^{0.4}(T_w/T_\infty)^{0.4} = 0.0296\ Re_x^{-0.2} \qquad (2)$$

If the wall-temperature variation is not too severe, the isothermal convective conductances, given by Equation (2), may be used to predict heat fluxes with fair accuracy. However, for severe temperature or heat-flux variations, and in particular for insulated surfaces, the isothermal conductances are inadequate, and the effects of nonisothermality must be considered (see Appendix). The superposition theory, using Equation (1*b*) as a base, is shown to correspond very closely to experiment for very severe surface temperature and heat-flux variations.

References

1 M. Tribus and J. Klein, "Forced Convection Through a Laminar Boundary Layer Over an Arbitrary Surface With an Arbitrary Temperature Variation," *Journal of the Aeronautical Sciences*, vol. 22, 1955, pp. 62–64.

2 M. W. Rubesin, "The Effect of an Arbitrary Surface Temperature Variation on the Convective Heat Transfer in an Incompressible Turbulent Boundary Layer," NACA TN 2345, April, 1951.

3 S. Scesa, "Experimental Investigation of Convective Heat Transfer to Air From a Flat Plate With a Stepwise Discontinuous Surface Temperature," MS thesis, University of California, Berkeley, Calif., February, 1951 (Seban analysis reported here).

4 M. Sibulkin, "Heat Transfer to an Incompressible Turbulent Boundary Layer and Estimation of Heat Transfer Coefficients at Supersonic Nozzle Throats," *Journal of the Aeronautical Sciences*, vol. 23, 1956, pp. 162–172.

5 C. Ferrari, "Determination of the Heat Transfer Properties of a Turbulent Boundary Layer in the Case of Supersonic Flow When the Temperature Distribution Along the Constraining Wall Is Arbitrarily Assigned," Report No. CAL/GM-807, Contract NOrd-14523, Cornell Aeronautics Laboratory, Buffalo, N. Y., March, 1954.

6 W. C. Reynolds, W. M. Kays, and S. J. Kline, "Heat Transfer in the Turbulent Incompressible Boundary Layer, II—Step Wall-Temperature Distribution," NASA Memorandum 12-2-58W, December, 1958.

7 R. Eichhorn, E. R. G. Eckert, and A. D. Anderson, "An Experimental Study of the Effects of Non-Uniform Wall Temperature on Heat Transfer in Laminar and Turbulent Axisymmetric Flow Along a Cylinder," WADC TR 58-33, University of Minnesota, Minneapolis, Minn., July, 1958.

8 W. C. Reynolds, W. M. Kays, and S. J. Kline, "Heat Transfer in the Turbulent Incompressible Boundary Layer, I—Constant Wall Temperature," NASA Memorandum 12-1-58W, December, 1958.

9 W. C. Reynolds, W. M. Kays, and S. J. Kline, "Heat Transfer in the Turbulent Incompressible Boundary Layer, III—Arbitrary Wall Temperature and Heat Flux," NASA Memorandum 12-3-58W, December, 1958.

10 S. J. Kline, A. V. Lisin, and B. W. Waitman, "An Experimental Investigation of the Effect of Free Stream Turbulence on the Turbulent Boundary Layer Growth," Final Report, Contract NAw-6500, Department of Mechanical Engineering, Stanford University, Stanford, Calif. (Report MD-2), May 15, 1958.

11 W. C. Reynolds, W. M. Kays, and S. J. Kline, "Heat Transfer in the Turbulent Incompressible Boundary Layer, IV—Effect of Location of Transition and Prediction of Heat Transfer in a Known Transition Region," NASA Memorandum 12-4-58W, December, 1958.

12 D. C. Baxter and W. C. Reynolds, "Fundamental Solutions for Heat Transfer From Nonisothermal Flat Plates," Readers Forum, *Journal of the Aeronautical Sciences*, vol. 25, 1958, pp. 403–404.

13 J. P. Hartnett, E. R. G. Eckert, R. Birkebak, and R. L. Sampson, "Simplified Procedures for Calculation of Heat Transfer to Surfaces With Non-Uniform Temperatures," Department of Mechanical Engineering, University of Minnesota, Minneapolis, Minn., WADC TR 56-373, December, 1956.

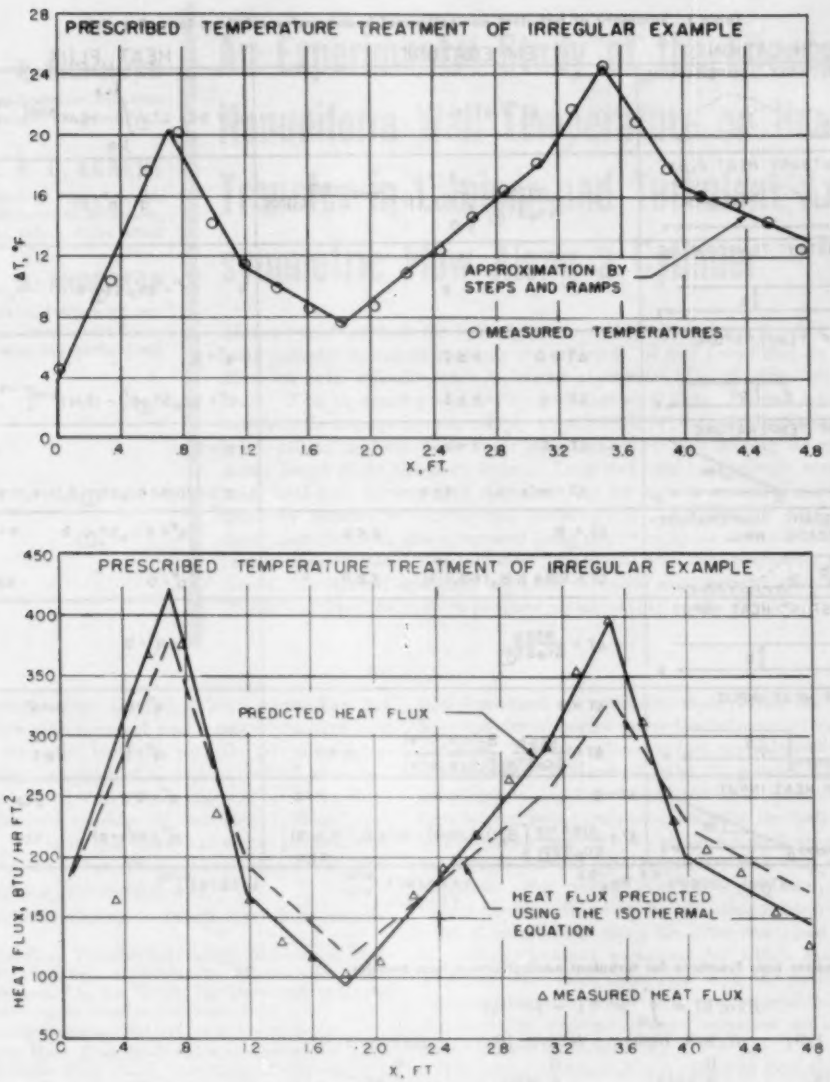
PRESCRIBED TEMPERATURE TREATMENT OF IRREGULAR EXAMPLE
ΔT, °F
X, FT
APPROXIMATION BY STEPS AND RAMPS
O MEASURED TEMPERATURES
PRESCRIBED TEMPERATURE TREATMENT OF IRREGULAR EXAMPLE
HEAT FLUX, BTU/HR FT²
X, FT
PREDICTED HEAT FLUX
HEAT FLUX PREDICTED USING THE ISOTHERMAL EQUATION
Δ MEASURED HEAT FLUX

Fig. 9 Irregular nonisothermal example

14 E. R. G. Eckert and R. M. Drake, Jr., "Heat and Mass Transfer," second edition, McGraw-Hill Book Company, Inc., New York, N. Y., 1959, pp. 179–183.

APPENDIX

Summary of Turbulent Nonisothermal Heat-Transfer Solutions for a Flat Plate

The wall-temperature and heat-flux variations for a number of important cases are summarized in Table 1. These solutions are derived in detail in reference [9], based on the superposition theorems [1, 2, 14].

Some of the solutions are presented in terms of the *incomplete beta functions*, defined by

$$B_s(a, b) = \int_0^s s^{a-1}(1 - s)^{b-1} ds$$

The *complete* beta function is related to the gamma function by

$$B_1(a, b) = \Gamma(a)\Gamma(b)/\Gamma(a + b)$$

A convenient relation useful in shifting the arguments of the beta function is

$$B_s(a, b) = B_1(a, b) - B_{1-s}(b, a)$$

The pertinent incomplete beta functions have been computed [9], and are tabulated in Table 2.

Table 3 serves to illustrate the qualitative effects of nonisothermality on the heat-transfer coefficient.

The foregoing cases can be considered as "fundamental solutions," and superimposed directly in ramp-step approximations for heat-transfer calculations in nonisothermal problems, references [9, 12, 13, 14].

Table 1 Summary of turbulent nonisothermal heat-transfer solutions for a flat plate

SPECIFICATION	TEMPERATURE	HEAT FLUX
ARBITRARY TEMPERATURE 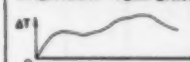	$\Delta T = \Delta T(x)$	$q'' = Gc_p S_{T_\textcircled{T}} \int_{\xi=0}^{\xi=x} \left[1 - (\xi/x)^{9/10}\right]^{-1/9} d\Delta T(\xi)$
ARBITRARY HEAT FLUX	$\Delta T = \frac{.0975/x}{Gc_p S_{T_\textcircled{T}}} \int_{\xi=0}^{\xi=x} \left[1 - (\xi/x)^{9/10}\right]^{-8/9} q''(\xi) d\xi$	$q'' = q''(x)$
CONSTANT TEMPERATURE 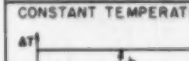	$\Delta T = b$	$q'' = Gc_p S_{T_\textcircled{T}} b$
STEP TEMPERATURE	$\Delta T = 0 \quad x \le \ell$ $\Delta T = b \quad x \ge \ell$	$q'' = 0 \quad x < \ell$ $q'' = Gc_p S_{T_\textcircled{T}} b\left[1 - (\ell/x)^{9/10}\right]^{-1/9} \quad x \ge \ell$
RAMP TEMPERATURE 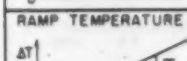	$\Delta T = 0 \quad x < a$ $\Delta T = m(x-a) \quad x \ge a$	$q'' = 0 \quad x < a$ $q'' = 1.111\, mx\, Gc_p S_{T_\textcircled{T}} B_r(8/9, 10/9) \quad x \ge a$
CONSTANT TEMPERATURE-ADIABATIC WALL 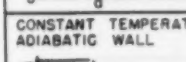	$\Delta T = b \quad x < a$ $\Delta T = .1084\, b\, B_s(8/9, 1/9) \quad x \ge a$	$q'' = G \cdot c_p S_{T_\textcircled{T}} b \quad x < a$ $q'' = 0 \quad x \ge a$
CONSTANT HEAT INPUT 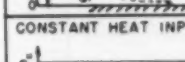	$\Delta T = \frac{.959\, b}{Gc_p S_{T_\textcircled{T}}}$	$q'' = b$
STEP HEAT INPUT 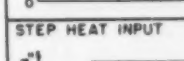	$\Delta T = 0 \quad x < \ell$ $\Delta T = \frac{.959\, b}{Gc_p S_{T_\textcircled{T}}} \frac{B_r(1/9, 10/9)}{B_s(1/9, 10/9)} \quad x \ge \ell$	$q'' = 0 \quad x < \ell$ $q'' = b \quad x \ge \ell$
RAMP HEAT INPUT 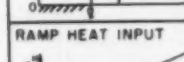	$\Delta T = 0 \quad x < a$ $\Delta T = \frac{.1084\, mx}{Gc_p S_{T_\textcircled{T}}} \left[B_r(1/9, 20/9) - (a/x) B_r(1/9, 10/9)\right] \quad x \ge a$	$q'' = 0 \quad x < a$ $q'' = m(x-a) \quad x \ge a$

$S_{T_\textcircled{T}} = .0296\, Pr^{-0.4}\, Re_x^{-0.2}$ $\quad r = 1 - (a/x)^{9/10} = 1 - (\ell/x)^{9/10}$ $\quad s = (a/x)^{9/10}$

Table 2 Incomplete beta functions for turbulent nonisothermal heat transfer

$$B_z(a, b) = \int_0^z s^{a-1}(1-s)^{b-1} ds$$

z	$B_z(8/9, 1/9)$	$B_z(8/9, 10/9)$	$B_z(1/9, 10/9)$	$B_z(1/9, 20/9)$
0	0	0	0	0
0.1	0.1518	0.1445	6.9604	6.8837
0.2	0.2948	0.2661	7.5087	7.3445
0.3	0.4457	0.3792	7.8447	7.5898
0.4	0.6109	0.4863	8.0886	7.7414
0.5	0.7971	0.5886	8.2796	7.8401
0.6	1.0151	0.6864	8.4357	7.9046
0.7	1.2833	0.7797	8.5664	7.9456
0.8	1.6412	0.8682	8.6772	7.9694
0.9	2.2089	0.9505	8.7702	7.9809
1.0	9.1853	1.0206	8.8439	7.9839

z	$B_z(1/9, 8/9)$	$B_z(1/9, 10/9)$	$B_z(1/9, 20/9)$
0	0	0	0
0.01	5.3960	5.3948	5.3887
0.02	5.8286	5.8260	5.8131
0.03	6.0979	6.0938	6.0735
0.04	6.2967	6.2910	6.2631
0.05	6.4555	6.4482	6.4125
0.06	6.5883	6.5794	6.5357
0.07	6.7029	6.6923	6.6406
0.08	6.8039	6.7916	6.7316
0.09	6.8943	6.8802	6.8119
0.10	6.9764	6.9604	6.8837

Table 3

Specification	$St\, Pr^{0.4}(T_w/T_\infty)^{0.4} Re_x^{0.2}$
Constant surface temperature	0.0296
Ramp temperature from leading edge	0.0336
Constant heat flux	0.0309
Ramp heat flux from leading edge	0.0342

R. EICHHORN
Assistant Professor, Princeton University, Princeton, N. J.

E. R. G. ECKERT
Professor and Director of Heat Transfer Laboratory, University of Minnesota, Minneapolis, Minn. Mem. ASME

A. D. ANDERSON
Lockheed Aircraft Corp., Missile and Space Division, Sunnyvale, Calif.

An Experimental Study of the Effects of Nonuniform Wall Temperature on Heat Transfer in Laminar and Turbulent Axisymmetric Flow Along a Cylinder[1]

Measurements of both the hydrodynamic and thermal characteristics of flow over an axial cylinder at subsonic speeds are reported. It was found that the boundary layer along an axial cylinder tends to become asymmetrical as it approaches the transition point. This asymmetry vanishes again in turbulent flow. For both laminar and turbulent flow, the average boundary-layer growth could be predicted by the standard flat-plate relationships, and simple methods were deduced for determining the effective hydrodynamic length of the boundary layers. Local and total heat-transfer measurements were made with both laminar and turbulent flow for various unheated starting lengths followed by linearly increasing wall temperatures. For laminar flow, agreement with theory was obtained, this agreement being improved by the Seban and Bond cylindrical curvature correction. The turbulent-flow results indicated preference for the theory of Seban. Isothermal equations represent turbulent heat transfer within approximately 20 per cent when the wall-temperature variations are not too abrupt.

THE relationships governing heat transfer to flat plates in uniform flow with constant wall temperature have long been established. Recently, however, with the advent of high-speed flight and other examples of a modern technological age, the design engineer is faced with a more exacting set of specifications and must perforce consider of importance effects once thought secondary. It is in this light that recent investigators have undertaken studies of the effects of nonuniform wall temperature on heat transfer in external flows.

For both laminar and turbulent-boundary-layer flows, calculation procedures are available which permit the determination of heat transfer to bodies under the influence of variable wall temperature. There have been, in fact, several excellent analyses, and a recent effort by Hartnett, et al. [2], parallel to this experimental investigation, has been completed which presents in a simplified form for the design engineer calculation methods for both laminar and turbulent flow. These calculation methods require analytical expressions for the heat transfer with a step wall-temperature variation. For neither flow have such expressions been obtained exactly. However, for the laminar boundary layer the results of calculations using the afore-mentioned methods applied to wall-temperature variations for which exact solutions are available show close agreement with the exact solutions. For turbulent-boundary-layer flow two semiempirical solutions for the step-type wall-temperature variation are available, that of Seban [3] and of Rubesin [4].

The first experimental investigations were those of Jakob and Dow [5] and Tessin and Jakob [6]. Both investigations were made in low-speed flow, and both used cylindrical test sections in axisymmetric flow. Unfortunately, only total heat-transfer measurements were made, and no strict accounting was taken of

[1] Publication of the Heat Transfer Laboratory, Mechanical Engineering Department, University of Minnesota, Minneapolis, Minn. This research was sponsored by the Wright Air Development Center and has been reported in more detail in Reference [1].[2]

[2] Numbers in brackets designate References at end of paper.

Contributed by the Heat Transfer Division and presented at the Annual Meeting, Atlantic City, N. J., November 29–December 4, 1959, of THE AMERICAN SOCIETY OF MECHANICAL ENGINEERS.

NOTE: Statements and opinions advanced in papers are to be understood as individual expressions of their authors and not those of the Society. Manuscript received at ASME Headquarters, August 12, 1959. Paper No. 59—A-151.

Nomenclature

a = cylinder radius
$b = 2\pi a$ = cylinder circumference
c_f = local skin-friction coefficient
$c_{f_{fp}}$ = local skin-friction coefficient, flat plate
h = local heat-transfer coefficient
h_{fp} = local heat-transfer coefficient, flat plate
k = thermal conductivity
L = heated length
$q(x)$ = local heat flux
$Q(x)$ = total heat flux
T = temperature
T_w = wall temperature
T_∞ = free-stream temperature
$dT_w/d\xi$ = wall temperature gradient
u = axial velocity
u_∞ = axial free-stream velocity
x = axial length
x_0 = hydrodynamic starting length (unheated)
y = normal distance from cylinder wall
Pr = Prandtl number
Re_x = Reynolds number, $u_\infty x/\nu$
G, H, S, R, M, N = tabulated integrals [2]
α = dimensionless axial length
δ = boundary-layer thickness
δ^* = boundary-layer displacement thickness
η = Blasius variable $\frac{y}{x}\left(\frac{u_\infty x}{\nu}\right)^{1/2}$
ξ = axial length
ν = kinematic viscosity
$\zeta = \frac{4}{9}\left(\frac{\nu x}{u_\infty}\right)^{1/2}$

the location of the transition point or the effect of the transverse curvature. Later measurements by Scesa [3] employed a flat plate with separately controlled ribbon-type heaters embedded in the surface. The results for step-type variations in wall temperature with various unheated starting lengths offered no firm support for either the turbulent-flow semiempirical analysis of Seban or that of Rubesin. Close inspection of Scesa's data, however, does reveal a slight preference for the analysis of Seban. In addition, more general types of wall-temperature variation were not investigated. No investigation heretofore reported has included measurements with laminar boundary layers.

It was, therefore, felt that a more complete study was warranted; one which would allow careful measurement and control of local wall temperature and heat flux, and at the same time permit a careful study of the hydrodynamic boundary layer so that questions of effective starting length could be answered.

The study described herein reports the heat-transfer results obtained on a cylinder in axial flow with nonuniform wall temperature. Careful measurements of the unheated boundary layers were made prior to the bulk of the heat-transfer investigation. The nonuniform wall temperatures reported involve unheated starting lengths followed by a linearly increasing wall temperature. The selection of this type of wall-temperature variation was dictated by the desirability of having the nonuniform wall-temperature effects continue undiminished in a downstream direction. In addition, corrections for conduction in the walls are then not required. All measurements reported herein were made in air (Pr = 0.7), the Reynolds number range covered was from 0.15×10^6 to 2.5×10^6.

After the completion of the bulk of the work described in this paper, it was found that a similar investigation was under way at Stanford University. A report on the latter work has since become available [7]. In the areas in which both investigations overlap, the results are compatible. More recently, a paper by Sogin [16] has appeared which considers laminar flow over ablating surfaces.

Experimental Apparatus

The Wind Tunnel. All experiments were conducted in the low-speed, low-turbulence wind tunnel of the Heat Transfer Laboratory, Mechanical Engineering Department, University of Minnesota. A schematic diagram of the wind tunnel is shown in Fig. 1. The test section of the wind tunnel is 12 in. by 24 in. in cross section and is 30 in. long. Test section speeds between 60 and 170 fps are possible. Upstream of the test section are mounted eight turbulence damping screens followed by a contraction section of area ratio 15 to 1. The turbulence level (ratio of root-mean-square fluctuation velocity to mean velocity) is less than 0.16 per cent at tunnel speeds up to 140 fps. Local variation in mean velocity, excluding side-wall boundary layers, is less than 1 per cent at all speeds. Due to developing side-wall boundary layers, the mean flow velocity increases about 2 per cent over the length of the test section. The length Reynolds number of natural transition is above 10^6.

The Test Model. A cylinder mounted axially in the wind-tunnel test section was selected for this study since the troublesome edge effects associated with flat plates can in this way be avoided. The effects of transverse curvature and the possibility of asymmetry of the boundary layer are considered in the text which follows.

A schematic diagram of the experimental model is shown in Fig. 2. The model consists basically of two parts, the outer shell, and the internal heater.

The shell is constructed of stainless-steel type 304 tubing nominal 2-in. OD by 0.05-in. wall thickness, 40-in. length. The shell was first normalized to relieve internal stresses and then lapped to a diameter of 2.002 ± 0.001. Eighteen circumferential slots $^1/_8$ in. wide and $^1/_2$ in. long were milled in the surface to receive thermocouples for surface-temperature measurement. The slots are so arranged on the model surface that no thermocouple is axially in a direct line with any other thermocouple. Iron-constantan, inconel-sheathed thermocouples were used and were calibrated in a constant-temperature bath prior to installation. The thermocouples were installed through holes drilled in the

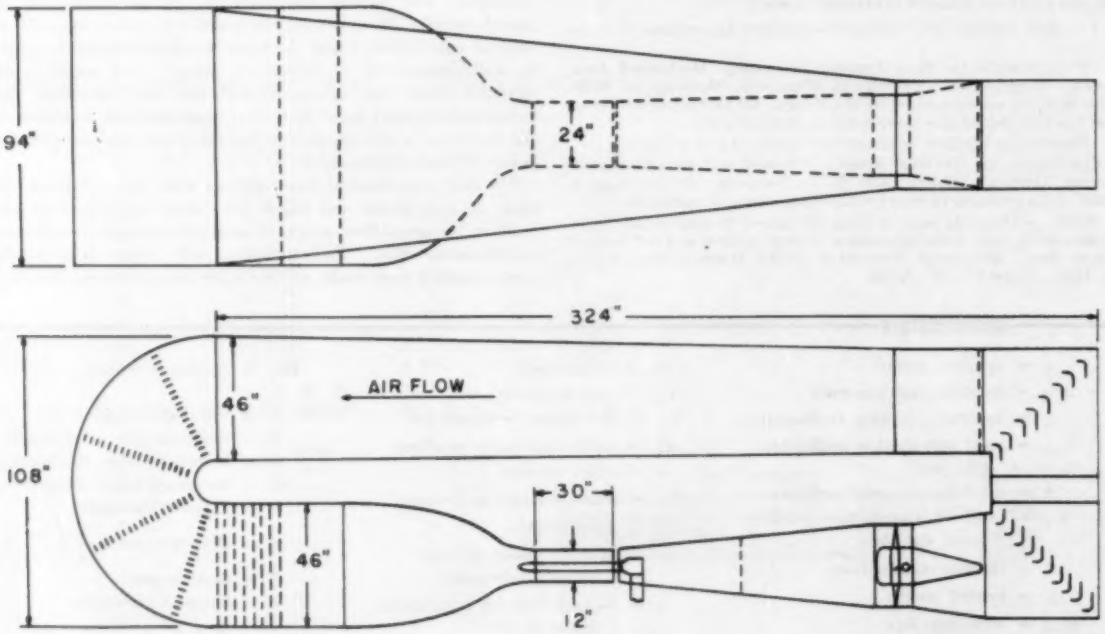

Fig. 1 Diagram of wind tunnel

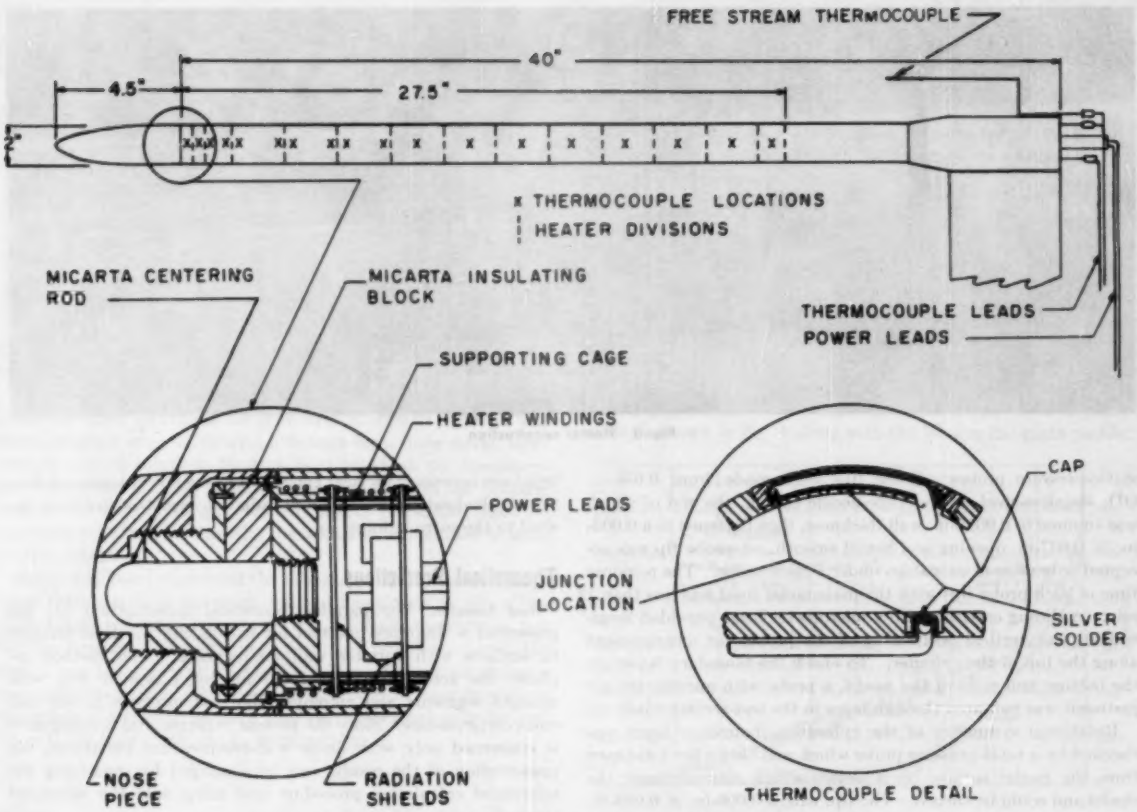

Fig. 2 Diagram of test model and thermocouple installation

bottom of the milled slots and stainless-steel caps were then silver-soldered in place. The sheathed thermocouples are led out the rear of the model and connection made to flexible lead wires of the same calibration furnished by the same manufacturer. A detailed sketch of the thermocouple installation is shown in Fig. 2.

At the heat-transfer rates encountered in this investigation, the resistance to heat flow through the tube wall is small compared to the heat-flow resistance of the boundary layer, so that the junction temperatures of the thermocouples installed in the tube wall should differ negligibly from the true surface temperatures.

Although some difficulties were experienced with the thermocouple calibration, it is reasonably certain that the temperatures reported are accurate within ± 1 deg F.

The shell preparation was completed by a finish lap followed by buffing to a high polish. The final dimensions of the shell are 2.001 $\pm$ 0.001 OD with a bow of less than 0.01 in. in the 40 in. length.

The total normal emissivity of a sample of the shell material similarly prepared was measured by the Radiation Section of the Heat Transfer Laboratory. At 200 deg F the total normal emissivity was 0.16.

The internal heater is 27.5 in. in length over-all and is supported from both ends. Designed to allow within limits an arbitrary variation in surface temperature, the heater is segmented longitudinally into fourteen individual heaters. The three front heaters are, respectively, 0.5, 0.6, and 1.2 in. long and the last heater is 1.2 in. long. Each of the other heaters is each 2.4 in. long.

Fig. 3 shows the heater construction. The internal heater is fabricated of stainless-steel, hypodermic-needle tubing held rigid by chromium-plated radiation shields which also separate and provide power terminals for the individual heaters. Thermocouples are located in alternate heater sections to allow an estimate of the heat conducted in the axial direction through the heater assembly. All electrical and thermocouple leads are brought out through the center of the heater and connected to junction blocks. To prevent free convection within the heater, the interstices are packed with glass-fiber insulation.

The heating elements are of nichrome wire wound over glass-fiber tape and covered by electric resistor cement. The cement prevents electrical contact between windings and provides a high-emissivity surface.

Heat exchange between the heater and the shell is principally by conduction through air and by radiation since the space between the heater and the shell is small to minimize free convection. The calculated longitudinal conductance for this heater assembly is about 0.004 Btu/hr deg F.

Power to the individual heaters was supplied by a d-c motor-generator and controlled by slide-wire rheostats. Voltage and current-metering jacks were mounted on a control panel along with the rheostats.

To promote as long a length of laminar boundary-layer flow as possible, an aluminum nosepiece was fitted to the model with auto-body refinishing cement covering the junction between nosepiece and model. The cement was smoothed until a surface continuous to touch was achieved. When turbulent results were desired, a 0.008-in. butt-welded wire ring was slipped over the nosepiece to about 1.75 in. ahead of the heated section.

Instrumentation. Boundary-layer profiles were measured with small flattened total-pressure probes with attached free-stream

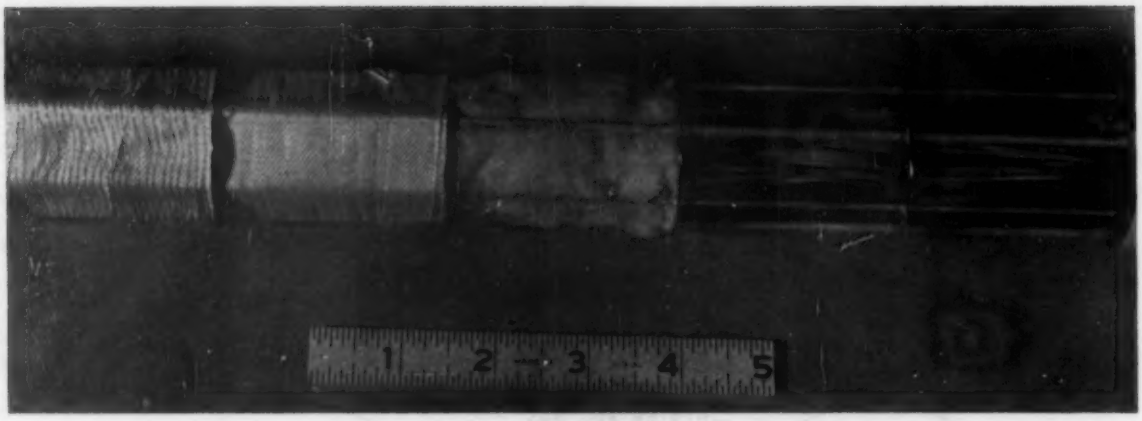

Fig. 3 Heater construction

static-pressure probes. Probe tips were made from 0.036-in. OD, stainless-steel, hypodermic-needle tubing, the end of which was thinned to 0.0015-in. wall thickness, then flattened to a 0.003-in. × 0.037-in. opening and honed smooth. A probe tip was accepted only after examination under a microscope. The response time of such probe tips with the manometer used was less than 1 min. A sliding carriage with a micrometer head provided longitudinal and vertical positioning of the probes for measurement along the top of the cylinder. To check the boundary layers on the bottom and sides of the model, a probe with micrometer adjustment was mounted through holes in the test-section windows.

Rotational symmetry of the cylindrical boundary layer was checked by a total-pressure probe which was held a fixed distance from the model surface by a device which clamped over the model and could be turned. The tip, with a 0.006-in. × 0.038-in. opening, was positioned 0.053 in. from the model surface by a solder teat resting on the surface behind the probe opening.

Pressure differences were indicated on a vertical manometer and read to less than 0.001 in. of fluid with a Gaertner telemicroscope and cathetometer. A model HWB, Flow Corporation hot-wire anemometer was used to indicate the presence of turbulence in the boundary layer. Thermoelectric emfs were measured with either a Brown-Rubicon, precision, self-balancing potentiometer or a Leeds and Northrup, portable Model 8662 potentiometer. The individual direct-current powers were measured with a Weston Model 1 volt-ammeter with voltboxes and shunts.

Experimental Procedure

Throughout the study, hydrodynamic measurements were made to determine the boundary-layer starting lengths and to study certain peculiarities which arose. This information is summarized in a later section.

For both the laminar and turbulent cases, a linear temperature distribution was imposed on the test surface. This situation was significantly different from the isothermal, and also exhibited sufficient difference between the Seban and Rubesin turbulent predictions. It also was well suited to the experimental model and, in addition, being linear simplified the theoretical predictions.

A heat distribution, estimated to result in a linear temperature profile, was set into the model. When equilibrium was reached, the temperature distribution on the test surface was recorded and plotted. The power to the individual heaters was then readjusted, using the temperature profile as a guide, until a linear wall-temperature profile was established. The power input, wall and heater temperatures, and tunnel operating conditions were then recorded.

Although at times negligible, corrections to the measured power input are necessary for heat generated in the power leads, conduction in the heater and shell, and radiation heat transfer from the shell to the surroundings.

Theoretical Predictions

Heat Transfer. The parallel theoretical investigation [2] has presented a simplified method for calculating the heat transfer to surfaces with variable wall temperature. This method replaces the actual temperature profile by a broken line with straight segments and employs tabulated integrals in the calculation procedure. Since the present experimental investigation is concerned only with linear wall-temperature variations, the presentation of the results can be simplified by modifying the referenced calculation procedure and using only the tabulated integrals.

For details of the procedure the reader is referred to [2]. For a linear wall temperature variation and Prandtl numbers not too far below 1 the results can be presented in the simple forms given in the following:

Laminar local heat flux

$$q(x) = 0.332k\,\mathrm{Pr}^{1/3}\mathrm{Re}_x^{1/2}\frac{dT_w}{d\xi}\left[G(1) - G\left(\frac{x_0}{x}\right)\right] \quad (1)$$

Laminar total heat flux

$$Q(x) = 0.664bk\,\mathrm{Pr}^{1/3}\mathrm{Re}_x^{1/2}\frac{dT_w}{d\xi}x\left[H(1) - H\left(\frac{x_0}{x}\right)\right] \quad (2)$$

Turbulent local heat flux (Seban)

$$q(x) = 0.0296k\,\mathrm{Pr}^{1/3}\mathrm{Re}_x^{0.8}\frac{dT_w}{d\xi}\left[S(1) - S\left(\frac{x_0}{x}\right)\right] \quad (3)$$

Turbulent local heat flux (Rubesin)

$$q(x) = 0.0296k\,\mathrm{Pr}^{1/3}\mathrm{Re}_x^{0.8}\frac{dT_w}{d\xi}\left[M(1) - M\left(\frac{x_0}{x}\right)\right] \quad (4)$$

Turbulent total heat flux (Seban)

$$Q(x) = 0.0370bk\,\mathrm{Pr}^{1/3}\mathrm{Re}_x^{0.8}\frac{dT_w}{d\xi}x\left[R(1) - R\left(\frac{x_0}{x}\right)\right] \quad (5)$$

Turbulent total heat flux (Rubesin)

$$Q(x) = 0.0370bk\,\mathrm{Pr}^{1/3}\mathrm{Re}_x^{0.8}\frac{dT_w}{d\xi}x\left[N(1) - N\left(\frac{x_0}{x}\right)\right] \quad (6)$$

The several functions G, H, S, M, R, N, represent incomplete Beta functions and are tabulated in [2]. In Equations (1) to (6), an unheated starting length x_0 has been assumed.

For purposes of comparison, the isothermal heat-transfer predictions are:

Laminar local

$$q(x) = 0.332 \frac{k}{x} \mathrm{Pr}^{1/3} \mathrm{Re}_x^{1/2} (T_w - T_\infty) \tag{7}$$

Turbulent local

$$q(x) = 0.0296 \frac{k}{x} \mathrm{Pr}^{1/3} \mathrm{Re}_x^{0.8} (T_w - T_\infty) \tag{8}$$

The corresponding total heat-flux quantities are simply obtained by integration over the length x.

Transverse Curvature Effects. No exact solution of the laminar-boundary-layer equations for flow over a circular cylinder has been obtained as yet. Several attempts have been made, however, to obtain solutions for situations in which the boundary-layer thickness is either small or large compared to the cylinder radius. Of these investigations, only that of Seban and Bond [8] considers heat transfer directly, the others being confined to skin-friction effects.

Seban and Bond considered the situation wherein the boundary-layer thickness is of the same order of magnitude as the radius and obtained a series solution to the differential equations, but for the heat-transfer case they calculated only two terms, the first being the same as for the flat plate, the second giving a curvature correction depending on the ratio of boundary-layer thickness to cylinder radius. For the isothermal cylinder and $\mathrm{Pr} = 0.715$ their result can be expressed by

$$h = h_{fp}(1 + 0.58\zeta) \tag{9}$$

where

$$\zeta = (4/a)(\nu x/u_\infty)^{1/2}$$

a being the cylinder radius.

The expression for the skin friction was carried out to three terms. As corrected by Kelly [9], it is

$$c_f = c_{fp}(1 + 0.525\zeta - 0.120\zeta^2) \tag{10}$$

The range of validity of Equation (9) is not known since only two terms in the series have been evaluated. However, Glauert and Lighthill [10] have estimated Equation (10) to be valid for $\zeta < 0.8$, and since Equations (9) and (10) would be identical for $\mathrm{Pr} = 1$, one can estimate for $\mathrm{Pr} = 0.715$ that the third term which is missing from Equation (9) should become negligible at about the value of ζ at which the third term in Equation (10) is negligible (say, less than 1 per cent of the second term). Thus assuming $0.120\zeta^2 < (1 + 0.525\zeta)$ (0.01) yields $\zeta < 0.12$, which for this problem ($u_\infty = 100$ fps, $\nu = 18 \times 10^{-5}$ sq ft per sec, $a = 1/12$ ft) leads to $x < 3.1$ ft as the range of validity of the first two terms of Equation (10) and thus of Equation (9).

It may be assumed that Equation (9), although holding strictly only for the isothermal-wall-temperature case holds approximately for the nonisothermal case as well.

Little information is available about the effect of transverse curvature on heat transfer in a turbulent boundary layer. In order to estimate this effect, it was assumed to be roughly the same as the effect of curvature upon friction. H. U. Eckert [11] gives the expression

$$\frac{c_f}{c_{fp}} = \left(1 + \frac{1}{3}\frac{\delta}{a}\right)^{1/4} \tag{11}$$

for a $1/7$-power profile at low Mach numbers. In the present study, $\delta/a \leq 0.5$, which would indicate a maximum correction of about 3 per cent. Since the effect is small and uncertain, it was neglected in the turbulent predictions.

Experimental Flow Study

The basic purpose of this study is a determination of the influence of variable wall temperature on convective heat transfer. For a proper evaluation of this effect, it is, however, extremely important that the nature of the hydrodynamic boundary layer be known. Therefore the program included the actual measurement of the characteristics of the laminar and turbulent boundary-layer flows. These results, obtained at various times throughout the study, are summarized in this section.

Velocity Profiles. Measurements of velocity profiles were made with the flattened pitot tubes. The contact of the probe with the model surface was indicated with an ohmmeter, distances from this point being measured with a micrometer. A sample laminar-velocity profile, corrected for displacement of the effective probe center, is shown in Fig. 4 along with the Blasius flat-plate profile.

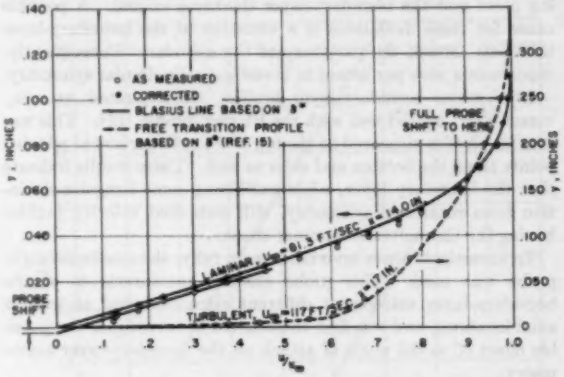
AS MEASURED
CORRECTED
BLASIUS LINE BASED ON δ*
FREE TRANSITION PROFILE BASED ON δ* (REF. 15)
FULL PROBE SHIFT TO HERE
PROBE SHIFT
LAMINAR, u_∞ = 81.3 FT/SEC x = 14.0 IN.
TURBULENT, u_∞ = 117 FT/SEC x = 17 IN.
y, INCHES
y, INCHES
y/x_∞

Fig. 4 Typical velocity profiles

A typical turbulent profile is also shown in Fig. 4. For turbulent profiles, a probe shift possibly is still present, but because of the profile fullness, measurements in the laminar sublayer are difficult, and no simple correction method is available. Because of these difficulties, and because the probe shifts have a smaller effect on the over-all contour of the turbulent profiles, this correction was neglected.

Boundary-Layer Development. *Laminar Flow:* In laminar flow along a flat plate, it is known that the boundary-layer thickness increases with the square root of the distance from the leading edge. This boundary-layer growth can be expressed in terms of the displacement thickness by the relationship (12)

$$\delta^* = 1.729 \left(\frac{\nu x}{u_\infty}\right)^{1/2} \tag{12}$$

where δ^* is defined by

$$\delta^* = \int_0^\infty \left(1 - \frac{u}{u_\infty}\right) dy \tag{13}$$

Equations (12) and (13) apply strictly only for flat plates, but should hold as well for axial cylinders in the length where nose-piece effects and transverse-curvature effects can be neglected. According to Seban and Bond [8], Scholkemeier [13] has shown that the boundary layer on a half-body, when the displacement thickness is small compared with the cylinder radius, will assume the characteristics of a flat plate $1\frac{1}{2}$ diameters from the stagnation point, measured along a meridian. These results should apply approximately for the present model, so that even very

near the beginning of the heating section the boundary layer should assume flat plate characteristics.

The effects of transverse curvature have been investigated by various authors, but as yet no conclusive experimental study has appeared. The analytical studies of Seban and Bond [8], Kelly [9], and Glauert and Lighthill [10] have shown that Equation (13) satisfactorily defines the displacement thickness, when δ^* is small compared to the cylinder radius a. In addition, and even more important, the results of these authors show that the displacement-thickness growth for the length of cylinder considered in this investigation will differ negligibly from that predicted by Equation (12).

To determine starting lengths from velocity-profile information, the profiles were planimetered to find the displacement thickness and the displacement thickness squared was plotted versus an arbitrary length co-ordinate. The extrapolation of the $(\delta^*)^2$ to zero then should yield the effective hydrodynamic starting length. It was found, however, that irregular deviations from the expected relation between distances from the effective starting point and the boundary-layer thickness existed. A possible cause for these deviations is a variation of the boundary-layer thickness around the periphery of the cylinder. Consequently, experiments were performed to investigate the circular symmetry.

All laminar boundary-layer profiles, when plotted as u/u_∞ versus y/δ^*, agreed well with the Blasius' profile [12]. This was true for profiles measured on the top of the cylinder and at selected points along the bottom and sides as well. These results indicate that the boundary layer, while exhibiting some irregular deviation from rotational symmetry, still embodied velocity profiles having the characteristic laminar shape.

To investigate these anomalies more fully, the constant-height probe was used. This probe enabled measurements of the boundary-layer velocity at different circumferential as well as axial locations, and was first constructed to investigate the possible effect of model angle of attack on the boundary-layer asymmetry.

The angle of attack was adjusted nearly to zero using the constant-height probe by balancing total pressure readings in the boundary layer on top and bottom, then on the two sides. It was found, however, from total-pressure measurements at other circumferential locations, that a boundary-layer asymmetry was still present which could not be removed by such adjustments.

At several longitudinal positions, eight circumferential readings of the total pressure at a fixed distance from the surface were taken. Fig. 5 shows the velocities which exist at a constant distance from the surface and at various circumferential and axial positions. From the knowledge of the probe height in the boundary layer and of the velocity ratio u/u_∞ at this position, one can determine a displacement thickness by assuming the profile shape to be described by Blasius' profile. For $x = 21$ in. in Fig. 5, the maximum deviation in y/δ^* as calculated by the foregoing method was ± 4 per cent. One might suspect a correlation between the variation in boundary-layer thickness and the rectangular cross section of the wind tunnel. This, however, is not obvious from Fig. 5. No other explanation can be offered since no asymmetries are detectable in the free-stream flow, and the model surface is circular within ± 0.001 in. and uniformly smooth so that no unequal roughness elements should be present.

When it was noted that a similarity in the velocity profiles existed in spite of the asymmetry, an average of the readings taken with the constant-height probe was used to determine the effective hydrodynamic length. Using an average value of u/u_∞ for a certain longitudinal position an η is obtained from the Blasius' profile. Then $1/\eta^2$ is plotted versus an x measured from an arbitrary point. A straight-line relation is expected on such a plot according to the equation $(1/\eta^2) = x(\nu/u_\infty y^2) = cx$. Fig. 6 shows that this expected linear relation is very well followed by the experimental results, indicating that, on the average, the boundary layer grows on the cylinder in the same way as on a flat plate. The position of $1/\eta^2 = 0$ determines the effective starting position.

Turbulent Flow. The nature of the turbulent boundary layer on an axial cylinder is not well known, the only reported experimental velocity profiles being those of Richmond [14]. Richmond's data were taken with much thicker boundary layers (relative to cylinder radius) than the ones in this investigation so no conclusions can be drawn from his results. H. U. Eckert [11] has published an analysis of the turbulent boundary layer which unfortunately has no experimental confirmation. The turbulent boundary layer was, therefore, treated as a flat-plate boundary layer, and measurements were undertaken to determine the characteristic shape of the velocity profiles, the rate of boundary-layer growth, and the degree of asymmetry present.

The model was aligned and the flow symmetry checked with the constant-height probe. The ratio of local to free-stream velocity as a function of circumferential position at several axial locations thus determined is shown in Fig. 5. It is of interest to note that the asymmetry in turbulent flow is not nearly as pronounced as in laminar flow.

Measurements of complete velocity profiles were made at successive axial locations along the top of the model and at selected locations on the bottom and sides. When plotted as u/u_∞ versus y/δ^* these profiles agreed well with the turbulent profiles of Klebanoff and Diehl [15] which were made under natural transition at Reynolds numbers about two to four times as large as in the present investigation. A representative measured profile is compared in Fig. 4 with the profile of Klebanoff and Diehl.

On a flat plate, the turbulent displacement thickness δ^* is proportional to $x^{0.8}$, and since δ^* can be determined by integration of the profiles, a plot of $(\delta^*)^{1.25}$ versus an arbitrary x should lead, on extrapolation to zero, to the effective turbulent starting position. Although this method was satisfactory, considerable time for measurement and calculation was required and it was found more expedient to use the constant-height probe in conjunction with the Klebanoff and Diehl profile as a standard to determine values of δ^*/y as a function of x. These values were used in the manner just described to determine the effective

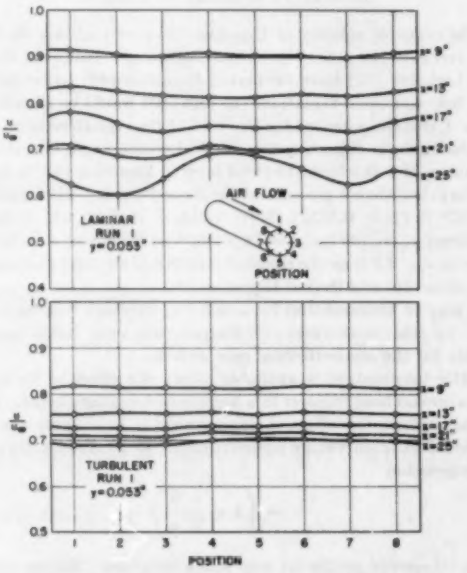

Fig. 5 Circumferential velocity variations

starting length. Fig. 6 shows $(\delta^*/y)^{1.25}$ plotted versus x for a typical run.

Experimental Heat-Transfer Study

Laminar Boundary Layer. Since the theory of heat transfer to laminar boundary layers under the influence of variable wall temperature is well established and since accurate predictions can be readily obtained [2], it was felt that an excellent check on the proper operation of the experimental equipment would be given by experiments in the laminar ranges. To establish the extent of this agreement between theory and experiment, the five laminar heat-transfer runs listed in Table 1 are reported.

Table 1 Laminar heat-transfer runs

Run no.	u_∞-fps	x_0, in.	$\frac{dT_w}{d\xi}$, deg F/ft	Re/ft
1	82.5	5.0	47.0	458000
2	83.1	4.8	47.5	449000
3	84.3	4.0	46.6	451000
4	82.4	5.0	49.0	455000
5	82.0	18.4	50.3	460000

Prior to each run, the effective starting point of the hydrodynamic boundary layer relative to a fixed point on the model surface was determined as discussed in the preceding section. Runs Nos. 1–4 were made before the turbulent runs discussed in the next section and run No. 5 after the turbulent runs.

The first four runs of Table 1 differ from each other in that the model was rotated in its mount through an angle of 90 deg for each run. Thus the top of the model in run No. 1 is the bottom of the model in run No. 3. The reasons for these changes are enumerated in the following.

Fig. 7 shows the temperature distribution for runs Nos. 1 and 5. The measured and predicted local and total heat fluxes are shown in Figs. 8 and 9. The total heat flux in Fig. 9 represents the total amount of heat transferred into the boundary layer up to any point x. The theoretical predictions are taken from Equations (1) and (2), using properties evaluated at the average film temperature, the measured free-stream velocity and the value x_0 determined as discussed previously. Of the experimental points, the open points represent the data as taken and the closed points represent the data as corrected for the effect of cylindrical curvature by Equation (9). Figs. 8 and 9 also show the heat-transfer rates for run No. 5 as predicted by the isothermal heat-transfer coefficient, Equation (7), based on the distances from the starting points of both the thermal and the hydrodynamic boundary layers, and on the local difference between fluid and wall temperature. It should be noted that in Figs. 8 and 9 only heat-transfer measurements in the region where the hydrodynamic characteristics have been studied are included. For runs Nos. 1–4, heat-transfer results are presented for 19.1 in. of heated surface, and for run No. 5, for 13.2 in. of heated surface.

Run No. 5 was made with the first two heaters turned off and a 12.3-in. unheated section placed between the nosepiece and the heating section to provide a longer unheated starting length. The effective starting point of the thermal boundary layer was determined by extrapolating the measured linear wall-temperature profile to intersect with the measured free-stream temperature, Fig. 7.

Due to a systematic error in the thermocouple circuit in runs Nos. 1–4, the values of the wall and free-stream temperatures and hence of the unheated starting lengths are known less exactly than in run No. 5 or the turbulent runs of the next section. However, since the results are to be compared with Equations (1) and (2), the only additional uncertainty incurred from this fact arises in the exact value of x_0, and the effect of this uncertainty diminishes as x_0/x becomes smaller. The value of x_0 is defined as the distance between the starting points of the hydrodynamic boundary layer and the beginning of the heating section.

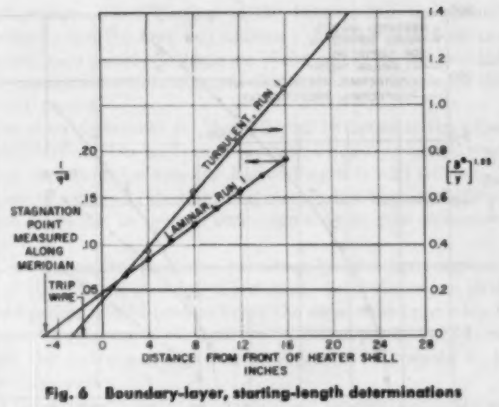
STAGNATION POINT MEASURED ALONG MERIDIAN
TRIP WIRE
TURBULENT, RUN 1
LAMINAR, RUN 1
DISTANCE FROM FRONT OF HEATER SHELL, INCHES

Fig. 6 Boundary-layer, starting-length determinations

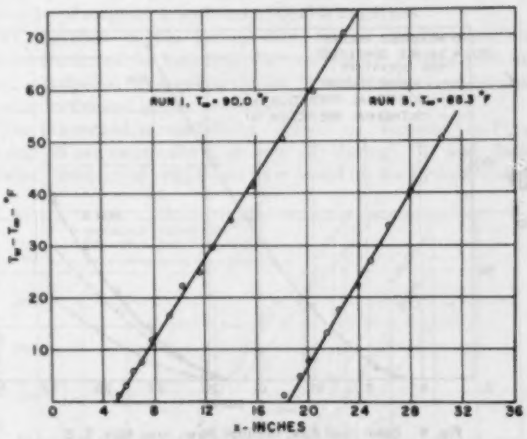

Fig. 7 Wall-temperature distributions, laminar flow, runs Nos. 1, 5

The data shown in Fig. 8 scatter about the theoretical line by about ±10 per cent. To investigate the extent to which this scatter might be a result of rotational asymmetry effects the checks discussed in the following paragraphs were made. Experimental errors resulting from errors in measurement are discussed in the Appendix of [1]. It is there shown that errors of the foregoing order of magnitude are comparable with the expected maximum indeterminant error.

Because of the variation of the heat-transfer coefficient with boundary-layer thickness around the periphery of the model, a thermocouple located where the boundary layer is abnormally thick or abnormally thin might not sense the average temperature for its longitudinal position. To investigate this possibility, an analysis was made of the circumferential temperature distribution around the shell, using a heat-transfer coefficient based on the measured local boundary-layer displacement thickness and taking into account conduction around the model skin. The displacement thickness variation determined from the velocity variation at $x = 21$ in. in Fig. 5 (laminar flow) with Equations (12) and (1) was used to calculate local circumferential heat-transfer coefficients corresponding to the flow and thermal conditions to run No. 1. From Equation (12), the effective hydro-

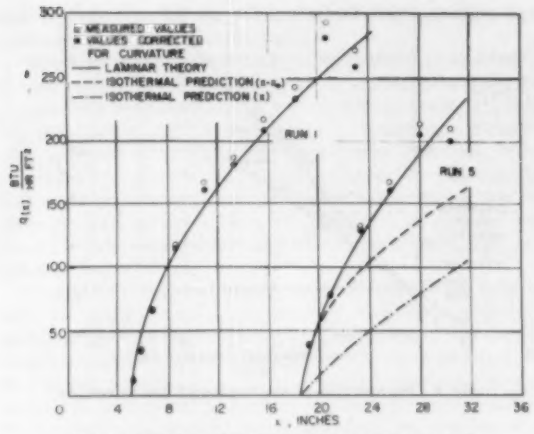

Fig. 8 Local heat flux, laminar flow, runs Nos. 1, 5

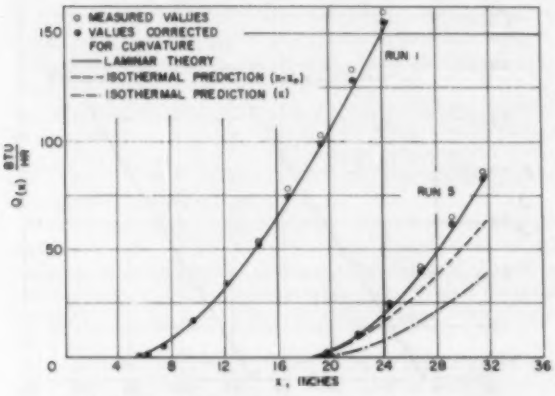

Fig. 9 Total heat flux, laminar flow, runs Nos. 1, 5

dynamic length varied between 19.8 and 22.5 in. The wall to free-stream temperature difference at this location was about 60 deg F. From Equation (1), the maximum variation in the heat-transfer coefficient was ±7 per cent.

If the heat input, circumferentially, was constant and the shell conduction negligible, the wall to free-stream temperature ratio would also vary by ±7 per cent (±4.2 deg F). The calculated variation allowing for circumferential heat conduction, but keeping the circumferential heat input to the shell constant, was less than ±1 per cent (±0.6 deg F). A further qualitative check for correlation between the measured thickness of the boundary layer at each thermocouple location and the local heat transfer was inconclusive.

In an effort to gain further insight into the problem, three heat-transfer runs were made with the model rotated 90 deg in its mount each time (runs Nos. 2–4). The conditions for each run were similar to the first run. Flow measurements were repeated at each position to determine whether the asymmetry was associated with the model or with the wind tunnel (see Experimental Flow Study). The asymmetry was unchanged at all four angular positions probably indicating that the tunnel was its cause. Through rotation of the model, fluctuations in the heat input by about ±10 per cent were obtained. The variations did not appear to be systematic in nature.

The total heat-input representation shown in Fig. 9 exhibits much less data scatter than does the corresponding local representation. In fact, for runs Nos. 1 and 5, the experimental values of $Q(x)$ as corrected for curvature differ by less than 4 per cent from the theoretical curve. Errors to this extent are less than the maximum indeterminant errors as discussed in the Appendix of [1].

The experimental data points in both Figs. 8 and 9 were corrected for the effects of cylindrical curvature with Equation (9). It is seen that the agreement with theory is generally improved by the correction. However, since the experiments were not designed to check the effect of cylindrical curvature, definitive conclusions as to the extent of this effect should not be drawn.

The theoretical curves as well as the measured points given in Figs. 8 and 9 are subject to experimental error through the property values, the Reynolds number, the wall-temperature gradient, and the starting length, all of which must be used to determine the theoretical curve. For this reason, the dimensionless representations of Figs. 10 and 11 are given. In these figures the experimental uncertainties affect only the location of the experimental points on the graph and not the position of the theoretical curves which are the integrals $G(x_0/x)$ and $H(x_t/x)$ of Equations (1) and (2).

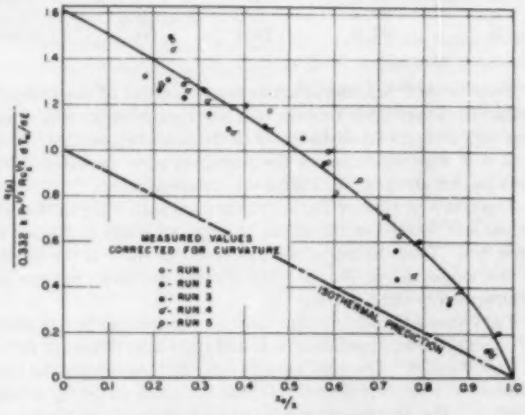

Fig. 10 Dimensionless local heat flux, laminar flow

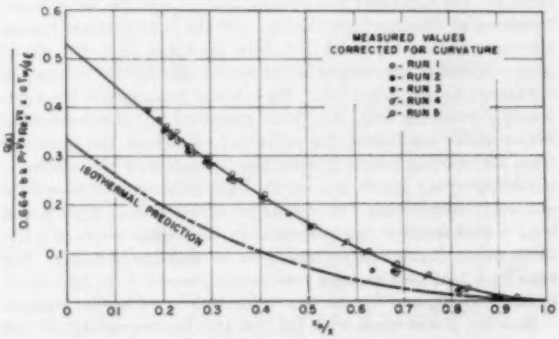

Fig. 11 Dimensionless total heat flux, laminar flow

In view of the improvement in the agreement with theory resulting from the cylindrical curve correction in Figs. 8 and 9, all data in Figs. 10 and 11 have been so corrected. The effect of the correction is small, however, and does not materially affect the scatter in the data.

The anticipated maximum indeterminant error for the ordinates of the local and total representations are about 10 and 12 per cent, respectively. The absolute indeterminant error in the abscissas of these curves is a maximum of 0.02 at $x_0/x = 0.5$ and is thus small compared to the errors in the ordinates.

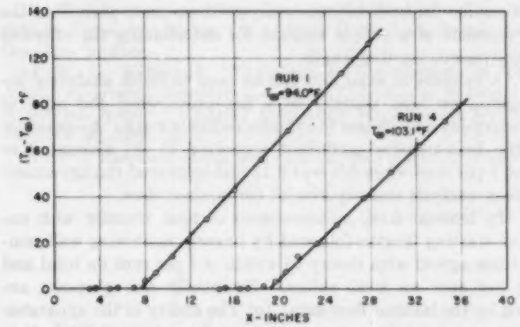

Fig. 12 Wall-temperature distributions, turbulent flow, runs Nos. 1, 4

As with Fig. 9 the total heat-flux plot of Fig. 11 exhibits less scatter of data than does the local heat-flux plot of Fig. 10.

Since it is the intention of the laminar study to establish the ability of the apparatus to detect and measure the effects of wall-temperature variation, the isothermal wall heat-transfer predictions, Equation (7), are for comparison shown in Figs. 10 and 11. It is evident from these graphs that the nonuniform wall effect is large enough to be investigated satisfactorily.

Turbulent Boundary Layer. Turbulent boundary-layer flow was imposed upon the model by means of an 0.008-in. butt-welded trip wire placed on the nosepiece 1.75 in. from the leading edge of the heater shell. Prior to each individual run, starting-length determinations were made as discussed previously. In all, five turbulent heat-transfer runs were made after it was determined that the equipment was functioning properly. The imposed conditions are summarized in Table 2.

Table 2 Turbulent heat-transfer runs

Run no.	u_∞, fps	x_0, in.	$\frac{dT_w}{d\xi}$, deg F/ft	Re/ft
1	86.5	7.7	63.0	473000
2	117.7	8.4	52.5	626000
3	116.2	14.6	42.5	612000
4	117.0	19.0	56.0	622000
5	168.7	9.5	40.0	847000

The imposed temperature distributions for runs Nos. 1 and 4 are shown in Fig. 12 and represent, respectively, the shortest and longest starting lengths used. Based on the known temperature distributions and free-stream velocities, the theoretical predictions for the distributions of the local and total heat-transfer rates were determined from Equations (3) through (6). The physical properties were evaluated at the local and average film temperature, respectively. Examples of these calculations along with the experimental data points are shown in Figs. 13 and 14 for runs Nos. 1 and 4. In addition to the theoretical predictions of Seban and Rubesin, Figs. 13 and 14 also present theoretical estimates based on an isothermal heat-transfer coefficient, Equation (8). In these figures the isothermal prediction based on the hydrodynamic length x is shown as a dash-dot line and that based on the heated length, $x - x_0$, is shown as a dashed line.

The data definitely show preference for the modified Seban prediction except for run No. 1 close to the beginning of heating where the Rubesin prediction appears to be preferred. However, these findings should be weighted less than the rest since the Reynolds number is quite low at this location ($Re_{x_0} = 305{,}000$), and since the temperature distribution begins to depart from linearity. A check of the effect of the initial departure from linearity of the wall-temperature distribution on heat-transfer predictions was made for run No. 4. This check showed a small effect close to the beginning of the heating but no appreciable effect after the first two heaters. For the turbulent runs, the data from heaters downstream of the end of the test section is not reported, since the characteristics of the boundary layer there are not known.

The close agreement in Figs. 13 and 14 between the experimental data and the isothermal prediction based on heated length is here fortuitous because the heated length is well defined. In the case of a general arbitrary temperature distribution the heated length could not be defined unambiguously to give accurate results.

A correction for transverse curvature has not been applied to any of the data presented in this section. Such correction, as discussed earlier, would tend to lower the data, thus improving the apparent preference of the data for the Seban prediction. In any event, the correction according to Equation (11) would be less than 3 per cent.

In the Appendix to [1] a calculation of the errors affecting $q(x)$ and $Q(x)$ shows for run No. 1 average indeterminant errors of 5.4 and 6.0 per cent, respectively. The data scatter in $q(x)$ is about this order of magnitude and that of $Q(x)$ is much less.

As discussed in the laminar-flow section, a dimensionless representation of the heat flux offers certain advantages from an error standpoint. Accordingly, Figs. 15 and 16 which combine all runs on individual graphs are presented.

The theoretical curves labeled "Seban" or "Rubesin" in Figs. 15 and 16 are essentially Equations (3) through (6) and those labeled "isothermal predictions" are based on the hydrodynamic

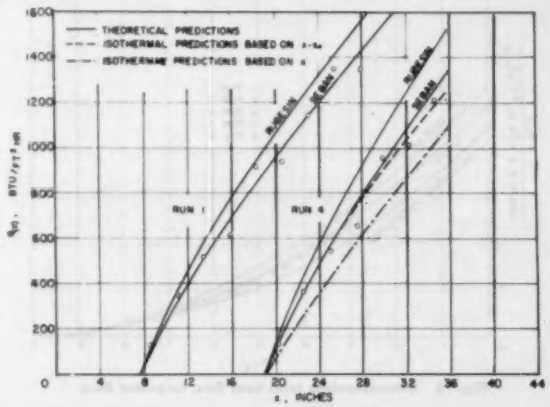

Fig. 13 Local heat flux, turbulent flow, runs Nos. 1, 4

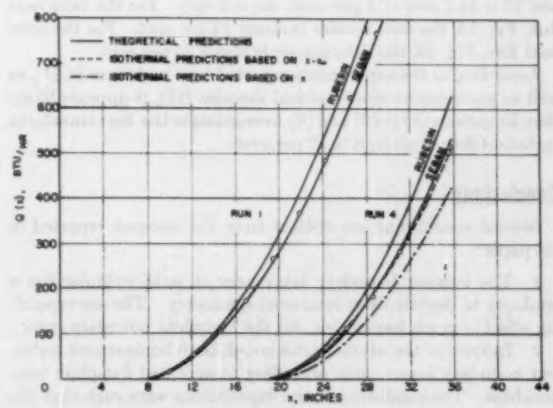

Fig. 14 Total heat flux, turbulent flow, runs Nos. 1, 4

length and calculated from Equation (8). The complete Reynolds number range of the data is 303,000 to 2,530,000. As before, no curvature correction has been applied.

Both the local heat-flux representation of Fig. 15 and the total heat-flux representation of Fig. 16 show a definite preference for the Seban prediction over either the Rubesin or the isothermal heat-transfer coefficient prediction.

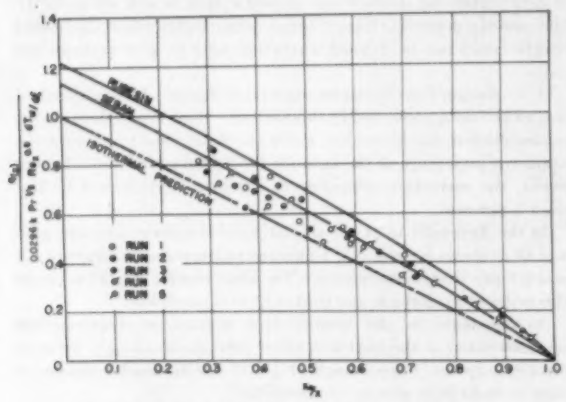

Fig. 15 Dimensionless local heat flux, turbulent flow

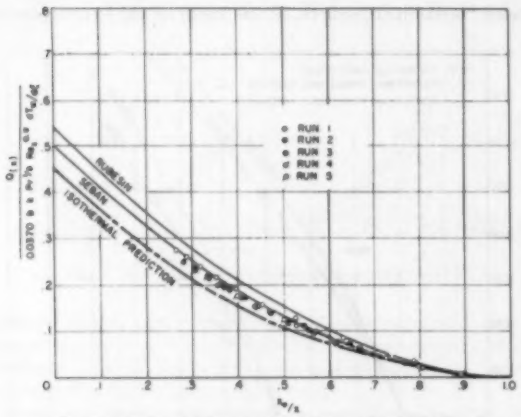

Fig. 16 Dimensionless total heat flux, turbulent flow

The maximum indeterminant error in the ordinates of Figs. 15 and 16 is 14.7 and 17.1 per cent, respectively. For the local heat flux, Fig. 15, the data scatter is about 15 per cent. For the total heat flux, Fig. 16, the data scatter is about 10 per cent.

According to the experiments reported here and those in [7], as well as more recent semiempirical theories [17], it appears likely that Equations (3) to (6) and (8) overestimate the heat transfer in turbulent flow of air by 8 to 10 per cent.

Conclusions

Several conclusions are evident from the research reported in the paper:

1 The laminar boundary layer over an axial cylinder has a tendency to deviate from rotational symmetry. The corresponding effect is much less evident for the turbulent boundary layer.

2 In spite of the asymmetries noted, both laminar and turbulent boundary layers grow according to accepted flat-plate relationships. The conditions of the experiments were such that the effects of transverse curvature on the boundary-layer thickness were small. In both boundary layers these facts permitted the development of a simple method for determining the effective hydrodynamic starting length.

3 A cylinder in axial flow can be used to check analytical information on heat transfer to a flat plate when the ratio of boundary-layer thickness to cylinder radius is small. A correction on the heat-transfer coefficient according to [8] amounted to about 7 per cent when δ/a was 0.17 and improved the agreement between analysis and experiment for laminar flow.

4 In laminar flow, measurements of heat transfer with unheated starting lengths followed by linearly increasing wall temperatures agreed with theory to within ±4 per cent on total and ±10 per cent on local values. Essentially two purposes are served by the laminar flow data: (*a*) The ability of the apparatus to make accurate measurements is confirmed; and (*b*) further support is given to the superposition principle on which nonuniform wall-temperature, heat-transfer calculations are based.

5 In turbulent flow, the measurements indicated preference for Seban's theory [3] with a modified Prandtl number dependence [2].

6 The isothermal equations predicted the turbulent results within 20 per cent and, since this type of calculation is quite easy to make, may be preferable as long as wall-temperature changes are not too abrupt.

Acknowledgment

The authors acknowledge the aid of Mr. P. A. Schoeck and Mr. J. P. Rosenwald during the initial phases of the research. Mr. R. Anderson and Mr. F. J. Bradac constructed the experimental apparatus and Mr. R. F. O'Neill made many of the measurements and performed much of the data reduction. The helpful suggestions of Dr. J. P. Hartnett are greatly appreciated.

References

1 R. Eichhorn, E. R. G. Eckert, and A. D. Anderson, "An Experimental Study of the Effects of Non-Uniform Wall Temperature on Heat Transfer in Laminar and Turbulent Axisymmetric Flow Along a Cylinder," WADC TR 58-33, July, 1958.

2 J. P. Hartnett, E. R. G. Eckert, and Roland Birkebak, "Calculation of Convection Heat Transfer to Non-Isothermal Surfaces Exposed to a Fluid Stream With Wedge Type Surface Pressure Gradient," WADC TR 57-753, ASTIA Doc. No. AD 142236, July, 1958.

3 S. Scesa, "Experimental Investigation of Convective Heat Transfer to Air From a Flat Plate With a Stepwise Discontinuous Surface Temperature," MS thesis, University of California, Berkeley, Calif., 1949.

4 M. W. Rubesin, "The Effect of an Arbitrary Surface Temperature Variation Along a Flat Plate on the Convective Heat Transfer in an Incompressible Turbulent Boundary Layer," NACA TN 2345, April, 1951.

5 M. Jakob and W. M. Dow, "Heat Transfer From a Cylindrical Surface to Air in Parallel Flow With and Without Unheated Starting Sections," TRANS. ASME, vol. 68, 1946, pp. 123–134.

6 W. Tessin and M. Jakob, "Influence of Unheated Starting Sections on the Heat Transfer From a Cylinder to Gas Streams Parallel to the Axis," TRANS. ASME, vol. 75, 1953, pp. 473–481.

7 W. C. Reynolds, W. M. Kays, and S. J. Kline, "Heat Transfer in Turbulent Incompressible Boundary Layers," NASA Memos 12-1-58W, 12-2-58W, 12-3-58W, 12-4-58W, December, 1958.

8 R. A. Seban and R. Bond, "Skin Friction and Heat Transfer Characteristics of a Laminar Boundary Layer on a Cylinder in Axial Incompressible Flow," *Journal of the Aeronautical Sciences*, vol. 18, 1951, pp. 671–675.

9 H. R. Kelly, "A Note on the Laminar Boundary Layer on a Cylinder in Axial Incompressible Flow," *Journal of the Aeronautical Sciences*, vol. 21, 1954, p. 634.

10 M. B. Glauert and M. J. Lighthill, "The Axisymmetric Boundary Layer on a Long Thin Cylinder," *Proceedings of The Royal Society*, London, England, series A, vol. 230, 1955, pp. 188–203.

11 H. U. Eckert, "Simplified Treatment of the Turbulent Boundary Layer Along a Cylinder in Compressible Flow," *Journal of the Aeronautical Sciences*, vol. 19, 1952, pp. 23–28, 38.

12 H. Schlichting, "Boundary Layer Theory," McGraw-Hill Book Company, Inc., New York, N. Y., 1955.

13 T. Scholkemeier, "The Laminar Friction Layer on Rotationally Symmetric Bodies," Technische Hochschule, Braunschweig, Germany, no date.

14 R. L. Richmond, "Experimental Investigation of Thick, Axially Symmetric Boundary Layers on Cylinders at Subsonic and Hypersonic Speeds," GALCIT Hypersonic Wind Tunnel Memorandum, No. 39, June, 1957.

15 P. S. Klebanoff and Z. W. Diehl, "Some Features of Artificially Thickened Fully Developed Turbulent Boundary Layers With Zero Pressure Gradient," NACA TR 1110, 1952.

16 H. H. Sogin, "Laminar Transfer From Isothermal Spanwise Strips on a Flat Plate," JOURNAL OF HEAT TRANSFER, TRANS. ASME, Series C, vol. 82, 1960, pp. 53–63.

17 E. M. Sparrow, T. M. Hallman, and R. Siegel, "Turbulent Heat Transfer in the Thermal Entrance Region of a Pipe With Uniform Heat Flux," *Applied Scientific Research*, series A, vol. 7, 1937, pp. 37–52.

Geometric Factors for Radiative Heat Transfer Through an Absorbing Medium in Cartesian Co-ordinates

A. K. OPPENHEIM
J. T. BEVANS
Shell Development Company, Emeryville, Calif.
Now with Space Technology Laboratories, Los Angeles, Calif.
Mem. ASME

Heat flux conveyed by diffuse radiation from surface A_1 and A_2 through an absorbing medium is expressed by the relation

$$Q_{1-2} = J_1 \int_{A_1 \times A_2} f(l_{12})(\cos\theta_1 \cos\theta_2/\pi l_{12}^2)dA_1 dA_2$$

where J_1 is the radiosity of A_1 (sum of the emitted, reflected, and transmitted flux per unit area), l_{12} is the radiation beam (the distance between surface elements dA_1 and dA_2), θ_1 and θ_2 are the angles between the radiation beam and the normals to the surface elements, and $f(l_{12})$ is the function describing the absorption law. The foregoing four-dimensional integral is transformed into a sum of one-dimensional integrals for the cases of opposite-parallel and adjoining-perpendicular rectangles. The results are suitable for numerical integration with any total absorption law obtained from the actual distribution of monochromatic absorptivities over the whole spectrum.

THE EVALUATION and prediction of process furnace performance requires an accurate determination of the heat transfer from the combustion gases and the furnace enclosure to absorbing surfaces. A primary mechanism for this transfer is the radiant exchange between the combustion gases, the enclosure walls, and the absorbing area. In the past, the methods of detailed analysis have been too complicated for practical application and sufficient information was not available regarding radiant properties to make an accurate analysis. As a consequence, methods of semiempirical form have been developed which represent by a single variable all the elements of the furnace that have a common function [4].[1] These procedures permit an overall system behavior to be determined but do not allow any examination of variations in such variables as heat flux or temperature occurring within the furnace.

The development of the network method of radiant exchange analysis [5] has provided a practical procedure for making a more detailed study of the radiation within a furnace. The application of this method is presently restricted by the lack of knowledge of the properties of radiant systems. In addition to the obvious physical properties of the surfaces and gases within the furnace, an important property of a radiation system is the geometrical relationship between the various surfaces which comprise the system. The geometrical factors for two surfaces separated by a nonabsorbing medium have been determined for a large number of geometries and reported in the literature [1, 2]. Computations for surfaces separated by an absorbing medium have not been performed for comparable varieties of geometries and dimensions. Only recently has a limited number of results been reported [3].

The paper describes a method for determining the geometric factors for parallel opposed equal rectangles and perpendicular adjacent unequal rectangles with an intervening absorbing medium. These two basic shapes can be used to compute the geometric factors for any arrangement of parallel or opposed rectangles with the aid of flux algebra.

Basic Relations

The net exchange between two completely absorbing diffuse surfaces separated by an absorbing medium is given by:

$$Q_{12} = A_1 \tau_{12} F_{12} \sigma (T_1^4 - T_2^4) \qquad (1)$$

The factor $\tau_{12}F_{12}$ is termed the geometric transmission factor and is expressed by (see Fig. 1):

[1] Numbers in brackets designate References at end of paper.

Contributed by the Heat Transfer Division and presented at the Annual Meeting, Atlantic City, N. J., November 29-December 4, 1959, of THE AMERICAN SOCIETY OF MECHANICAL ENGINEERS.
Manuscript received at ASME Headquarters, September 11, 1959. Paper No. 59—A-206.

Nomenclature

A_1, A_2 = heat-transfer area of surface 1 or surface 2, respectively, ft²

$A = \frac{X}{h}$, equation (13)

$B = \frac{X}{h}$, equation (13) or $= \frac{Z}{h}$, equation (61)

$C = BK = kY$, equation (28) or $= BK = kZ$, equation (71)

$D = AK = kX$, equation (28) or $= AK = kY$, equation (71)

$E = C^2 + D^2$, equation (28) or equation (71)

F = geometrical shape factor

$K = kh$, equation (26) or $= kX$, equation (71)

Q = heat flow, Btu/hr

T = temperature, deg R

X, Y, Z = dimensions of the rectangles, ft

a, b = x, y co-ordinates, respectively, of the position of one rectangle relative to the other, see Fig. 3(*a*)

$f(l)$ = parallel beam transmission function

h = perpendicular distance between parallel rectangles, ft

(Continued on next page)

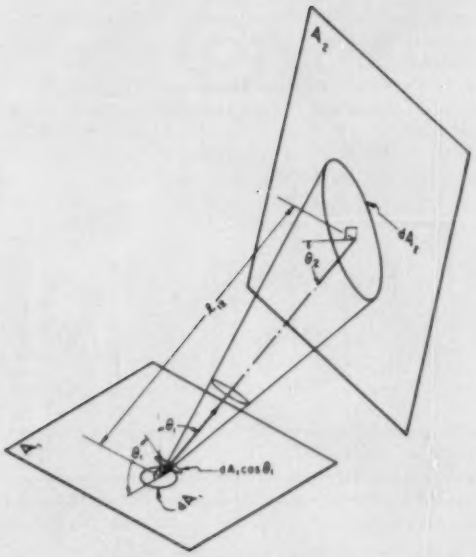

Fig. 1 Geometrical relationships for two radiative surfaces

$$\tau_{12}F_{12} = \frac{1}{A_1}\int_{A_1}\int_{A_2}\frac{f(l)\cos\theta_1\cos\theta_2}{\pi l^2}\,dA_1dA_2 \qquad (2)$$

For an absorption of zero ($f(l) = 1$), this equation reduces to the conventional geometric shape factor and values may be found in the literature for most geometries of practical interest [1, 2]. The extension of these factors to include attenuation by the medium using $f(l) = e^{-kl}$ has recently been reported for both perpendicular and parallel squares [3]. These values were obtained by numerical integration of equation (2) and are for a limited range of the pertinent variables.

Equation (2) can also be used to define the absorption by the intervening gas by setting $f(l)$ equal to absorption factor of the gas. If this is done, equation (1) then represents the energy absorbed by the gas from the energy exchange between the two surfaces. The derivation to be given will consider geometric transmission factors and the geometric absorption factors are obtained by defining $f(l)$ as the absorption function rather than the transmission function.

Evaluation of equation (2) requires a specification of the geometries of the two surfaces A_1 and A_2, the relative orientation of the two surfaces, and the functional behavior of the function $f(l)$. The first two factors are determined by the physical system considered, whereas $f(l)$ depends upon the nature of the absorption process.

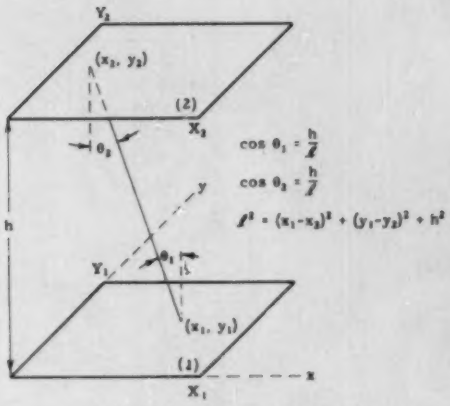

Fig. 2 Parallel opposed rectangles

Method of Analysis

The explanation of the method is best given by example and the procedures used for reducing the four-dimensional integral [equation (2)] for the particular case of parallel rectangles will be given here. The derivation for parallel adjacent rectangles is presented in the Appendix.

The general case of parallel opposed unequal rectangles will be considered initially and later restricted to equal rectangles as a simplification. The relationships between θ_1, θ_2, and l are indicated in Fig. 2, and when substituted in equation (2) give:

$$\tau_{12}F_{12} = \frac{1}{A_1}\int_{A_1}\int_{A_2}\frac{f(l)h^2}{\pi l^4}\,dA_1dA_2 \qquad (3)$$

where

$$l^2 = (x_1 - x_2)^2 + (y_1 - y_2)^2 + h^2 \qquad (4)$$

The integral is the gist of the problem and may be written in terms of the limits of the two areas A_1 and A_2, as (see Fig. 3):

$$I = \frac{\pi}{h^2}\tau_{12}A_1F_{12} = \int_0^{X_1}dx_1\int_0^{Y_1}dy_1\int_a^{X_2}dx_2\int_b^{Y_2}dy_2\left\{\frac{f(l)}{l^4}\right\} \qquad (5)$$

Fig. 3(a) represents a superposition of the planes containing the two rectangles and indicates the relationship between the various limits.

First Transformation of Variables. The variables are first transformed as follows:

$x = x_1$	or	$x_1 = x$
$y = y_1$	or	$y_1 = y$
$\xi = x_2 - x_1$	or	$x_2 = \xi + x$
$\eta = y_2 - y_1$	or	$y_2 = \eta + y$

Nomenclature

k = absorption coefficient, ft^{-1}
l = length of line connecting any point on one surface with any point on the other surface
$u = \frac{x}{h}$, equation (13) or $\frac{x}{X}$ equation (61)
$w = Kz$, equation (27) or equation (71)
x, y = co-ordinates
ξ, η = transformed co-ordinates (parallel rectangles)
$z = \frac{l}{h}$, equation (13) or $\frac{l}{X}$, equation (61)
α, β, ρ = transformed co-ordinates, equation (53)
θ = angle between the normal to a surface and l
π = 3.141592 . . .
σ = Stefan-Boltzman constant
τ = geometrical transmission factor
$\phi(z)$ = transformed transmission function; $f(l/h)$, equation (13) or $f(l/X)$, equation (61)
$\Phi(w)$ = transformed transmission function = $\phi(kz)$

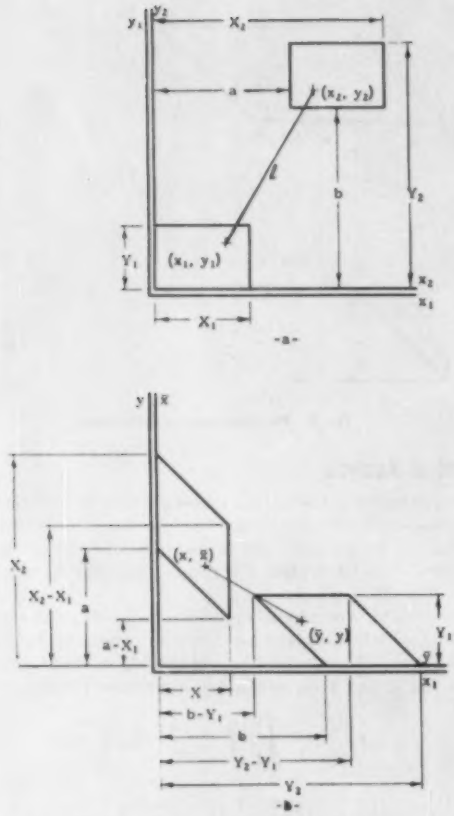

Fig. 3 Transformations of domains of integration for parallel rectangles

The Jacobian of this transformation is equal to unity, i.e., the transformation is area preserving.

The transformation is preceded by an exchange of co-ordinates which corresponds to a change in the order of integration. This is possible by virtue of the symmetric form of the integrand. The transformation is applied and the new co-ordinates (x, ξ) and (y, η) obtained. The limits of the new variables are determined by the transformation of the limits as follows: The boundary $x_2 = X_2 = \text{const}$ becomes $\xi = X_2 - x$ in Fig. 3(b); boundary $x_2 = a$ becomes $\xi = a - x$; boundary $y_2 = Y_2$ becomes $\eta = Y_2 - y$; and boundary $y_2 = b$ becomes $\eta = b - y$. The other boundaries remain unchanged.

Equation (5) in the new co-ordinates is:

$$I = \left[\int_{X_2-X_1}^{X_2} d\xi \int_0^{X_2-\xi} dx + \int_a^{X_2-X_1} d\xi \int_0^{X_1} dx + \int_{a-X_1}^{a} d\xi \int_{a-\xi}^{X_1} dx\right] \left[\int_{Y_2-Y_1}^{Y_2} d\eta \int_0^{Y_2-\eta} dy + \int_b^{Y_2-Y_1} d\eta \int_0^{Y_1} dy + \int_{b-Y_1}^{b} d\eta \int_{b-\eta}^{Y_1} dy\right] \left\{\frac{f(l)}{l^4}\right\} \quad (6)$$

where

$$l^2 = \xi^2 + \eta^2 + h^2 \quad (7)$$

Equations (6) and (7) are the generalized form for parallel opposed unequal rectangles (not directly opposed). There are six parameters which must be considered in evaluating the integral, X_1, X_2, Y_1, Y_2, a, and b. The function $f(l)$ has not been specified and remains unchanged under the transformation since l is an even function.

Restriction to Directly Opposed Rectangles. The geometric factors for unequal rectangles not directly opposed may be obtained from the factors for directly opposed equal rectangles when there is no absorption by the intervening medium. This can also be shown to be true for the case of absorption and no generality is lost by setting $a = b = 0$, $X_1 = X_2 = X$, and $Y_1 = Y_2 = Y$. Equation (6) then becomes:

$$I = \left[\int_0^X d\xi \int_0^{X-\xi} dx + \int_{-X}^0 d\xi \int_{-\xi}^X dx\right] \left[\int_0^Y d\eta \int_0^{Y-\eta} dy + \int_{-Y}^0 d\eta \int_{-\eta}^Y dy\right] \left\{\frac{f(l)}{l^4}\right\} \quad (8)$$

The most general case for parallel rectangles can be reduced to the evaluation of equation (8).

Since the variable l is not dependent upon the variables x and y, the first integration indicated in equation (8) can be performed without regard to the form of the transmission function. This gives:

$$I = \left[\int_0^X (X-\xi)d\xi + \int_{-X}^0 (X-\xi)d\xi\right]\left[\int_0^Y (Y-\eta)d\eta + \int_{-Y}^0 (Y+\eta)d\eta\right]\left\{\frac{f(l)}{l^4}\right\} \quad (9)$$

The second term of each bracketed term is simplified by changing the sign of the variable of integration:

$$I = \left[\int_0^X (X-\xi)d\xi - \int_X^0 (X-\xi)d\xi\right]\left[\int_0^Y (Y-\eta)d\eta - \int_Y^0 (Y-\eta)d\eta\right]\left\{\frac{f(l)}{l^4}\right\}$$

or

$$I = 4\left[\int_0^X (X-\xi)d\xi\right]\left[\int_0^Y (Y-\eta)d\eta\right]\left\{\frac{f(l)}{l^4}\right\} \quad (10)$$

Second Transformation of Variables. Equation (10) is reduced to an explicit function of two variables by the following transformation:

$$\begin{aligned} x &= \xi \quad \text{or} \quad \xi = x \\ l^2 &= \xi^2 + \eta^2 + h^2 \quad \text{or} \quad \eta^2 = l^2 - \xi^2 - h^2 \end{aligned} \quad (11)$$

The Jacobian of this transformation is equal to l/y. The new limits of integration in the x-l plane are shown in Fig. 4; the limits for x remain the same as for ξ; the limits of $y = 0$ become $l = \sqrt{x^2 + h^2}$ and for $\eta = Y$, the limits are $l = [x^2 + Y^2 + h^2]^{1/2}$.

The resulting expression is:

$$I = 4\left[\int_{\sqrt{Y^2+h^2}}^{\sqrt{X^2+Y^2+h^2}} dl \int_{\sqrt{l^2-Y^2-h^2}}^{X} dx + \int_{\sqrt{X^2+h^2}}^{\sqrt{Y^2+h^2}} dl \int_0^X dx + \int_h^{\sqrt{X^2+h^2}} dl \int_0^{\sqrt{l^2-h^2}} dx\right] \left[(X-x)\left(Y - \sqrt{l^2-x^2-h^2}\right)\frac{f(l)}{l^2(l^2-x^2-h^2)}\right] \quad (12)$$

Nondimensional Form. The perpendicular distance between the two rectangles is a convenient length to use as a nondimensionaliz-

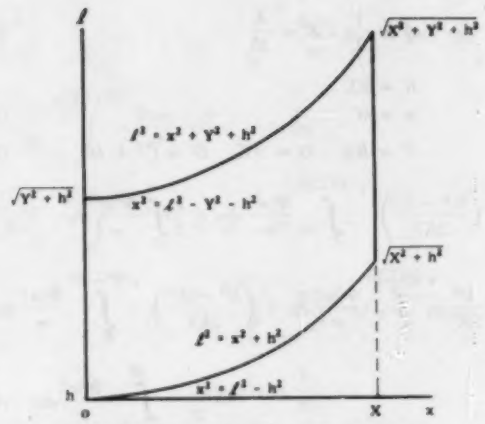

Fig. 4 Domain of integration in the (x,l)-plane

ing factor. The limits and variables may be redefined thus:

$$z = \frac{l}{h} \qquad u = \frac{x}{h} \qquad f(l) = \phi(z)$$
$$A = \frac{X}{h} \qquad B = \frac{Y}{h} \tag{13}$$

The limits are altered correspondingly. For example:

when $l = \sqrt{X^2 + Y^2 + h^2}$ then $z = \sqrt{A^2 + B^2 + 1}$

and when $x = \sqrt{l^2 - y^2 - h^2}$ then $u = \sqrt{z^2 - B^2 - 1}$

The function $f(l)$ has been changed to account for the change of variable.

The expression for the integral then becomes:

$$I = 4\left[\int_{\sqrt{B^2+1}}^{\sqrt{A^2+B^2+1}} dz \int_{\sqrt{z^2-B^2-1}}^{A} du + \int_{\sqrt{A^2+1}}^{\sqrt{B^2+1}} dz \int_{0}^{A} du + \int_{1}^{\sqrt{A^2+1}} dz \int_{0}^{\sqrt{z^2-1}} du\right]$$
$$\left[(A-u)(B-\sqrt{z^2-u^2-1})\frac{\phi(z)}{z^2\sqrt{z^2-u^2-1}}\right] \tag{14}$$

Reduction to a Function of a Single Variable. The preceding equation may be integrated with respect to u without specification of the transmission function $\phi(z)$. The result is an expression consisting of six terms:

$$I = 4\sum_{n=1}^{6} i_n \tag{15}$$

$$i_1 = AB\int_{\sqrt{A^2+1}}^{\sqrt{A^2+B^2+1}} \frac{\phi(z)}{z^3}\sin^{-1}\left[\frac{A}{\sqrt{z^2-1}}\right]dz \tag{16}$$

$$i_2 = -AB\int_{\sqrt{B^2+1}}^{\sqrt{A^2+B^2+1}} \frac{\phi(z)}{z^3}\cos^{-1}\left[\frac{B}{\sqrt{z^2-1}}\right]dz \tag{17}$$

$$i_3 = \left[\left(\frac{\pi AB-1}{2}\right)\int_{1}^{\sqrt{A^2+1}}\frac{\phi(z)}{z^3}dz\right]$$
$$-\left[\left(\frac{A^2}{2}\right)\int_{\sqrt{A^2+1}}^{\sqrt{A^2+B^2+1}}\frac{\phi(z)}{z^3}dz\right]$$
$$-\left[\left(\frac{B^2}{2}\right)\int_{\sqrt{B^2+1}}^{\sqrt{A^2+B^2+1}}\frac{\phi(z)}{z^3}dz\right]$$
$$+\left[\left(\frac{1}{2}\right)\int_{\sqrt{B^2+1}}^{\sqrt{A^2+B^2+1}}\frac{\phi(z)}{z^3}dz\right] \tag{18}$$

$$i_4 = \frac{1}{2}\int_{1}^{\sqrt{A^2+1}}\frac{\phi(z)}{z}dz - \frac{1}{2}\int_{\sqrt{B^2+1}}^{\sqrt{A^2+B^2+1}}\frac{\phi(z)}{z}dz \tag{19}$$

$$i_5 = B\int_{\sqrt{A^2+1}}^{\sqrt{A^2+B^2+1}}\frac{\phi(z)}{z^3}[z^2-(A^2+1)]^{1/2}dz$$
$$+ A\int_{\sqrt{B^2+1}}^{\sqrt{A^2+B^2+1}}\frac{\phi(z)}{z^3}[z^2-(B^2+1)]^{1/2}dz \tag{20}$$

$$i_6 = -A\int_{1}^{\sqrt{A^2+1}}\frac{\phi(z)}{z^3}\sqrt{z^2-1}\,dz$$
$$- B\int_{1}^{\sqrt{B^2+1}}\frac{\phi(z)}{z^3}\sqrt{z^2-1}\,dz \tag{21}$$

No additional simplification is possible without specifying the transmission function $\phi(z)$. A confirmation of the validity of the transformation and algebra is possible by setting the transmission equal to unity in equations (16) through (21). After integrating and combining terms, the result is:

$$I = 2\log\left\{\left[\frac{(A^2+1)(B^2+1)}{(A^2+B^2+1)}\right]^{1/2} + (B\sqrt{A^2+1})\tan^{-1}\frac{B}{\sqrt{A^2+1}} + (A\sqrt{B^2+1})\tan^{-1}\frac{A}{\sqrt{B^2+1}} - A\tan^{-1}A - B\tan^{-1}B\right\} \tag{22}$$

Equation (5) defines the relation between I and the geometrical transmission factor $\tau_{12}F_{12}$. Setting τ_{12} equal to unity gives:

$$F_{12} = \frac{I}{\pi AB} \tag{23}$$

Substitution of equation (22) into equation (23) yields the same relation as found in the literature for parallel directly opposed rectangles [1].

The function $f(l)$ represents either the absorption or transmission behavior of the intervening gas. In most cases, this behavior is directly proportional to the path length, i.e.,

$$f(l) = \bar{f}(kl) \tag{24}$$

or

$$\phi(z) = \Phi(kl) \tag{25}$$

If this situation exists, the preceding equations (15) through (21) can be modified by introducing the definitions:

$$K = kh \tag{26}$$

$$w = Kz = kl \tag{27}$$

The limits of the integrals may also be altered to conform with the new variable as follows:

$$\begin{aligned} C &= BK \\ D &= AK \\ E^2 &= C^2 + D^2 \end{aligned} \tag{28}$$

The relations given in equations (27) and (28) when applied to equations (15) through (21) yield:

$$i_1 = CD \int_{\sqrt{K^2+D^2}}^{\sqrt{K^2+E^2}} \frac{\Phi(w)}{w^3} \sin^{-1}\left(\frac{D}{\sqrt{w^2 - K^2}}\right) dw \tag{29}$$

$$i_2 = -CD \int_{\sqrt{K^2+C^2}}^{\sqrt{K^2+E^2}} \frac{\Phi(w)}{w^3} \cos^{-1}\left(\frac{C}{\sqrt{w^2 - K^2}}\right) dw \tag{30}$$

$$i_3 = \left(\frac{\pi CD - K^2}{2}\right) \int_K^{\sqrt{K^2+D^2}} \frac{\Phi(w)}{w^3} dw + \left(\frac{K^2 - C^2}{2}\right) \int_{\sqrt{K^2+C^2}}^{\sqrt{K^2+E^2}} \frac{\Phi(w)}{w^3} dw - \left(\frac{D^2}{2}\right) \int_{\sqrt{K^2+D^2}}^{\sqrt{K^2+E^2}} \frac{\Phi(w)}{w^3} dw \tag{31}$$

$$i_4 = -\frac{1}{2} \int_{\sqrt{K^2+C^2}}^{\sqrt{K^2+E^2}} \frac{\Phi(w)}{w} dw + \frac{1}{2} \int_K^{\sqrt{K^2+D^2}} \frac{\Phi(w)}{w} dw \tag{32}$$

$$i_5 = D \int_{\sqrt{K^2+C^2}}^{\sqrt{K^2+E^2}} \frac{\Phi(w)}{w^3} \sqrt{w^2 - (K^2 + C^2)}\, dw + C \int_{\sqrt{K^2+D^2}}^{\sqrt{K^2+E^2}} \frac{\Phi(w)}{w^3} \sqrt{w^2 - (K^2 + D^2)}\, dw \tag{33}$$

$$i_6 = -D \int_K^{\sqrt{K^2+D^2}} \frac{\Phi(w)}{w^3} \sqrt{w^2 - K^2}\, dw - C \int_K^{\sqrt{K^2+C^2}} \frac{\Phi(w)}{w^3} \sqrt{w^2 - K^2}\, dw \tag{34}$$

The expression for the geometrical transmission or absorption factor becomes:

$$A_1\tau_{12}F_{12} = \frac{h^2 I}{\pi} \quad \text{or} \quad \tau_{12}F_{12} = \frac{K^2 I}{\pi CD} \tag{35}$$

where

$$I = 4 \sum_{n=1}^{6} i_n \tag{36}$$

The foregoing equations are for the case of parallel opposed equal rectangles. The results for perpendicular, adjacent unequal rectangles is given by the following equations for the case of absorption or transmission directly proportional to path length (see Appendix):

$$A = \frac{Y}{X}; \quad B = \frac{Z}{X} \tag{37}$$

$$\begin{aligned} K &= kX \\ w &= kl \end{aligned} \tag{38}$$

$$C = BK, \quad D = AK, \quad E^2 = C^2 + D^2 \tag{39}$$

$$i_1 = \left(\frac{K^2 - C^2}{2K^2}\right) \int_C^{\sqrt{K^2+C^2}} \frac{\Phi(w)}{w} dw + \frac{1}{2} \int_K^C \frac{\Phi(w)}{w} dw - \frac{D^2}{2K^2} \int_D^{\sqrt{K^2+D^2}} \frac{\Phi(w)}{w} dw + \left(\frac{E^2 - K^2}{2K^2}\right) \int_E^{\sqrt{K^2+E^2}} \frac{\Phi(w)}{w} dw - \frac{1}{2} \int_{\sqrt{K^2+D^2}}^E \frac{\Phi(w)}{w} dw \tag{40}$$

$$i_2 = \left(\frac{3C^4 - K^4}{12K^2}\right) \int_C^{\sqrt{K^2+C^2}} \frac{\Phi(w)}{w^3} dw - \frac{K^2}{12} \int_K^C \frac{\Phi(w)}{w^3} dw + \left(\frac{2C^2K^2 + D^4}{4K^2}\right) \int_D^{\sqrt{K^2+D^2}} \frac{\Phi(w)}{w^3} dw - \frac{C^2}{2} \int_D^{\sqrt{K^2+C^2}} \frac{\Phi(w)}{w^3} dw + \left(\frac{6K^2E^2 + K^4 - 3E^4}{12K^2}\right) \int_E^{\sqrt{K^2+E^2}} \frac{\Phi(w)}{w^3} dw + \left(\frac{6E^2 + K^2}{12}\right) \int_{\sqrt{K^2+D^2}}^E \frac{\Phi(w)}{w^3} dw \tag{41}$$

$$i_3 = \frac{1}{4K^2} \int_C^{\sqrt{K^2+C^2}} w\Phi(w)dw - \frac{1}{4K^2} \int_0^K w\Phi(w)dw - \frac{1}{4K^2} \int_E^{\sqrt{K^2+E^2}} w\Phi(w)dw + \frac{1}{4K^2} \int_D^{\sqrt{K^2+D^2}} w\Phi(w)dw \tag{42}$$

$$i_4 = \frac{2}{3K} \int_0^K \Phi(w)dw \tag{43}$$

$$i_5 = -\frac{1}{K} \int_C^{\sqrt{K^2+C^2}} \frac{\Phi(w)}{w} \sqrt{w^2 - C^2}\, dw + \frac{1}{K} \int_E^{\sqrt{K^2+E^2}} \frac{\Phi(w)}{w} \sqrt{w^2 - E^2}\, dw - \frac{1}{K} \int_D^{\sqrt{K^2+D^2}} \frac{\Phi(w)}{w} \sqrt{w^2 - D^2}\, dw \tag{44}$$

$$i_6 = \frac{1}{3K} \int_C^{\sqrt{K^2+C^2}} \frac{\Phi(w)}{w^3} (w^2 - C^2)^{3/2} dw + \frac{1}{3K} \int_D^{\sqrt{K^2+D^2}} \frac{\Phi(w)}{w^3} (w^2 - D^2)^{3/2} dw$$

$$- \frac{1}{3K} \int_{E}^{\sqrt{K^2+E^2}} \frac{\Phi(w)}{w^3} (w^2 - E^2)^{3/2} dw \quad (45)$$

$$i_7 = \frac{D^2}{K} \int_{D}^{\sqrt{K^2+D^2}} \frac{\Phi(w)}{w^3} \sqrt{w^2 - D^2}\, dw$$

$$+ \frac{C^2}{K} \int_{C}^{\sqrt{K^2+C^2}} \frac{\Phi(w)}{w^3} \sqrt{w^2 - C^2}\, dw$$

$$- \frac{E^2}{K} \int_{E}^{\sqrt{K^2+E^2}} \frac{\Phi(w)}{w^3} \sqrt{w^2 - E^2}\, dw \quad (46)$$

$$A_1 \tau_{12} F_{12} = \frac{I}{\pi} \quad (47)$$

$$I = \sum_{n=1}^{7} i_n \quad (48)$$

Discussion

The method presented here for the evaluation of geometric absorption or transmission factors is an alternative method to the direct evaluation of equation (2). The difference between the two procedures is the reduction in the complexity of the integration process required by the method given herein. This has been replaced by the mathematics of transforming equation (2) into expressions such as equations (36) through (41). However, once this has been performed for a specific geometry, this method permits the introduction of any desired absorption or transmission function without interfering with the previous mathematics. In contrast to this, with equation (2), each function requires a new computation of a four-dimensional integral. Geometries other than the rectangular one have been successfully reduced by the procedure described and the technique is not limited to the rectangular system.

The use of different functions is important to the subject of geometric absorption and transmission factors. The use of an exponential transmission function has been subject to question and additional experimental evidence may indicate other functions should be used. Under these circumstances, the method given here may provide analytical expressions quickly without resorting to numerical computations. For example, the use of $f(l) = 1 - kl$ is directly integrable with equations (36) through (41) whereas substitution of this in equation (2) would necessitate an involved integration process. The complexity of integrating equation (2) for $f(l) = 1$ and a simple geometry is well demonstrated by Hamilton and Morgan [1].

The conventional methods of flux algebra [1, 2] may be used with the geometric absorption and transmission factors. This eliminates the need for additional calculations for surfaces not directly opposed or adjacent. Hottel and Cohen [3] confined their attention to a system composed of squares and, consequently, computed the case of squares offset from each other. However, the use of flux algebra necessitates computation of rectangles rather than squares. This increases the number of computations required but increases the applicability of the results since the surfaces do not have to be restricted to squares.

Numerical computation with the method given here is direct and less difficult than numerical calculation with equation (2). Instead of a quadruple numerical integration necessary with equation (2), single integrals involving simple functions are integrated. The use of the digital computer for evaluation of these integrals is facilitated by these conditions.

References

1 D. C. Hamilton and W. R. Morgan, "Radiant-Interchange Configuration Factors," NACA TN 2836, December, 1952.

2 H. C. Hottel, "Radiant Heat Transmission," chapter IV of W. H. McAdams, "Heat Transmission," McGraw-Hill Book Company, Inc., New York, N. Y., 1954.

3 H. C. Hottel and E. S. Cohen, "Radiant Heat Exchange in a Gas-Filled Enclosure," *Journal AIChE*, vol. 4, 1958, pp. 3–14.

4 W. E. Lobo and J. E. Evans, "Heat Transfer in the Radiant Section of Petroleum Heaters," *Trans. AIChE*, vol. 35, 1939, pp. 743–778.

5 A. K. Oppenheim, "Radiation Analysis by the Network Method," TRANS. ASME, vol. 78, 1956, pp. 725–735.

APPENDIX

Perpendicular Adjacent Rectangles With a Common Edge

The configuration to be considered is shown in Fig. 5. Substitution of the relations for θ_1, θ_2, and l into the general equation for the geometrical transmission factor (equation (2) or text) gives:

$$\tau_{12} F_{12} = \frac{1}{A_1} \int_{A_1} \int_{A_2} \frac{z_2 y_1}{\pi l^4} f(l)\, dA_1 dA_2 \quad (49)$$

where

$$l^2 = (x_1 - x_2)^2 + y_1^2 + z_2^2 \quad (50)$$

As discussed previously, the function $f(l)$ can also be an absorption function but the geometric transmission will be used to demonstrate the procedure. Rewriting in terms of the integral:

$$I = \pi A_1 \tau_{12} F_{12} = \int_0^X dx_1 \int_0^Y dy_1 \int_0^X dx_2 \int_0^Z dz_2 \left\{ \frac{z_2 y_1 f(l)}{l^4} \right\} \quad (51)$$

The order of integration is not important and the above integral may be written as:

$$I = \int_0^X dx_1 \int_0^X dx_2 \int_0^Y dy_1 \int_0^Z dz_2 \left\{ \frac{z_2 y_1 f(l)}{l^4} \right\} \quad (52)$$

First Transformation. The variables of integration are changed by the following transformation:

$$\begin{array}{llll} \alpha = x_1 & \text{or} & x_1 = \alpha \\ \beta = y_1 & \text{or} & y_1 = \beta \\ \bar{x} = x_2 - x_1 & \text{or} & x_2 = \bar{x} + \alpha \\ \rho^2 = y_1^2 + z_2^2 & \text{or} & z_2^2 = \rho^2 - \beta^2 \\ l^2 = \bar{x}^2 + \rho^2 & & \end{array} \quad (53)$$

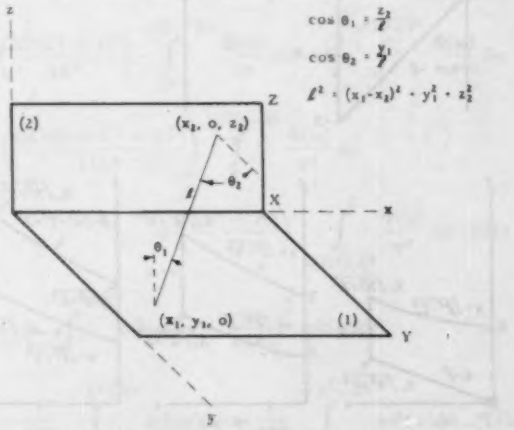

Fig. 5 Perpendicular adjacent rectangles

The Jacobian of this is equal to ρ/z_3.

$$I = \left[\int_0^X d\bar{x} \int_0^{X-\bar{x}} d\alpha + \int_{-X}^0 d\bar{x} \int_{-\bar{x}}^X d\alpha\right]$$

$$\left[\int_Y^{\sqrt{Y^2+Z^2}} d\rho \int_{\sqrt{\rho^2-Z^2}}^Y d\beta + \int_Z^Y d\rho \int_{\sqrt{\rho^2-Z^2}}^{\rho} d\beta + \int_0^Z d\rho \int_0^{\rho} d\beta\right]$$

$$\left\{\frac{\rho\beta f(l)}{l^4}\right\} \quad (54)$$

Since the transmission function $f(l)$, is not a function of the variables α and β, the first integration may be performed. This yields:

$$I = \frac{1}{2}\left[\int_0^X (X-\bar{x})d\bar{x} + \int_{-X}^0 (X+\bar{x})d\bar{x}\right]$$

$$\left[\int_Y^{\sqrt{Y^2+Z^2}} (Y^2+Z^2-\rho^2)d\rho + \int_Z^Y Z^2 d\rho + \int_0^Z \rho^2 d\rho\right]\left\{\frac{\rho f(l)}{l^4}\right\} \quad (55)$$

This expression may be simplified by noting:

$$\int_{-X}^0 (X+\bar{x})f(\bar{x}^2)d\bar{x} = \int_0^X (X-x)f(x^2)dx$$

Then

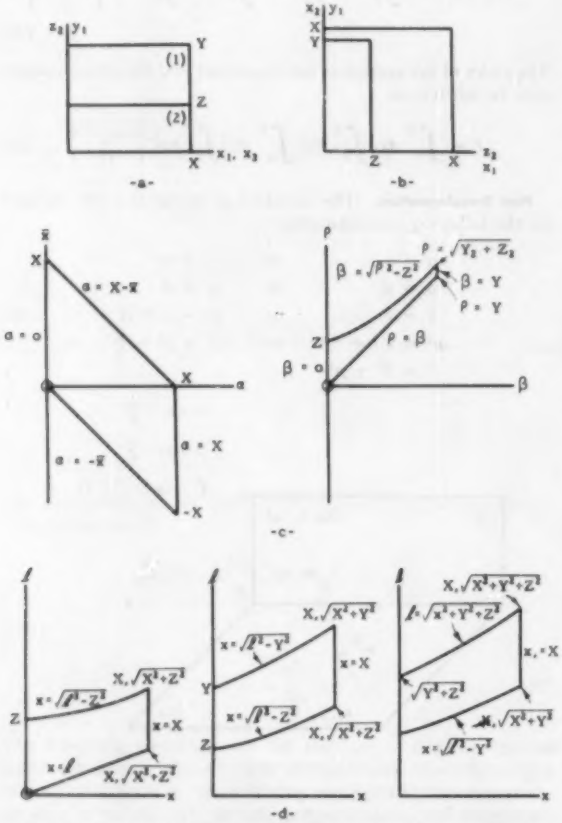

Fig. 6 Domains of integration for perpendicular adjacent rectangles

$$I = \left[\int_0^X (X-\bar{x})dx\right]\left[\int_0^Z \rho^2 d\rho + \int_Z^Y Z^2 d\rho + \int_Y^{\sqrt{Y^2+Z^2}} (Y^2+X^2-\rho^2)d\rho\right]\left\{\frac{\rho f(l)}{l^4}\right\} \quad (56)$$

Second Transformation. Equation (55) is further simplified by the following transformation:

$$x = \bar{x} \quad \text{or} \quad \bar{x} = x$$
$$l^2 = x^2 + \rho^2 \quad \text{or} \quad \rho^2 = l^2 - \bar{x}^2 = l^2 - x^2 \quad (57)$$

The Jacobian for this transformation is equal to $1/\rho$. The expression for the integral after multiplying by the value of the Jacobian is:

$$I = \left[\int_Z^{\sqrt{X^2+Y^2}} dl \int_{\sqrt{l^2-Z^2}}^X dx + \int_X^Z dl \int_0^X dx + \int_0^X dl \int_0^l dx\right]\left\{\frac{(X-x)(l^2-x^2)f(l)}{l^3}\right\}$$

$$+\left[\int_Y^{\sqrt{X^2+Y^2}} dl \int_{\sqrt{l^2-Y^2}}^X dx + \int_{\sqrt{X^2+Z^2}}^Y dl \int_0^X dx + \int_Z^{\sqrt{X^2+Z^2}} dl \int_0^{\sqrt{l^2-Z^2}} dx\right]\left\{(X-x)Z^2\frac{f(l)}{l^3}\right\}$$

$$+\left[\int_{\sqrt{Y^2+Z^2}}^{\sqrt{X^2+Y^2+Z^2}} dl \int_{\sqrt{l^2-Y^2-Z^2}}^X dx + \int_{\sqrt{X^2+Y^2}}^{\sqrt{Y^2+Z^2}} dl \int_0^X dx + \int_Y^{\sqrt{X^2+Y^2}} dl \int_0^{\sqrt{l^2-Y^2}} dx\right]\left\{\frac{(X-x)(Y^2+Z^2-l^2-x^2)f(l)}{l^3}\right\} \quad (58)$$

The various transformations are indicated in Fig. 6.

Nondimensional Variables. The length of the mutual edge is the most convenient nondimensionalizing factor. The variables are redefined as follows:

$$z = \frac{l}{X} \quad A = \frac{Y}{X} \quad u = \frac{x}{X} \quad B = \frac{Z}{X} \quad f(l) = \phi(z)$$

The nondimensional form of equation (58) is:

$$\frac{I}{X^2} = \left[\int_B^{\sqrt{B^2+1}} dz \int_{\sqrt{z^2-B^2}}^1 du + \int_1^B dz \int_0^1 du + \int_0^1 dz \int_0^z du\right]\left\{\frac{(1-u)(z^2-u^2)\phi(z)}{z^3}\right\}$$

$$+\left[\int_A^{\sqrt{A^2+1}} dz \int_{\sqrt{z^2-A^2}}^1 du + \int_{\sqrt{B^2+1}}^A dz \int_0^1 du + \int_B^{\sqrt{B^2+1}} dz \int_0^{\sqrt{z^2-B^2}} du\right]\left\{\frac{(1-u)B^2\phi(z)}{z^3}\right\} \quad (59)$$

$$+\left[\int_{\sqrt{A^2+B^2}}^{\sqrt{A^2+B^2+1}} dz \int_{\sqrt{z^2-(A^2+B^2)}}^{1} du + \int_{\sqrt{A^2+1}}^{\sqrt{A^2+B^2}} dz \int_0^1 du + \int_A^{\sqrt{A^2+1}} dz \int_0^{\sqrt{z^2-A^2}} du\right]\left\{\frac{(1-u)(A^2+B^2-z^2+u^2)\phi(z)}{z^3}\right\}$$

Reduction to a Function of a Single Variable. The transmission function $\phi(z)$ is not dependent upon the variable u. Therefore equation (62) may be integrated with respect to u without specifying the form of $\phi(z)$. Performing this and collecting terms,

$$I = X^2 \sum_{n=1}^{7} i_n \tag{60}$$

$$i_1 = \left(\frac{1-B^2}{2}\right)\int_B^{\sqrt{B^2+1}} \frac{\phi(z)}{z}\,dz + \frac{1}{2}\int_1^B \frac{\phi(z)}{z}\,dz - \frac{A^2}{2}\int_A^{\sqrt{A^2+1}} \frac{\phi(z)}{z}\,dz + \left(\frac{E^2-1}{2}\right)\int_E^{\sqrt{A^2+B^2+1}} \frac{\phi(z)}{z}\,dz - \frac{1}{2}\int_{\sqrt{A^2+1}}^{\sqrt{A^2+B^2}} \frac{\phi(z)}{z}\,dz \tag{61}$$

$$i_2 = \left(\frac{3B^4-1}{12}\right)\int_B^{\sqrt{B^2+1}} \frac{\phi(z)}{z^3}\,dz - \frac{1}{12}\int_1^B \frac{\phi(z)}{z^3}\,dz + \left(\frac{2B^2+A^4}{4}\right)\int_A^{\sqrt{A^2+1}} \frac{\phi(z)}{z^3}\,dz - \frac{B^2}{2}\int_A^{\sqrt{B^2+1}} \frac{\phi(z)}{z^3}\,dz + \left[\frac{6(A^2+B^2)+1-3(A^2+B^2)^2}{12}\right]\int_{\sqrt{A^2+B^2}}^{\sqrt{A^2+B^2+1}} \frac{\phi(z)}{z^3}\,dz + \left[\frac{6(A^2+B^2)+1}{12}\right]\int_{\sqrt{A^2+1}}^{\sqrt{A^2+B^2}} \frac{\phi(z)}{z^3}\,dz \tag{62}$$

$$i_3 = \frac{1}{4}\int_B^{\sqrt{B^2+1}} z\phi(z)dz - \frac{1}{4}\int_0^1 z\phi(z)dz - \frac{1}{4}\int_{\sqrt{A^2+B^2}}^{\sqrt{A^2+B^2+1}} z\phi(z)dz + \frac{1}{4}\int_A^{\sqrt{A^2+1}} z\phi(z)dz \tag{63}$$

$$i_4 = \frac{2}{3}\int_0^1 \phi(z)dz \tag{64}$$

$$i_5 = -\int_B^{\sqrt{B^2+1}} \frac{\phi(z)\sqrt{z^2-B^2}}{z}\,dz + \int_{\sqrt{A^2+B^2}}^{\sqrt{A^2+B^2+1}} \frac{\phi(z)\sqrt{z^2-A^2-B^2}}{z}\,dz - \int_A^{\sqrt{A^2+1}} \frac{\phi(z)\sqrt{z^2-A^2}}{z}\,dz \tag{65}$$

$$i_6 = \frac{1}{3}\int_B^{\sqrt{B^2+1}} \frac{\phi(z)}{z^3}(z^2-B^2)^{3/2}dz + \frac{1}{3}\int_A^{\sqrt{A^2+1}} \frac{\phi(z)}{z^3}(z^2-A^2)^{3/2} - \frac{1}{3}\int_{\sqrt{A^2+B^2}}^{\sqrt{A^2+B^2+1}} \frac{\phi(z)}{z^3}(z^2-A^2-B^2)^{3/2}dz \tag{66}$$

$$i_7 = A^2\int_A^{\sqrt{A^2+1}} \frac{\phi(z)}{z^3}\sqrt{z^2-A^2}\,dz + B^2\int_B^{\sqrt{B^2+1}} \frac{\phi(z)}{z^3}\sqrt{z^2-B^2}\,dz - (A^2+B^2)\int_{\sqrt{A^2+B^2}}^{\sqrt{A^2+B^2+1}} \frac{\phi(z)}{z^3}\sqrt{z^2-A^2-B^2}\,dz \tag{67}$$

If the absorption or transmission function may be written as:

$$\phi(z) = \Phi(kl) \tag{68}$$

then the following modification of the variables can be made:

$$K = kX \tag{69}$$

$$w = zK = kl \tag{70}$$

$$C = BK; \quad D = AK; \quad E^2 = C^2 + D^2 \tag{71}$$

Equations (61) through (67) become:

$$i_1 = \left(\frac{K^2-C^2}{2K^2}\right)\int_C^{\sqrt{K^2+C^2}} \frac{\Phi(w)}{w}\,dw + \frac{1}{2}\int_K^C \frac{\Phi(w)}{w}\,dw - \frac{D^2}{2K^2}\int_D^{\sqrt{K^2+D^2}} \frac{\Phi(w)}{w}\,dw + \left(\frac{E^2-K^2}{2K^2}\right)\int_E^{\sqrt{K^2+E^2}} \frac{\Phi(w)}{w} - \frac{1}{2}\int_{\sqrt{K^2+D^2}}^E \frac{\Phi(w)}{w}\,dw \tag{72}$$

$$i_2 = \left(\frac{3C^4-K^4}{12K^2}\right)\int_C^{\sqrt{K^2+C^2}} \frac{\Phi(w)}{w^3}\,dw - \frac{K^2}{12}\int_K^C \frac{\Phi(w)}{w^3}\,dw + \left(\frac{2C^2K^2+D^4}{4K^2}\right)\int_D^{\sqrt{K^2+D^2}} \frac{\Phi(w)}{w^3}\,dw - \frac{C^2}{2}\int_D^{\sqrt{K^2+C^2}} \frac{\Phi(w)}{w^3}\,dw + \left(\frac{6K^2E^2+K^4+3E^4}{12K^2}\right)\int_E^{\sqrt{K^2+E^2}} \frac{\Phi(w)}{w^3}\,dw + \left(\frac{6E^2+K^2}{12}\right)\int_{\sqrt{K^2+D^2}}^E \frac{\Phi(w)}{w^3}\,dw \tag{73}$$

$$i_4 = \frac{1}{4K^2}\int_C^{\sqrt{K^2+C^2}} w\Phi(w)dw - \frac{1}{4K^2}\int_0^K w\Phi(w)dw - \frac{1}{4K^2}\int_E^{\sqrt{K^2+E^2}} w\Phi(w)dw + \frac{1}{4K^2}\int_D^{\sqrt{K^2+D^2}} w\Phi(w)dw \tag{74}$$

$$i_4 = \frac{2}{3K}\int_0^K \Phi(w)\,dw \tag{75}$$

$$i_5 = -\frac{1}{K}\int_C^{\sqrt{K^2+C^2}} \frac{\Phi(w)}{w}\sqrt{w^2 - C^2}\,dw + \frac{1}{K}\int_E^{\sqrt{K^2+E^2}} \frac{\Phi(w)}{w}\sqrt{w^2 - E^2}\,dw - \frac{1}{K}\int_D^{\sqrt{K^2+D^2}} \frac{\Phi(w)}{w}\sqrt{w^2 - D^2}\,dw \tag{76}$$

$$i_6 = \frac{1}{3K}\int_C^{\sqrt{K^2+C^2}} \frac{\Phi(w)}{w^3}(w^2 - C^2)^{3/2}\,dw + \frac{1}{3K}\int_D^{\sqrt{K^2+D^2}} \frac{\Phi(w)}{w^3}(w^2 - D^2)^{3/2}dw - \frac{1}{3K}\int_E^{\sqrt{K^2+E^2}} \frac{\Phi(w)}{w^3}(w^2 - E^2)^{3/2}dw \tag{77}$$

$$i_7 = \frac{D^2}{K}\int_D^{\sqrt{K^2+D^2}} \frac{\Phi(w)}{w^3}\sqrt{w^2 - D^2}\,dw + \frac{C^2}{K}\int_C^{\sqrt{K^2+C^2}} \frac{\Phi(w)}{w^3}\sqrt{w^2 - C^2}\,dw - \frac{E^2}{K}\int_E^{\sqrt{K^2+E^2}} \frac{\Phi(w)}{w^3}\sqrt{w^2 - E^2}\,dw \tag{78}$$

$$A_1\tau_{12}F_{12} = \frac{I}{\pi} \tag{79}$$

DISCUSSION

D. K. Edwards[2]

The authors are to be commended for their simplification of the geometric transmission or absorption factor for two technically important geometries. Such work is needed to make possible application of the network method[3] for real gases through use of the band energy approximation.[4]

One important outcome of the authors' work should be comparison of the accuracy of using the *geometric mean beam length* defined by

$$\bar{l}_G = \frac{\frac{1}{\pi}\int_{A_1}\int_{A_2} l\,\frac{\cos\theta_1\cos\theta_2}{l^2}\,dA_1dA_2}{\frac{1}{\pi}\int_{A_1}\int_{A_2}\frac{\cos\theta_1\cos\theta_2}{l^2}\,dA_1dA_2}$$

in place of the *true mean beam length* defined by the expression

$$f(\bar{l}) = \frac{\frac{1}{\pi}\int_{A_1}\int_{A_2} f(l)\,\frac{\cos\theta_1\cos\theta_2}{l^2}\,dA_1dA_2}{\frac{1}{\pi}\int_{A_1}\int_{A_2}\frac{\cos\theta_1\cos\theta_2}{l^2}\,dA_1\,dA_2}$$

Present industrial practice[5] is to use the geometric mean beam length multiplied by a factor of 0.9 or so in place of the true mean beam length. For the case of parallel rectangles the error involved in using the geometric mean beam length is less than 6 per cent.

It would be interesting to see the authors carry out the indicated integration for perpendicular adjacent rectangles with technically important absorption functions such as $Cl^{1/3}$ and $Cl^{2/3}$ and determine the error in using the geometric mean beam length in place of the true mean beam length.

In connection with the above comparison, it should be noted that the network method should be applied only to surfaces which are uniformly irradiated by each other, since it is assumed that the same geometric transmission function applies for reflected as well as emitted energy. It would appear that, if an enclosure is sufficiently subdivided so that the nodal surfaces are uniformly irradiated by each other, the geometric mean beam length would always be a quite good approximation to the true mean beam length.

If the comparison suggested shows this situation to be the case, it is suggested also that the authors carry out integration with $f(l) = l$ and present tables or graphs of the geometric mean beam length as functions of their parameters A and B.

Authors' Closure

The authors wish to express their appreciation for the thoughtful discussion contributed by Professor Edwards. His suggestions are indeed very pertinent to our own views and we are, in fact, planning to carry them out. However, the only way to proceed from now on is by numerical computation. The present paper sets up only the background for such purpose. In the meantime, some of the geometric factors have been evaluated by the use of the Electrodata 204 computer, and we are certainly planning to present the results in the near future.

---

[2] Asst. Professor of Engineering, University of California, Los Angeles, Calif. Assoc. Mem. ASME.

[3] Authors' Reference [5].

[4] R. V. Dunkle and J. T. Bevans, "Radiant Interchange Within an Enclosure," JOURNAL OF HEAT TRANSFER, TRANS. ASME, Series C, vol. 82, 1960, pp. 1–19.

[5] Authors' Reference [2].

C. M. USISKIN
Lewis Research Center, NASA, Cleveland, Ohio. At present, Radio Corporation of America, Astro-Electronic Products Division, Princeton, N. J. Assoc. Mem. ASME

R. SIEGEL
Lewis Research Center, NASA, Cleveland, Ohio. Assoc. Mem. ASME

Thermal Radiation From a Cylindrical Enclosure With Specified Wall Heat Flux

Thermal radiation is considered from the inside surface of a heated cylindrical enclosure. A specified heat input is imposed at the enclosure wall and the surface temperature distribution is determined. The analysis considers both black and diffuse gray-body radiation and obtains a simple relation between the two. The energy equation, which is a linear integral equation, is solved by three methods: (a) Use of a separable kernel; (b) numerical integration; and (c) variational methods.

Introducing radiation into heat-transfer problems results in changing the energy equation from a differential equation to an integro-differential equation. For the case where heat transfer is only by radiation, which we consider here, the energy equation simplifies to a linear integral equation in the variable U representing the total radiation flux leaving the surface or, for black bodies, σT^4. Although we consider only a special case in pure radiation, the methods presented here could be applied to other similar radiation problems.

Specifically, we consider thermal radiation from the internal surface of a cylindrical enclosure open at both ends as shown in Fig. 1. The internal surface is heated by a specified heat flux which is a function of axial position, and the wall temperature is found from the analysis. The radiation from the surface may either be black or diffuse gray body. Heat conduction within the enclosure wall is assumed negligible compared with the radiation fluxes, and the enclosure is assumed to be in a vacuum so that heat convection does not enter the problem. Each end of the cylinder sees an outside environment which may each be at a different specified temperature.

Contributed by the Heat Transfer Division and presented at the Annual Meeting, Atlantic City, N. J., November 29–December 4, 1959, of The American Society of Mechanical Engineers.

Note: Statements and opinions advanced in papers are to be understood as individual expressions of their authors and not those of the Society. Manuscript received at ASME Headquarters, August 26, 1959. Paper No. 59—A-159.

With the foregoing assumptions the energy equation governing the radiation process is found to be a linear integral equation, and the linearity permits building more general solutions by superposition of elementary situations. The necessary elementary solutions are found by three different methods: (*a*) Use of an approximate separable kernel; (*b*) numerical integration; and (*c*) a variational method.

In the analysis we first consider the black-body case and then extend the results to include the more general situation of diffuse gray-body radiation.

Energy Balance (Black Body)

Consider the heat quantities entering and leaving an element dA_1, Fig. 1, located at position x on the internal surface of the

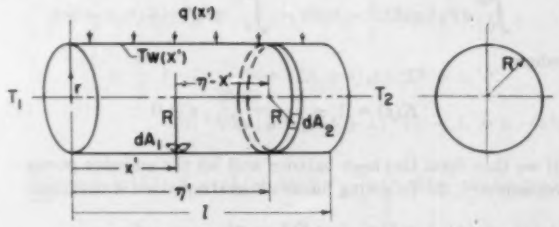

Fig. 1 Hollow cylinder enclosure

Nomenclature

A, B, C, D, E = coefficients determined by the variational method
dA_1, dA_2 = elementary areas on cylindrical surface, Fig. 1
F = configuration factor for a circular element radiating to a perpendicular element
J = variational principle for Φ; J_q, variational principle for $\Phi_q{}^*$
K = area-factor kernel in integral equation
l = length of cylindrical enclosure
L = dimensionless length, $l/2R$
M, N, P = functions of L defined in Equation (13)
q = heat added per unit area at enclosure wall
R = radius of cylindrical enclosure
r = radial co-ordinate measured from cylinder axis
T = absolute temperature; T_w, absolute wall temperature; T_1, T_2, temperatures of environments seen at ends of enclosure
U = total radiation leaving surface per unit area
x = dimensionless axial co-ordinate, $x'/2R$
x' = axial length co-ordinate measured from one end of enclosure
z = length defined as $|x - \eta|$
α = exponent in approximate separable kernel
β = exponent in approximation for F
ϵ = emissivity
η' = dummy integration variable; η, dimensionless variable $\eta'/2R$
ρ = reflectivity
σ = Stefan-Boltzmann constant
Φ = wall emissive power for $q = 0$ and one end of enclosure exposed to unit emissive power
Φ_q = wall emissive power for specified q at walls; $\Phi_q{}^*$, defined as Φ_q/q
φ = emissive power (σT^4); φ_w, wall emissive power; φ_1, φ_2, emissive powers of environments seen at ends of enclosure

cylindrical enclosure. The heat radiated from the element per unit area is given by the emissive power (we are here considering only black-body radiation),

$$\sigma T_w^4(x) \tag{1}$$

The heat input to the surface element is composed of four quantities. The first is the imposed heat flux at the wall, which on a unit area basis is simply $q(x)$. The second and third are the heat inputs q_1 and q_2 from the constant environment temperatures T_1 and T_2 at the ends of the enclosure. These environments can be replaced by fictitious black-body surfaces at the ends of the cylinder. The configuration factor which then applies is for a circular area radiating to an element in a plane perpendicular to the circle and this has been given elsewhere.[1,2] Hence we can immediately write

$$q_1 = \sigma T_1^4 F(x) \tag{2a}$$

$$q_2 = \sigma T_2^4 F(L - x) \tag{2b}$$

where

$$F(x) = \left[\frac{x^2 + (1/2)}{(x^2 + 1)^{1/2}} - x\right]$$

Note that throughout the analysis, all length quantities have been made dimensionless by dividing by the tube diameter. The fourth heat input is the radiation to dA_1 from all other elements such as dA_2 on the internal surface of the cylinder. This is obtained by integrating, over the enclosure, the product of the emissive power of dA_2 and the configuration factor between dA_2 and dA_1. From the previous references[1,2] this results in the following expression:

$$\int_0^x \sigma T_w^4(\eta) K(x - \eta) d\eta + \int_x^L \sigma T_w^4(\eta) K(\eta - x) d\eta$$

where

$$K(z) = 1 - \frac{z^2 + 3z/2}{(z^2 + 1)^{1/2}} \quad z \geq 0 \tag{3}$$

If we then form the heat balance and let the emissive power φ replace σT^4, the following linear integral equation is obtained:

$$\varphi_w(x) = q(x) + \varphi_1 F(x) + \varphi_2 F(L - x) + \int_0^x \varphi_w(\eta) K(x - \eta) d\eta + \int_x^L \varphi_w(\eta) K(\eta - x) d\eta \tag{4}$$

We now proceed to solve this equation for $\varphi_w(x)$ when $q(x)$ is specified.

Superposition of Solutions (Black Body)

Since the energy equation is linear in φ, a complete solution can be formed by superposing three elementary solutions as illustrated in Fig. 2. In the first problem the surroundings are all at φ_2 and there is no imposed heat input at the enclosure surface. The surface must then come to equilibrium at the same temperature as the surroundings, and we have the trivial result that φ at the wall is equal to φ_2. In the second problem the surroundings are at absolute zero temperature and there is a heat input $q(x)$ at the wall. The solution for this situation will be designated by $\Phi_q(x)$. For the third problem the environment at one end of the enclosure is at a constant emissive power, $\varphi_1 - \varphi_2$, and $q(x)$ is zero.

[1] H. Buckley, "On the Radiation From the Inside of a Circular Cylinder," Part I, *Philosophical Magazine*, vol. 4, 1927, pp. 753–762. Part II, *Philosophical Magazine*, vol. 6, 1928, pp. 447–457.

[2] H. C. Hottel and J. D. Keller, "Effect of Reradiation on Heat Transmission in Furnaces and Through Openings," TRANS. ASME, vol. 55, 1933, pp. 39–49.

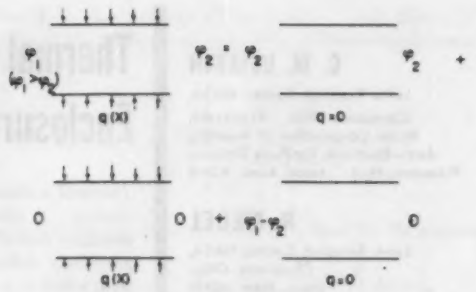

Fig. 2 Superposition of elementary solutions

For the case when $\varphi_1 - \varphi_2$ has a value of unity the solution is termed $\Phi(x)$. By superposition the general solution to Equation (4) is then

$$\varphi_w(x) = \varphi_2 + \Phi_q(x) + (\varphi_1 - \varphi_2)\Phi(x) \tag{5}$$

We shall first consider the solution for $\Phi_q(x)$ and then discuss the function $\Phi(x)$.

Solution for Specified Heat Input With Surroundings at Zero (Black Body)

In this section the solution for $\Phi_q(x)$ will be found. We shall limit the discussion to the case where $q(x)$ is a constant, although the methods used can be applied for the more general case of variable heat input with length. With $\varphi_1 = \varphi_2 = 0$, and letting $\Phi_q^*(x) = \Phi_q(x)/q$, Equation (4) reduces to the following relation for $\Phi_q^*(x)$:

$$\Phi_q^*(x) = 1 + \int_0^x \Phi_q^*(\eta) K(x - \eta) d\eta + \int_x^L \Phi_q^*(\eta) K(\eta - x) d\eta \tag{6}$$

Equation (6) will now be solved using three different methods.

Approximate Separable Kernel. The kernel $K(z)$ in Equation (6) has been plotted in Fig. 3, and it is seen that it has the general shape of an exponential function. We then try to approximate $K(z)$ by the more convenient function $e^{-\alpha z}$.[3] To choose the constant α, consider an infinite isothermal cylindrical enclosure. Then by imposing the condition that there be a heat balance on any element of the internal surface it is seen that

$$2 \int_0^\infty K(z) dz = 1 \tag{7}$$

This condition is then applied to the approximate kernel so that

$$\int_0^\infty e^{-\alpha z} dz = 1/2 \tag{7a}$$

or $\alpha = 2$. The kernel e^{-2z} is given in Fig. 3, and it is seen that the agreement with the exact kernel is quite good. The approximation is then substituted into Equation (6) with the result

$$\Phi_q^*(x) = 1 + \frac{1}{e^{2x}} \int_0^x \Phi_q^*(\eta) e^{2\eta} d\eta + e^{2x} \int_x^L \Phi_q^*(\eta) \frac{1}{e^{2\eta}} d\eta \tag{8}$$

The advantage of this method is now evident since by means of the separable kernel the quantities involving x have been taken out from under the integral signs, and the integral equation can

[3] This approximation has been used, with good results, by Buckley.[1] As shown there, the solution can be obtained to increasing degrees of accuracy by employing a series of exponential terms to approximate $K(z)$.

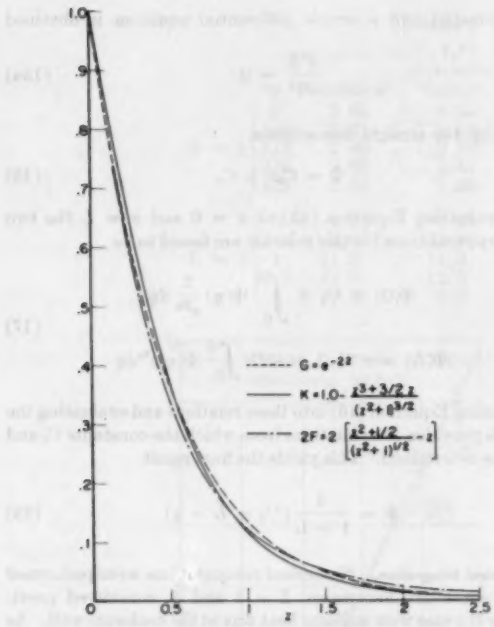

Fig. 3 Exact and approximate configuration factors

now be solved quite easily. By differentiating the equation twice, the integrals can be removed and a simple differential equation is obtained

$$\frac{d^2\Phi_q^*}{dx^2} = -4 \tag{8a}$$

This has the general solution

$$\Phi_q^* = -2x^2 + C_1x + C_2 \tag{9}$$

From symmetry we know that, at $x = L/2$, $d\Phi_q^*/dx = 0$, and hence $C_1 = 2L$. To determine C_2 we evaluate the integral Equation (8) at $x = 0$ and $x = L$ and utilize the fact that $T_w(0) = T_w(L)$. This yields the boundary condition,

$$\int_0^L \Phi_q^*(\eta)\frac{1}{e^{2\eta}}\,d\eta = \frac{1}{e^{2L}}\int_0^L \Phi_q^*(\eta)e^{2\eta}d\eta$$

Inserting $\Phi_q^* = -2x^2 + 2Lx + C_2$ into this relation gives $C_2 = L + 1$, so that the final result for Φ_q^* is the parabola

$$\Phi_q^* = L + 1 + 2(xL - x^2) \tag{9a}$$

The next step in the analysis was to test this simple expression by performing a direct numerical integration of Equation (6) for a few sample cases.

Numerical Integration. The integrals in Equation (6) were placed in finite-difference form and numerical computations were carried out for enclosures with length-diameter ratios of 1 and 4. In the numerical method the enclosure length was divided into equal increments and the wall temperature at each position was expressed in terms of the temperatures at the other positions. This resulted in a system of simultaneous equations which were solved on an IBM 704 digital computer. The increment sizes were cut in half until convergence was obtained. Some of the final results are given in Table 1, and it is seen that although the temperatures obtained numerically deviate by several per cent from the parabola obtained in the previous section, the curves are still very close to being parabolic in shape. It appears then, that a parabola provides a good approximation, at least in the range of small L which was considered, to the solution of the integral equation. With this in mind we then turn to variational methods which provide a means for determining the parabola which will best approximate the solution.

Variational Method. As shown elsewhere,[4] an integral equation of the Fredholm type, such as Equation (6), can be solved by obtaining an extremum of the associated variational principle,

$$J_q = \int_0^L\int_0^L K(|\eta - x|)\Phi_q^*(\eta)\Phi_q^*(x)dx\,d\eta - \int_0^L [\Phi_q^*(x)]^2dx + 2\int_0^L \Phi_q^*(x)dx \tag{10}$$

Since $\Phi_q^*(x)$ may be simply approximated by a parabola (a higher order polynomial could be used if necessary) we let

$$\Phi_q^*(x) = A + Bx + Cx^2 \tag{11}$$

Actually from symmetry about $x = L/2$ we know that $B = -CL$, but we shall use Equation (11) in its present form since this will enable part of the work to be utilized again in a later section. Equation (11) is then substituted into Equation (10) and the integration is carried out. The algebra involved in the double integral is considerable and very lengthy expressions are obtained which will not be given here. The resulting expression gives J_q in terms of the three coefficients A, B, and C. To obtain an extremum we follow the Ritz procedure (see for example Hildebrand,[5] or Courant and Hilbert[6] and differentiate J_q separately with respect to each of the coefficients and set each of the three resulting equations equal to zero. This yields,

$$\frac{\partial J_q}{\partial A} = 0 \rightarrow AL[-L + (L^2+1)^{1/2}] + \frac{B}{2}L^2[-L + (L^2+1)^{1/2}] + \frac{C}{3}\{-L^3 - L + (L^2 + {}^1/_4L)(L^2+1)^{1/2} + {}^3/_4\ln[L + (L^2+1)^{1/2}]\} - L = 0 \tag{12a}$$

$$\frac{\partial J_q}{\partial B} = 0 \rightarrow AL[-L + (L^2+1)^{1/2}] + \frac{B}{2}\left\{-L^2 + {}^1/_3(L^2+1)^{1/2} - \frac{1}{2L}\ln[L + (L^2+1)^{1/2}] + L^2(L^2+1)^{1/2}\right\} + \frac{C}{3}L[-L^2 - 1 + (L^2+1)^{1/2}] - L = 0 \tag{12b}$$

$$\frac{\partial J_q}{\partial C} = 0 \rightarrow A\{2L^2 + 2L - {}^3/_2\ln[L + (L^2+1)^{1/2}] - (2L^2 + {}^1/_2L)(L^2+1)^{1/2}\} + BL^2[(L^2+1) - (L^2+1)^{3/2}] + C\{{}^3/_8L^3 + {}^4/_4L^2 - ({}^3/_8L^3 + {}^7/_8L^2 + {}^1/_4L)(L^2+1)^{1/2} + {}^1/_4\ln[L + (L^2+1)^{1/2}]\} + 2L^2 = 0 \tag{12c}$$

If Equation (12a) is subtracted from (12b) the result immediately gives the relation $B = -CL$, which was mentioned before as necessary for the wall-temperature distribution to be symmetric about $x = L/2$. Equations (12) are then solved simultaneously for A and C which gives the final form,

[4] R. Courant and D. Hilbert, "Methods of Mathematical Physics," first English edition, vol. 1, Interscience Publishers, Inc., New York and London, 1953, p. 205.

[5] F. B. Hildebrand, "Methods of Applied Mathematics," Prentice-Hall, Inc., New York, N. Y., 1952, p. 187.

[6] Loc. cit., p. 175.

$$\Phi_q^* = \frac{M(L)}{P(L)} + \frac{N(L)}{P(L)}(xL - x^2) \tag{13}$$

where

$$M(L) = {}^2/_3L^4 + {}^1/_3L^2(L^2+1)^{1/2} - \left(L^2 + \frac{L}{2}\right)\ln\left[L + (L^2+1)^{1/2}\right]$$

$$N(L) = -4L^2 + 3L\ln\left[L + (L^2+1)^{1/2}\right] + L^2(L^2+1)^{1/2}$$

$$P(L) = {}^1/_6L^6 + {}^7/_{12}L^4 - {}^{11}/_{12}L^2 + \left[-{}^1/_6L^5 - {}^1/_3L^3 + {}^5/_6L^3\right](L^2+1)^{1/2} + \left[{}^1/_3L^4 + {}^1/_3L^2 + 2L\right]\ln\left[L + (L^2+1)^{1/2}\right] - \left\{({}^1/_3L^3 + L)(L^2+1)^{1/2} \ln\left[L + (L^2+1)^{1/2}\right] - {}^3/_4\left\{\ln\left[L + (L^2+1)^{1/2}\right]\right\}^2\right.$$

The distributions calculated from Equation (13) are compared with the previous methods in Table 1, and good agreement is obtained. The coefficients $M(L)/P(L)$ and $N(L)/P(L)$ are plotted for L from 0 to 10 in Fig. 4(*a*), and are compared with the coefficients $L + 1$ and 2 from Equation (9*a*). The results of the simple method using the separable kernel provide a good approximation.

Solution for Zero Heat Input and One End Reservoir Heated (Black Body)

Now the function $\Phi(x)$ is considered, which is the solution for an enclosure with zero heat input at the walls, and with one end exposed to a reservoir at zero temperature and the other to an emissive power $\varphi = 1$. In this case $q(x) = 0$, $\varphi_2 = 0$, and $\varphi_1 = 1$ so that Equation (4) reduces to

$$\Phi(x) = F(x) + \int_0^x \Phi(\eta)K(x-\eta)d\eta + \int_x^L \Phi(\eta)K(\eta - x)d\eta \tag{14}$$

This problem has already been treated by Hottel and Keller[3] in connection with radiation from a hole in a furnace wall. As a further example illustrating the variational method and for completeness in the presentation, the solution is briefly outlined here using the present methods. The results are found to be in good agreement with those of Hottel and Keller[3] and the reader is referred to that work for more details on this type of configuration.

Approximate Separable Kernel. Since the kernel K is being approximated by e^{-2x}, we make a similar approximation for the configuration factor $F(x)$. The quantity $2F(x)$ is plotted in Fig. 3 and it is seen to be quite close to an exponential function so we let $2F(x) = e^{-\beta x}$. To determine β we impose the condition that the total radiant exchange by the exact and approximate form factors would be the same for a cylinder of infinite length. This gives

$$2\int_0^\infty \left[\frac{x^2 + 1/2}{(x^2+1)^{1/2}} - x\right]dx = \int_0^\infty e^{-\beta x}dx$$

which yields $\beta = 2$. Equation (14) then becomes

$$\Phi(x) = \frac{1}{2}e^{-2x} + \frac{1}{e^{2x}}\int_0^x \Phi(\eta)e^{2\eta}d\eta + e^{2x}\int_x^L \Phi(\eta)\frac{1}{e^{2\eta}}d\eta \tag{15}$$

By differentiating this integral equation twice, the integrals are eliminated and a simple differential equation is obtained

$$\frac{d^2\Phi}{dx^2} = 0 \tag{15a}$$

This yields the straight line solution

$$\Phi = C_3x + C_4 \tag{16}$$

By evaluating Equation (15) at $x = 0$ and $x = L$ the two boundary conditions for this solution are found to be

$$\Phi(0) = {}^1/_2 + \int_0^L \Phi(\eta)\frac{1}{e^{2\eta}}d\eta$$
$$\Phi(L) = e^{-2L}/2 + e^{-2L}\int_0^L \Phi(\eta)e^{2\eta}d\eta \tag{17}$$

Substituting Equation (16) into these relations and evaluating the integrals provides two equations from which the constants C_3 and C_4 can be determined. This yields the final result

$$\Phi = \frac{1}{1+L}({}^1/_2 + L - x) \tag{18}$$

Numerical Integration. Numerical computations were performed for the same two enclosures, $L = 1$ and 4, considered previously for the case with uniform heat flux at the enclosure wall. As seen from Table 1 the results are in very good agreement with the simple expression given in Equation (18). To obtain numerical values for $x > L/2$ note that the Φ-function is asymmetric about $L/2$ so that $\Phi(L - x) = 1 - \Phi(x)$.

Variational Method. To find the best straight-line relation for Φ we again employ the variational method. The variational principle for this case is

$$J = \int_0^L\int_0^L K(|\eta - x|)\Phi(\eta)\Phi(x)dx\,d\eta - \int_0^L [\Phi(x)]^2dx + 2\int_0^L \Phi(x)F(x)dx \tag{19}$$

We then let $\Phi = D + Ex$ and carry out the indicated operations. Most of the necessary algebra has already been performed in relation to Equations (10) and (11). This yields J as a function of the constants D and E, and we now obtain an extremum by differentiating J separately with respect to D and E and setting the resulting equations equal to zero. This yields,

$$\frac{\partial J}{\partial D} = 0 \rightarrow D[-L^2 + L(L^2+1)^{1/2}] + \frac{E}{2}[-L^3 + L^2(L^2+1)^{1/2}] + \frac{L^2}{2} - \frac{L}{2}(L^2+1)^{1/2} = 0 \tag{20a}$$

$$\frac{\partial J}{\partial E} = 0 \rightarrow D[-L^2 + L(L^2+1)^{1/2}] + \frac{E}{2}\left\{-L^3 + ({}^1/_2 + L^2)(L^2+1)^{1/2} - \frac{1}{2L}\ln\left[L + (L^2+1)^{1/2}\right]\right\} + \frac{(2L^2-1)(L^2+1)^{1/2} + 1 - 2L^2}{-3L} = 0 \tag{20b}$$

Solving simultaneously we obtain

Table 1 Distributions of Φ_q^* and Φ

		Φ_q^*			Φ		
	x	Numerical	Separable kernel	Variational	Numerical	Separable kernel	Variational
$L = 1$	0	2.06	2.00	2.06	0.759	0.750	0.759
	1/8	2.31	2.22	2.31	0.696	0.688	0.694
	1/4	2.49	2.38	2.49	0.631	0.625	0.630
	3/8	2.60	2.47	2.60	0.566	0.563	0.565
	1/2	2.64	2.50	2.63	0.500	0.500	0.500
$L = 4$	0	4.95	5.00	4.98	0.900	0.900	0.896
	1/2	8.61	8.50	8.60	0.797	0.800	0.797
	1	11.2	11.0	11.2	0.697	0.700	0.698
	3/2	12.6	12.5	12.7	0.599	0.600	0.599
	2	13.2	13.0	13.2	0.500	0.500	0.500

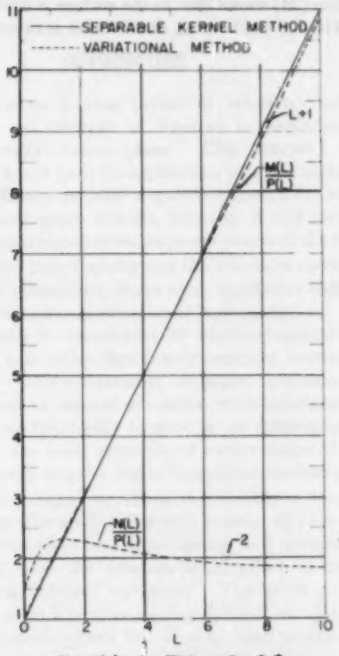

Fig. 4(a) Coefficients for Φ_q^*

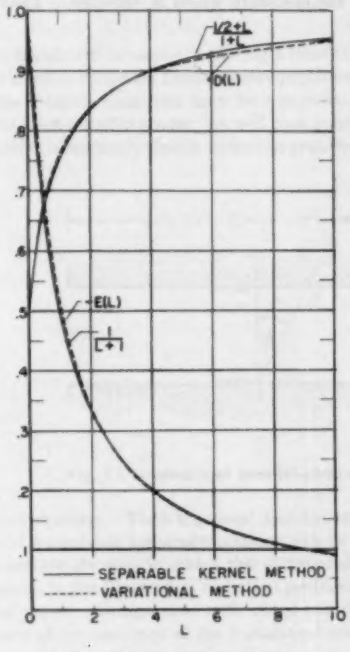

Fig. 4(b) Coefficients for Φ

$$D(L) = \frac{-4L^3 + 5L^2 + 4L^2 + 7L + (4L^4 - 7L^2 - 4L)(L^2 + 1)^{1/2} + 3[L - (L^2 + 1)^{1/2}] \ln [L + (L^2 + 1)^{1/2}]}{6\{L^3 + L - L^2(L^2 + 1)^{1/2} + [L - (L^2 + 1)^{1/2}] \ln [L + (L^2 + 1)^{1/2}]\}}$$

and

$$E(L) = \frac{2}{3}\left\{\frac{-L^2 + 2 + (L^2 - 2)(L^2 + 1)^{1/2}}{L(L^2 + 1)^{1/2} - \ln [L + (L^2 + 1)^{1/2}]}\right\} \quad (21)$$

The coefficients D and E are plotted in Fig. 4(b) and compared with the more simple coefficients resulting from the separable kernel method. The values of Φ for $L = 1$ and 4 are shown in Table 1 and agree quite well with the previous solutions. Hottel and Keller[2] mention that $\Phi(x)$ begins to deviate slightly from a straight line for $L > 5$, and hence the expressions presented here should not be applied for large L without being first checked by further numerical computations.

Nonblack Surface

We shall now consider surfaces which are gray and are diffuse reflectors. For the cases considered in this paper, where the heat flux is specified and the wall temperature is found, a simple relation will be determined relating the solution for the black-body problem to the diffuse gray-body case. Consider a function $U(x)$ which is defined as the total amount of energy leaving a surface element by radiation. If we form a heat balance on an element of area, the total energy leaving is equal to the imposed heat flux plus the radiation coming from the ends of the enclosure and the enclosure wall. This gives

$$U(x) = q(x) + \varphi_1 F(x) + \varphi_2 F(L - x) + \int_0^x U(\eta)K(x - \eta)d\eta + \int_x^L U(\eta)K(\eta - x)d\eta \quad (22)$$

This equation is of exactly the same form as Equation (4) and hence $U(x)$ is equal to the solution for the emissive power previously obtained for the case of black-body surfaces.

Now that $U(x)$ is known we have to relate it to the surface temperature. To do this consider in detail the quantities which contribute to the energy leaving the surface. One term is the energy emitted directly from the surface. A second term is the energy arriving from the ends of the enclosure which is reflected by the surface, and the final term is the energy arriving from the other portions of the enclosure which is reflected. Thus $U(x)$ can be written as

$$U(x) = \epsilon(x)\varphi_w(x) + \rho(x)\left[\varphi_1 F(x) + \varphi_2 F(L - x) + \int_0^x U(\eta)K(x - \eta)d\eta + \int_x^L U(\eta)K(\eta - x)d\eta\right] \quad (23)$$

If we multiply Equation (22) by $\rho(x)$ and subtract Equation (23) we can then obtain the solution for the wall emissive power

$$\varphi_w(x) = \frac{\rho}{\epsilon} q + U \quad (24)$$

where, for constant q, we have by using the black-body solution Equation (5)

$$U(x) = \varphi_2 + q\Phi_q^*(x) + (\varphi_1 - \varphi_2)\Phi(x)$$

Equation (24) shows that as the surface is made a better reflector ($\epsilon \to 0$ and $\rho \to 1$) the φ_w distribution is raised to a higher level.

E. M. SPARROW

Lewis Research Center, NASA, Cleveland, Ohio. At present, professor of Mechanical Engineering, University of Minnesota, Minneapolis, Minn. Assoc. Mem. ASME

Application of Variational Methods to Radiation Heat-Transfer Calculations

A variational method is presented for solving a class of integral equations which arise in radiation heat-transfer problems. First, to demonstrate the formulation of radiation problems in terms of integral equations, consideration is given to a system consisting of two nonblack, finite, parallel plates. After a general description of the variational method, its use is illustrated by application to the parallel-plate system. Comparisons are made which show very good agreement with exact solutions.

Introduction

Following a long period of relatively moderate research activity, an upsurge of interest in radiation heat transfer has recently taken place. This renewed importance of radiation arises from its application to space technology. Not only does radiation provide a workable means for transferring waste heat from space vehicles, but also it will serve as a dominant heat-transfer mechanism in power plants of the future.

Between radiation heat transfer and the alternate mechanisms of conduction and convection, there exist significant differences in physical concepts and in mathematical representation. Physically, radiant energy is transferred by electromagnetic waves; while conduction and convection involve contact between particles of matter. Mathematically, radiation problems must often be formulated as *integral equations*, while conduction and convection are most frequently formulated as differential equations. Of course, the basic principle of conservation of energy interrelates the energy transfer due to these three mechanisms.

The solution of integral equations is generally a formidable task even for those who are familiar with them. In view of this, it is of first importance to find approximate, but accurate techniques which will ease the computational effort in radiation problems involving integral equations. The great utility of variational methods as a tool for solving differential equations in many areas of applied science has already been demonstrated. It is the aim of this paper to present and apply a variational procedure which will be useful in solving a class of integral equations which arise in radiation heat-transfer problems.

Since integral equations may be somewhat unfamiliar to the general heat-transfer reader, we will first consider, by way of illustration, a relatively simple radiation problem and its governing integral equation. Then a general description of the variational method for solving integral equations will be given. Finally, to demonstrate the way in which the variational procedure is used, we return to the illustrative radiation problem of the first section of the paper. Comparison with exact solutions will provide a measure of the accuracy of the variational method.

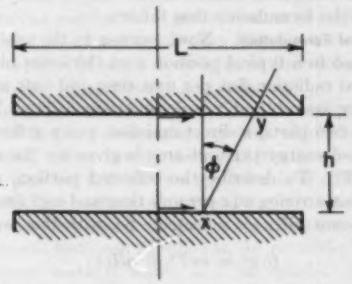

Fig. 1 Schematic of parallel-plate system

A Radiation Problem and Its Integral Equation

Description of Problem. Since our purpose here is to demonstrate the manner in which integral equations may arise in heat-radiation problems, it is reasonable to select a simple physical situation. In this way, we retain the essential features of the formulation while avoiding the distractions of complex geometrical relation-

Contributed by the Heat Transfer Division and presented at the Annual Meeting, Atlantic City, N. J., November 29-December 4, 1959, of The American Society of Mechanical Engineers.

Note: Statements and opinions advanced in papers are to be understood as individual expressions of their authors and not those of the Society. Manuscript received at ASME Headquarters, August 13, 1959. Paper No. 59—A-120.

Nomenclature

A = surface area
$a_1, a_2, \ldots$ = constants which depend only on γ
$B(x)$, $B(y)$ = combined radiant flux (emitted and reflected) leaving a position x or y per unit time and unit area
C_1, C_2 = coefficients in equation (16)
$D_1, D_2, \ldots$ = coefficients in equation (21)
F = angle factor
f = function of X
$G(X)$ = arbitrary function of X
$H(x)$ = radiant energy arriving at x per unit time and area
h = spacing between plates
I = variational expression, equation (13)
K = kernel of integral equation
L = plate length
Q = over-all net heat-transfer rate
q = local net heat-transfer rate per unit area
T = absolute temperature
X = dimensionless co-ordinate, x/L
x = co-ordinate measuring distance along lower plate from center plane
Y = dimensionless co-ordinate, y/L
y = co-ordinate measuring distance along upper plate from center plane
β = dimensionless combined flux, $B/\epsilon\sigma T^4$
γ = gap spacing ratio, h/L
ϵ = emissivity, $1 - \rho$
λ = constant parameter in equation (12)
ρ = reflectivity, $1 - \epsilon$
σ = Boltzmann's constant
ϕ = angle defined in Fig. 1

ships. Consideration is given to the parallel-plate system pictured in Fig. 1. Each plate is of length L and extends indefinitely in the direction normal to the plane of the figure. The surfaces of both plates radiate and reflect in a diffuse manner, and they possess identical *gray-body* emissivity values ($\epsilon = \alpha = 1 - \rho$). The space between the plates may contain a nonparticipating gas or else a vacuum. The thermal-boundary conditions, chosen on the basis of simplicity, are that both plate surfaces are maintained at the same uniform temperature, and that negligible radiant energy passes inward from the external environment into the gap between the plates.[1] It is clear that radiant energy will pass out the ends of the gap to the environment, and this will constitute the net heat transfer from the system.

For this and related systems, there are several results which may be of interest. First, it may be desired to know the distribution of the net heat flux along the surface of the plate, since it is this energy which must be locally supplied to maintain the prescribed plate temperature. Also of importance is the over-all heat transfer from the system. On the other hand, if various positions on the surface of a plate are being viewed by a pyrometer, then it is necessary to know the distribution of the combined (emitted and reflected) radiant flux. All of these results are furnished by the formulation that follows.

Mathematical Formulation. Now, turning to the analysis, attention is directed to a typical position x on the lower plate, Fig. 1. The combined radiation flux per unit time and unit area leaving an elementary area dA_x at x is designated as $B(x)$. This flux is composed of two parts, a direct emission and a reflection. The rate of emitted energy per unit area is given by the well-known relation: $\epsilon\sigma T^4$. To describe the reflected portion, we denote[2] the radiant flux arriving at x per unit time and unit area by $H(x)$; then the amount $\rho H(x)$ is reflected. So, with this, we can write

$$B(x) = \epsilon\sigma T^4 + \rho H(x) \tag{1}$$

As it stands equation (1) contains two unknowns, B and H. However, it is easy to see that the energy arriving at x must be related to the energy which leaves positions on the upper plate. Consider a typical point y on the upper plate. The energy leaving an elementary area dA_y is

$$B(y)dA_y$$

Of this, an amount

$$B(y)dA_y dF_{y-x} \tag{2a}$$

arrives at position x on the lower plate, where dF_{y-x} is the angle factor of dA_x as viewed from y. Using the reciprocity relation

$$dF_{y-x}dA_y = dF_{x-y}dA_x$$

equation (2a) becomes

$$B(y)dA_x dF_{x-y} \tag{2b}$$

From this, it follows that the energy impinging per unit area at x due to radiation leaving y is

$$B(y)dF_{x-y} \tag{3}$$

But, x receives energy from all positions y on the upper surface, and the total contribution is found by integrating equation (3). So,

$$H(x) = \int_{y=-L/2}^{y=L/2} B(y)dF_{x-y} \tag{4a}$$

From Jakob,[3] it follows that the angle factor dF_{x-y} is given by the remarkably simple expression

$$dF_{x-y} = \tfrac{1}{2}d(\sin\phi)$$

From Fig. 1, it is easy to see that

$$\sin\phi = \frac{y - x}{[(y - x)^2 + h^2]^{1/2}}$$

and with this equation (4a) becomes

$$H(x) = \frac{h^2}{2}\int_{-L/2}^{L/2} B(y)\frac{1}{[(y - x)^2 + h^2]^{3/2}}dy \tag{4b}$$

Finally, the governing equation for B is obtained by introducing this expression for H into equation (1), giving

$$B(x) = \epsilon\sigma T^4 + \frac{\rho h^2}{2}\int_{-L/2}^{L/2} B(y)\frac{1}{[(y - x)^2 + h^2]^{3/2}}dy \tag{5}$$

or, in dimensionless form

$$\beta(X) = 1 + \frac{\rho\gamma^2}{2}\int_{-1/2}^{1/2} \beta(Y)\frac{1}{[(Y - X)^2 + \gamma^2]^{3/2}}dY \tag{6}$$

where γ now represents the aspect ratio h/L. Because of the symmetry of the problem, it is clear that the distribution of B (or of β) will be the same along the upper plate as along the lower plate. So, $\beta(X)$ and $\beta(Y)$ are the same functions, the only difference being that X and Y are interchanged as independent variables.

Equation (6) is called an integral equation since the unknown function β appears under the integral sign as well as in other parts of the equation.[4] The factor

$$\frac{1}{[(Y - X)^2 + \gamma^2]^{3/2}}$$

is called the kernel of the integral equation and is usually identified by the notation $K(Y, X)$. In the particular case under consideration here, the kernel is symmetric since Y and X can be interchanged without any effect whatsoever. It is interesting to note that, for an integral equation, there are no boundary conditions as there are in differential equations.

Once the integral equation has been solved, all quantities of interest immediately become available. The solution itself directly furnishes the distribution of the combined radiant flux B, which is useful in pyrometry. The net heat flux q at any position is the difference between the leaving and arriving radiation, that is

$$q = B - H \tag{7}$$

Eliminating H by use of equation (1) and noting that $1 - \rho = \epsilon$, the expression for q becomes

$$\frac{q}{\epsilon\sigma T^4} = \frac{1 - \beta\epsilon}{\rho} \tag{7a}$$

So, once the variation of β with X is known, the variation of q is easily computed. Finally, the over-all heat transfer Q (per unit width) is obtained by integrating equation (7a), giving the result

$$\frac{Q/L}{\epsilon\sigma T^4} = \frac{1 - \epsilon\int_{-1/2}^{1/2}\beta dX}{\rho} \tag{8}$$

[1] The extension to nonuniform (but identical) plate temperatures and to a radiating environment can easily be made without adding anything basically new to the formulation.

[2] The B, H notation has been taken from E. R. G. Eckert, "Heat and Mass Transfer," McGraw-Hill Book Company, Inc., New York, N. Y., 1959, pp. 409–411 and pp. 416–418.

[3] Max Jakob, "Heat Transfer," John Wiley & Sons, Inc., New York, N. Y., 1957, vol. 2, pp. 19–21.

[4] Mathematically speaking, equation (6) is classified as a Fredholm equation of the second kind.

It is clearly seen that a knowledge of B (or β) is the key to the problem.

Before leaving this illustrative situation, it is well to make mention of the way this problem would have been treated using standard textbook methods. There, the gross assumption would have been made that the impinging energy H is the same for all points x. With this, it follows from equation (1) that B is also independent of x. To replace our equation (4*a*), the simple theory would substitute

$$H = BF_{-} \tag{9}$$

where F_{-} is the angle factor for two finite parallel plates.[5] The combination of equations (9) and (1) gives

$$\frac{B}{\epsilon\sigma T^4} = \frac{1}{1 - \rho F_{-}} \tag{10}$$

and

$$q = \frac{Q}{L} = \frac{1 - F_{-}}{1 - \rho F_{-}} \epsilon\sigma T^4 \tag{11}$$

where the heat transfer has been evaluated from equation (7*a*). The approximate formulation cannot give the variations of q or of B with x. It is only able to supply some sort of average value, whose accuracy depends on the complexity of the configuration. For the illustrative situation considered here, it is expected that the simple formulation would predict reasonably good Q-values when $h \geq L$, with the accuracy decreasing as h/L decreases. For complex geometries with re-entrant corners, the simple formulation would be expected to lead to serious errors.

However, it is not our purpose here to evaluate the relative merits of the approximate versus the more exact integral formulation. It is clear that there are situations where both local information and more exact values of over-all results are needed and, in these, integral equations will be involved.

We now turn to the description of a variational method for solving a class of integral equations which arise in radiation problems.

The Variational Procedure

Suppose that a physical problem is governed by the following integral equation

$$\beta(X) = G(X) + \lambda \int_a^b \beta(Y) K(Y, X) dY \tag{12}$$

where G is a given function of X, λ a constant parameter, and $K(Y, X)$ a *symmetrical* kernel. Now, according to the calculus of variations,[6] there corresponds to this integral equation the following variational expression I, which has a very special property

$$I = \lambda \int_a^b \int_a^b K(Y, X)\beta(X)\beta(Y) dX\, dY - \int_a^b [\beta(X)]^2 dX + 2 \int_a^b \beta(X) G(X) dX \tag{13}$$

namely, that the value of I is an extremum (a maximum for our radiation problem) when it is evaluated using that function which satisfies the integral equation (12). This characteristic suggests a procedure for obtaining approximate solutions of the integral equation by using the variational expression I. The simplest scheme would be to select several trial functions for β and introduce them successively into equation (13). That function which gives the maximum value for I would be regarded as the closest approximation to the correct solution. A more systematic and satisfactory procedure for finding an extremum of the variational expression is the Ritz method. According to this approach, a set of functions $f_1(X)$, $f_2(X)$, . . . is selected, and with these, β is written as the following sum

$$\beta(X) = C_1 f_1(X) + C_2 f_2(X) + \ldots = \sum_{n=1}^{r} C_n f_n(X) \tag{14a}$$

$$\beta(Y) = C_1 f_1(Y) + C_2 f_2(Y) + \ldots = \sum_{n=1}^{r} C_n f_n(Y) \tag{14b}$$

where $C_1, C_2, \ldots$ are constants which remain to be determined. With this choice for β, the integrations indicated in equation (13) can be carried out. The result is an expression for I containing the $C_1, C_2, \ldots$. To find an extremum for I, the expression is differentiated successively with respect to each C and each resulting equation is set equal to zero. This provides r simultaneous equations for the unknown constants $C_1, \ldots, C_r$. In practice, this procedure may be applied successively using an increasing number of terms in the series (14) until convergence to a desired accuracy is achieved. The choice of functions $f_n(X)$ may be arbitrary, but better results (for a given number of terms) and more rapid convergence are achieved when the selections are made in accordance with any physical insight or knowledge which one may have about the problem (e.g., symmetry).

To fix these ideas about the variational procedure, application will be made to the parallel-plate system which has previously been discussed. It is readily seen that the governing equation (6) for that problem is actually a special case of the general form (12) to which the variational method applies. As a matter of fact, if variable (but identical) surface temperatures and a radiating environment had been included in the parallel-plate problem, the variational method would still be usable. These added effects would contribute nonintegral terms containing functions of X to the right side of equation (6); and these would correspond to $G(X)$ in equation (12).

Application to the Parallel-Plate System

As has already been noted, the parallel-plate system is ideally suited for illustrating the way in which the variational procedure is used in solving a class of integral equations which arise in radiation problems. The parallel-plate problem is governed by the integral equation (6), and the first step in obtaining its variational solution is to find the variational expression I. Comparing equation (6) to the general form (12), it follows that

$$\lambda = \frac{\rho\gamma^2}{2}, \qquad G(X) = 1, \qquad a = -1/2, \qquad b = 1/2$$

$$K(Y, X) = \frac{1}{[(Y - X)^2 + \gamma^2]^{3/2}}$$

Substituting these into equation (13), the variational expression corresponding to equation (6) takes the form

$$I = \frac{\rho\gamma^2}{2} \int_{-1/2}^{1/2} \int_{-1/2}^{1/2} \frac{\beta(X)\beta(Y) dX\, dY}{[(Y - X)^2 + \gamma^2]^{3/2}} - \int_{-1/2}^{1/2} [\beta(x)]^2 dX + 2 \int_{-1/2}^{1/2} \beta(X) dX \tag{15}$$

To find an extremum of equation (15), we use the Ritz method as previously outlined. In selecting the functions $f_n(X)$ in equation (14), cognizance is taken of the fact that symmetry exists about the points $X = 0$ and $Y = 0$; that is, $\beta(X) = \beta(-X)$ and $\beta(Y) = \beta(-Y)$. Functions which immediately suggest themselves as candidates for the role of f_n are $X^0, X^2, X^4, \ldots$ Other

[5] Footnote 3, eq. (31-49).

[6] F. B. Hildebrand, "Methods of Applied Mathematics," Prentice-Hall, Inc., New York, N. Y., 1952, p. 494.

Table 1 Numerical values of C_n and D_n

(a) Values of C_1 and C_2, for quadratic, equation (16)

	$\gamma = 1$		$\gamma = 0.5$		$\gamma = 0.1$	
ϵ	C_1	$-C_2$	C_1	$-C_2$	C_1	$-C_2$
0.1	1.642	0.5549	2.479	2.367	7.388	16.54
0.3	1.441	0.3801	1.890	1.403	3.192	4.726
0.5	1.282	0.2423	1.518	0.8045	1.992	1.832
0.7	1.153	0.1315	1.262	0.4013	1.433	0.6996
0.9	1.047	0.03998	1.075	0.1139	1.113	0.1624

(b) Values of D_1, D_2, and D_3, for quartic, equation (21)

	$\gamma = 0.5$			$\gamma = 0.1$		
ϵ	D_1	$-D_2$	D_3	D_1	$-D_2$	$-D_3$
0.1	2.486	2.644	1.284	7.205	10.06	27.81
0.3	1.893	1.548	0.6726	3.095	1.128	15.92
0.5	1.519	0.8754	0.3306	1.942	−0.06314	8.564
0.7	1.263	0.4322	0.1440	1.411	−0.1774	4.024
0.9	1.076	0.1210	0.03261	1.107	−0.06997	1.079

possibilities exist (e.g., the cosines), but none appears quite as attractive as these power functions. So, as a first approximation for β in the form of equation (14), we try

$$\beta(X) = C_1 + C_2X^2, \qquad \beta(Y) = C_1 + C_2Y^2 \tag{16}$$

The constants C_1 and C_2 are determined so as to provide an extremum for I. Introducing these expressions for β into the variational expression (15) and carrying out the indicated integrations lead to

$$I = \rho(C_1^2a_1 + C_1C_2a_2 + C_2^2a_3) - C_1^2 - {}^1/_6C_1C_2 - {}^1/_{90}C_2^2 + 2C_1 + \frac{C_2}{6} \tag{17}$$

where the a_1, a_2, and a_3 depend only on the gap ratio γ and are given in the Appendix. To find the values of C_1 and C_2 which give an extremum for I, we differentiate equation (17) with respect to each C and set the resulting equations to zero. Carrying out this operation, there is obtained

$$\left.\begin{aligned} \frac{\partial I}{\partial C_1} = 0 &\rightarrow 2C_1(\rho a_1 - 1) + C_2(\rho a_2 - {}^1/_6) = -2 \\ \frac{\partial I}{\partial C_2} = 0 &\rightarrow C_1(\rho a_2 - {}^1/_6) + 2C_2(\rho a_3 - {}^1/_{90}) = -{}^1/_6 \end{aligned}\right\} \tag{18}$$

Simultaneous solution of this simple pair of linear algebraic equations gives C_1 and C_2. Once the C-values have been found, the local and over-all heat transfer are easily computed by using equations (7a) and (8), giving

$$\frac{q}{\epsilon\sigma T^4} = \frac{1 - \epsilon(C_1 + C_2X^2)}{\rho} \tag{19}$$

$$\frac{Q/L}{\epsilon\sigma T^4} = \frac{1 - \epsilon(C_1 + C_2/12)}{\rho} \tag{20}$$

As a specific numerical example, consider the case of $\gamma = 0.5$. Then, evaluating equations (26), (27), and (28), there is obtained: $a_1 = 0.61803$, $a_2 = 0.091237$, $a_3 = 0.0038127$. For $\rho = 0.9$, equation (18) becomes

$$0.88755C_1 + 0.084554C_2 = 2$$

$$0.084554C_1 + 0.018137C_2 = 1/6$$

from which it is found that $C_1 = 2.4789$ and $C_2 = -2.3673$. With these, the results for $B(X)$, $q(X)$, and Q follow from equations (16), (19), and (20), as

$$\beta = \frac{B}{\epsilon\sigma T^4} = 2.4789 - 2.3673X^2$$

$$\frac{q}{\epsilon\sigma T^4} = 0.8357 + 0.2630X^2, \qquad \frac{Q/L}{\epsilon\sigma T^4} = 0.85759$$

where we have used $\epsilon = 1 - \rho = 0.1$. These results illustrate two characteristics which are generally true for the parallel-plate problem regardless of the specific values of γ and ρ: (*a*) The combined radiant flux B (emitted plus reflected) is a maximum at the mid-point of the plate ($X = 0$) and decreases steadily to a minimum value at the ends of the gap ($X = \pm 1/2$). (*b*) The local heat transfer q is smallest at the mid-section and largest at the ends of the gap.

Values of C_1 and C_2 have been evaluated from equation (18) for gap spacings γ of 1, 0.5, and 0.1 for a wide range of reflectivities. The C-values thus obtained are presented in Table 1.

The quadratic form for $\beta(X)$, as given by equation (16), was selected as a first approximation. It is desirable to know how well the resulting predictions compare with those of a more exact solution. Fortunately, there are available some solutions[7] of equation (6) which were obtained by direct iteration on an electronic computer. Using these as a standard, we proceed to test the accuracy of the quadratic variational solution. It may be first observed that, for a given spacing γ, the variation of the combined flux β along the plate is greater as ρ increases. Consequently, for a given γ, it was found that the most severe test of the variational procedure is at the larger ρ-values. For this reason, detailed comparisons will only be presented for $\rho = 0.9$. Such comparisons are made in Table 2(*a*), (*b*), and (*c*) for γ-values of 1, 0.5, and 0.1, respectively, at X-values of 0, 0.1, 0.2, 0.3, 0.4, and 0.5. Attention is directed to the first and last lines of each table. The accuracy of the variational quadratic is seen to be remarkably good for $\gamma = 1$. As the gap ratio γ decreases, the predictions of the quadratic become somewhat less precise; but still are quite good. For the case of $\gamma = 0.1$, the errors range from 2 per cent at $X = 0$ (center point) to 9 per cent at $X = \pm 1/2$ (end points), with even smaller errors at some in-between points. The performance of the variational quadratic must be regarded as particularly gratifying, especially in view of its simplicity and ease of application.

In practice, the next step would be to carry out a second variational computation using a more complex form for β. From this, there would be obtained a more accurate set of radiation predictions. Further, in the absence of an exact solution, more than

[7] J. L. Gregg, personal communication.

Table 2 Comparison of $\beta(x)$ from various computations

(a) $\gamma = 1, \rho = 0.9$

$X \rightarrow$	0	0.1	0.2	0.3	0.4	0.5
Quadratic	1.642	1.637	1.620	1.592	1.554	1.504
Exact	1.644	1.638	1.620	1.590	1.552	1.508

(b) $\gamma = 0.5, \rho = 0.9$

$X \rightarrow$	0	0.1	0.2	0.3	0.4	0.5
Quadratic	2.479	2.455	2.384	2.266	2.100	1.887
Quartic	2.486	2.460	2.382	2.258	2.096	1.905
Exact	2.485	2.459	2.383	2.259	2.095	1.908

(c) $\gamma = 0.1, \rho = 0.9$

$X \rightarrow$	0	0.1	0.2	0.3	0.4	0.5
Quadratic	7.39	7.22	6.73	5.90	4.74	3.25
Quartic	7.21	7.10	6.76	6.07	4.88	2.95
Exact	7.22	7.11	6.75	6.07	4.90	2.97

one variational computation is needed in order to define the accuracy of the results.

To demonstrate how the performance of the variational method can be improved, the procedure is repeated with the following quartic representation for β:

$$\beta(X) = D_1 + D_2X^2 + D_3X^4, \qquad \beta(Y) = D_1 + D_2Y^2 + D_3Y^4 \tag{21}$$

This form is a logical refinement of equation (16) and continues to incorporate the symmetry properties of β. Introducing equation (21) into the variational expression I gives

$$I = \rho(D_1^2a_1 + D_1D_2a_2 + D_2^2a_3 + D_1D_3a_4 + D_2D_3a_5 + D_3^2a_6) - D_1^2 - {}^1/_6\, D_1D_2 - {}^1/_{40}\, D_1D_3 - \frac{D_2^2}{80} - \frac{D_2D_3}{224} - \frac{D_3^2}{2304} + 2D_1 + \frac{D_2}{6} + \frac{D_3}{40} \tag{22}$$

where again, the $a_1, \ldots, a_6$ depend only on γ and are given in the Appendix. To find the extremum of I, equation (22) is differentiated successively with respect to each D and the resulting equations set to zero. So,

$$\begin{aligned}
\frac{\partial I}{\partial D_1} = 0 &\rightarrow 2D_1(\rho a_1 - 1) + D_2(\rho a_2 - {}^1/_6) + D_3(\rho a_4 - {}^1/_{40}) = -2 \\
\frac{\partial I}{\partial D_2} = 0 &\rightarrow D_1(\rho a_2 - {}^1/_6) + 2D_2(\rho a_3 - {}^1/_{80}) + D_3(\rho a_5 - {}^1/_{224}) = -{}^1/_6 \\
\frac{\partial I}{\partial D_3} = 0 &\rightarrow D_1(\rho a_4 - {}^1/_{40}) + D_2(\rho a_5 - {}^1/_{224}) + 2D_3(\rho a_6 - {}^1/_{2304}) = -{}^1/_{40}
\end{aligned} \tag{23}$$

Once γ (i.e., a_1 through a_6) and ρ have been prescribed, then these equations can be readily solved for D_1, D_2, and D_3. With these, the local and over-all heat-transfer results take the form

$$\frac{q}{\epsilon\sigma T^4} = \frac{1 - \epsilon(D_1 + D_2X^2 + D_3X^4)}{\rho} \tag{24}$$

$$\frac{Q}{\epsilon\sigma T^4} = \frac{1 - \epsilon(D_1 + D_2/12 + D_3/80)}{\rho} \tag{25}$$

Solutions of equations (23) have been carried out for γ-values of 0.5 and 0.1[8] for a wide range of ρ-values. The D_1, D_2, and D_3 thus computed are given in Table 1(b). Using these values, we can now proceed to compare predictions of the variational quartic with those of the quadratic and of the exact solution. Turning to Table 2(b) and (c), it is observed that, indeed, the quartic is closer to the exact solution than is the quadratic. For example, at $X = 0.5$ for $\gamma = 0.1$, the prediction as given by the quadratic is in error by 9 per cent; while the quartic has cut the error to 0.6 per cent.

Even closer agreement with the exact solution would be achieved if a sixth-degree polynomial were to be used in place of the quartic. With an exact solution available for comparison purposes, it is clear that such a step is quite unnecessary for γ-values of 0.1 and greater. However, in the absence of an exact solution, it might be necessary (depending on the precision desired) to use the sixth-degree equation to verify the accuracy of the variational solution.

Concluding Remarks: Limitations

It has been demonstrated that a variational method can be used with considerable advantage to solve integral equations which may arise in thermal-radiation problems. The important restriction which must be met is that the governing integral equation of the radiation problem have the form of equation (12). The note of caution to be sounded here is that the $\beta(Y)$ which appears under the integral must be the same function as the $\beta(X)$ which appears on the left side of the equation.

APPENDIX

Expressions for $a_1, \ldots, a_6$

$$a_1 = (1 + \gamma^2)^{1/2} - \gamma \tag{26}$$

$$a_2 = \left({}^1/_6 - \frac{4\gamma^2}{3}\right)(1 + \gamma^2)^{1/2} + \gamma^2\{\ln [1 + (1 + \gamma^2)^{1/2}] - \ln \gamma\} + \frac{4\gamma^2}{3} - \frac{\gamma}{2} \tag{27}$$

$$a_3 = \left({}^1/_{80} - \frac{2\gamma^2}{45} + \frac{4\gamma^4}{45}\right)(1 + \gamma^2)^{1/2} + \frac{\gamma^2}{12}\{\ln [1 + (1 + \gamma^2)^{1/2}] - \ln \gamma\} - \frac{\gamma}{16} - \frac{4\gamma^3}{45} \tag{28}$$

[8] No solution was obtained for $\gamma = 1$, since the quadratic approximation has already provided exceedingly good results for that situation.

$$a_4 = \left(\tfrac{1}{60} - \frac{31\gamma^2}{30} + \frac{16\gamma^4}{15}\right)(1+\gamma^2)^{1/2} + \left(\frac{\gamma^2}{2} - \frac{3\gamma^4}{2}\right)\{\ln[1+(1+\gamma^2)^{1/2}] - \ln\gamma\} - \frac{\gamma}{8} + 2\gamma^2 - \frac{16\gamma^4}{15} \quad (29)$$

$$\frac{a_5}{2} = \left(\tfrac{1}{480} - \frac{726\gamma^2}{8400} + \frac{4468\gamma^4}{8400} - \frac{296\gamma^6}{525}\right)(1+\gamma^2)^{1/2} + \left(\frac{7\gamma^2}{160} - \frac{5\gamma^4}{16} + \frac{3\gamma^6}{4}\right)\{\ln[1+(1+\gamma^2)^{1/2}] - \ln\gamma\} - \frac{\gamma}{64} + \frac{3\gamma^2}{16} - \gamma^4 + \frac{296\gamma^7}{525} + \frac{\gamma^2 a_4}{2} \quad (30)$$

$$a_6 = \frac{\gamma^2}{2}\int_{-1/2}^{1/2} \xi^4 g(\xi)\,d\xi \quad (31)$$

$$g(\xi) = [(\tfrac{1}{2}-\xi)^2+\gamma^2]^{1/2}[\tfrac{1}{2}(\tfrac{1}{2}-\xi)+4\xi] + [(\tfrac{1}{2}-\xi)^2+\gamma^2]^{-1/2}\left[(\tfrac{1}{2}-\xi)\left(\gamma^2 - 6\xi^2 + \frac{\xi^4}{\gamma^2}\right) + 4\xi(\gamma^2-\xi^2)\right] + [(\tfrac{1}{2}+\xi)^2+\gamma^2]^{1/2}[\tfrac{1}{2}(\tfrac{1}{2}+\xi)-4\xi] + [(\tfrac{1}{2}+\xi)^2+\gamma^2]^{-1/2}\left[(\tfrac{1}{2}+\xi)\left(\gamma^2 - 6\xi^2 + \frac{\xi^4}{\gamma^2}\right) - 4\xi(\gamma^2-\xi^2)\right] + \left(6\xi^2 - \frac{3\gamma^2}{2}\right)\ln\left\{\frac{(\tfrac{1}{2}-\xi)+[(\tfrac{1}{2}-\xi)^2+\gamma^2]^{1/2}}{-(\tfrac{1}{2}+\xi)+[(\tfrac{1}{2}+\xi)^2+\gamma^2]^{1/2}}\right\}$$

With respect to the a_6 computation, it was found expedient to evaluate the integral numerically (by Simpson's rule) rather than analytically.

DISCUSSION

R. Viskanta[9]

The application of the variational method to the solution of integral equations encountered in the radiant heat-transfer problems is a welcome addition to the variational techniques already developed for the solution of Milne's integral equation [1].[10] Integration of equation (15) as well as the evaluation of a's and D's is quite involved even for a simple function $G(X)$ and kernel $K(X,Y)$. The extension of variational method to the solution of more complicated integral equations [2, 3] becomes extremely complex.

A solution of the Freedholm integral equation of the second kind (12) can also be obtained by the method of successive substitutions, due to Neumann and Liouville, which gives the unknown function $\beta(X)$ as an integral series in λ [4],

$$\beta(X) = G(X) + \lambda\int_a^b K(X,Y)\,G(Y)dY + \lambda^2\int_a^b K(X,Y)dY\int_a^b K(Y,Z)G(Z)dZ + \ldots + \quad (32)$$

where Z is a dummy integration variable.

[9] Reactor Engineering Division, Argonne National Laboratory Lemont, Ill.

[10] Numbers in brackets designate References at end of discussion.

The convergence of the Neumann series as well as the existence and uniqueness of the solution can readily be demonstrated [5]. Now turning to the specific example in the analysis, the solution of equation (6) can simply be written as

$$\beta(X) = 1 + \lambda\int_{-1/2}^{1/2}\frac{dY}{[(X-Y)^2+\gamma^2]^{1/2}} + \lambda^2\int_{-1/2}^{1/2}\frac{dY}{[(X-Y)^2+\gamma^2]^{1/2}}\int_{-1/2}^{1/2}\frac{dz}{[(Y-Z)^2+\gamma^2]^{1/2}} + \ldots + \quad (33)$$

From the form of the solution it is evident that the convergence of the series is rapid when $\lambda \ll 1$. For case (a) numerical calculations yield the following values for the combined dimensionless flux $\beta(X) = 1.570$, 1.618 and 1.546 for $X = 0$, 0.2, and 0.4, respectively. Thus at $X = 0$ the prediction, as given by the three terms of the series (33), is in error by 4 per cent.

Both the variational method and the method of successive substitutions can give only approximate solutions, though the order of approximation can be extremely high. However, before attempting to solve a specific problem it is more advantageous to investigate the integral equation and the parameters to ascertain which of the several available methods is more suitable from the viewpoint of engineering accuracy and the effort expended in the calculations.

References

1 V. Kourganoff, "Basic Methods in Transfer Problems," Oxford, at the Clarendon Press, Oxford, England, 1952, pp. 126–52.

2 N. C. Francis, J. C. Stewart, L. S. Bohl, and T. J. Krieger, "Variational Solutions of the Transport Equation," Progress in Nuclear Energy, series I, Physics and Mathematics, vol. I, Pergamon Press, London, England, 1959, pp. 360–388.

3 R. Viskanta, "Heat Transfer in Thermal Radiation Absorbing and Scattering Medium," dissertation, Purdue University (in preparation).

4 E. T. Whittaker and G. N. Watson, "Modern Analysis," Cambridge University Press, Cambridge, England, fourth edition, 1952, p. 221.

5 E. Hopf, "Mathematical Problems of Radiative Equilibrium," Cambridge University Press, Cambridge, England, 1934, p. 37.

Author's Closure

Sincere thanks are extended to Mr. Viskanta for pointing out the procedure of successive approximations. As he has indicated, this is a fairly standard method and may be found in such well-known books as Hildebrand's "Methods of Applied Mathematics."[11]

In appraising the numerical results which Mr. Viskanta has presented, the author is surprised by their modest level of accuracy. The particular case considered was (a) in Table 2. As has already been stated in the paper, this is the least testing of all the cases shown in the table. Yet, the results from the successive approximate procedure are much less accurate than are those of the simple variation quadratic. But, even more surprising is that the β valves from the successive approximate method do not decrease monotonically from $X = 0$ to $X = 0.5$, as they should. Instead, a maximum is achieved somewhere between. In view of this, it would appear that further investigation is needed to clarify the utility of the successive approximation procedure.

[11] Prentice-Hall, Inc., Englewood-Cliffs, N. J., 1952, pp. 421–427.

W. E. IBELE
Associate Professor,
Mechanical Engineering Department,
University of Minnesota,
Minneapolis, Minn.
Assoc. Mem. ASME

T. F. IRVINE, JR.
Associate Professor,
Mechanical Engineering Department,
University of Minnesota,
Minneapolis, Minn.

Certain Thermodynamic and Transport Properties of the Atmospheres of Venus, Mars, and Jupiter[1]

Aerodynamic, heat transfer, biological, and other scientific investigations related to planetary systems require a knowledge of atmospheric properties. In the absence of direct measurements within these atmospheres, which is the situation existing for all planets except Earth, the properties must be estimated from the best available data by suitable methods. Since atmospheres may be considered as mixtures of constituent gases, it is possible, in principle, to calculate their properties using basic-mixture theory.

The chief difficulty in this approach lies in the uncertainty of present physical models of atmospheres; i.e., the number, type, and concentration of the constituent gases. For example, it has been concluded in [1][2] that present planetary atmospheric models are only order-of-magnitude estimates. This situation is comparable to the state of knowledge regarding the upper regions of Earth's atmosphere prior to the 1957–1959 International Geophysical Year. Nevertheless, the predictions available until that time served a useful purpose in stimulating research in various atmospheric phenomena. In this spirit, the atmospheric calculations in the present study were undertaken.

In addition to altitude variations of pressure, density, and temperature, planetary atmospheric properties of interest include thermodynamic energy functions (internal energies, enthalpies, entropies, and so on) and transport properties such as viscosities, coefficients of diffusion, and thermal conductivities. Also useful for certain applications are supersonic shock tables and atmospheric radiation properties. The purpose of this paper is to present certain of the thermodynamic and transport properties for the selected atmospheres of Venus, Mars, and Jupiter. Information is given on the specific heat, acoustic velocity, dynamic viscosity, thermal conductivity, and Prandtl number over a temperature range from 200 to 1500 deg Kelvin (K). The property variation with temperature was included so that phenomena occurring under temperature extremes likely to be encountered in the atmospheres could be considered.

Description of the Planets

Although the planetary atmospheres are treated in detail elsewhere [2–4], in order to gain some perspective for the atmospheric calculations a brief discussion will be presented here.

Venus, which is one of the two interior planets, i.e., those whose orbits lie between the Earth and the Sun, shares enough similarities with Earth to be referred to as a sister planet. Although these similarities encompass such physical characteristics as mass, size, gravitational field, and length of day, their atmospheres show marked differences. The surface of Venus is covered with clouds so dense and continuous that no satisfactory surface observation has ever been reported. Spectroscopic measurements have identified carbon dioxide in the atmosphere but a large uncertainty regarding other constituents exists.

Unlike Venus, the atmosphere of Mars is not opaque, although it too is believed to contain carbon dioxide. Great difficulty has been encountered identifying other constituents though they are known to exist from independent pressure measurements made by spectral line-broadening and other techniques. It is, therefore, generally proposed that the other important constituent is nitrogen.

Jupiter, which is the largest planet in the solar system, is believed to have an atmosphere consisting primarily of hydrogen and methane. The large gravitational attraction and low temperatures, however, make it probable that the lower regions of Jupiter's atmosphere are compressed to the extent that the constituents are in the liquid and solid state. The calculations which follow, therefore, can apply only to that portion of the atmosphere existing in the gaseous state.

Table 1 lists some of the planetary properties which are of interest, including the atmospheric properties which will be used in the calculations to follow. The atmospheric data for Mars and Venus were obtained from [5] and for Jupiter from [6]. Both references include a discussion and quantitative information on the density variation with altitude calculated on the basis of an isothermal atmosphere.

Methods of Analysis

Heat Capacity. The heat capacities of the various planetary atmospheres are of direct interest as well as being required for determining the acoustic velocity and Prandtl number. In dimensionless form, the heat capacity at constant pressure for the planets was determined from the constant-pressure heat capacities of the pure gaseous components comprising the atmosphere according to

$$C_p/R = \sum_i x_i (C_p/R)_i \qquad (1)$$

In equation (1) x_i and $(C_p/R)_i$ represent the mole fraction and dimensionless constant-pressure heat capacity, respectively, for the ith constituent. The units of C_p are prescribed by the units chosen for the gas constant R.

Acoustic Velocity. The acoustic velocities for the atmosphere were determined from the perfect-gas relation and expressed in dimensionless form by

[1] Publication from the Heat Transfer Laboratory, University of Minnesota.

[2] Numbers in brackets designate References at end of paper.

Contributed by the Heat Transfer Division and presented at the Annual Meeting, Atlantic City, N. J., November 29–December 4, 1959, of The American Society of Mechanical Engineers.

Note: Statements and opinions advanced in papers are to be understood as individual expressions of their authors and not those of the Society. Manuscript received at ASME Headquarters, August 12, 1959. Paper No. 59—A-102.

Table 1 Atmospheric data for the planets

		Composition		Molecular weight, g per mole	Gravitational constant (relative to Earth[a])	Average atm temp, deg K
		Mass fraction	Mole fraction			
Venus..	CO_2	0.90	0.85	41.6	0.87	266
	N_2	0.10	0.15			
Mars...	N_2	0.95	0.97	28.5	0.38	237
	CO_2	0.05	0.03			
Jupiter...	H_2	0.63	0.93	3.0	2.63	170
	CH_4	0.37	0.07			

[a] g_{earth} = 9.807 m per sec.

$$a/a_0 = (\gamma T/\gamma_0 T_0)^{1/2} \tag{2}$$

a, the reference velocity, being given by

$$a_0 = \left(\gamma_0 g \frac{R}{M} T_0\right)^{1/2} \tag{3}$$

and determined for a temperature of 273.16 K. The remaining quantities are defined as follows:

a = acoustic velocity
γ = heat-capacity ratio = $\dfrac{C_p/R}{C_p/R - 1}$
g = gravitational constant from Table 1
R = universal gas constant
M = molecular weight from Table 1
T = temperature, deg K

Viscosity. The viscosities of the various atmospheres were determined by the method proposed by Hirschfelder, et al. [7], for binary mixtures. An earlier investigation [8] of the various available procedures for determining viscosities of binary gas mixtures found this method to reproduce the experimental data with reasonable accuracy and, because of its semitheoretical nature, to lend itself better to extrapolation procedures. The equations are reported clearly and completely by [7] and will not be repeated here. Briefly, the method considers the contribution of interactions[a] between molecules of the pure components and that due to interactions of unlike molecules. The molecular parameters of this latter contribution are determined from those of the pure components by the use of empirical combining laws. The collision diameter for unlike interacting pairs is given by $\sigma_{12} = (\sigma_1 + \sigma_2)/2$, the minimum potential by $\epsilon_{12} = (\epsilon_1\epsilon_2)^{1/2}$. The molecular parameters for the pure components are determined from experimental viscosity measurements, the values employed for the viscosity calculations of this work being given in Table 2.

Table 2 Intermolecular force constants

Gas	From viscosity data [7] σ(Å)	From viscosity data [7] ϵ/k(°K)	From thermal-conductivity data σ(Å)	From thermal-conductivity data ϵ/k(°K)
Hydrogen	2.968	33.3	2.605	123.0
Nitrogen	3.749	79.8	3.767	93.0
Carbon dioxide	3.897	213.0	3.721	309.0
Methane	3.796	144.0	3.962	127.0

Thermal Conductivity. Thermal conductivities for the planetary atmospheres were also determined by the method set forth by Hirschfelder, et al. [7], for binary mixtures. As in the case of viscosity, a previous study [8] determined the validity of this representation for helium-air mixtures. The equations employed will not be given since they are set forth and clearly described in [7]. The method considers contributions to energy transport arising from the interactions of molecules in like and unlike pairs. These interactions are characterized by σ and ϵ as with viscosity, their values for like interactions being determined from an analysis of the pure gas thermal-conductivity data and for unlike interactions by the same empirical combining rules given for viscosity. The parameters determined for the pure gases are given in Table 2.

Prandtl Number. This dimensionless quantity plays such an important role in heat-transfer calculations that it was determined from the values of heat capacity, viscosity, and thermal conductivity for each of the planetary atmospheres. These properties are combined as given by

$$\mathrm{Pr} = \eta C_p/\lambda \tag{4}$$

Results for Pure Gases

The sources of data employed in this work are summarized in Table 3. All calculations were performed on an electronic computer. Heat-capacity data were taken from NBS Circular 564 [9] with the exception of methane which were obtained from [10].

As indicated earlier, the viscosities for the pure gases were determined according to [7] using the force constants reported there. The calculated results shown as solid lines are compared, Fig. 1, in the case of hydrogen, nitrogen, and carbon dioxide

Table 3 Sources of data

Gas	Heat capacity, C_p	Viscosity	Thermal conductivity
Hydrogen	[9]	According to [7] using force constants given there	[16, 24]
Nitrogen	[9]		[19, 25, 26, 27, 28]
Carbon dioxide	[9]		[13, 14, 15, 16, 17, 18, 19, 20, 21, 22, 23, 27]
Methane	[10]		[16, 29, 30]

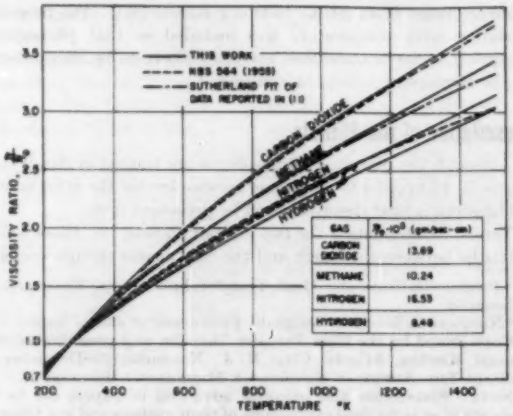

Fig. 1 Comparison of calculated component viscosities (solid lines) with curves fit to experimental data

[a] The molecular interactions are characterized by two constants, σ the collision diameter and ϵ the minimum potential energy of two interacting molecules.

with the best experimental curve given by [9]. For methane, the statistical predictions are compared with a Sutherland-formula representation of the viscosity which reproduces the experimental data [11] within the limits of experimental error for the temperature range (90 to 300 K). Satisfactory agreement is obtained between the two representations over the range for which experimental data exist with the possible exception of hydrogen where a difference at 1000 deg K amounts to 5 per cent. Because some of the experimental data considered in [9] scatter from the final curve by this magnitude and because of the inherent uncertainty in the knowledge of the atmospheric compositions, it was decided to retain the statistical predictions in order to have them consistent with the thermal-conductivity predictions.

Thermal conductivities for the pure gases were determined according to Hirschfelder [7] using the force constants calculated from conductivity data given in Table 2. The results are shown as solid lines in Figs. 2 and 3. In the case of nitrogen, hydrogen, and carbon dioxide they are compared in the figures with the best fit of the experimental data given by [9]. Recent experimental data published on carbon dioxide [19, 20, 23, 27] and not included in [9] also appear in Fig. 2. The methane predictions are shown in Fig. 3 together with experimental data [16, 29, 30]. For all four gases, the statistical representation appears to be entirely satisfactory, the average disagreement with the experimental data being of the order of 2 to 3 per cent.

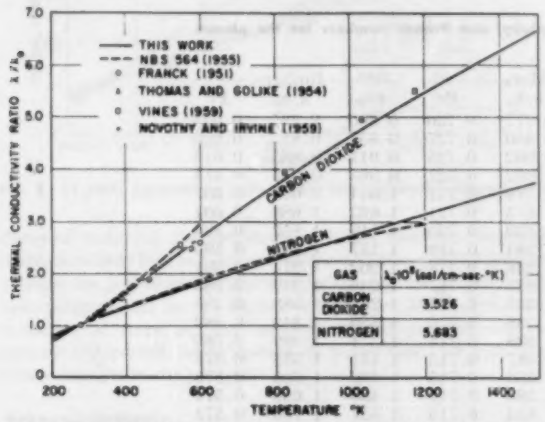

Fig. 2 Comparison of calculated carbon-dioxide and nitrogen thermal conductivity with experimental data

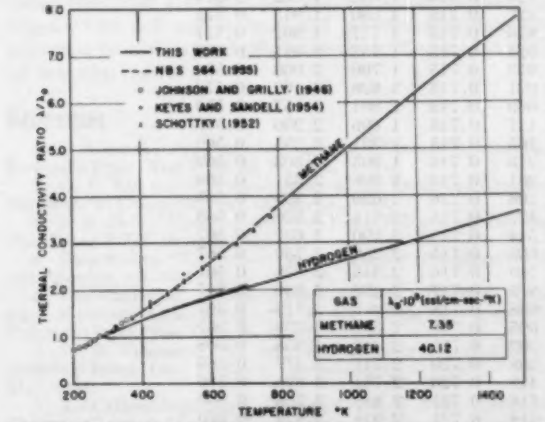

Fig. 3 Comparison of calculated methane and hydrogen thermal conductivity with experimental data

Atmospheric Properties

Dimensionless heat capacities and acoustic velocities for the planets Venus, Mars, and Jupiter as a function of the temperature are given, respectively, by Figs. 4, 5, and 6. The heat capacity may be converted to cal/gm mole deg K by taking R equal to 1.9872 cal/gm mole deg K. The acoustic velocity may be converted to meters per second using the values for a_0 at 273.16 K given in Table 4.

Dimensionless viscosities, thermal conductivities, and Prandtl numbers for the three planets are reported in Table 5 at 20-deg increments from 200 to 800 K and at 50-deg increments from 800 to 1500 K.

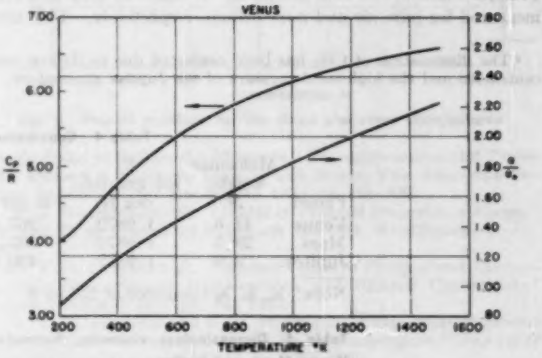

Fig. 4 Dimensionless heat capacity and sound velocity for Venus

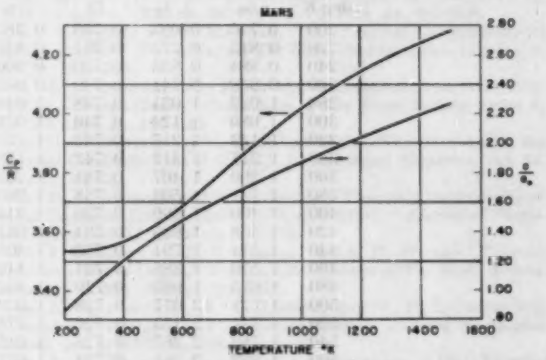

Fig. 5 Dimensionless heat capacity and sound velocity for Mars

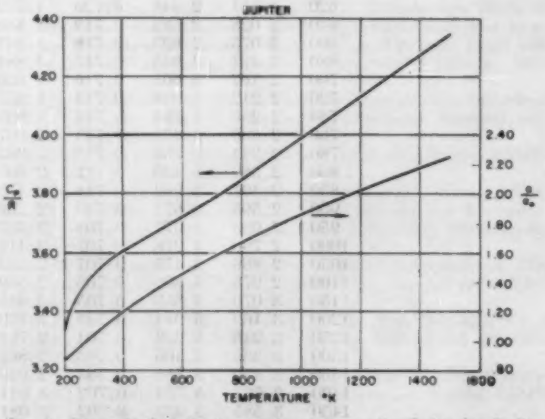

Fig. 6 Dimensionless heat capacity and sound velocity for Jupiter

The calculations were terminated at 1500 K where dissociation effects would be negligible.[4] Plots of the viscosity and conductivity in dimensionless form are given in Figs. 7 and 8. These may be converted to dimensional values by using the appropriate reference values given in Table 4 and in Figs. 7 and 8. The variation of Prandtl number with temperature is shown in Fig. 9. The Prandtl numbers for the planet Jupiter are seen to be significantly lower than for those of Mars and Venus, and for pure hydrogen [12] which comprises 93 volume per cent of the Jupiter atmosphere. The experimental results reported for helium-air mixtures [8] show a similar behavior, however. There, at 270 K, and a helium molar concentration of 90 per cent, the measured Prandtl number was 0.51 compared to values of 0.71 and 0.66 measured for pure air and pure helium, respectively. This mixture effect coupled with the influence of the large thermal conductivity of hydrogen would account for the Prandtl-number behavior for the Jupiter atmosphere.

[4] The dissociation of CH_4 has been neglected due to its low concentration and the high total pressure of the Jupiter atmosphere.

Summary and Conclusions

It should be recognized clearly that the thermodynamic and transport properties reported here refer to the atmospheric compositions chosen for the various planets. Since uncertainties remain regarding these compositions and since the atmospheric compositions enter directly into the calculation of the various properties, these properties will necessarily be subjected to an uncertainty. Under these circumstances, the reported atmospheric properties should be used judiciously.

Once having this reservation clearly understood, however, it is reasonable to expect that careful analysis of existing data for various pure gases when combined with well-established proce-

Table 4 Conversion constants for Figs. 4 to 8

Planet	Molecular weight, M	R, cal/gm mole deg K	a_0, m per sec	η_0, gm/sec cm	λ_0, cal/cm sec deg K
Venus..	41.6	1.9872	267.03	14.15×10^{-6}	3.828×10^{-5}
Mars...	28.5	1.9872	333.12	16.46×10^{-6}	5.612×10^{-5}
Jupiter..	3.0	1.9872	490.05	9.15×10^{-6}	34.6×10^{-5}

NOTE: a_0, η_0, λ_0 calculated at 273.16 K.

Table 5 Dimensionless viscosity, thermal-conductivity, and Prandtl numbers for the planets Venus, Mars, and Jupiter

T,	Venus			Mars			Jupiter		
deg K	η/η_0	λ/λ_0	Pr	η/η_0	λ/λ_0	Pr	η/η_0	λ/λ_0	Pr
200	0.740	0.693	0.755	0.785	0.777	0.730	0.800	0.735	0.635
220	0.813	0.773	0.751	0.847	0.840	0.727	0.857	0.812	0.626
240	0.884	0.855	0.750	0.906	0.902	0.725	0.911	0.885	0.619
260	0.954	0.941	0.749	0.963	0.962	0.723	0.963	0.956	0.614
280	1.022	1.031	0.748	1.018	1.019	0.722	1.014	1.024	0.607
300	1.089	1.124	0.746	1.071	1.075	0.721	1.063	1.089	0.601
320	1.153	1.217	0.744	1.123	1.130	0.720	1.110	1.152	0.597
340	1.217	1.312	0.742	1.173	1.183	0.719	1.157	1.214	0.594
360	1.280	1.407	0.741	1.222	1.236	0.718	1.202	1.274	0.591
380	1.341	1.503	0.738	1.269	1.287	0.717	1.246	1.332	0.588
400	1.400	1.599	0.736	1.316	1.338	0.717	1.288	1.388	0.585
420	1.458	1.695	0.734	1.361	1.388	0.716	1.330	1.443	0.582
440	1.514	1.791	0.733	1.405	1.438	0.716	1.371	1.499	0.580
460	1.570	1.886	0.731	1.449	1.487	0.715	1.411	1.553	0.578
480	1.625	1.982	0.729	1.492	1.536	0.715	1.450	1.605	0.576
500	1.678	2.077	0.728	1.533	1.584	0.715	1.490	1.658	0.574
520	1.731	2.173	0.726	1.575	1.633	0.715	1.527	1.709	0.573
540	1.783	2.267	0.725	1.615	1.682	0.715	1.567	1.761	0.572
560	1.833	2.361	0.724	1.655	1.731	0.715	1.605	1.812	0.572
580	1.884	2.455	0.723	1.695	1.779	0.715	1.643	1.862	0.571
600	1.933	2.548	0.721	1.733	1.827	0.715	1.680	1.913	0.571
620	1.981	2.641	0.720	1.772	1.876	0.715	1.717	1.962	0.571
640	2.028	2.732	0.719	1.810	1.924	0.715	1.753	2.011	0.570
660	2.075	2.823	0.718	1.847	1.973	0.715	1.790	2.060	0.570
680	2.121	2.915	0.717	1.884	2.021	0.715	1.826	2.109	0.570
700	2.167	3.005	0.716	1.920	2.069	0.715	1.861	2.157	0.570
720	2.212	3.094	0.715	1.957	2.117	0.715	1.896	2.206	0.570
740	2.256	3.183	0.714	1.992	2.165	0.715	1.931	2.255	0.569
760	2.300	3.273	0.714	2.027	2.213	0.716	1.965	2.303	0.569
780	2.344	3.359	0.713	2.062	2.261	0.716	1.998	2.351	0.569
800	2.386	3.446	0.712	2.097	2.308	0.716	2.030	2.399	0.568
850	2.491	3.662	0.711	2.178	2.427	0.715	2.111	2.520	0.568
900	2.593	3.871	0.710	2.258	2.544	0.715	2.190	2.639	0.567
950	2.693	4.077	0.708	2.337	2.658	0.715	2.268	2.759	0.567
1000	2.790	4.278	0.707	2.416	2.769	0.716	2.345	2.878	0.567
1050	2.886	4.475	0.707	2.493	2.879	0.717	2.420	2.998	0.567
1100	2.978	4.669	0.706	2.569	2.988	0.718	2.495	3.118	0.567
1150	3.070	4.859	0.705	2.645	3.095	0.718	2.569	3.238	0.567
1200	3.160	5.044	0.704	2.720	3.202	0.719	2.640	3.358	0.568
1250	3.248	5.223	0.704	2.794	3.308	0.720	2.711	3.477	0.568
1300	3.335	5.406	0.703	2.867	3.412	0.720	2.781	3.593	0.569
1350	3.420	5.581	0.703	2.939	3.516	0.721	2.851	3.708	0.569
1400	3.503	5.754	0.702	3.011	3.618	0.721	2.919	3.824	0.570
1450	3.585	5.923	0.702	3.081	3.720	0.721	2.987	3.939	0.571
1500	3.667	6.090	0.701	3.152	3.819	0.722	3.054	4.054	0.571

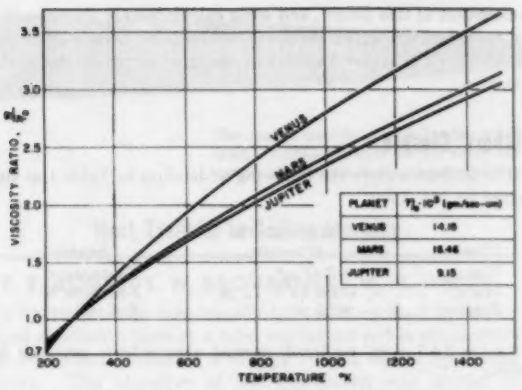

Fig. 7 Viscosity ratio for the three planetary atmospheres

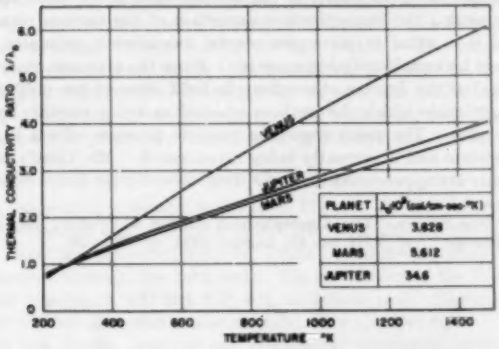

Fig. 8 Thermal conductivity ratio for the three planetary atmospheres

dures of statistical thermodynamics should yield the best estimates available for the thermodynamic and transport properties.

Since the procedure for determining the various properties has been programmed for the electronic computer, the future determination of more accurate atmospheric information for the planets will permit the properties to be re-evaluated with only minor changes in the program.

Acknowledgments

The authors gratefully acknowledge the assistance of Mr. Gangu Hingorani who developed and supervised the computer program with skill and patience, and Mr. Bruce Lindahl who performed the tedious hand-calculation checks necessary to verify the computer results.

References

1 G. Solomon, "Planetary Atmospheres," Vistas in Astronautics, Pergamon Press, New York, N. Y., 1958.

2 G. P. Kuiper, "The Atmosphere of the Earth and Planets," University of Chicago Press, Chicago, Ill., 1949.

3 S. H. Dole, "The Atmosphere of Venus," The Rand Corporation, Paper P-978, October, 1956.

4 Otto Struve, "The Atmospheres of Jupiter and Saturn," *Sky and Telescope*, vol. 13, 1954, pp. 336–338.

5 Carl Gazley, Jr., "Deceleration and Heating of a Body Entering a Planetary Atmosphere From Space," Vistas in Astronautics, Pergamon Press, New York, N. Y., 1958, p. 8.

6 D. R. Chapman, "An Approximate Analytical Method for Studying Entry Into Planetary Atmospheres," NACA TN 4279, May, 1958.

7 J. O. Hirschfelder, C. F. Curtiss, and R. B. Bird, "Molecular Theory of Gases and Liquids," John Wiley & Sons, Inc., New York, N. Y., 1954, pp. 529–537.

8 E. R. G. Eckert, W. E. Ibele, and T. F. Irvine, Jr., "Thermal Conductivity of Helium-Air Mixtures," Thermodynamics and Transport Properties of Gases, Liquids, and Solids, The American Society of Mechanical Engineers, 1959, pp. 295–300.

9 J. Hilsenrath, et al.; "Tables of Thermal Properties of Gases," Circular U. S. Bureau of Standards No. 564, Washington, D. C., 1955.

10 F. D. Rossini, et al., "Selected Values of Physical and Thermodynamic Properties of Hydrocarbons and Related Compounds," Carnegie Press, Pittsburgh, Pa., 1953.

11 H. L. Johnston and K. E. McCloskey, "Viscosities of Several Common Gases Between 90°K and Room Temperature," *Journal of Physical Chemistry*, vol. 44, 1940, pp. 1038–1058.

12 J. Hilsenrath and Y. S. Touloukian, "The Viscosity, Thermal Conductivity, and Prandtl Number for Air, O_2, N_2, NO, H_2, CO, CO_2, H_2O, He, and A," Trans. ASME, vol. 76, 1954, pp. 967–985.

13 H. Gregory and S. Marshall, "The Thermal Conductivity of Carbon Dioxide," *Proceedings of The Royal Society*, series A, vol. 114, 1927, pp. 354–366.

14 B. G. Dickens, "The Effect of Accommodation on Heat Conduction Through Gases," *Proceedings of The Royal Society*, series A, vol. 143, 1934, pp. 517–540.

15 G. G. Sherratt and E. Griffiths, "A Hot-Wire Method for the Thermal Conductivities of Gases," *Philosophical Magazine*, vol. 27, 1939, pp. 68–75.

16 H. L. Johnston and E. R. Grilley, "Thermal Conductivity of Eight Common Gases Between 80°K and 380°K," *Journal of Chemical Physics*, vol. 14, 1946, pp. 233–238.

17 J. D. Lambert, E. N. Staines, and S. D. Woods, "Thermal Conductivities of Organic Vapors," *Proceedings of The Royal Society*, series A, vol. 200, 1950, pp. 262–271.

18 E. A. Stolyarov, V. V. Ipatiev, and V. P. Teodorovitch, "Transfer Phenomena in Compressed Gases," *Zhurnal Fizicheskoy Khimii*, vol. 24, 1950, pp. 166–176.

19 E. U. Franck, "Temperature Dependence of the Thermal Conductivity of Several Gases, "*Zeitschrift für Elektrochemie*, vol. 55, 1951, pp. 636–643.

20 L. B. Thomas and R. C. Golike, "A Comparative Study of Accommodation Coefficients by the Temperature-Jump and Low-Pressure Methods and Thermal Conductivities of Helium, Neon, and Carbon Dioxide," *Journal of Chemical Physics*, vol. 22, 1954, pp. 300–305.

21 C. T. Archer, "The Thermal Conductivity and the Accommodation Coefficient of Carbon Dioxide," *Philosophical Magazine*, vol. 19, 1935, pp. 901–918.

22 F. G. Keyes, "Thermal Conductivity of Gases," Trans. ASME, vol. 77, 1955, pp. 1395–1396.

23 J. Novotny and T. F. Irvine, Jr., "Viscosity, Thermal Conductivity, and Prandtl Number of Carbon Dioxide—Air Mixtures," Heat Transfer Laboratory, University of Minnesota, Minneapolis, Minn., 1959.

24 N. B. Vargaftik and I. Parfenov, "Heat Conductivity of Hydrogen at High Temperatures," *Zhurnal Eksperimental noi i Teoreticheskoi Fiziki*, vol. 8, 1935, p. 189.

25 F. G. Keyes, "Measurements of the Heat Conductivity of Nitrogen-Carbon Dioxide Mixtures," Trans. ASME, vol. 73, 1951, pp. 597–603.

26 F. G. Keyes, "Additional Measurements of Heat Conductivity of Nitrogen, Carbon Dioxide, and Mixtures," Trans. ASME, vol. 74, 1952, pp. 1303–1306.

27 R. G. Vines, "Measurement of the Thermal Conductivities of

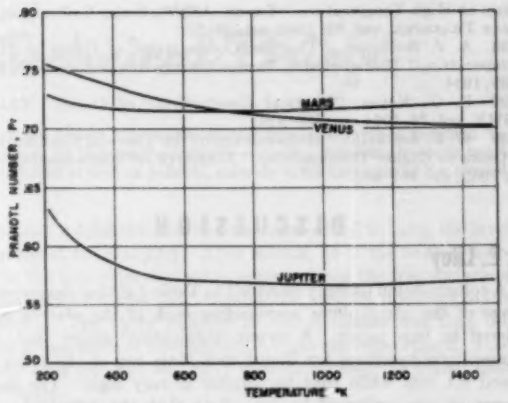

Fig. 9 Prandtl numbers for the three planetary atmospheres

Gases at High Temperature," TRANS. ASME, Series C, JOURNAL OF HEAT TRANSFER, vol. 82, 1960, pp. 48–52.

28 A. J. Rothman, "Thermal Conductivity of Gases at High Temperature," United States Atomic Energy Commission, UCRL-2339, 1954.

29 F. G. Keyes, "Thermal Conductivity of Gases," TRANS. ASME, vol. 76, 1954, pp. 809–816.

30 W. F. Schottky, "Measurement of the Thermal Conductivity of Gases at Higher Temperatures," *Zeitschrift für Elektrochemie*, vol. 56, 1952, pp. 889–892.

DISCUSSION

P. E. Liley[6]

A column could usefully be added to Table 1 giving the pressure range of the atmosphere surrounding each of the planets considered in this paper. A recent publication[6] states that the atmospheric pressures for Venus and Mars are of the order of 3 and 0.1 atm while that for Jupiter is very high. The same source quotes evidence[7] to the effect that the principal constituents of the atmosphere of Jupiter are hydrogen and helium with methane and ammonia present as minor constituents. This differs from the authors' assumption of a hydrogen-methane atmosphere for this planet.

The data calculated by the authors for Jupiter must be considered only approximate in view of the high pressure of the atmosphere of this planet, and some calculations of the properties for considerably higher pressures would have been most useful to determine whether significant changes occur at the higher densities.

[6] Assistant Professor of Mechanical Engineering, Purdue University, Lafayette, Ind.

[6] "Space Handbook: Astronautics and Its Applications," Government Printing Office, Washington, D. C., 1959.

[7] H. C. Urey, "The Planets, Their Origin and Development," Yale University Press, New Haven, Conn., 1952.

Authors' Closure

The authors supply the following addendum to Table 1 as suggested by Mr. Liley.

Planet	Atmospheric pressure	Source
Venus	$\approx 3.0\ p_0$*	Footnote 6
Mars	0.08 to 0.12 p_0	Footnote 6
Jupiter	$\approx 20\ p_0$	Ref. [6]

* p_0 = 14.7 psia, sea-level, normal atmospheric pressure for earth.

There is, as indicated in the introduction, much uncertainty concerning the atmospheric composition of the various planets, and it is usual to encounter several inconsistent estimates, all made by equally reliable scientists. Since the estimate made by Urey[7] of the Jupiter atmosphere in 1952, Struve[8] has published an estimate which the authors selected as being possibly more accurate. The point regarding possible pressure effects is appropriate and is currently being investigated. Mr. Liley's comments are appreciated.

[8] Otto Struve, "The Atmosphere of Jupiter and Saturn, Sky and Telescope," vol. XIII, no. 10, August, 1954, pp. 336–338.

Journal of HEAT TRANSFER — Technical Briefs

This section consists of contributions of 750 words or less (about 2½ double-spaced typewritten pages, including figures). Technical Briefs will be reviewed and approved by the specific division's reviewing committee prior to publication. After approval such contributions will be published as soon as possible, normally in the next issue of the Journal.

Heat Transfer to Boiling Mercury

F. E. ROMIE,[1] S. W. BROVARNEY,[1] W. H. GIEDT[1]

AN EXPERIMENT on heat transfer to boiling mercury flowing by natural circulation through a tube was carried out in conjunction with evaluation studies of a nuclear reactor cooled by boiling mercury. The objective of the experiment was limited to demonstrating that very high heat fluxes could be sustained by boiling mercury. Despite this limited objective, sufficient measurements were made to permit estimation of quality and density of the two-phase mixture leaving the test section. The maximum heat flux attained in the experiments was 600,000 Btu/hr-ft^2; higher fluxes were prevented by equipment limitations rather than by transition from the nucleate boiling regime. The maximum flux previously reported [1][2] is 200,000 Btu/hr-ft^2.

Experimental Apparatus and Operation

The apparatus schematic is shown in Fig. 1. The test section proper consisted of a 1018 steel tube $^7/_{16}$-in. OD with a 0.109-in. wall. Heat was generated in a 4-in. length by conduction of electric current through the tube wall. The remainder of the flow conduit was $^7/_{16}$-in. OD 304 S/S with an 0.05-in. wall. The condenser and water-cooled condenser tube were also 304 S/S.

The test section material and dimensions correspond to the generation of 89 per cent of the heat in the tube wall with the tube filled with liquid mercury. During boiling, the area of the mercury conduction path is diminished and the fraction of heat generated in the wall is, of course, higher than the above value. (In reduction of the boiling data, it was considered that all of the heat was generated in the wall.)

Power input to the test section was determined by measuring the voltage drop between two voltage taps connected to the test section wall. The electrical resistance of the test section was computed from the resistivity of the steel evaluated at the average wall temperature. Measurement of the flow rate of the naturally circulating mercury was afforded by a thermal flow meter in which the temperature change of the flowing mercury and the electrically supplied heat input to the meter are measured variables. The flow rate of the liquid mercury is related to these two variables by a simple heat balance made across the electric heater. The primary measurement of mercury pressure (under conditions of net boiling) was obtained by measuring the (saturation) temperature of the mercury leaving the test section. A Bourdon pressure gage was provided to permit rapid visual notification of possible pressure abnormalities during operation. Temperature measurements were made with chromel-alumel thermocouples welded to the external surfaces of the loop.

Magnesium and titanium hydride (8 gm of Mg and 0.5 gm of TiH) were added to the mercury after the loop had been filled to a level within the condenser. Evidence [2] exists that these two additives are necessary for attainment of high nucleate boiling fluxes. Additional mercury was then added to bring the level to the top of the seal plug. After sealing, 65 of the 85 lb of mercury in the loop were drained in order to bring the free surface of the mercury to a level just covering the loop leg openings to the condenser. The vapor pressure in the condenser was thus the saturation pressure of mercury at the condenser conditions. Subsequent runs (on any one day) were at successively higher heat input rates.

Initial operation of the loop revealed that the steel test section wall was not wet by the mercury. However, it was found possible to attain wetting by mechanically cleaning the surface and then depositing a thin copper layer by dipping the surface in a copper sulfate solution. Following this treatment, the mercury readily wet the surface.

During the course of the experiment, hydrodynamic oscillations of the mercury flow were occasionally indicated by the Bourdon pressure gage. In all cases, these oscillations could be made to cease by increasing the heat input or by increasing the system pressure. Increasing the heat input was effective at the lower heat flux level at which boiling in the test section was beginning. At the higher heat fluxes, an increase in system pressure was required to stop the oscillations. System pressure was increased by decreasing the water rate to the mercury condenser. Lack of an effective means of metering the low water rates required for stability at the high heat fluxes and also concern over safety in the event of a system rupture at the higher pressures required for high heat fluxes led to termination of the experimental work at a flux of 600,000 Btu/hr-ft^2.

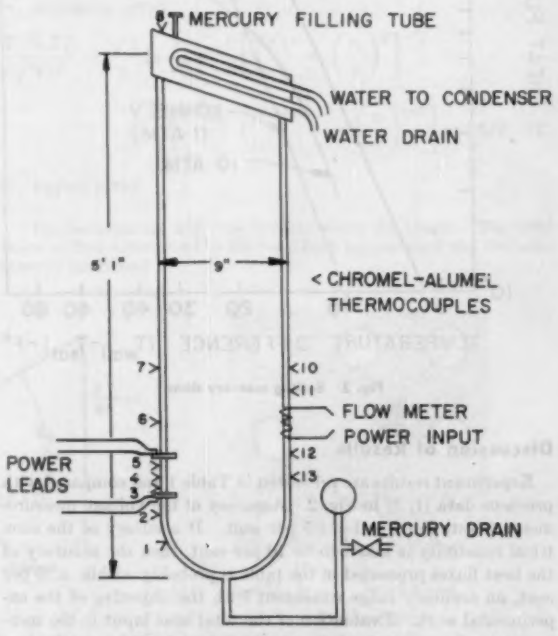

Fig. 1 Schematic of heat-transfer loop

[1] Advanced Technology Laboratories, a Division of American-Standard, Mountain View, Calif. F. E. Romie and W. H. Giedt, Mem. ASME.

[2] Numbers in brackets designate References at end of paper.

Contributed by the Heat Transfer Division of THE AMERICAN SOCIETY OF MECHANICAL ENGINEERS. Manuscript received at ASME Headquarters, June 6, 1960.

Table 1

Run	Heat flux Btu / hr ft² × 10⁻²	Test section pressure psia	Flow velocity at inlet to test section ft/sec	Inlet temp deg F	Temp increase through test section deg F	Inside wall temp at TC 5 deg F	Inside wall temp less saturation temp deg F	Heat out / Heat in	Exit quality
1	...	...	...	...	...	...	...	...	...
2	24	...	2.9	66	137	647	...	2.16	...
3	92	...	0.67	282	169	468	...	1.65	...
4	150	...	1.0	256	217	504	...	2.0	...
5	190	...	1.1	293	227	562	...	1.78	...
6	230	...	1.9	320	221	587	...	2.50	...
7	260	...	1.5	355	221	629	...	1.66	...
8	400	...	1.3	386	240	701	...	1.0	...
9	460	10	1.1	392	249	741	110	...	0.015
10	67	...	...	247	214	453	...	...	...
11	210	...	1.3	480	135	674	...	1.03	...
12	280	10	1.4	488	153	710	69	...	0.001
13	340	14	1.1	506	122	759	88	...	0.032
14	470	17	0.89	524	168	776	84	...	0.061
15	550	19	0.74	536	165	776	75	...	0.10
16	600	33	1.5	649	112	825	64	...	0.049

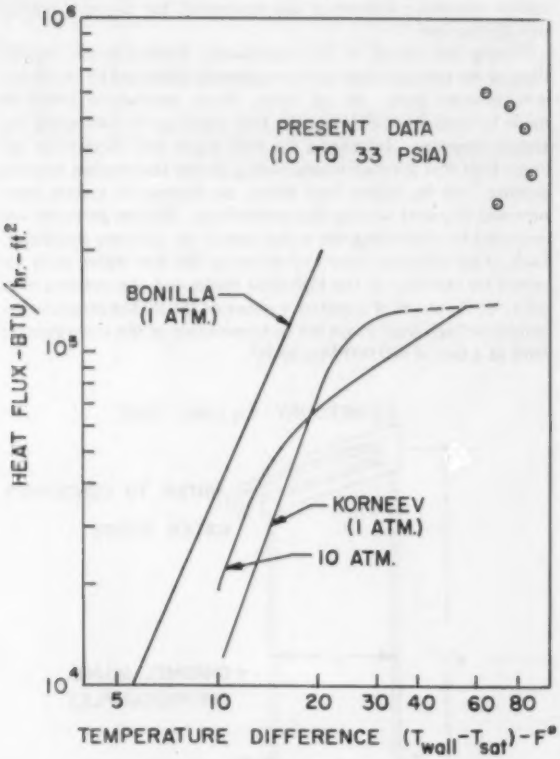

Fig. 2 Boiling mercury data

Discussion of Results

Experiment results are presented in Table 1 and compared with previous data [1, 3] in Fig. 2. Accuracy of the voltage measurements is estimated to be ±5 per cent. If accuracy of the electrical resistivity is taken to be 10 per cent, then the accuracy of the heat fluxes presented in the table is probably within ±20 per cent, an accuracy range consistent with the objective of the experimental work. Evaluation of the total heat input to the mercury (the denominator of the entries in the second from the last column of Table 1) has a considerably lower accuracy because the rate of heat conduction to or from the test section via the electrodes is unknown. The product of the heat flux and the inside surface area of the 4-in. free length of the test section was used for an estimate of the total heat input. The heat output is calculated as the product of the mass rate and the enthalpy change of the mercury. The enthalpy change of the mercury (under conditions of no net boiling) was based on the temperature change of the mercury: $T_6 - T_2$.

The test section pressure for runs with net vapor generation is the saturation pressure corresponding to the temperature indicated by thermocouple number 6.

The exit quality of the mercury liquid-vapor mixture is calculated using the equation

$$\chi_e = \frac{1}{\Delta h}\left[\frac{(\text{Heat in})}{(\text{Mass rate})} - C_p(T_{sat} - T_2)\right]$$

in which T_2 is the inlet temperature to the section. Based on this exit quality and an assumed slip ratio of two, the computed density of the liquid-vapor mixture leaving the test section is 5.5 and 17.9 lb/ft³ for runs 15 and 16, respectively. The computed vapor volume fraction is in excess of 97 per cent for both runs.

No calibration of the thermal flow meter was made. Errors in flow measurements can be expected due, primarily, to heat losses from the metering section. These errors would make the computed mass rate (inlet velocity in Table 1) higher than the true value. If a lower mass rate is used, the heat balance would be improved and the exit qualities would be higher than those listed. There is, therefore, reason to believe that the density of the liquid-vapor mixture was even lower than the values quoted above.

A more complete description of the apparatus and tests is given in reference [2].

References

1 C. F. Bonilla, et al., "Pool Boiling Heat Transfer With Mercury," Reactor Heat Transfer Conference, November 1–2, 1956, New York, N. Y. (Nuclear Development Corporation of America, White Plains, N. Y.)

2 J. O. Bradfute, et al., "An Evaluation of Mercury Cooled Breeder Reactors," AEC Report ATL-A-102, 31, October, 1959.

3 M. I. Korneev, "Heat Transfer in Mercury and Magnesium Amalgams During Boiling Under Conditions of Free Convection," (Translation) *Teploenergetika*, vol. 2, no. 4, 1955, p. 44.

Temperature Distribution and Heat-Transfer Results for an Internally Cooled, Heat-Generating Solid

E. M. SPARROW[1]

Introduction

In internally heat-generating solids such as a nuclear reactor or a carrier of electric current, cooling may be provided to remove heat for power generation purposes or to maintain the temperature within tolerable limits. One approach toward cooling such systems is to pass fluid through parallel flow passages which are arranged in a regular pattern throughout the solid. Such a cooling arrangement utilizing circular passages is pictured in Fig. 1. The left-hand sketch (*a*) shows the passages in an equilateral triangular array, while the right-hand sketch (*c*) shows a square pattern. It is clear that the material immediately adjacent to the passages will be most strongly cooled and that the temperature will be higher in the interior. Such temperature nonuniformities may serve to produce significant thermal stresses and additionally, for a reactor, certain temperature-dependent nuclear characteristics may be affected.

The aim of the present investigation is to provide information on the temperature distribution and heat transfer in heat-generating solids which are internally cooled by circular flow passages arranged in either equilateral triangular or square array. Results will be presented over a range of spacing ratios[2] s/r_0 from 1.05 (passages almost touching) to indefinitely large values. The rate of heat generation per unit volume Q will be taken to be uniform, and the flow fully developed. The purpose of this brief report is to record in the permanent literature the main results of reference [1][3] which is available only in preprint form.

For the triangular array, analytical results appropriate to relatively large spacings have been given in references [2] and [3]. Smaller spacings were considered in reference [4], but the temperature distribution is given only for $s/r_0 = 1.2$. For the square array, no heat-transfer studies have previously been carried out. But, as was pointed out during the review of reference [1] the problem of neutron diffusion has the same governing equation as the temperature problem. The neutron diffusion problem has been treated in reference [5] by an analytical technique which is best suited to large spacings.

Summary of the Analysis and Results

Under the conditions of hydrodynamically and thermally fully developed flow and uniform internal heat generation in the solid, the temperature rises linearly in the direction of fluid flow. So, as far as the solid is concerned, there is no net heat transfer normal to the plane of Fig. 1. The conduction problem thus becomes two-dimensional. Because of the symmetry inherent in the configurations under consideration it is necessary to study only a representative portion of the solid. The typical elements appropriate to the triangular and square arrays are shown blackened in Figs. 1 (*a* and *c*), respectively. The center sketch (*b*) isolates the element and shows the boundary conditions. The angle θ_0 is 30 deg for the triangular array and 45 deg for the square array. The statement that $\partial T/\partial\theta = 0$ on the radial boundaries is an expression of the symmetry condition as is the statement $\partial T/\partial n = 0$ (n = normal) on the right-hand boundary. At the surface of the passage, $r = r_0$, we impose the condition that the temperature is uniform around the periphery[4] and has a value T_0 at the cross section under consideration.

The heat-conduction problem is governed by Laplace's equation plus an additional term for the volume heat source Q. In cylindrical co-ordinates, we get

$$\frac{\partial^2 T}{\partial r^2} + \frac{1}{r}\frac{\partial T}{\partial r} + \frac{1}{r^2}\frac{\partial^2 T}{\partial \theta^2} = -\frac{Q}{k} \tag{1}$$

As shown in reference [1], it is possible to find a solution of equation (1) which exactly satisfies the boundary conditions at $r = r_0$, and along the radial lines $\theta = 0$ deg and $\theta = \theta_0$. But, because the typical element is a mixture of cylindrical and rectangular geometry, it is not possible to satisfy exactly the conditions on all the boundaries. Consequently, on the right-hand boundary, the condition $\partial T/\partial n = 0$ was satisfied at a finite number of points, rather than at all points. However, a sufficient number of points were selected so that the temperature distribution results were not significantly affected by the use of additional points. In addition, over-all energy conservation was also satisfied. The details of the analysis are available in reference [1]. The final expressions for the temperature distribution have been found to be

(*a*) triangular array

$$\frac{T - T_0}{(Q/k)s^2} = \frac{\sqrt{3}}{\pi}\ln\frac{r}{r_0} - \frac{1}{4}\left[\left(\frac{r}{s}\right)^2 - \left(\frac{r_0}{s}\right)^2\right] + \sum_{J=1}\frac{\Delta_J}{6J}\left(\frac{r}{s}\right)^{6J}\left[1 - \left(\frac{r_0}{r}\right)^{12J}\right]\cos 6J\theta \tag{2}$$

(*b*) square array

[1] Professor of Mechanical Engineering, University of Minnesota, Minneapolis, Minn. Assoc. Mem. ASME.

[2] See Fig. 1 for Nomenclature.

[3] Numbers in brackets designate References at end of paper.

Contributed by the Heat Transfer Division of The American Society of Mechanical Engineers. Manuscript received at ASME Headquarters, June 6, 1960.

[4] The temperature will vary linearly along the length. The local value of T_0 is determined by the local bulk temperature and the heat-transfer coefficient.

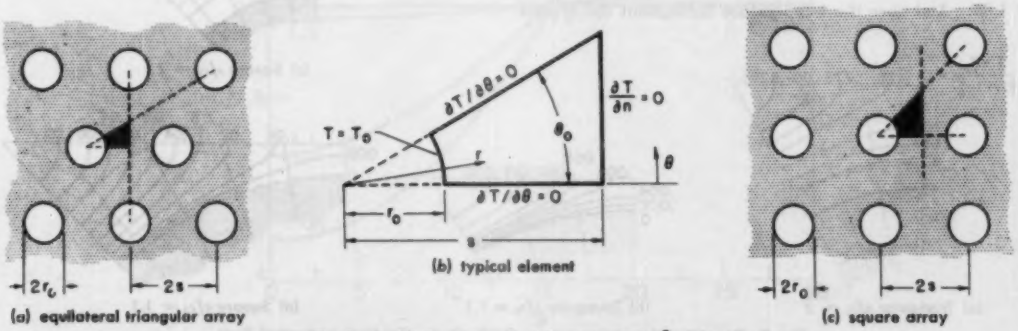

Fig. 1 Cooling passages in a heat-generating solid

Table 1 Values of δ_j for square cooling arrangement

s/r_0	δ_1	δ_2	δ_3	δ_4	δ_5	δ_6	δ_7
4.0	$-1.25382(10^{-1})$	$-1.0583(10^{-2})$	$-6.120(10^{-4})$	$-3.898(10^{-5})$	$-2.42(10^{-6})$	$-1.5(10^{-7})$	$-8\ (10^{-9})$
2.0	$-1.25098(10^{-1})$	$-1.0429(10^{-2})$	$-5.713(10^{-4})$	$-3.177(10^{-5})$	$-1.39(10^{-6})$	$-2\ (10^{-8})$	$3\ (10^{-9})$
1.5	$-1.22597(10^{-1})$	$-9.060\ (10^{-3})$	$-2.08\ (10^{-4})$	$5.33\ (10^{-5})$	$6.1\ (10^{-6})$	$1\ (10^{-6})$	$1\ (10^{-7})$
1.3	$-1.17022(10^{-1})$	$-5.995\ (10^{-3})$	$6.13\ (10^{-4})$	$1.65\ (10^{-4})$	$3.1\ (10^{-5})$	$4\ (10^{-6})$	$4\ (10^{-7})$
1.2	$-1.10421(10^{-1})$	$-2.387\ (10^{-3})$	$1.566(10^{-3})$	$5.50\ (10^{-4})$	$5.3\ (10^{-5})$	$6\ (10^{-6})$	$5\ (10^{-7})$
1.15	$-1.05352(10^{-1})$	$3.172\ (10^{-4})$	$2.233(10^{-3})$	$4.44\ (10^{-4})$	$5.8\ (10^{-5})$	$4.3(10^{-6})$	$1\ (10^{-6})$
1.1	$-9.8721\ (10^{-2})$	$3.6596(10^{-3})$	$2.911(10^{-3})$	$4.655(10^{-4})$	$2.44(10^{-5})$	$-1.1(10^{-5})$	$-5.5(10^{-6})$
1.05	$-9.0358\ (10^{-2})$	$7.310\ (10^{-3})$	$3.210(10^{-3})$	$2.06\ (10^{-4})$	$-1.20(10^{-4})$	$-3.8(10^{-5})$	$-1.6(10^{-5})$

s/r_0	δ_8	δ_9	δ_{10}
1.10	$-1.5(10^{-6})$	$-3(10^{-7})$	$-4(10^{-8})$
1.05	$-3.2(10^{-6})$	$-4(10^{-7})$	$-2(10^{-8})$

Table 2 Values of Δ_j for triangular cooling array

s/r_0	Δ_1	Δ_2	Δ_3	Δ_4	Δ_5	Δ_6	Δ_7
4.0	$-5.05072(10^{-2})$	$-6.0881(10^{-4})$	$-1.262(10^{-5})$	$-1.97(10^{-7})$	$-3.08(10^{-9})$	$-4.8(10^{-11})$	$-7(10^{-13})$
2.0	$-5.04988(10^{-2})$	$-6.0542(10^{-4})$	$-1.217(10^{-5})$	$-1.84(10^{-7})$	$-1.33(10^{-9})$	$2.8(10^{-11})$	$2(10^{-12})$
1.5	$-5.02447(10^{-2})$	$-6.9920(10^{-4})$	$1.374(10^{-6})$	$8.54(10^{-7})$	$5.23(10^{-8})$	$2.4(10^{-9})$	$8(10^{-11})$
1.3	$-4.90792(10^{-2})$	$-2.1203(10^{-4})$	$6.354(10^{-5})$	$5.42(10^{-6})$	$2.99(10^{-7})$	$1.3(10^{-8})$	$4(10^{-10})$
1.2	$-4.69598(10^{-2})$	$8.7812(10^{-4})$	$1.749(10^{-4})$	$1.51(10^{-5})$	$6.27(10^{-7})$	$1.7(10^{-8})$	$-1(10^{-10})$
1.175	$-4.60073(10^{-2})$	$1.0819(10^{-3})$	$2.205(10^{-4})$	$+1.56(10^{-5})$	$8.32(10^{-7})$	$9.8(10^{-10})$	$-2(10^{-9})$
1.15	$-4.48345(10^{-2})$	$1.5384(10^{-3})$	$2.736(10^{-4})$	$1.76(10^{-5})$	$4.21(10^{-7})$	$-5\ (10^{-8})$	$-7(10^{-9})$
1.10	$-4.15694(10^{-2})$	$2.8029(10^{-3})$	$3.782(10^{-4})$	$1.09(10^{-5})$	$-2.40(10^{-6})$	$-5\ (10^{-7})$	$-5(10^{-8})$
1.05	$-3.68059(10^{-2})$	$4.3358(10^{-3})$	$3.169(10^{-4})$	$-5.67(10^{-5})$	$-1.51(10^{-5})$	$-1.7(10^{-6})$	$-9(10^{-8})$

$$\frac{T - T_0}{(Q/k)s^2} = \frac{2}{\pi} \ln \frac{r}{r_0} - \frac{1}{4}\left[\left(\frac{r}{s}\right)^2 - \left(\frac{r_0}{s}\right)^2\right] + \sum_{j=1} \frac{\delta_j}{4J}\left(\frac{r}{s}\right)^{4J}\left[1 - \left(\frac{r_0}{r}\right)^{4J}\right] \cos 4J\theta \quad (3)$$

where the δ_j and Δ_j represent numerical constants which are listed in Tables 1 and 2, respectively, over the range from $s/r_0 = 1.05$ to $s/r_0 = 4.0$. Two aspects of the tables are worthy of note: First, the δ_j and Δ_j decrease with increasing j; with the decrease being more rapid at the larger values of s/r_0. Second, the dependence of any particular δ_j or Δ_j on the spacing ratio s/r_0 becomes quite small at the larger s/r_0; especially for the more important coefficients $j = 1, 2, 3, 4$. Additionally, it was found that with increasing s/r_0, fewer and fewer terms of the series are needed. For $s/r_0 > 4$, only Δ_1, δ_1, and possibly δ_2 are required, and these have achieved essentially constant values. Using equations (2) and (3) in conjunction with the tables, the temperature distribution within the typical element can be calculated for any value of $s/r_0 \geq 1.05$. And once the temperature throughout the typical element has been found, then it is known throughout the entire cross section by symmetry.

To illustrate the results, temperature contours (lines of constant temperature) are displayed in Fig. 2 for two representative cases: $s/r_0 = 2.0$ and 1.1, with (a) and (b) applying to the triangular array and (c) and (d) to the square array. In appraising these figures, it may be noted that with increasing spacing, the temperature field about any passage will be less and less influenced by the neighboring passages and, hence, will become

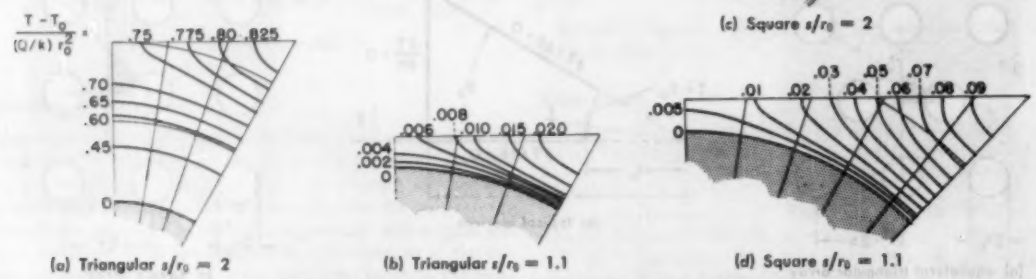

(a) Triangular $s/r_0 = 2$ (b) Triangular $s/r_0 = 1.1$ (c) Square $s/r_0 = 2$ (d) Square $s/r_0 = 1.1$

Fig. 2 Representative temperature distributions, showing isothermal lines

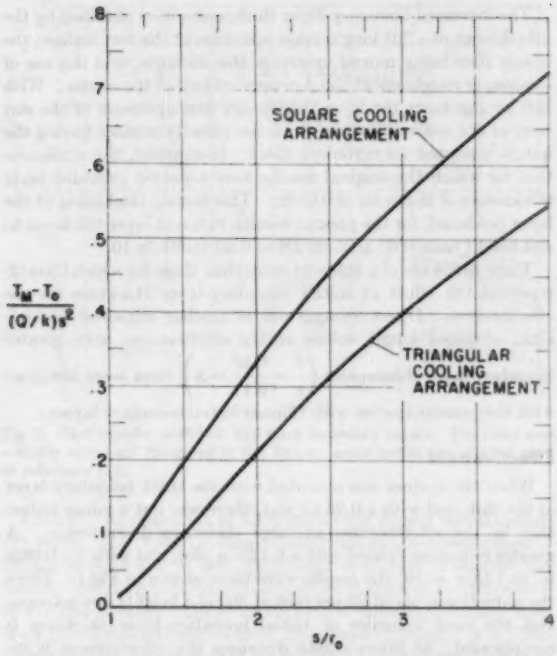

Fig. 3 Maximum (hot spot) temperatures in the cross section of a heat-generating solid

more circularly symmetric. This is borne out by comparing Fig. 2 (*a*) with 2 (*b*), and also by comparing 2 (*c*) with 2 (*d*).

Of great practical interest is the maximum temperature T_M (hot spot) in the cross section. For the triangular array, this

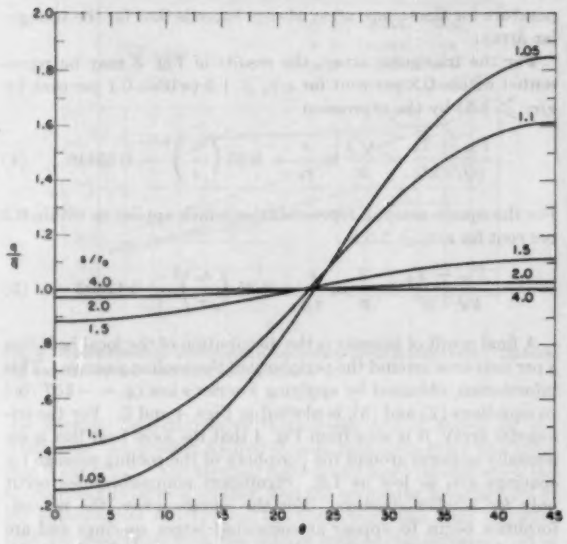

Fig. 5 Local wall heat flux distribution for square cooling arrangement

occurs at $\theta = 30$ deg and $r = s/\cos 30$ deg; and for the square array at $\theta = 45$ deg and $r = s/\cos 45$ deg. Hot spot temperatures evaluated from equations (2) and (3) are plotted in Fig. 3. In interpreting this figure, it is important to note that the spacing appears in the ordinate. With this in mind, it is seen that for a fixed spacing s, the hot spot temperature increases as the radius of the cooling passage decreases. This finding is in accord with intuition. It is also interesting to note that for fixed values of spacing s, passage radius r_0, and heat source Q, the hot spot tem-

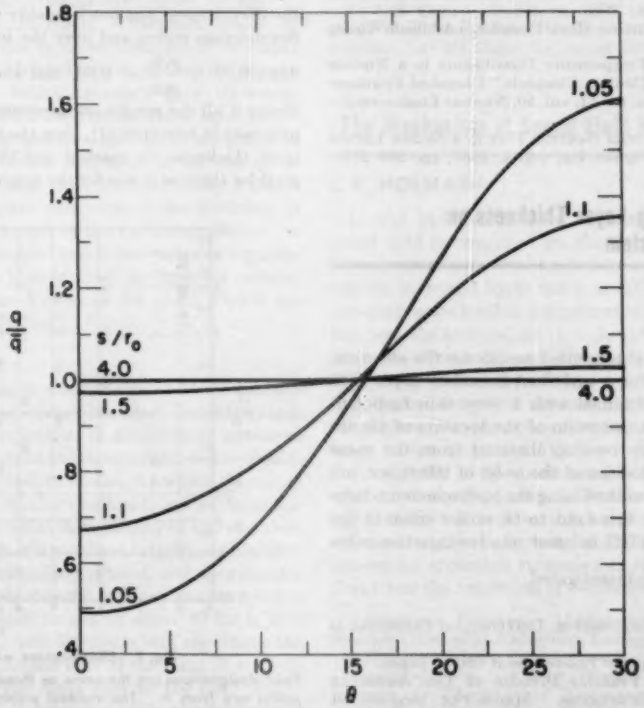

Fig. 4 Local wall heat flux distribution for triangular cooling arrangement

perature for the square array always exceeds that for the triangular array.

For the triangular array, the results of Fig. 3 may be represented within 0.8 per cent for $s/r_0 \geqslant 1.3$ (within 0.1 per cent for $s/r_0 \geqslant 1.5$) by the expression

$$\frac{T_M - T_0}{(Q/k)s^2} = \frac{\sqrt{3}}{\pi} \ln \frac{s}{r_0} + 0.25 \left(\frac{r_0}{s}\right)^2 - 0.23446 \qquad (4)$$

For the square array, a representation which applies to within 0.3 per cent for $s/r_0 \geqslant 1.5$ is

$$\frac{T_M - T_0}{(Q/k)s^2} = \frac{2}{\pi} \ln \frac{s}{r_0} + 0.25 \left(\frac{r_0}{s}\right)^2 - 0.17352 \qquad (5)$$

A final result of interest is the distribution of the local heat flux q per unit area around the periphery of the cooling passage. This information, obtained by applying Fourier's law ($q = -k\partial T/\partial r$) to equations (2) and (3), is plotted in Figs. 4 and 5. For the triangular array, it is seen from Fig. 4 that the local heat flux is essentially uniform around the periphery of the cooling passage for spacings s/r_0 as low as 1.5. Significant nonuniformities occur only for smaller spacings. For the square array, the nonuniformities begin to appear at somewhat larger spacings and are larger for any given spacing. But even at $s/r_0 = 1.5$, q varies by only ±12 per cent around the mean. So, except for the smaller spacings, uniform peripheral wall temperature and uniform peripheral wall heat flux are almost identical.

To give perspective to these results, it should be remembered that for a given total cross-sectional area (solid plus cooling passages) and a fixed s/r_0, more of the area is occupied by solid when the holes are in square array.

References

1 E. M. Sparrow, "Temperature Distribution in an Internally Cooled, Heat-Generating Solid," ASME paper No. 60—SA-15.

2 F. A. Fend, E. M. Baroody, and J. C. Bell, Battelle Memorial Institute report T-42, October, 1950.

3 P. J. Schneider, "Conduction Heat Transfer," Addison-Wesley Book Co., 1955, pp. 206–212.

4 P. B. Richards, "The Temperature Distribution in a Nuclear Reactor Pierced by Circular Cooling Channels," Chemical Engineering Progress Symposium Series, no. 11, vol. 50, Nuclear Engineering—Part I, 1954, pp. 127–133.

5 E. R. Cohen, "The Thermal Neutron Flux in a Square Lattice Cell," *Nuclear Science and Engineering*, vol. 1, 1956, pp. 268–279.

Effects of Initial Boundary-Layer Thickness on a Tangential Injection System

R. A. SEBAN[1]

Introduction

A RECENT PUBLICATION[1][2] presented results for the effectiveness and the heat transfer for a turbulent boundary layer with tangential fluid injection, obtained with a very thin turbulent boundary layer existing just upstream of the location of the injection slot. Supplementary results, obtained from the same system, with free-stream velocities of the order of 100 ft/sec, are given here to show the effect of increasing the upstream boundary-layer thickness. The effect turns out to be rather small in the range of slot sizes, 0.25 to 0.063 in., and relative injection rates $0.25 < \frac{\rho_s u_s}{\rho_1 u_1} < 0.80$, that were investigated.

[1] Professor of Mechanical Engineering, University of California at Berkeley, Calif. Mem. ASME.

[2] Numbers in brackets designate References at end of paper.

Contributed by the Heat Transfer Division of THE AMERICAN SOCIETY OF MECHANICAL ENGINEERS. Manuscript received at ASME Headquarters, June 27, 1960.

The increased boundary-layer thicknesses were obtained by the attachment of a 2 ft long section upstream of the test surface, the nozzle thus being moved upstream this distance, and the use of sandpaper roughness at the downstream end of the nozzle. With this arrangement the layer thicknesses just upstream of the slot were of the order of 0.60 in., with the velocity profiles having the nature accepted for turbulent flows. In contrast, the configuration for which the original results were reported provided layer thicknesses of the order of 0.06 in. This tenfold thickening of the layer produced, for the present results, ratios of layer thickness to slot height from $0.60/0.25 \cong 2.4$ to $0.60/0.063 \cong 10$.

These ratios are of a different order than those for which Chin [2] reported the effect of initial boundary-layer thickness on the effectiveness. Direct comparison is further impaired because Chin obtained larger values of the effectiveness with greater boundary-layer thicknesses $\left(\frac{\delta}{s} \approx \frac{0.80}{0.11} \approx 8\right)$ than were obtained with the present system with thinner initial boundary layers.

Effectiveness

When the system was operated with the thick boundary layer at the slot, and with a 0.25-in. slot, there was but a minor reduction in the effectiveness at large distances downstream. A greater reduction existed with a 0.125-in. slot, and with the 0.063-in. slot [$\delta/s \approx 10$] the results were those shown in Fig.1. There the reduction is about 20 per cent at 300 slot heights downstream. But the local influence of initial boundary-layer thickness is complicated; at intermediate distances the effectiveness is increased slightly and the final reduction is attained by a more rapid decay at large distances. (In terms of the power law regime specified in reference [1], the results for larger boundary-layer thickness would require a larger negative exponent for the dependence on the distance x, downstream of the slot, and a greater initial distance $(x/s)_i$.)

Despite the maximum diminution of 20 per cent the change in the effectiveness was much smaller when averaged over the whole downstream region and over the investigated range of injection flows $0.25 < \frac{\rho_s u_s}{\rho_1 u_1} < 0.80$, and slot heights $0.063 < s < 0.25$. Hence if all the results are presented in terms of the correlation proposed in reference [1], then the effects of increased boundary-layer thickness are masked and the correlation of results is as good for these as it was for the original results.

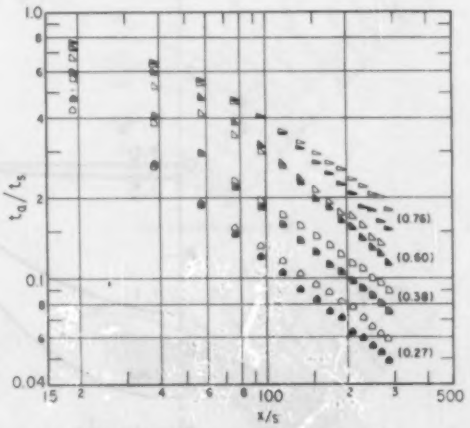

Fig. 1 Effectiveness with 0.063 in. slot

Point designations are the same as those of reference [1] and the open points are from it. The shaded points are for the thicker boundary layer. Mass velocity ratios are indicated by numbers next to the curves.

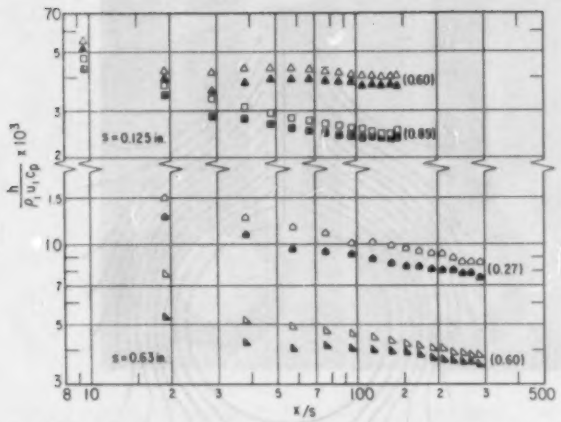

Fig. 2 Heat transfer with thin and thick boundary layers. Slot sizes and velocity ratios are indicated in the figure; open points are original runs of reference [1].

Chin [2], by operation of his system with thicker initial boundary layers, $\delta/s \approx 20$, produced reductions in the effectiveness of 30 per cent at $x/s = 200$, with lesser reduction at shorter distances. No direct comparison is possible because of the differences in δ/s and because Chin's results with a thinner boundary layer were above those obtained from the present system. It is interesting to note, however, that his results for the thicker layer were about the same as those for the present system with a thin layer.

Heat Transfer

As for the effectiveness, an increase in the upstream boundary-layer thickness produces a slight decrease in the heat-transfer coefficient. This was not examined as extensively as was the effectiveness, but some typical results are shown in Fig. 2. These show a reduction over the whole downstream length, so that even the final values do not agree with the prediction from the Colburn equation based on heated length, as they did for the values obtained with small initial boundary-layer thickness. This implies the production, with the greater initial layer thickness, of an effective upstream length great enough to be significant in the context of the kind of results that apply in the case of an unheated starting length. In that case, if the initial layer thickness is not too great, an effective prediction of the coefficient is possible by using the heated length in the usual formulation for that coefficient. But if the unheated length becomes much greater than the heated one then the heat-transfer coefficient is reduced primarily because of the reduced shear at the wall. This is apparently the effect that is indicated in Fig. 2.

Discussion

The relatively small changes in effectiveness and heat transfer produced by the increase in upstream boundary-layer thickness might be considered as an indication of a relatively unaltered hydrodynamic behavior. Such an inference might well be associated with the operation with the 0.25 in. slot, for which the values of the effectiveness were practically unaltered, but examination of that case shows that the relative invariability of the effectiveness arises from the interaction of a number of significant changes. The velocity profiles were substantially altered, and approximate similarity on a power law basis was not attained until a relative distance of $x/s > 60$, compared to one of about 40 for a thin boundary layer. In contrast, with adiabatic wall conditions the temperature profiles at all locations were of the form $[t = t_a \exp(-ky^2)]$ and were similar even quite close to the slot. Fig. 3 gives a qualitative view of the situation by showing hydrodynamic

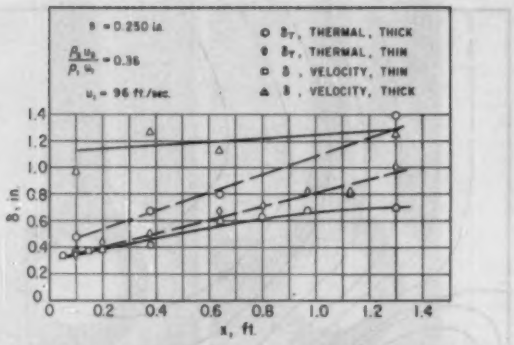

Fig. 3 Hydrodynamic and thermal boundary-layer thicknesses. Operating conditions are indicated in the figure.

and thermal boundary-layer thicknesses, and it shows for the latter case the greater hydrodynamic boundary-layer thickness that is expected. The thermal layer grows more rapidly when the hydrodynamic layer is thicker, and the surprising invariability of the effectiveness results from the lower velocities, near the wall, that are associated with the thicker hydrodynamic layer. It is remarkable that the two effects are in such proportion. When the slot size is reduced, this relation apparently fails, but only at large distances downstream of the slot.

Acknowledgment

The research from which these results were derived was supported by the National Science Foundation by Grant 4631.

References

1 R. A. Seban, "Heat Transfer and Effectiveness for a Turbulent Boundary Layer With Tangential Fluid Injection," published in this issue, pp. 303-312.

2 J. H. Chin, S. C. Skirvin, L. E. Hayes, and A. H. Silver, "Adiabatic Wall Temperature Downstream of a Single, Tangential Injection Slot," ASME Paper No. 58—A-107.

The Mechanism of Sound Field Effects on Heat Transfer

J. P. HOLMAN[1]

IT HAS BEEN determined experimentally that when a strong sound field is impressed on the free convection boundary-layer flow about a horizontal heated cylinder, the heat-transfer rates may be increased by as much as 300 per cent depending on the sound pressure level and temperature difference between the surface and the ambient air [1, 2, 3, 4].[2] This note will seek to explain this effect in terms of the interaction of acoustical streaming with the boundary-layer flow.

A typical acoustical streaming system is shown in Fig. 1 and the typical free convection flow field may be seen in Fig. 2. The inner vortex system of Fig. 1 is called the d-c boundary layer. For a cylinder of $^3/_4$ in. diameter it is only about 0.001 in. thick when air is the fluid used. The theory for the acoustical streaming flow field is well established for the case of the adiabatic cylinder, i.e., no heat transfer [5, 6, 7]. The important point concerning acoustical streaming as it pertains to heat transfer is that when the amplitude of oscillation of the sound field is raised

[1] Associate Professor, Mechanical Engineering Department, Southern Methodist University, Dallas, Texas.

[2] Numbers in brackets designate References at end of paper.

Contributed by the Heat Transfer Division of THE AMERICAN SOCIETY OF MECHANICAL ENGINEERS. Manuscript received at ASME Headquarters, May 23, 1960.

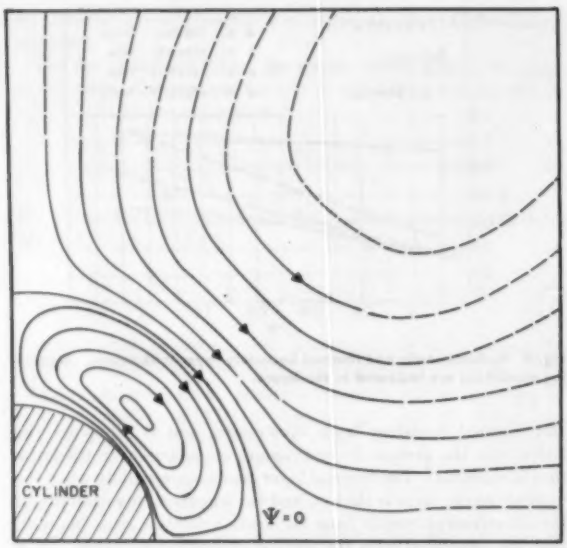

Fig. 1 A typical acoustical streaming flow field

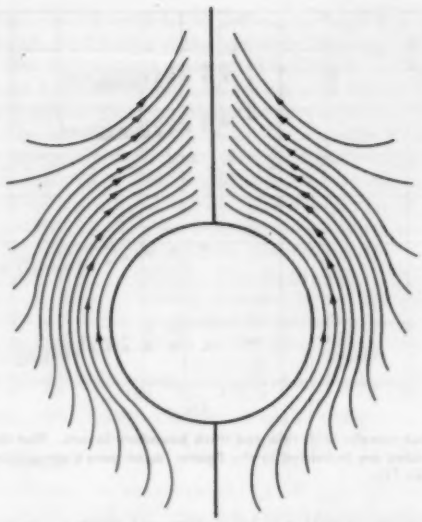

Fig. 2 A typical convection flow field around a horizontal cylinder

above a certain critical value the streaming patterns become intensified and deviate from theory. An intense churning action is observed and at sufficiently high amplitudes the d-c boundary layer collapses entirely.

For low intensity sound waves the acoustical streaming velocities are very small (of the order of 0.1 in./sec) and no effect on heat transfer would be expected. When the amplitude of the sound field is raised above the critical value it would be expected that the heat-transfer rates would be increased for the following reasons:

1 The churning action of the d-c vortex system would introduce an eddy conductivity effect very close to the heat-transfer surface and thereby increase the heat-transfer rate.

2 The higher streaming velocities of the outer system of Fig. 1 when added to the free convection field of Fig. 2 would produce a flow separation and a circulatory or vortex-shedding motion on the upper side of the cylinder. Accompanying this flow separation would be increased turbulence which would also tend to increase the heat-transfer rate.

3 The higher streaming velocities of the outer system of Fig. 1 will add to the free-convection boundary-layer velocities in the lower quadrants of the cylinder, thereby producing higher heat-transfer rates due to the increased energy transport. Correspondingly, it would be expected that the thickness of the thermal boundary layer would be reduced on the lower side of the cylinder.

4 The percentage increase in heat transfer over the value for no-sound should be markedly dependent on the temperature difference between the surface and the ambient air. It would be expected that the largest percentage changes in the heat-transfer coefficient would be observed for large temperature differences with the effect becoming less pronounced as the temperature difference is decreased. This is expected because the boundary layer is more easily disturbed when the temperature difference is large and it is easier for eddy motions to be generated. The experimental results of Fand and Kaye [3] show the expected temperature dependence.

5 Identical results should be obtained for a vibrating cylinder in an ambient environment as for a sound field impressed on a stationary cylinder. It may be noted that the streaming patterns will be different depending on whether the cylinder is vibrated in a vertical or horizontal direction. For a horizontal vibration the patterns would be like Fig. 1, while vertical oscillations would produce streaming currents in just the opposite direction. Thus one would not expect the vortex patterns or flow separation effect to exist on the upper side of the cylinder when the oscillatory motion is in the vertical direction. Some recent preliminary results of Fand and Kaye [8] verify this expectation.

Some shadowgraph pictures of the free convection flow around a horizontal cylinder under the influence of a strong progressive sound field are shown in Fig. 3. In these photographs the sound field moves from right to left. The boundary-layer flow is unaffected until the critical sound pressure level is attained. At higher intensities, a rather distinct flow separation process is observed and a vortex shedding motion was observed in the motion pictures of the flow processes, in agreement with the discussion in paragraph number two of this paper. This type of vortex shedding was also observed by Fand and Kaye [3] using smoke.

Measurements of the boundary-layer thickness at the stagnation point in shadowgraphs like those of Fig. 3 show that the thickness is reduced for all frequencies between 1000 cps and 5000 cps when the critical sound pressure level is exceeded. A larger reduction is observed for low frequencies than for high frequencies. However, the measurements at the higher frequencies were influenced by spherical wave fronts so that the frequency effect was partially obscured. Nevertheless, the boundary-layer thickness is markedly reduced by as much as 50 per cent and this fact is believed to corroborate the qualitative analysis in paragraph number three above.

Westervelt [9] has recently made some analytical estimates of the critical sound pressure level. The criterion

$$S/\delta_{As} \simeq 1 \tag{1}$$

was used; where S is the amplitude of the sound field and δ_{As} is the a-c boundary-layer thickness defined by

$$\delta_{As} \equiv \sqrt{\nu/\omega} \tag{2}$$

ν is the kinematic viscosity and ω is the circular frequency of the sound wave. The a-c boundary-layer thickness has the physical significance of a viscous-wave influence distance. The criterion in (1) specifies the point where the d-c boundary-layer thickness becomes functionally dependent on the amplitude and the in-

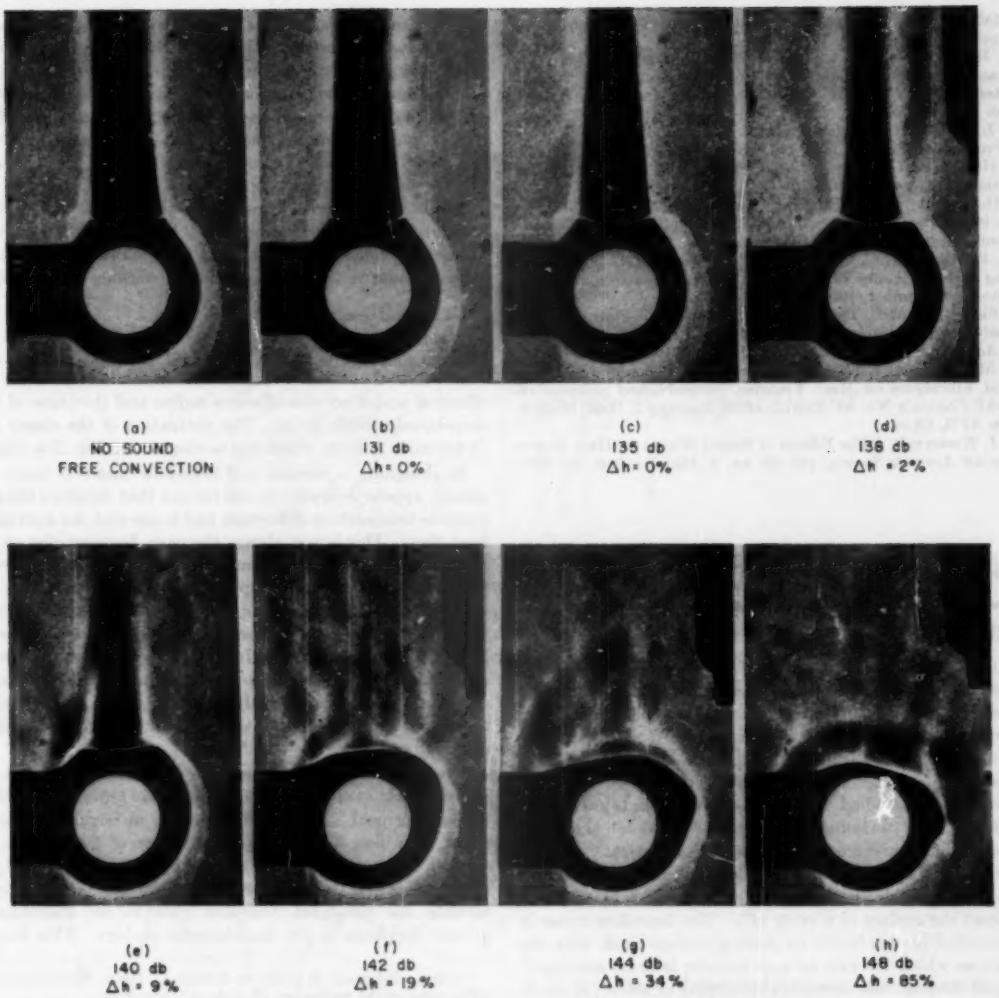

Fig. 3 Effect of sound pressure level on free convection boundary layer
1660 cps, $T_w - T_a = 152$ deg F
$Gr_f \sim 3 \times 10^4$

tensification mentioned above begins at this point. The criterion may be expressed in terms of sound pressure level as

$$\text{S.P.L.} = 136 + 10 \log F \quad \text{decibels} \qquad (3)$$

where F is in kilocycles. The accompanying table shows comparisons of this relation with the experiments of Sprott, Holman, and Durand [4]. The agreement is good. The relation does not predict the frequency effect but this is believed to be influenced strongly by the diameter of the cylinder. The effect of cylinder diameter was not included in the derivation of equation (3). Also, the accuracy of the experimental data is probably of the order of ±2 db so that the specific frequency dependence could easily be obscured.

Comparison of critical sound pressure levels with equation (3)

Frequency cps	Equation (3)	Experimental values
1000	136 decibels	134 decibels
1660	138	137
2720	140	135
3220	141	135
3720	141.7	138
4220	142.2	134
5000	143	135

In view of the many points of agreement of the qualitative analysis with experimental data, it seems reasonable to accept its validity. At the time that acoustical streaming was first proposed to be the cause of the increased heat-transfer rates (reference [2]) the experimental data available were not conclusive. Subsequent data which have been obtained point to this physical mechanism as the correct one.

Acknowledgment

The author wishes to thank Mr. Erich Soehngen for discussing this problem with him at some length.

References

1 P. N. Kubanskii, "Effects of Acoustic Vibrations of Finite Amplitude on the Boundary Layer," *Zhurnal Technich Eskoi Fiziki*, vol. 22, 1953, pp. 585–592.

2 J. P. Holman and T. P. Mott-Smith, "The Effects of Constant-Pressure Sound Fields on Free Convection Heat Transfer From a

Horizontal Cylinder," *Journal of the Aero/Space Sciences*, vol. 26, no. 3, 1959, pp. 188–189.

3 R. M. Fand and J. Kaye, "The Effect of High Intensity Stationary and Progressive Sound Fields on Free Convection From a Horizontal Cylinder," WADC Tech. Note 59-18, May, 1959, Wright-Patterson AFB, Ohio.

4 A. L. Sprott, J. P. Holman, and F. L. Durand, "The Effects of Strong Progressive Sound Fields on Free Convection Heat Transfer From a Horizontal Cylinder," WADC Tech. Rpt. 59-717, October, 1959, Wright-Patterson AFB, Ohio.

5 J. Holtsmark, et al., "Boundary Layer Flow Near a Cylindrical Obstacle in an Oscillating Incompressible Fluid," *Journal Acoustic Society*, vol. 26, no. 1, January, 1954, pp. 26–39.

6 W. P. Raney, J. C. Corelli, and P. J. Westervelt, "Acoustical Streaming in the Vicinity of a Cylinder," *Journal Acoustic Society*, vol. 26, no. 6, November, 1954, pp. 1006–1014.

7 S. Skavelm and S. Tjotta, "Steady Rotational Flow of an Incompressible Fluid Enclosed Between Two Coaxial Cylinders," *Journal Acoustic Society*, vol. 27, no. 1, January, 1955, pp. 26–33.

8 R. M. Fand and J. Kaye, "The Influence of Sound Fields and Acoustical Vibrations on Heat Transfer," unpublished progress report, USAF Contract No. AF 33(616)-6076, January 1, 1960, Wright-Patterson AFB, Ohio.

9 P. J. Westervelt, "The Effects of Sound Waves on Heat Transfer," *Journal Acoustic Society*, vol. 32, no. 3, March, 1960, pp. 337–338.

A Transducer for the Measurement of Heat-Flow Rate

ROBERT GARDON[1]

IT IS OFTEN REQUIRED to measure the rate of heat transfer across the surface of a solid. In some applications it may also be desired that the measuring instrument be small, in order that the measured heat-transfer rate can be associated with some particular location on the surface, and that the instrument have a rapid response, in order that temporal variations of the heat-transfer rate can be studied. Both these requirements are met by an adaptation of a transducer originally devised for the rapid measurement of high intensities of thermal radiation.[2]

The principle of operation of what might be called the "circular foil heat-flow meter" is illustrated in Fig. 1. Heat is being transferred across the surface of a body (P). The heat-flow meter is shown mounted in this body, its sensing surface flush with the surface across which the rate of heat transfer is to be measured. The body of the heat-flow meter is a small plug or screw (B) made of copper It has a small central hole which is closed off by a circular foil of constantan (F). The dimensions of the heat-flow meter are such that, for all practical purposes, it is always in thermal equilibrium with the body in which it is mounted. When the surface of the body loses heat, the heat lost from the foil F is replaced by a radial flow of heat from the body into the foil. As a result of this radial heat flow, the center of the foil assumes a temperature sl tly lower than that of its circumference. The resulting radial temperature distribution in the foil is schematically shown in Fig. 1. (Similar considerations apply for heat flow in the opposite direction, which entails an elevation of the central temperature of the foil.) The temperature difference ΔT_m between the center and circumference of the foil can be related to the rate of heat loss from the foil, and it can readily be measured by attaching a thin copper wire (W) to the center of the foil. Thus a thermocouple is obtained—consisting of the copper wire, constantan foil and copper body—which directly measures the temperature difference of interest. By a favorable coincidence, variations with temperature in the thermal conductivity of constantan and in the thermoelectric power of copper-constantan thermocouples are such as to produce a linear heat-flow rate versus emf relation for circular foil heat-flow meters made of these two materials.[2] Also, the sensitivity of such instruments is independent of their temperature.

Mechanically these transducers differ from the circular foil radiometers described in footnote 2 by their miniaturization and all-metallic construction, which permit their installation in various objects under test.[2] The equations governing their performance are:

$$\text{Sensitivity} = E/q = 0.183\ R^2/S\ [mv/(\text{cal/cm}^2\cdot\text{sec})]$$
$$\text{Time constant} = \tau = 3.7\ R^2\ [\text{sec}]$$

where R and S are the effective radius and thickness of the foil, respectively, both in cm. The derivation of the above is given in footnote 2, from which the nomogram of Fig. 2 is also taken.

In designing a circular foil heat-flow meter it may, at first glance, appear desirable to aim for one that develops the greatest possible temperature difference, and hence emf, for a given rate of heat flow. This is not always the case, however, for an unduly large depression (or elevation) of the central temperature of the foil would disturb the temperature distribution of the surface under study. In other words, ΔT_m must be kept small in relation to ΔT, the temperature difference that is the driving force for the heat transfer under study. In some instances it may therefore be advantageous to design a relatively insensitive transducer, i.e., one that generates a relatively small ΔT_m for a given rate of heat flow, and to make up for this by suitably amplifying its small electrical output.

The instrument differs from other heat-flow transducers in that it is mounted *in* the body under study, *not between* the two media exchanging heat. Its use thus entails no significant series resistance to heat flow and no disturbance of fluid flow over the surface under study. This makes it especially valuable for the study of convective heat-transfer coefficients. Its small size permits the measured heat-flow rate to be associated with definite locations on the heat-transfer surface. This is of value

[2] Acknowledgment is made to Arthur C. Ruge Associates for their refinement of the technique of making these units.

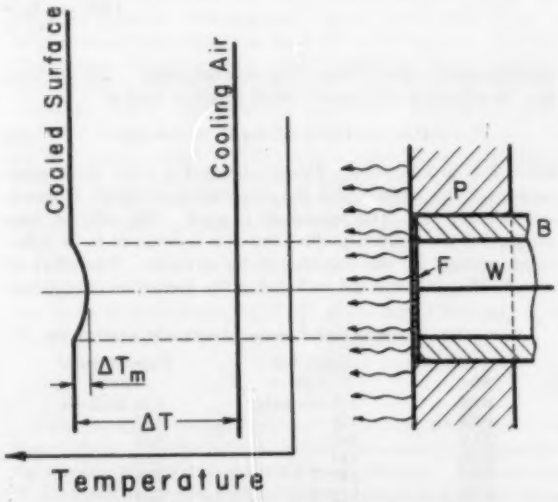

Fig. 1 Principle of operation of heat-flow meter

[1] Senior Group Leader, Basic Engineering Research, Glass Research Center, Pittsburgh Plate Glass Co., Pittsburgh, Pa. Mem. ASME.

[2] R. Gardon, "An Instrument for the Direct Measurement of Intense Thermal Radiation," *Review of Scientific Instruments*, vol. 24, 1953, pp. 366–370.

Contributed by the Heat Transfer Division of THE AMERICAN SOCIETY OF MECHANICAL ENGINEERS. Manuscript received at ASME Headquarters, June 9, 1960.

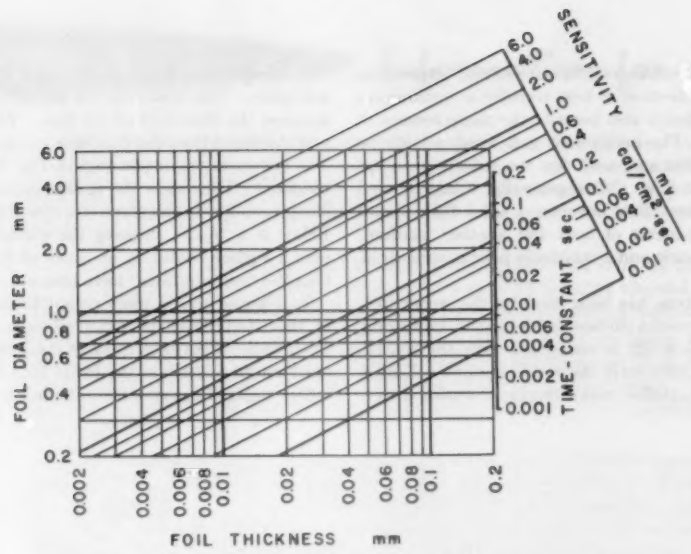

Fig. 2 Chart for design of copper-constantan circular foil heat-flow meters

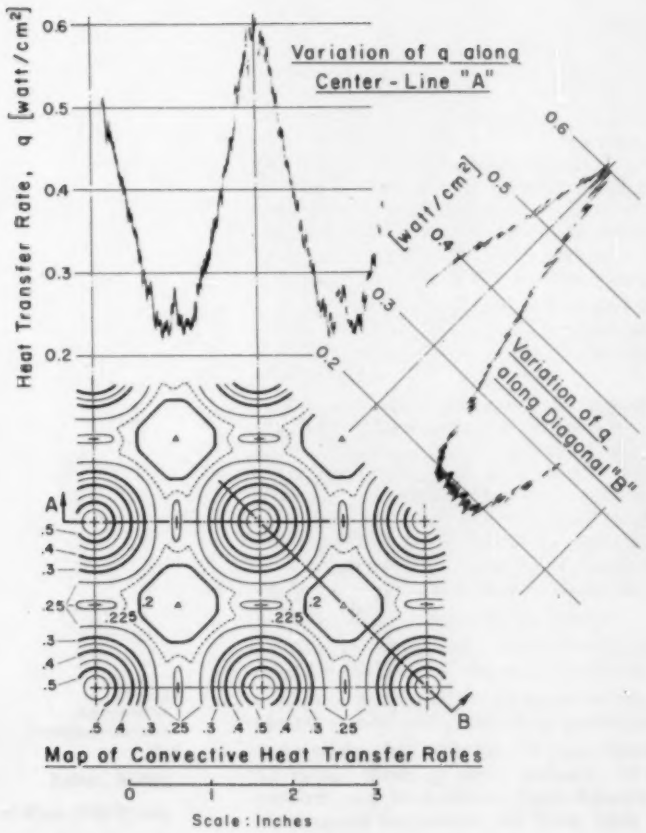

Fig. 3 Variation of local convective heat-transfer rates

Maxima in heat-transfer rate occur opposite the centers of nozzles and are shown thus +
Minima shown thus Δ
Lines of constant heat-flow rate marked in watt/cm²
Conditions:

Nozzles:	1/8 in. diam × 4 in. long
Arrangement:	Nozzles laid out on a square pitch at 2 in. centers
	Nozzle exits distant 3 in. from hot plate
Temperature of hot plate:	19.2 deg C above ambient air
Air rate:	150 lb/hr·ft² of hot plate

where spatial variations in heat-transfer rate are of interest, as in the study of entrance effects or of heat transfer in nonuniform flow fields. Its rapid response also permits the measurement of heat-transfer transients. The instrument can most readily be mounted in metallic bodies and used for the measurement of convective or radiant heat flow. More generally, it can be used to measure the rate of heat flow between a solid that should preferably be a good conductor of heat and another medium, solid or fluid, that is dielectric and a relatively poor conductor of heat.

An instrument of this type has been used by the writer in a study of heat transfer between a surface and jets of air impinging on it. In particular, this study is concerned with the spatial variation of heat-transfer rates over the cooled surface. This is measured by means of a heat-flow meter having a sensing area 1 mm in diameter, which is mounted in the center of an electric hot plate. The plate can be moved in its own plane so as to traverse the flow field of the jets. The movement of the plate and the signal from the heat-flow meter are fed to an x-y recorder. The curves in the upper part of Fig. 3 are typical of the results obtained. They show the spatial variation of heat-transfer rates along (*a*) a line in the plane of a row of nozzles and (*b*) a diagonal. Below is a "map" showing the variation of heat-transfer rates over a surface cooled by an array of jets, idealized to the extent that the "contour lines" have been smoothed.

It is hoped that a more comprehensive account of the results of this study may be rendered in a forthcoming publication. Meanwhile, it is the purpose of this brief to describe the circular foil heat-flow meter in the belief that this may be of interest to others engaged in experimental studies of heat transfer.

Journal of HEAT TRANSFER

Information for Authors

• Manuscripts should be submitted in final form to the Editor. Each manuscript must be accompanied by a statement that it has not been published elsewhere nor has it been submitted for publication elsewhere. A paper which would occupy more than 8 pages of the Journal may be returned to the author for abridgment.

• The author should state his business connection, the title of his position, and his mailing address. A short abstract (50 to 100 words) should be included on the first page immediately preceding the introductory paragraph of the paper.

Three copies of the manuscript are required. One of these must be a carefully prepared printer's copy, typed in double spacing, on one side of the page only, with wide margins, on $8^1/_2$ by 11-in. opaque white paper. Mimeographed manuscripts, if prepared with exceptional care, can be accepted provided they are completely edited.

• As far as possible, all mathematical expressions should be typewritten. Greek letters and other symbols not available on the typewriter should be carefully inserted in ink. Care should be taken to distinguish between capital and lowercase letter, between zero (0) and the letter (*O*), between the numeral (1) and the letter (*l*), etc. A letter representing a vector cannot be printed with an arrow above or below it. The letter should be underscored with a single wavy line, wherever it appears in the text, to designate boldface type.

• A list of symbols carefully marked for the use of the editor (thus: κ, Greek l.c. kappa), if it has not been included in the body of the paper, should accompany the manuscript on a separate page.

• Before preparing a manuscript the author should study printed articles in the Journal, with special attention to the form and style of mathematical expressions, tables, footnotes, references, and abstract. Numbers that identify mathematical expressions should be enclosed in parentheses. Numbers that identify references at the end of the paper should be enclosed in brackets. Care should be taken to arrange all tables and mathematical expressions in such a way that they will fit into a single column when set in type. Equations that might extend beyond the width of one column (fractions that should not be broken or long expressions enclosed in parentheses) should be rephrased to go on two or more lines within column width. Fractional powers are preferred to root signs and should always be used in more elaborate formulas. The solidus should be used instead of the horizontal line for fractions wherever possible.

• A normal paper should not exceed 8 pages in the Journal. It is about 8000 words or 20 double-spaced typewritten pages exclusive of drawings. A Technical Brief should not exceed 750 words or about one page in the Journal inclusive of drawings.

• Originals and two copies of figures must accompany the manuscript. Line drawings should not be larger than $8^1/_2 \times 11$ in. and should be planned for reduction to column width. Lettering should be large enough to be clearly legible when the illustration is reduced. The originals of line drawings must be in India ink on white or pale blue tracing paper or tracing cloth. Photographs of equipment or test specimens must be glossy prints and should be used sparingly. Captions for figures should be typed double-spaced and included as the last page of the manuscript. The figure number and author's name should be written in the margin or on the back of each illustration.

• Titles of papers should be brief.

• Authors can obtain copies of the ASME Manual MS-4, "An ASME Paper," from the Editor and are urged to do so before drafting their papers in final form.

• Papers published in Journals of the Transactions of the ASME must be presented at a Meeting, either in person or by title.

• An author is entitled to 25 preprints free of charge (in the case of two authors, 15 each; three or more authors, 10 each). Larger quantities of preprints or reprints can be ordered from Editorial Department, The American Society of Mechanical Engineers, 29 West 39th Street, New York 18, N. Y. Quotations will be sent on request.

Please address all communications to:

Editor, ASME,

29 West 39th Street,

New York 18, N. Y.

ASME Publications Committee